DOKUZ EYLÜL UNIVERSITY

GRADUATE SCHOOL OF NATURAL AND
APPLIED SCIENCES

STRATIGRAPHY, TECTONIC EVOLUTION AND PETROGENESIS OF THE VOLCANIC ROCKS IN THE GÖRDES, DEMİRCİ AND EMET BASINS (WESTERN ANATOLIA)

by

E. Yalçın ERSOY

October, 2011

İZMİR

STRATIGRAPHY, TECTONIC EVOLUTION AND PETROGENESIS OF THE VOLCANIC ROCKS IN THE GÖRDES, DEMİRCİ AND EMET BASINS (WESTERN ANATOLIA)

A Thesis Submitted to the
Graduate School of Natural and Applied Sciences of Dokuz Eylül University
In Partial Fulfillment of the Requirements for the Degree of Doctor of
Philosophy in Geological Engineering, Economic Geology Program

by
E. Yalçın ERSOY

October, 2011
İZMİR

Ph.D. THESIS EXAMINATION RESULT FORM

We have read the thesis entitled **"STRATIGRAPHY, TECTONIC EVOLUTION AND PETROGENESIS OF THE VOLCANIC ROCKS IN THE GÖRDES, DEMİRCİ AND EMET BASINS, WESTERN ANATOLIA"** completed by **EMRAH YALÇIN ERSOY** under supervision of **PROF. DR. CAHİT HELVACI** and we certify that in our opinion it is fully adequate, in scope and in quality, as a thesis for the degree of Doctor of Philosophy.

Prof. Dr. Cahit HELVACI
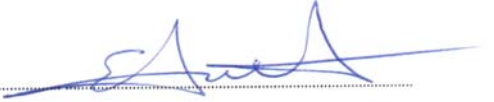
Supervisor

Prof. Dr. Uğur İNCİ

Thesis Committee Member

Prof. Dr. KADİR YURDAKOÇ

Thesis Committee Member

Prof. Dr. Osman CANDAN

Examining Committee Member
Member

Doç. Dr. Ercan ALDANMAZ

Examining Committee

Prof. Dr. Mustafa SABUNCU
Director
Graduate School of Natural and Applied Sciences

ii

ACKNOWLEDGMENTS

STRATIGRAPHY, TECTONIC EVOLUTION AND PETROGENESIS OF THE VOLCANIC ROCKS IN THE GÖRDES, DEMİRCİ AND EMET BASINS (WESTERN ANATOLIA)

ABSTRACT

New stratigraphic, structural, geochemical (whole rock major and trace elements, and Sr, Nd, Pb and O isotopes) and Ar/Ar age data from the NE–SW-trending Gördes, Demirci and Emet basins are presented. The data show that the different types of extensional to transtensional basins were superimposed, and they were all developed under N–S-directed extension as the Menderes Massif is episodically exhumed as a core complex.

The early-middle Miocene volcanic rocks are classified as high-K calc-alkaline (felsic), and shoshonitic and ultrapotassic (mafic), with the late Miocene basalts being transitional between the early-middle Miocene volcanites and the Na-alkaline Quaternary Kula volcanites (QKV). The geochemical characteristics of the most primitive rocks indicate that (1) early-middle Miocene volcanic rocks were derived from a Primitive Mantle-like mantle source underwent to enrichment processes, (2) the mantle source of these rocks was distinct from those of the Eocene volcanic rocks located further north, and of the other volcanic provinces in the region. The mantle source of the shoshonitic and ultrapotassic mafic volcanic rocks was influenced by enrichment processes related to subduction and "multi-stage melting and melt percolation" processes in the lithospheric mantle. The influence of the latter event increases from west to east. Geochemical features of the high-K calc-alkali felsic rocks indicate that they were derived mainly from lower continental crustal melts which then mixed with mantle-derived lavas. These rocks then underwent differentiation from andesites to rhyolites via nearly pure fractional crystallization processes in the upper crust.

Keywords: Western Anatolia; NE-SW-trending basins; Neogene volcanism; magmatic petrogenesis; core complex

GÖRDES, DEMİRCİ VE EMET HAVZALARINDAKİ (BATI ANADOLU) VOLKANİK KAYALARIN STRATİGRAFİSİ, TEKTONİK EVRİMİ VE PETROJENEZİ

ÖZ

KD-GB uzanımlı Gördes, Demirci ve Emet havzasından elde edilen yeni stratigrafik, yapısal, jeokimyasal (toplam kaya ana ve iz element, Sr, Nd, Pb ve O izotopları) ve Ar/Ar yaş verileri sunulmuştur. Veriler, farklı tiplerde genişlemeli ve transtensiyonal havza tiplerinin farklı evrelerde ve Menderes Masifi'nin çekirdek kompleksi şeklinde episodik olarak yüzeylemesi sırasında K-G yönlü genişlemeli tektonik rejim altında meydana geldiğini gösterir.

Erken-orta Miyosen volkanik kayaları yüksek-K kalk-alkali, şoşonitik ve ultrapotasik olarak sınıflanır. Geç Miyosen bazaltları erken-orta Miyosen volkanitleri ile Na-alkali Kuvaterner Kula volkanitleri (KKV) arasında geçişli jeokimyaya sahiptir. En ilksel kayaların jeokimyasal özellikleri; (1) erken-orta Miyosen volkanik kayalarının orijinal olarak İlksel Manto benzeri olan ve daha sonra zenginleşmiş olan bir manto kaynağından türediğini ve bu kayaların manto kaynağının, kuzeydeki Eosen volkanitlerinden ve çevredeki diğer volkanik kayalardan farklı olduğunu gösterir. Şoşonitik ve ultrapotasik mafik volkanik kayaların manto kaynağı yitim ilişkili ve litosferik manto içinde meydana gelen "çok evreli ergime ve ergiyik etkileşimi" işlevler ile zenginleşmiştir. Bu zenginleşmenin etkisi batıdan doğuya doğru artar. Yüksek-K, kalk-alkali feslik volkanik kayaların iz element özellikleri bunların başlıca alt kabuğun ergimesinden türeyen magmaların mantodan türeme magmalar ile karışarak oluştuklarını gösterir. Bu kayalar daha sonra üst kabuktaki ayrımlaşmalı kristalizasyon işlevleri ile andezitlerden riyolitlere evrilmiştir ve iki evreli petrojenetik evrime sahiptir.

Anahtar kelimeler: Batı Anadolu; KD-GB gidişli havzalar; Neojen volkanizması; magmatic petrojenez; çekirdek kompleksi

CONTENTS

CHAPTER ONE
INTRODUCTION

Igneous activity along converging plate margins is typically characterized by K-rich magmas with calc-alkaline to high-K affinities. Geochemical features of the igneous rocks in such geodynamic settings suggest that their origin involves a series of geochemical processes; including metasomatism of the mantle source by melts, and/or fluid fluxes from the descending slab (e.g., Pearce, 1982, 1983; Hawkesworth et al., 1991, 1995; Saunders et al., 1991; Turner et al., 1997, 1999; Elliot et al., 1997; Kelemen et al., 2004), variable degrees of melting of the metasomatized mantle (e.g., Pearce & Parkinson, 1993) and subsequent differentiation processes at shallower depths, such as magma mixing, assimilation and fractional crystallization. Magmatic rocks along post-collisional regions have also similar geochemical features which are mainly inherited from subduction related processes developed just before the collision, and include high-K calc-alkaline, shoshonitic and ultrapotassic rocks.

In the circum Mediterranean, several volcanic provinces host to post-collisional high-K calc-alkaline, shoshonitic and ultrapotassic rocks. The main volcanic regions are located in SE Spain (e.g., Benito et al., 1999; Turner et al., 1999; Coulon et al., 2002; Duggen et al., 2004, 2005; Seghedi et al., 2007), Central Italy (Roman Volcanic Province; e.g., Peccerillo, 1998; Di Battistini et al., 1998, 2001; Conticelli, 1998; Conticelli et al., 2002, 2009b; Boari et al., 2009), East European Alpine belt (including Dinarides) and Carpathian-Pannonian Region (e.g., Seghedi et al., 2001; Harangi et al., 2007; Cvetković et al., 2004a, b), Dinarides and Rhodopes (Alther et al., 2004; Marchev et al., 2004; Cvetković et al., 2004a, b; Prelević et al., 2004, 2005), and Aegean-Anatolia region (Yılmaz, 1989, Güleç, 1991; Ercan et al., 1996; Yılmaz et al., 1998; Keskin et al., 1998; Aldanmaz et al., 2000; Yılmaz et al., 2001; Pe-Piper & Piper, 2001; Parlak et al., 2001; Keskin, 2003; Alıcı-Şen et al., 2004; Innocenti et al., 2005; Tonarini et al., 2005; Alpaslan, 2007; Ersoy et al., 2008; Keskin et al., 2008; Pe-Piper & Piper, 2009; Dilek & Altunkaynak, 2010; Ersoy et al., 2010b) (Figure 1.1).

Figure 1.1 GoogleEarth view of Mediterranean area showing the locations of main Cenozoic igneous provinces. SES: SE Spain; MC: Massif Central; RVP: Roman Volcanic Province; DR: Dinarides; CPR: Carpathian-Pannonian Region; RH: Rhodopes; SAVA: South Aegean Volcanic Arc; WAVP: Western Anatolian Volcanic Province; GVP: Galatian Volcanic Province; CAVP: Central Anatolian Volcanic Province; EAVP: Eastern Anatolian Volcanic Province.

In the Cenozoic volcanic provinces, shown in Figure 1.1, the volcanic products are mainly high-K to shoshonitic calc-alkaline including basalts-andesites-dacites and rhyolites, which are accompanied by local occurrences of high-MgO shoshonitic to ultrapotassic rocks including lamproites (e.g., Ersoy et al., 2008, 2010b; Conticelli et al., 2009b; Prelević et al., 2010a, b; Tomassini et al., 2011). Among these, the high-MgO rocks are especially important as they serve their mantle source characteristics. Most striking features of these magmas are that (1) they have high compatible element contents such as Mg, Ni, Cr (i.e., they are relatively primitive); (2) they are anomalously enriched in fluid-compatible elements such as LILE (large ion lithophile elements) and LREE (light rare earth elements) over HFSE (high field strength elements); (3) they have anomalously enriched in radiogenic Sr and non-radiogenic Nd, even they have crustal Sr-Nd isotopic compositions.

In Aegean-Anatolia region that formed by subduction and collisional events between several continental blocks at the easternmost part of the Mediterranean, volcanic provinces have developed during the last ~50 Ma (Figure 1.2). The main

volcanic provinces in the Aegean-Anatolia region are, from west to east, (1) South Aegean Volcanic Arc (SAVA), that formed in response to active northward subduction along Hellenic trench (Buettner et al., 2005; Bailey et al., 2009); (2) Western Anatolian volcanic province including Aegean islands to the west (WAVP; Fytikas et al., 1984; Yılmaz, 1989, Güleç, 1991; Aldanmaz et al., 2000; Pe-Piper & Piper, 2001, 2007; Erkül et al., 2005b, Innocenti et al., 2005; Agostini et al., 2005, 2007, 2008; Altunkaynak & Genç, 2008; Dilek & Altunkaynak, 2009; Helvacı et al., 2009; Pe-Piper et al., 1995, 2002, 2009; Ersoy et al., 2008, 2010b); (3) N–S-trending Eskişehir-Afyon-Isparta volcanic area (EAIVA; Floyd et al., 1998; Alıcı et al., 1998; Francalanci et al., 2000; Çoban & Flower, 2006; Akal, 2008; Dilek & Altunkaynak, 2010; Elitok et al., 2010); (4) Galatian Volcanic Province (GVP; Wilson et al., 1997; Tankut et al., 1998; Koçyiğit et al., 2003); (5) Central Anatolian Volcanic Province including Konya area (CAVP; Temel et al., 1998; Yurtmen & Rowbotham, 2002; Alıcı-Şen et al., 2004; Alpaslan et al., 2006; Kürkçüoğlu 2010); (6) Eastern Anatolian Volcanic Province (EAVP; Buket & Temel, 1998; Yalçın et al., 1998; Yılmaz et al., 1998; Keskin, 2003; Alpaslan et al., 2005; Karaoğlu et al., 2005; Özdemir et al., 2006); and (7) Eocene magmatic belt throughout the northern Anatolia (Ercan et al., 1995, 1998; Altunkaynak, 2007; Altunkaynak & Genç, 2008; Keskin et al., 2008; Ustaömer et al., 2009) (Figure 1.2).

Western Anatolia is one of the best regions in the world in which to examine the origin and petrologic evolution of the post-collisional K-rich volcanic activity, as the region includes huge amount of high-K calc-alkaline to shoshonitic and locally developed high-MgO shoshonitic to ultrapotassic (sometimes lamproitic) volcanic rocks (Figure 1.1). The volcanism in the region mostly emplaced synchronously with the lacustrine deposition in Neogene extensional basins that developed on a basement including both metamorphic and non-metamorphic rocks. The NE–SW-trending basins in the region are the most famous among the Neogene extensional volcano-sedimentary basins. These basins were developed on lower- to mid-crustal metamorphic rocks of the Menderes Massif which widely accepted as an extensional core-complex exhumed synchronously with Neogene lacustrine deposition.
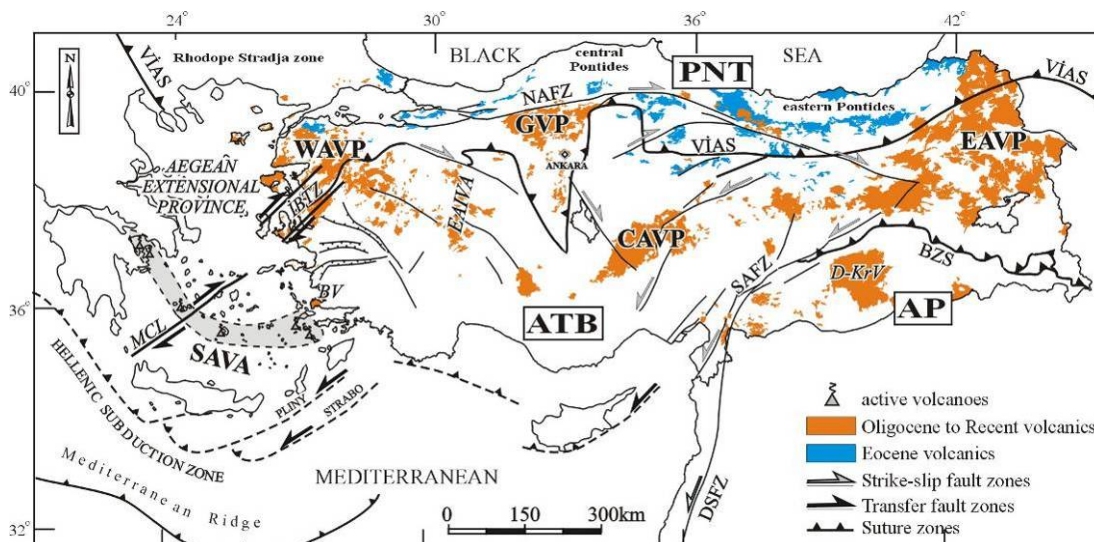
Figure 1.2 Tectonic map of Turkey showing distribution of Eocene to recent volcanic rocks in Turkey and Aegean (Modified from Geological Map of Turkey (1:500000), 2002). Major continental fragments: PNT–Pontides, ATB–Anatolia-Tauride Block, AP–Arabian Platform. Volcanic provinces: SAVA–South Aegean Volcanic Arc (~4–0 Ma), WAVP–Western Anatolian Volcanic Province (Eocene to recent), GVP–Galatian Volcanic Province (~22–9 Ma), CAVP–Central Anatolian Volcanic Province (late Miocene–Quaternary), Eastern Anatolian Volcanic Province (late Miocene–Quaternary), BV–Bodrum volcanites (~11 Ma); EAIVA–Eskişehir-Afyon-Isparta volcanic area (~23–5 Ma), KV–Konya volcanites (~20–18 Ma), DKrV–Diyarbakır-Karacadağ volcanites (Pliocene–Quaternary). Tectonic elements: VİAS–Vardar-İzmir-Ankara Suture, BZS–Bitlis-Zagros Suture, NAFZ–North Anatolian Fault Zone, SAFZ–South Anatolian Fault Zone, DSFZ–Dead Sea Fault Zone, MCL–Mid-Cycladic lineament, İBTZ–İzmir-Balıkesir Transfer Zone. MCL and İBTZ are from (Walcott & White, 1998; Pe-Piper et al., 2002; Uzel & Sözbilir, 2008).

1.1 Objectives of This Thesis

The late Cenozoic volcanic activity in western Anatolia, especially in NE–SW-trending Neogene basins, is closely associated with extensional basin formation and lacustrine deposition. In this respect, tectonic control over the volcanism must be evaluated in terms of the formation of these basins; the tectonic control on the volcano-sedimentary basins is a useful key to understand the geodynamic evolution of the region as a cause of magmatic activity. Hence, in addition to description and discussion of the geochemical features of the Neogene volcanic units, their stratigraphies have also been studied. The major objectives of this thesis are: (1) to document the Neogene stratigraphy of the NE–SW-trending volcano-sedimentary

basins and to correlate the volcano-sedimentary units in different basins; (2) to document the Neogene tectonic characteristics of the basins and to discuss their tectonic evolution in a regional scale and in terms of extensional exhumation of the Menderes Massif; (3) to describe the volcanic units in the study area, and correlate them on the basis of their stratigraphy and geochemical features; (4) to document the major and trace element compositions and Sr-Nd-O and Pb isotopic characteristics of the volcanic rocks; (5) to compare the geochemical features with the volcanic rocks in adjacent areas; (6) to define the petrologic evolution and the mantle source characteristics of the volcanic rocks; (7) to achieve a reasonable geodynamic evolution of the region.

1.2 Description of the Thesis

The thesis has been built on five chapters and three appendices:

Chapter I gives a general information about the aim and scope of the study. Also, tectonic framework of the region is described in this chapter.

Chapter II documents the Neogene stratigraphy of the NE–SW-trending basins. Neogene volcanic units are also described and correlated. Stratigraphic and tectonic correlation of the basins are given and discussed to reveal a tectonic model. The purposes of this chapter are; (1) to establish the depositional history of Miocene sedimentary and volcanic units in the NE–SW-trending Gördes, Demirci and Emet basins, (2) to show the structural relationships between the supra-detachment extensional basins and the transtensional basin formation on the basis of stratigraphic and structural criteria, and (3) compare the volcanic rocks in the basin fills, on the basis of their geochemical characteristics. Geochemical features of the volcanic rocks will be discussed in detail in the following sections. To accomplish this, 1/25000 scale geological maps of the key areas in these basins have been prepared and their volcano-sedimentary fills established. During the detailed mapping, the mesoscale faults that controlled and deformed the basin fill units have been investigated and defined on the basis of brittle and ductile features of the fault zones. The data from

this chapter has been published as *"Stratigraphic, structural and geochemical features of the NE-SW-trending Neogene volcano-sedimentary basins in western Anatolia: implications for associations of supradetachment and transtensional strike-slip basin formation in extensional tectonic setting"* in *Journal of Asian Earth Science (vol., 41, 159-183. doi: 10.1016/j.jseaes.2010.12.012)*.

Chapter III gives the whole rock geochemical data for the Neogene volcanic units. Petrogenetic model for felsic units have also been discussed in this chapter. In order to resolve some uncertainties in petrogenetic evolution of the Miocene volcanic rocks and to develop a better understanding of the geodynamic evolution of the region, it has been studied the isotope geochemistry ($\delta^{18}O$, Sr, Nd, and Pb) of the Miocene volcanic units in the NE-SW-trending Neogene basins, and compared our results with previously published data from the Northern Anatolian Eocene volcanites (NAEV), Quaternary Kula volcanites (QKV), Eskişehir-Afyon-Isparta volcanites (EAIV), Galatian volcanic province (GVP) and Saouth Aegean Volcanic Arc (SAVA). The data from this chapter has been published as *"Petrogenesis of the Neogene volcanic units in the NE-SW-trending basins in western Anatolia, Turkey"* in *Contribution to Mineralogy and Petrology* (*in press*; *doi: 10.1007/s00410-011-0679-3*).

Chapter IV gives the detailed geochemical features of the high-Mg potassic volcanic rocks in the NE–SW-trending basins, and compare them with the high-Mg potassic volcanic rocks located further west of the western Anatolian. A detailed petrogenetic model for the high-Mg potassic volcanic rocks is developed in this chapter. The data from this chapter has been published as "Mantle source characteristics and melting models for the early-middle Miocene mafic volcanism in Western Anatolia: implications for enrichment processes of mantle lithosphere and origin of K-rich volcanism in post-collisional settings" in *Journal of Volcanology and Geothermal Research* (*vol 198, 112-128. doi:10.1016/j.jvolgeores.2010.08.014*).

Chapter V discusses the general conclusions of this thesis coupling them with the previous studies. A general tectonic model for development of the NE–SW-trending basins and geodynamics for the Neogene volcanic rocks is developed.

Appendix 1 gives information on quantative modeling of fractional crystallization and contamination processes. This chapter has been published as "*FC-AFC-FCA and mixing modeler: a Microsoft® Excel© spreadsheet program for modeling geochemical differentiations of magma by crystal fractionations, crustal assimilation and mixing*" in *Computers and Geosciences* (*vol. 36, 383-390. doi:10.1016/j.cageo.2009.06.007*).

Appendix 2 gives analytical techniques of measurements of major-trace element contents and Sr, Sm-Nd, O and Pb isotopic compotisions.

Appendix 3 gives the major and trace element data of the volcanic rocks coupled with the some previously published analyses from the studied volcanic units.

1.3 An Overview of Tectonic Framework of Western Anatolia Region

The western Anatolia is the easternmost part of the Aegean orogenic belt. The region includes several continental blocks and suture zones and was shaped by Alpine orogeny related to Neo-Tethyan events (Figure 1.3) (e.g., Carey, 1958; Şengör & Yılmaz, 1981; Okay et al., 1996; Okay & Tüysüz, 1999).

The western Anatolian region includes two main continental blocks or fragments: (1) Rhodope-Pontide Fragment and (2) Anatolide-Tauride block (Figure 1.3). The Rhodope-Pontide Fragment comprises the Rhodope-Strandja Massif, Thrace Basin, İstanbul Zone and Sakarya Zone. The Rhodope-Strandja Massif (Okay et al., 2001) composed of crystalline basement of granite and gneisses and is tectonically overlain by allochthonous Triassic units. Okay et al. (1996) regarded that the Strandja Zone is part of the Mesozoic Laurasian active continental margin. The Thrace Basin is a Tertiary sedimentary basin developed during Middle Eocene (Görür et al., 1984).

The İstanbul Zone is characterized by non-metamorphic Palaeozoic sedimentary sequence, corresponding with a typical Atlantic-type continental margin (Okay et al., 1994). The Sakarya Zone is separated from the İstanbul and the Strandja zones by Intra-Pontide Suture (Figure 1.3). At regional scale, it consists of the Sakarya Continent (Şengör & Yılmaz, 1981) and the central-eastern Pontides. The Sakarya Continent was located between the Palaeo-Tethyan and the northern branch of the Neo-Tethys. The Sakarya Zone comprises Paleozoic granitic and metamorphic rocks of Carboniferous ages at the base (Okay et al., 1996). These crystalline rocks are tectonically overlain by a Late Palaeozoic to Triassic accretionary complex with intra-oceanic fore-arc deposits. All these rocks are unconformably overlain by Liassic detritals and middle Jurassic–early Cretaceous limestones and late Cretaceous flysch (Okay et al., 1996).
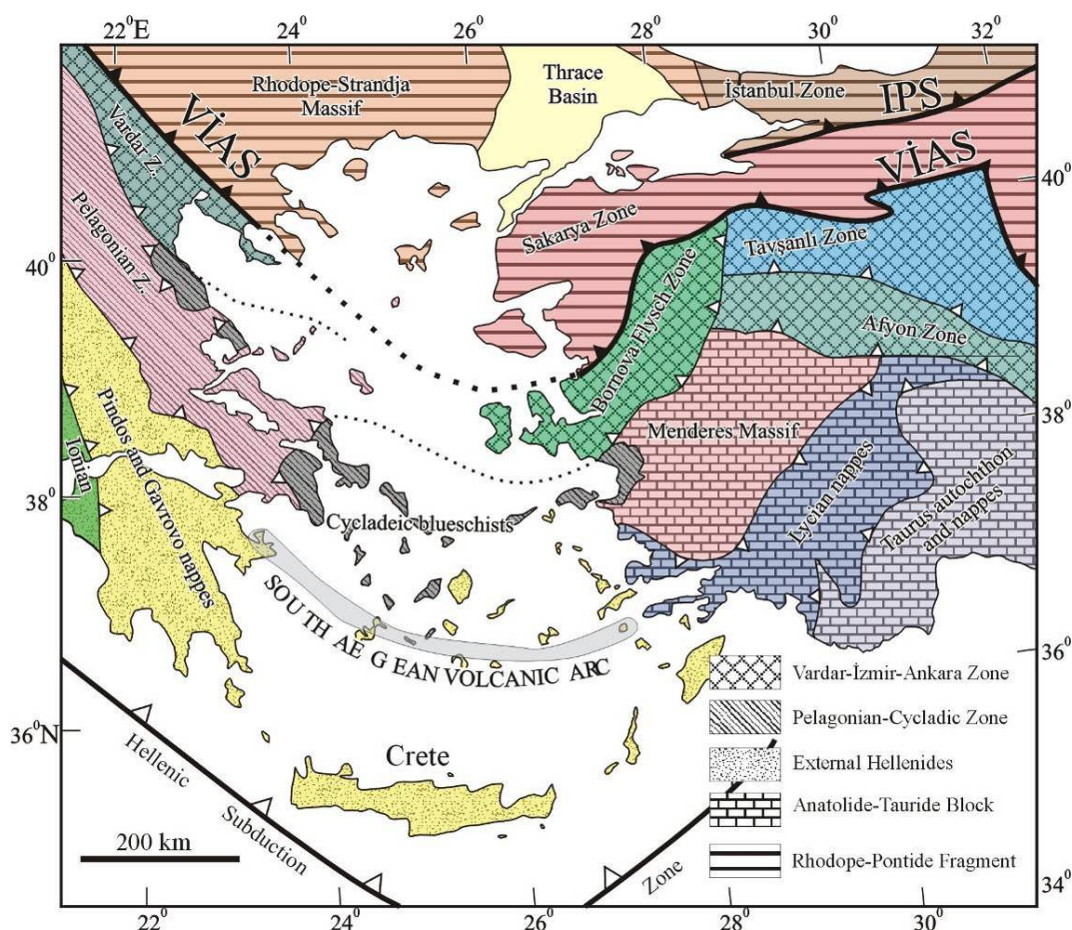
Figure 1.3 Tectonostratigraphic units of the Aegean region (after Lips, 1998; Okay & Tüysüz, 1999; Jolivet and Patriat, 1999; Ring et al., 1999a; Okay et al., 2001). IPS: Intra-Pontide Suture; VİAS: Vardar-İzmir-Ankara Suture zone.

The Anatolide-Tauride block made up of several tectonostratigraphic units which amalgamated during middle Eocene in the western Anatolia (Şengör & Yılmaz, 1981; Okay et al., 1996). These are, from north to south, Vardar-İzmir-Ankara zone, Menderes Massif and Lycian Nappes. The Vardar-İzmir-Ankara zone, made up of Vardar zone, Bornova Flysch zone, Afyon zone and Tavşanlı zone, represents the closure of the northern branch of the Neo-Tethys. The closure of the ocean was diachronous; it started in late Cretaceous in the west and proceeded until the early Eocene in the east (Görür et al., 1983; Tüysüz, 1993).

The Vardar zone, which is correlated with the İzmir-Ankara zone, separates the Rhodope continental block from the Pelagonian zone in Greece. It is represented by ophiolitic occurrences tectonically overlying the Pelagonian zone (Walcott & White, 1998). In the western Anatolia, the Vardar-İzmir-Ankara Suture Zone separates the Rhodope-Pontide Fragment from Anatolides. The Bornova Flysch Zone comprises chaotically deformed late Maastrichtian–Paleocene greywacke and shale with Mesozoic neritic limestone blocks of several kilometers large (Erdoğan, 1990; Erdoğan et al., 1990; Okay & Siyako, 1993; Okay et al., 1996). Okay (1996) suggested that it was formed in a transfer zone during Late Cretaceous owing mainly to its non-metamorphic character. The Tavşanlı Zone forms a blueschist belt, representing the northward subducted passive continental margin of the Anatolide-Tauride platform (Okay et al., 1996). The blueschists metamorphism occurred in Turonian-Coniacian (Okay & Kelley 1994). The Afyon zone comprises shelf-type Devonian to Paleocene sedimentary sequence metamorphosed in greenschist facies (Göncüoğlu et al., 1992; Okay et al., 1996).

The Menderes Massif forms the westernmost part of the Anatolides and is a large metamorphic massif with an exhumed ellipsoidal shape. The massif has traditionally been divided into two sequences: a "core" composed of augen gneisses, metagranites, schists, paragneisses and metagabbros; and a "cover" composed of schists, quartzites, amphibolites, phyllites and marbles (Dürr, 1975; Akkök, 1983; Şengör et al., 1984; Candan, 1995, 1996; Oberhänsli et al., 1997, 1998; Candan et al., 1997, 1998, 2001; Bozkurt & Oberhänsli, 2001; Régnier et al., 2003, 2007). Based

on Bryzoan assemblages and zircon radiometric analyses, the cover schists have been dated as Ordovician–Devonian (Konak et al., 1987; Loos & Reischmann, 1999). The schists are overlain by the fosiliferous grey marbles which are dated as Permian (Özer, 1998). Marbles starts with basal meta-conglomerate (Dürr, 1975), and consist of late Triassic–Liassic marbles intercalated with schists and metavolcanites. The succession continues upward with Jurassic–early Cretaceous massive marbles and late Cretaceous rudist-bearing marbles. The Menderes Massif shows a polyphase metamorphism: (M1) granulite, eclogite, amphibolite facies (pre-550 Ma / pre-Alpine, Candan et al., 2001), (M2) greenschist facies (pre-230 Ma / pre-Alpine, Ma; Akkök, 1983), (M3) blueschist facies (40 Ma / middle Alpine, Oberhänsli et al., 1998), (M4) amphibolite-greenschist facies which is known as main Menderes Metamorphism (35–36 Ma / middle Alpine, Lips et al., 2001), (M5) greenschist facies (12,2–19,5 Ma / late Alpine, Hetzel et al., 1995a). Alpine deformation history of the Menderes Massif includes contractional (M3 and M4; Eocene; Hetzel et al., 1998) and extensional events (M5; Bozkurt & Park, 1994; Hetzel et al., 1995a,b; Bozkurt, 2000; Lips et al., 2001). The late Alpine extensional deformation exhumed the Menderes Massif along crustal-scale low-angle detachment faults, accompanied by core complex formation. Based on sedimentological and radiometric data, recent studies showed that the late Alpine extensional deformation commenced ca. 23–20 Ma and continued by ca. 12 Ma (Bozkurt & Park, 1994, Hetzel et al., 1995a,b, 1998; Emre, 1996; Emre & Sözbilir, 1997; Koçyiğit et al., 1999; Bozkurt, 2000; Gessner et al., 2001a,b; Işık & Tekeli, 2001; Lips et al., 2001; Sözbilir, 2002a; Özer & Sözbilir, 2003; Ring et al., 2003, Işık et al., 2003, 2004; Bozkurt & Sözbilir, 2004; Seyitoğlu et al., 2000, 2002, 2004; Catlos & Çemen, 2005; Ring & Collins, 2005; Çemen et al., 2006; Glodny & Hetzel, 2007; Catlos et al., 2008; Ersoy et al., 2010a). This deformation was accompanied by basin formation in the upper plate, in which lacustrine sedimentation occurred with the extensive volcanism.

Detachment faulting and related supra-detachment volcano-sedimentary basin formation with magmatic activity characterize highly extended terrains such as the United States Cordillera and Aegean Extensional Province (Davis & Coney, 1979; Lister & Davis, 1989; Asmerom et al., 1994; Friedmann & Burbank, 1995;

Wernicke, 1995; Wernicke & Snow, 1998). The term "supra-detachment basin" refers to a sedimentary or volcano-sedimentary basin developed on a low-angle normal fault that can accommodate very large amounts of extension (Friedmann & Burbank, 1995). Deposition in such basins may occur; (a) actively during the extensional detachment faulting, (b) or passively after faulting. In the first case, syn-tectonic sedimentation occurs, giving rise to faulted contact between the deposits and the footwall. In the second case, the sediments overlay an eroded detachment fault (see Friedmann & Burbank, 1995).

The late Tertiary volcano-sedimentary basins in Western Anatolia (the eastern part of the Aegean Extensional Province) can be grouped as follows: (a) the Oligocene-Miocene molasse basins (Sözbilir, 2002b, 2005); (b) the Neogene volcano-sedimentary basins (Ercan et al., 1978; Şengör, 1987; Seyitoğlu & Scott, 1991, 1994a; Helvacı, 1995; Helvacı & Yağmurlu, 1995; Seyitoğlu, 1997a; Helvacı & Alonso, 2000; Yılmaz et al., 2000; Purvis & Robertson, 2004; Ersoy et al., 2010a); and (c) the Pliocene-Quaternary E–W-trending grabens (e.g., Cohen et al., 1995; Emre, 1996; Hakyemez et al., 1999; Bozkurt & Sözbilir, 2004; Çiftçi & Bozkurt, 2009) (Figure 1.4). The Neogene volcano-sedimentary deposits, which are located on the northern part of the Menderes Massif, were mainly developed in NE–SW-trending basins that are cut and displaced by nearly E–W-trending active high-angle normal faults bounding the Pliocene–Quaternary grabens.

Although many studies have been carried out in the NE–SW-trending basins, the stratigraphic and tectonic evolution of these basins remains controversial, and hence different evolutionary models have been proposed by various authors. According to Şengör (1987) the Neogene basins developed in two distinct stages. The first stage was related to the collision between the Sakarya continent and the Anatolide-Tauride platform that resulted in formation of paleo-tectonic Tibet-type cross-grabens under N-S-directed contractional events, and continued until the middle Miocene. The second stage commenced after the middle Miocene, and was related to N–S-directed extension that resulted in formation of neo-tectonic Aegean-type cross-grabens which overprinted the earlier grabens.
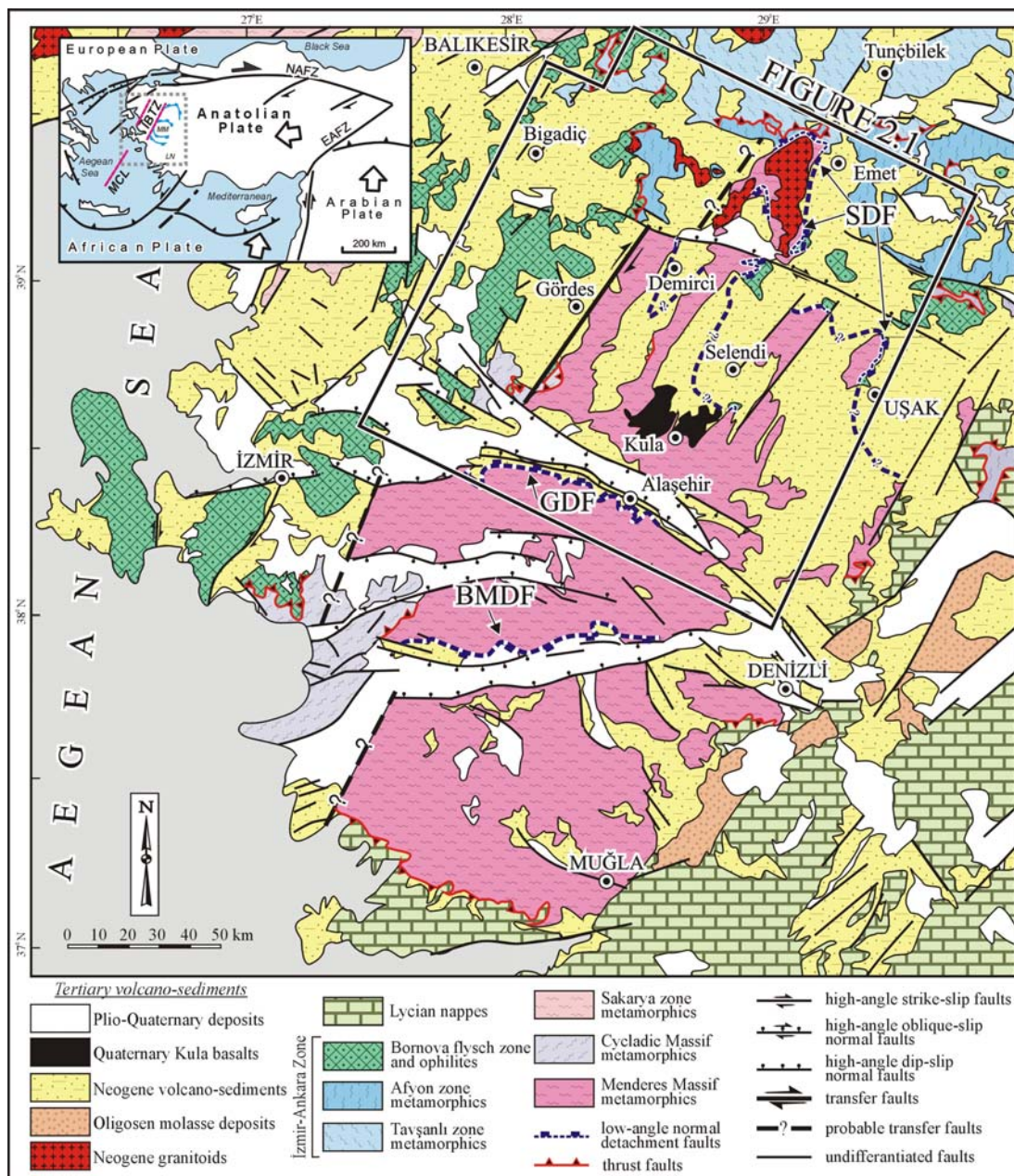
Figure 1.4 Simplified geological map of western Anatolia, showing the main tectono-stratigraphic units and tectonic elements (Modified from Geological Map of Turkey (1:500000), 2002). NAFZ-North Anatolian Fault Zone, EAFZ-East Anatolian Fault Zone, MCL- mid-Cycladic lineament, İBTZ-İzmir-Balıkesir Transfer Zone, SDF-Simav detachment fault, GDF-Gediz detachment fault, BMDF-Büyük Menderes detachment fault.

On the other hand, it has been suggested that extensional tectonics in the region commenced as early as the latest Oligocene (Seyitoğlu & Scott, 1991). According to Seyitoğlu & Scott (1991), the basins in western Anatolia started to develop synchronously during the post-orogenic collapse of the anomalously thickened

orogenic crust, whereas İnci (1998) suggested that the Neogene basins in the region formed as intermontane depocenters. The different views on the mode and timing of the extension in the area have been reviewed by Bozkurt (2003).

In addition, studies that have taken into account the Oligocene-Miocene tectonic exhumation of the Menderes Massif, suggest that the Miocene NE-SW-trending volcano-sedimentary basins formed on corrugated and eroded low-angle normal detachment fault planes that accommodated the exhumation of the Menderes Massif (Purvis & Robertson, 2004; Çemen et al., 2006, Ersoy et al., 2010a). Hence, from this perspective the exhumation style of the Menderes Massif is very important in understanding the basin formation in the upper plate of the detachment faults. Therefore, careful study is required of; (1) the detailed stratigraphy and correlations between the Neogene units in different basins, (2) the contact relationships between the Neogene units and the underlying basement rocks, and (3) the relative ages and kinematics of the faults that controlled the deposition of the Neogene units.

The tectonic contacts between the tectono-stratigraphic units have long been interpreted as thrusts. However, after the discovery of low-angle normal faults between; (a) the core and the cover rocks of the Menderes Massif (Bozkurt & Park, 1994); (b) the metamorphic rocks of the Menderes Massif and the non-metamorphic rocks of the İzmir-Ankara Zone (Lips et al., 2001; Işık & Tekeli, 2001); and (c) the metamorphic rocks of the Menderes Massif and the Neogene volcano-sedimentary units (Hetzel et al., 1995b; Emre, 1996; Emre & Sözbilir, 1997; Purvis & Robertson, 2004; Ersoy et al., 2010a), it is now widely accepted that the massif was exhumed along low-angle normal detachment faults or shear zones. The main low-angle detachment faults are; (1) the Simav detachment fault to the north (SDF; Işık & Tekeli, 2001; Ersoy et al., 2010a), (2) the Gediz detachment fault (GDF; Emre, 1996; Ring et al., 1999a, 2003; Lips et al., 2001; Gesner et al., 2001a,b; Sözbilir, 2001, 2002a; Bozkurt & Sözbilir, 2004; Çiftçi & Bozkurt, 2009), (3) the Büyük Menderes detachment fault (BMDF; Emre & Sözbilir, 1997; Lips et al., 2001; Gessner et al., 2001b) (Figure 1.4).

The SDF lies in the northern part of the Menderes Massif (Işık & Tekeli, 2001; Işık et al., 2003, 2004; Ersoy et al., 2010a; Figure 1.4). The footwall of the SDF comprises migmatitic-banded gneiss, biotite gneiss, mica schists and amphibolite which are intruded by syn-extensional Eğrigöz (20.7-20.0 Ma; Işık et al., 2004; Ring & Collins, 2005) and Koyunoba (21.0 Ma; Ring & Collins, 2005) granitoids. The hanging-wall rocks are composed of schists and marbles with ophiolitic mélange rocks. The GDF is located at the southern margin of the Gediz graben (Hetzel et al., 1995b; Emre, 1996; Emre & Sözbilir, 1997; Lips et al., 2001; Sözbilir, 2001, 2002a; Işık et al., 2003; Bozkurt & Sözbilir, 2004). The footwall units of the GDF are composed of schists of the Menderes Massif which are intruded by syn-extensional Salihli and Turgutlu granitoids (Hetzel et al., 1995a,b; Glodny & Hetzel, 2007; Catlos et al., 2008). The study area is focused on the area lying between SDF and GDF (Figure 1.4).

1.4 An Overview of the Neogene Magmatic Activity in the Region

The Western Anatolian Volcanic Province (WAVP) is one of the major volcanic belts that developed during the late Cenozoic in the Aegean-Western Anatolian region (Figures 1.1 and 1.5). On the basis of time and space relations, the magmatic rocks of the WAVP can be grouped as; (1) the Northwest Anatolian Eocene volcanic rocks (NAEV), (2) Oligocene volcanic and plutonic rocks just to the south of the NAEV, and (3) the more extensive Miocene volcanic and plutonic rocks that lie further south (Figure 1.5). In the literature, the Eocene and Miocene magmatic events have generally been evaluated as the result of a common petrogenetic history. There are, however, indications in previous studies that are discussed below which suggest there are some important geological and geochemical distinctions between them, such that they should be considered separately if we are to fully understand the geodynamic evolution of the region.

The NAEV is dominantly represented by medium- to high-K calc-alkaline series and less developed tholeiitic basalts which are thought to represent either; (1) the final products of the northward subduction (Ustaömer et al., 2009), or (2) the

products of post arc-continent collision (Genç & Yılmaz, 1997; Altunkaynak, 2007; Altunkaynak & Genç, 2008; Dilek & Altunkaynak, 2007, 2009). The Miocene volcanism produced considerable compositional diversity. In particular, there are more potassic rocks than the NAEV, including a dominantly K-alkaline (high-K, shoshonitic and ultrapotassic) series. In contrast to the NAEV, the Miocene volcanic rocks also interfinger with lacustrine sediments in extensional basins (Figure 1.5; Aldanmaz et al., 2000; Innocenti et al., 2005; Karacık et al., 2007; Ersoy & Helvacı, 2007; Ersoy et al. 2008; Pe-Piper et al., 2009; Helvacı et al., 2009; Altunkaynak et al., 2010; Karaoğlu et al., 2010; Ersoy et al., 2010b; Ersoy et al., 2011). These extensional basins developed as either; (a) strike-slip basins along the İzmir-Balıkesir transfer zone in the west, or (b) supra-detachment basins on the metamorphic rocks of the Menderes Massif that exhumed as a core-complex during early-middle Miocene in the east (Ersoy et al., 2010a, 2011).

The Miocene volcanic rocks in the NE–SW-trending supra-detachment basins, which are the main focus of this study, are especially important for the understanding of the geochemical evolution of the magmatism developed during core-complex formation. In this region, Na-alkali basalts were emplaced during the Quaternary (Quaternary Kula volcanites, QKV; Güleç, 1991; Alıcı et al., 2002). The other large volcanic occurrences in the region are present as the N–S-trending Eskişehir-Afyon-Isparta volcanic rocks (EAIV) located east of the WAVP, and as the Galatian Volcanic Province (GVP), located further northeast (Figure 1.2).

The causes and controls of Eocene and Miocene volcanic activity in the region have generally been evaluated together and subject to considerable debate. Enriched LILE/HFSE ratios, high $^{87}Sr/^{86}Sr$ and low $^{143}Nd/^{144}Nd$ ratios of the Eocene and Miocene volcanic rocks have all generally been attributed to two-stage enrichment by; (1) subduction-related metasomatism of their mantle sources, and (2) crustal contamination or hybridisation of the mantle-derived magmas with crustal melts during post-collisional orogenic thickening (Güleç, 1991; Aldanmaz et al., 2000; Altunkaynak, 2007; Altunkaynak & Genç, 2008; Dilek & Altunkaynak, 2007, 2009).
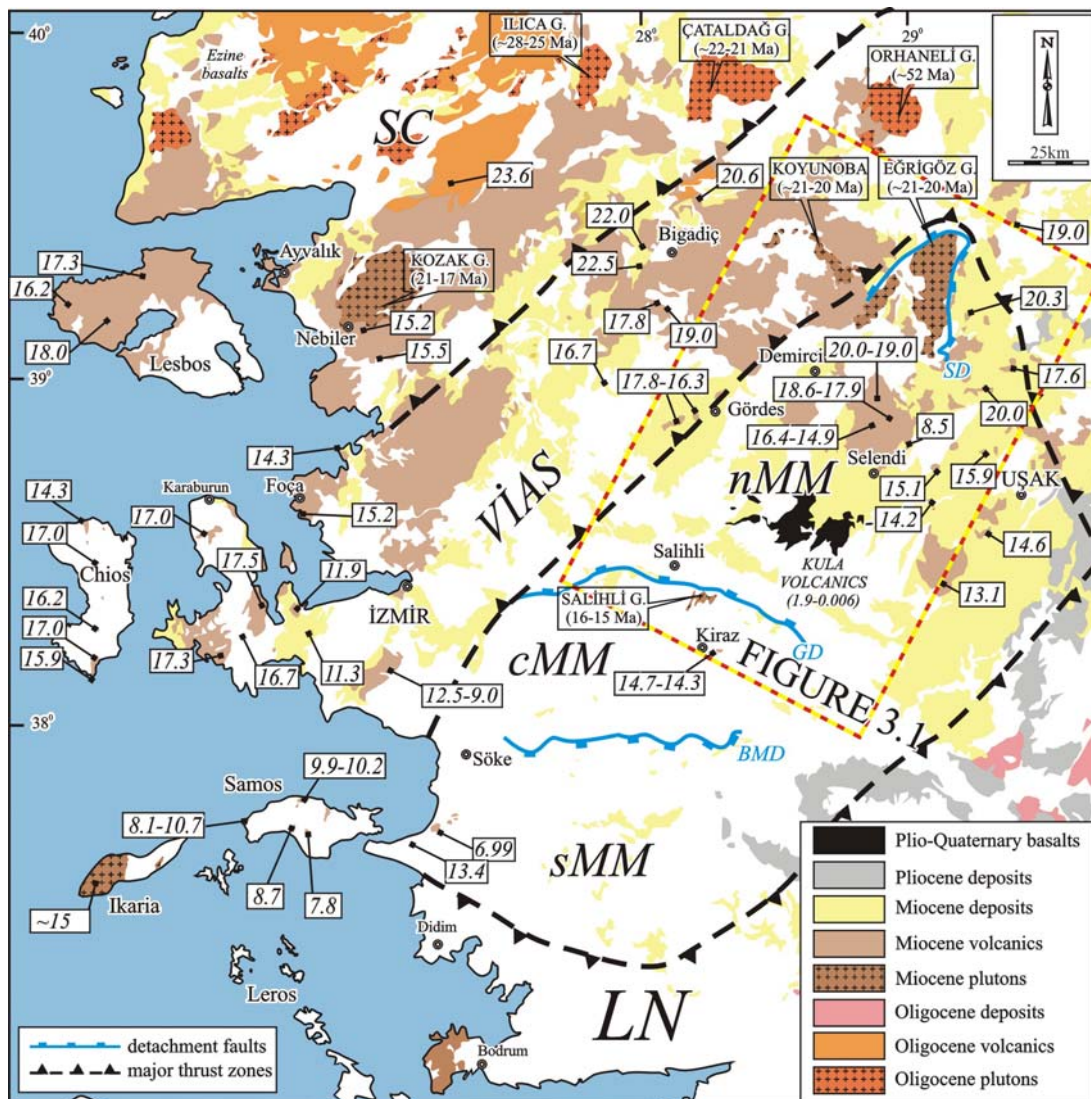
Figure 1.5 Simplified map of Western Anatolia, showing the Neogene volcanic and sedimentary rocks and main tectonic structures. The detachment faults are indicated by blue solid lines and comprise (from north to south) the Simav detachment (SD), Gediz detachment (GD) and Büyük Menderes detachment (BMD).

In more detail, the subduction-related metasomatism of the mantle sources of the Eocene to Miocene volcanic rock groups in the WAVP has been attributed to either; (a) closure of the northern Neo-Tethys along the Vardar-İzmir-Ankara Suture (VIAS) (cf. Güleç, 1991; Aldanmaz et al., 2000), or (b) northward subduction of the African Plate along the Hellenic trench (cf. Innocenti et al., 2005). Subduction along the VIAS may be responsible for mantle metasomatism of the NAEV, as they are located on the Sakarya Continent in an arc or back-arc setting. The Miocene volcanic rocks, on the other hand, are mainly located on the Anatolide-Tauride block in a

fore-arc setting (Figure 1.5). Hence, any subduction-related metasomatism of the Miocene source regions must have either been due to undocumented events during the Proterozoic-Mesozoic, and/or to recent Aegean subduction to the south (e.g., Pe-Piper & Piper, 2001). In the case of the latter, this would imply that there has been southward migration (slab roll-back) of the Hellenic trench over time (cf. Ring et al., 2010). Although this interpretation is compatible with mantle tomographic sections (Faccenna et al., 2003; Hafkenscheid et al., 2006), it contradicts hypotheses invoking near-horizontal Aegean slab subduction (Innocenti et al., 2005; Prelević et al., 2010).

CHAPTER TWO
STRATIGRAPHY AND TECTONIC EVOLUTION OF THE NE–SW-TRENDING NEOGENE BASINS

2.1 Volcano-stratigraphy of the NE–SW-Trending Basins

The NE–SW-trending Miocene basins in the region are, from west to east, the Bigadiç (Helvacı, 1995; Helvacı & Yağmurlu, 1995; Erkül et al., 2005a,b), Soma (İnci, 1998), Gördes (Seyitoğlu & Scott, 1994a,b; Purvis & Robertson, 2004), Demirci (Yılmaz et al., 2000), Akdere (Seyitoğlu, 1997b); Emet (Helvacı, 1986; Seyitoğlu et al., 1997); Selendi (Ercan et al., 1983; Seyitoğlu, 1997a; Westaway et al., 2004; Purvis & Robertson, 2004, Ersoy & Helvacı, 2007; Ersoy et al., 2010a) and Uşak-Güre basins (Ercan et al., 1978; Seyitoğlu, 1997a; Westaway et al., 2004; Seyitoğlu et al., 2009; Karaoğlu et al., 2010). The E-W-trending Pliocene-Quaternary grabens include, the Simav half-graben (Seyitoğlu, 1997b), and the Gediz (Cohen et al., 1995; Emre, 1996; Hakyemez et al., 1999; Bozkurt & Sözbilir, 2004; Çiftçi & Bozkurt, 2009), Küçük Menderes (Rojay et al., 2005; Emre & Sözbilir, 2007), and Büyük Menderes (Hakyemez et al., 1999) grabens which are actively deformed by basin-facing normal faults (Figure 2.1). In this chapter the stratigrapy of the Gördes, Demirci and Emet basins will be given, and then, the data will be compared with those of the other basins.
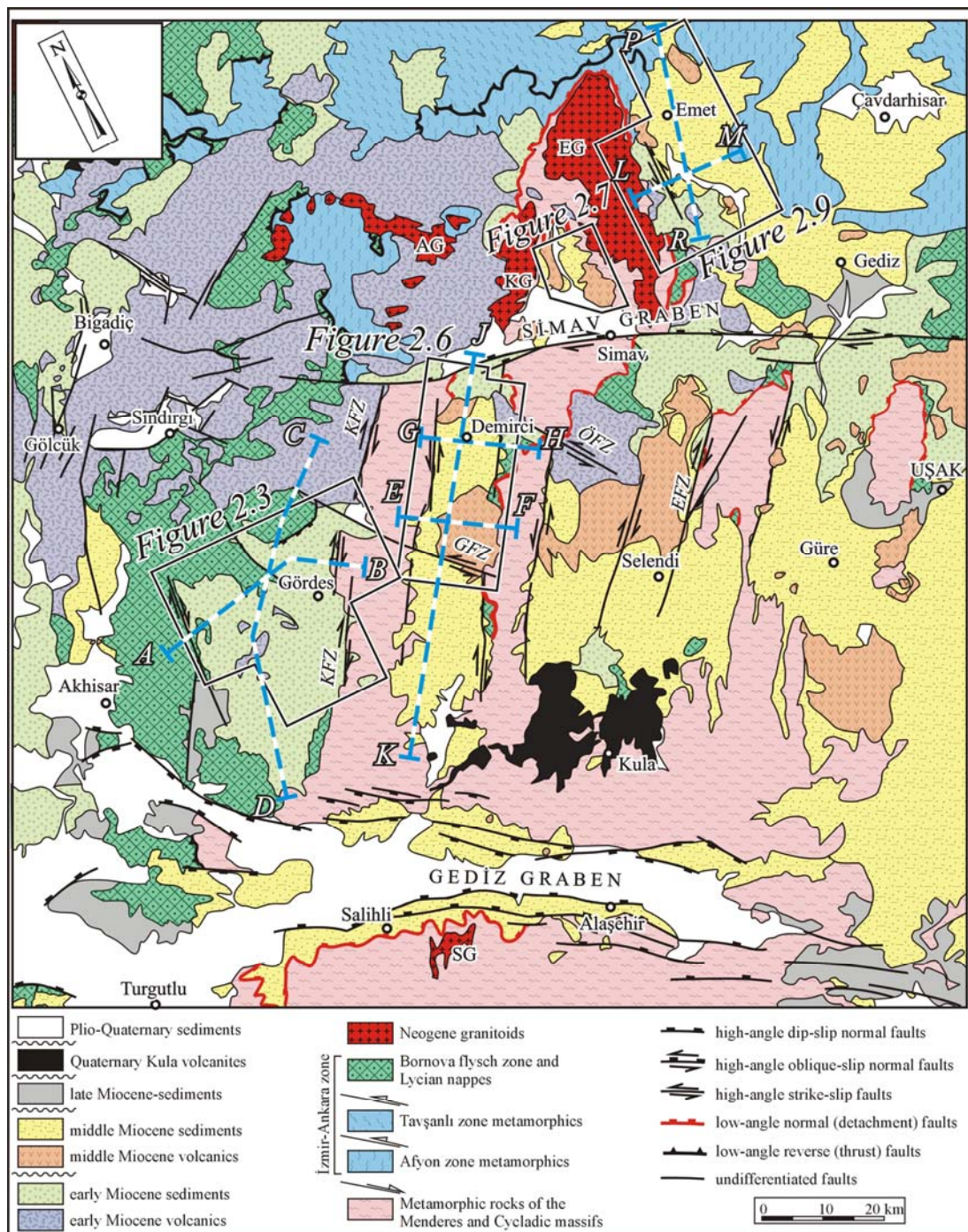
Figure 2.1 Simplified geological map of the NE–SW-trending Neogene basins (Compiled from this study; Geological Map of Turkey (1:500000), 2002; Okay & Tüysüz, 1999; Koçyiğit et al., 1999; Sözbilir, 2001; Işık & Tekeli, 2001; Ersoy et al., 2010a). EG-Eğrigöz granitoid, KG-Koyunoba granitoid, AG-Alaçam granitoid, SG-Salihli granitoids, KFZ-Kızıldam fault zone, GFZ-Güneşli fault zone, ÖFZ-Ören fault zone, EFZ-Eskin fault zone. Also shown are the locations of the detailed geological maps and cross-sections carried out in this study. The lines A-B to P-R indicate the section traces shown on Figure 2.4.

2.1.1 Gördes Basin

Gördes basin is confined by the Menderes Massif to the east and by ophiolitic mélange units of the Bornova flysch zone to the west (Figure 2.1), and has previously been studied by Nebert (1961), Yağmurlu (1984), Seyitoğlu & Scott (1994a,b), Purvis & Robertson (2004). Nebert (1961), divided the basin fill into two sections: an lower sedimentary unit starting with a boulder conglomerate and coarse-medium sandstones passing upwards to marls of early-middle Miocene, and an unconformably overlying upper sedimentary unit comprising basal conglomerate, alternations of tuff, marl and silicified limestone of Pliocene. According to Yağmurlu (1984) the basin fill starts with early Miocene alluvial fans (Göcek formation) and pass unconformably upward to middle Miocene Yeniköy formation and Küçükderbent formation. Küçükderbent formation is cut by late Miocene acidic volcanic rocks and overlain by tuffs (Karaboldere formation). These formations are overlain by late Miocene Ahmetler formation that is composed of alluvial fans.

According to Seyitoğlu & Scott (1994a,b) the stratigraphy of Gördes basin is characterized by three main sedimentary units. The basal part of the sequence is represented by the conglomerates and sandstones of the Dağdere Formation in the north and the Tepeköy Formation in the south, which are overlain by the sandstone-mudstone alternation of the Kuşlukköyü Formation that is also intercalated with acidic tuff (Figure 2.2a). The basin fill is cut by dacitic-rhyolitic volcanic necks (central volcanites; Seyitoğlu & Scott, 1994b). Gördes basin has previously been interpreted as either; (1) a classic graben bounded by normal faults (Seyitoğlu & Scott, 1994a,b), or (2) as a hanging wall basin passively formed above the corrugation of a low-angle normal fault (Purvis & Robertson, 2004).

In this study, the stratigraphy of Gördes basin has been revised on the basis of new field data. According to field studies, the stratigraphy of the basin begins with Kızıldam Formation which is conformably overlain by the Kuşlukköyü Formation. The Kuşlukköyü Formation interfingers with the Güneşli Volcanites and are also cut by the Kayacık Volcanites in the centre of the basin (Figures 2.2a and 2.3). These

units are unconformably overlain by the Gökçeler Formation and late Miocene to recent sediments.

The Kızıldam Formation crops out along the basin-bounding faults in Gördes basin (Figure 2.3). In the eastern margin of Gördes basin, the Kızıldam Formation is made up of reddish-brown conglomerates of alluvial fan origin, which are mainly derived from the underlying metamorphic rocks of the Menderes Massif. Here, the Kızıldam Formation unconformably overlies the metamorphic rocks and is composed of metamorphic clasts such as gneisses, schists and migmatites. In the western part of Gördes basin, the Kızıldam Formation starts with well-lithified carbonate-cemented conglomerates with mainly limestone-dominated clasts derived from the rocks of the İzmir-Ankara suture zone. The type section of the Kızıldam Formation is best seen around the Kızıldam village (Figure 2.3). To the centre of the basin, the unit passes laterally into the Kuşlukköy Formation. The Kızıldam Formation is regionally correlated with the Lower Miocene Kürtköyü Formation in the Demirci and Selendi basins, and is equivalent of the lower parts of the Dağdere and Tepeköy formations of Seyitoğlu & Scott (1994a, b). It is also correlated with the alluvial fan facies of Purvis & Robertson (2004).

Seyitoğlu & Scott (1994a) obtained 24.2±0.8 to 21.1±1.1 Ma K-Ar ages from tourmaline leucogranite pebbles in the Kızıldam Formation. The age of the Kızıldam Formation is accepted to be early Miocene on the basis of radiometric age data from the volcanic intercalations in the conformably overlying Kuşlukköy Formation. Alluvial fans of the Kızıldam Formation were deposited; (a) on the hanging-wall of N-S- to NE-SW-trending right-lateral strike-slip faults (Kızıldam and Göcek fault zones), and (b) along the nearly E-W-trending normal faults located north of the Salur and Börez villages (Börez fault zone, Figure 2.3).
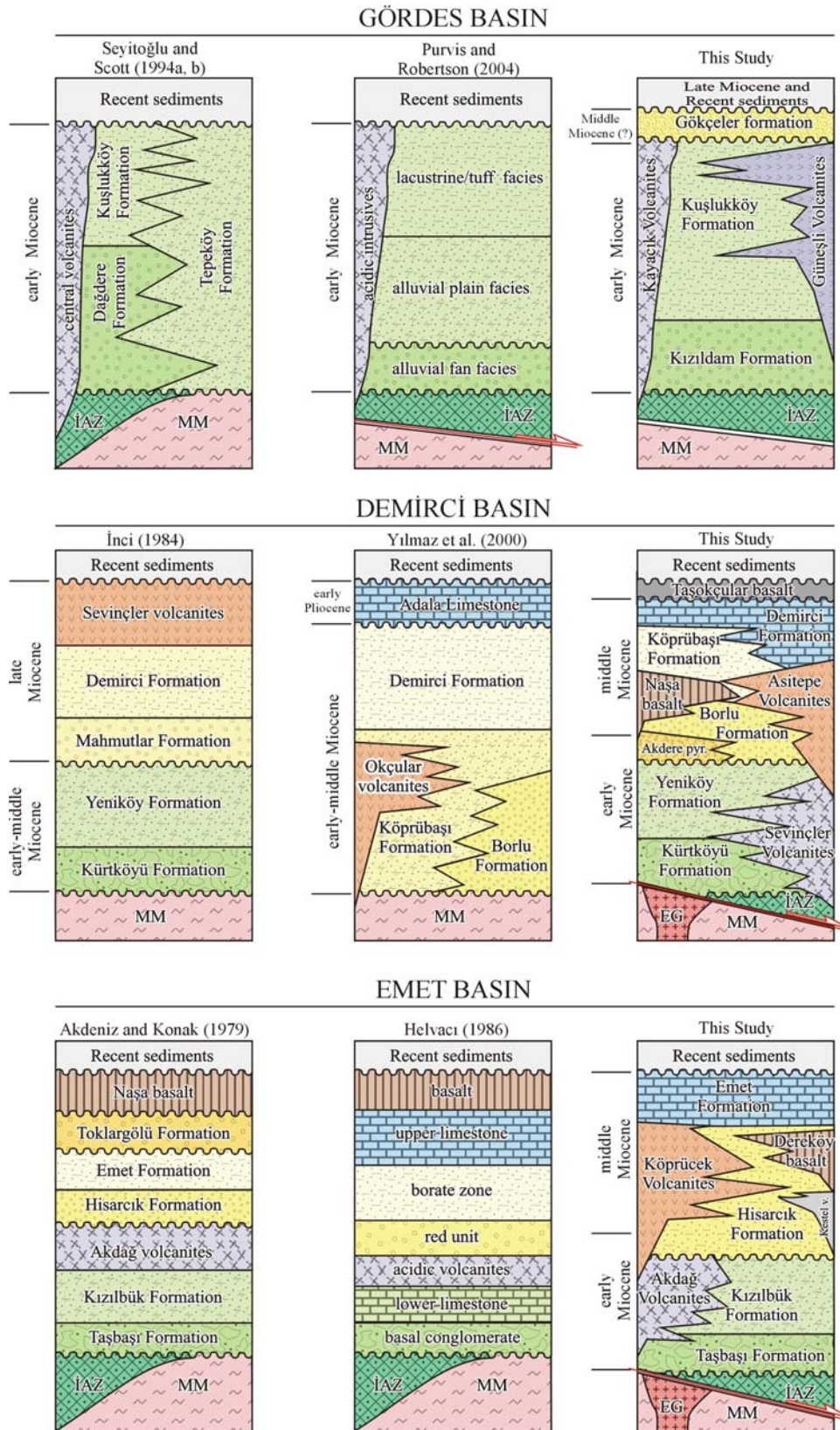
Figure 2.2 Comparison of stratigraphic sections proposed for the NE–SW-trending Gördes, Demirci and Emet basins. MM-Menderes Massif, İAZ-İzmir-Ankara Zone rocks, EG-Eğrigöz granitoid.

The Kuşlukköy Formation (Seyitoğlu & Scott, 1994a,b) crops out in a large area throughout the Gördes basin (Figure 2.3). The unit is composed of conglomerate-sandstone and sandstone-claystone alternations of fluvio-lacustrine origin (Figures 2.5b and 2.5c). The upper section of the Kuşlukköy Formation is represented by marl and limestone to the north of the Korubaşı village. The Kuşlukköy Formation contains coal occurrences in the western part of the basin (around Çıtak and Dağdere villages) and is also intercalated with acidic tuffs that can be followed from the northern to the southern parts of the basin. This formation is correlated with the alluvial plain and lacustrine/tuff facies of Purvis & Robertson (2004). The age of the unit is early Miocene on the basis of radiometric age data from the volcanic intercalations.
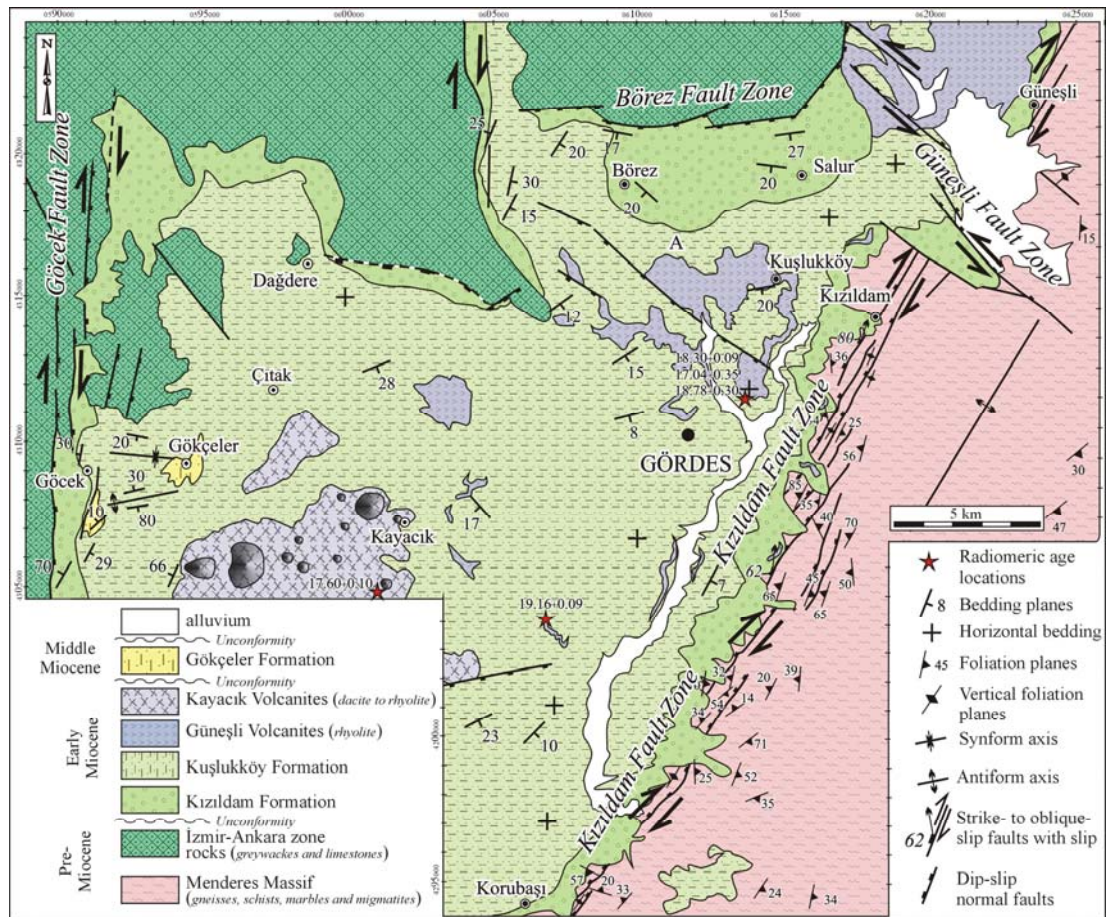
Figure 2.3 Geological map of Gördes basin. See Figure 2.2 for location.
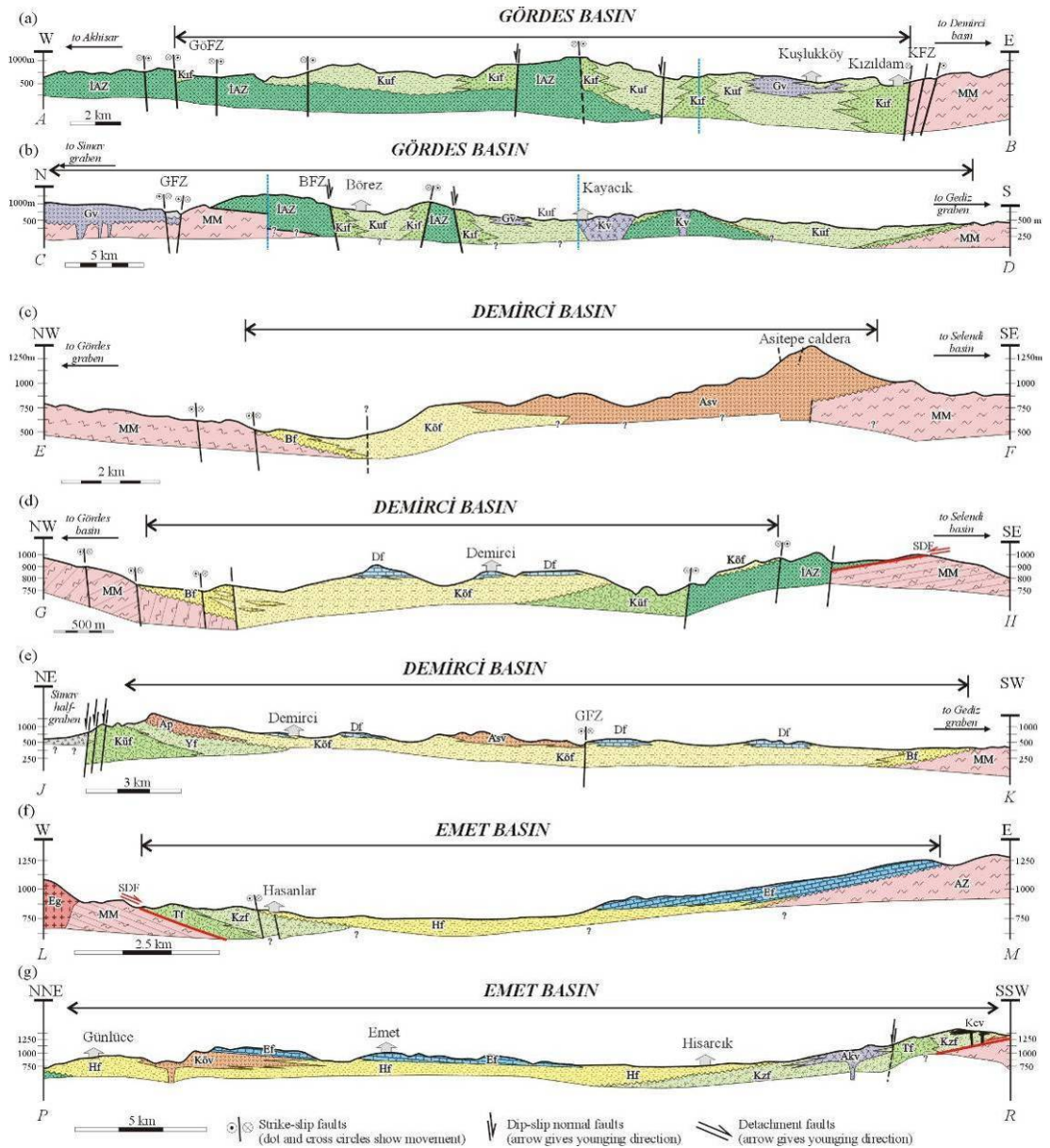
Figure 2.4 (a-g) Geological cross-sections across the Gördes, Demirci and Emet basins (see Figure 2.1 for section locations). MM-Menderes Massif, AZ-Afyon zone rocks, İAZ-İzmir-Ankara Zone rocks, Eg-Eğrigöz granite, Kıf-Kızıldam Formation, Kuf-Kuşlukköy Formation, Gv-Güneşli Volcanites, Kv-Kayacık Volcanites, Küf-Kürtköyü Formation, Yf-Yeniköy Formation, Tf-Taşbaşı Formation, Kzf-Kızılbük Formation, Kev-Kestel volcanites, Akv-Akdağ Volcanites, Bf-Borlu Formation, Köf-Köprübaşı Formation, Ap-Akdere pyroclastics, Asv-Asitepe Volcanites, Df-Demirci Formation, Hf-Hisarcık Formation, Ef-Emet Formation, Köv-Köprücek volcanites, SDF-Simav detachment fault, GöFZ-Göcek faulz zone, Gfz-Güneşli fault zone, KFZ-Kızıldam fault zone.
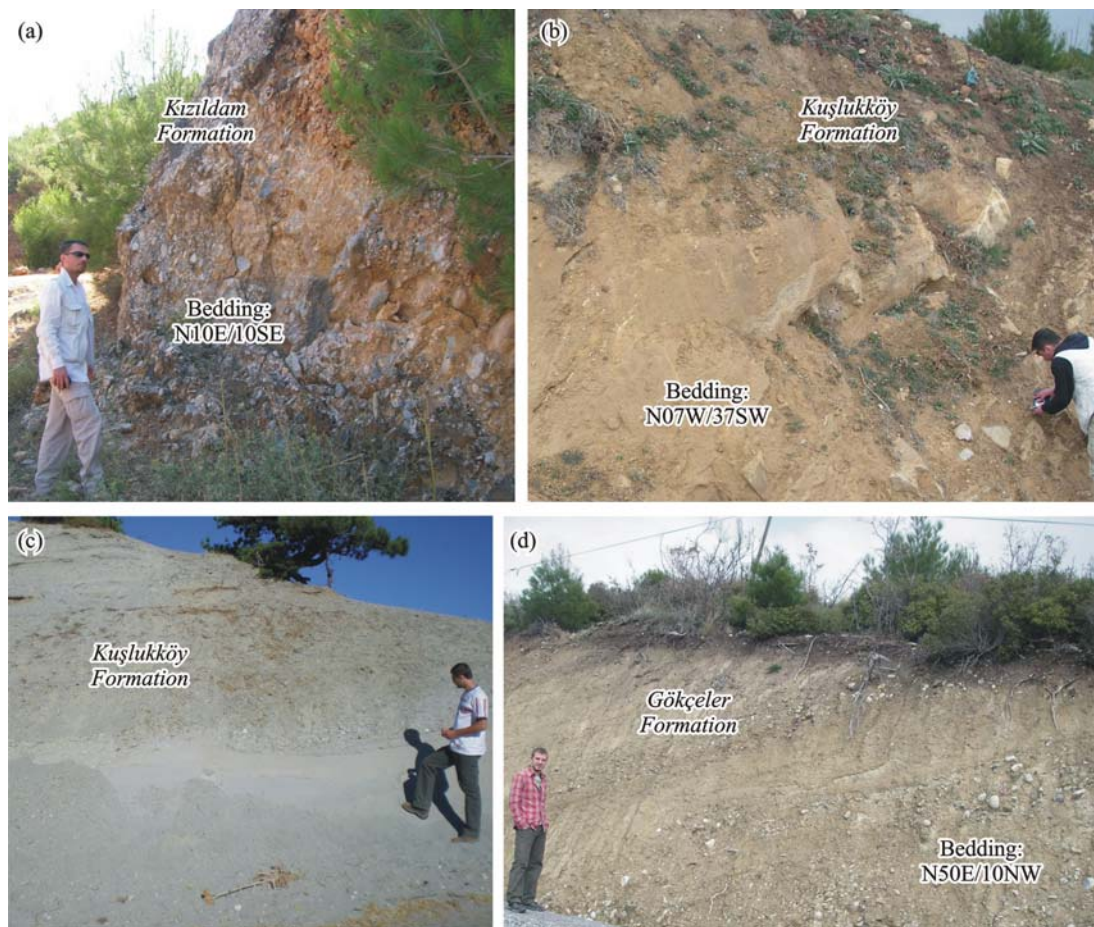
Figure 2.5 Field photographs from Gördes basin: (a) the Kızıldam Formation composed of well-lithified conglomerates derived mainly from limestone rocks of the İzmir-Ankara zone at the western margin of the basin; sandstone-mudstone alternations (b) and tuffaceous sandstone-siltstone (c) alternations of the Kuşlukköy Formation, (d) pebblestone-sandstone alternations of the Gökçeler Formation.

The Güneşli Volcanites cover a large area to the north of the basin and are cut by the E-W-trending oblique-slip normal faults of the Simav half-graben (Figure 2.1). This unit is composed of several pink to white colored rhyolitic dykes and lava flows and associated rhyolitic pyroclastic rocks to the north of the Gördes basin. The volcanic products are best observed around Güneşli (Figure 2.3). The pyroclastic rocks of the unit interfinger with the fine-grained sedimentary rocks of the Kuşlukköy Formation. The thickness of the tuff intercalations increases towards the northern part of the basin (1-2 m in the south and ~30m to the north of the Gördes town) where rhyolitic volcanic rocks crop out, suggesting that the pyroclastic flows in the basin fill deposits originated from the rhyolitic volcanic centers to the north of

the basin (Figure 2.4b). These acidic volcanic rocks are correlated with the dacitic to rhyolitic volcanic rocks of the Kayacık Volcanites in the centre of Gördes basin and the Sevinçler and Eğreltidağ volcanites in the Demirci and Selendi basins, respectively. Purvis et al. (2005) obtained 19.16±0.09 to 17.04±0.35 Ma biotite and feldspar Ar/Ar ages from the pyroclastic rocks of the Güneşli Volcanites. In this study 20.86±0.08 and 17.63±0.07 Ma whole rock Ar/Ar ages obtained from the Kayacık volcanites. 18.906±0.026 (MSWD = 1.90) and 18.763±0.890 Ma (MSWD = 9.50) sanidine Ar/Ar ages obtained from the Güneşli Volcanites (Table 2.1).

The Kayacık Volcanites crop out in the centre of Gördes basin. They are composed of mainly green colored dacitic to rhyolitic volcanic necks and associated lava flows and minor pyroclastic rocks interfingering with the Kuşlukköy Formation. The volcanic necks cut and deform the sandstones of the Kuşlukköy Formation. These volcanic rocks have previously been described as central volcanites (Seyitoğlu & Scott, 1994a). The volcanic products of the unit yielded 18.4±0.6 to 16.3±0.5 Ma K-Ar (Seyitoğlu & Scott, 1994b) and 21.71±0.04 to 17.6±0.1 Ma Ar/Ar ages (Purvis et al., 2005) (Table 2.1).

The Gökçeler Formation crops out in a limited area at the western margin of Gördes basin. The unit is best observed along the road-section from Gökçeler to Kayacık village. The unit is composed of conglomerates, pebblestones, sandstones, siltstones and marls which have a fluvio-lacustrine origin (Figures 2.3 and 2.5d). The conglomerates at the base of the unit include several conglomerate blocks derived from the underlying Kızıldam Formation. The Gökçeler Formation overlies the Kuşlukköy Formation along an angular unconformity and is tentatively identified as middle Miocene according to its stratigraphic position and lithological similarities to other middle Miocene units in adjacent basins (e.g., the İnay group in Demirci and Selendi basins). The early-middle Miocene units in Gördes basin are also unconformably overlain by late Miocene(?) to Recent sediments in the southwestern part of the basin.

Table 2.1 Published age data from the Neogene volcanic units in the NE–SW-trending basins. (1): Erkül et al. (2005a); (2) Seyitoğlu et al. (1997); (3) Purvis et al. (2005); (4) Ersoy et al. (2008); (5) Ersoy et al. (2010a); (6) Helvacı & Alonso (2000); (7) Ercan et al. (1996); (8) Innocenti et al. (2005)

Volcanic Units	Basin	Age Data	Refference
Early-middle Miocene felsic volcanic units			
Kocaiskan volcanites	Bigadiç basin	23.60±0.60–23.00±2.80	(1)
Sındırgı volcanites	Bigadiç basin	20.80±0.70–19.00±0.40	(1)
Kayırlar volcanites	Bigadiç basin	20.60±0.70	(1)
Şahinkaya volcanites	Bigadiç basin	17.80±0.40	(1)
Kayacık volcanites	Gördes basin	21.71±0.04–16.30±0.50	(2) and (3)and (3)
Güneşli volcanites	Gördes basin	19.16±0.09–17.04±0.35	(3)
		18.906±0.026	*This study*
		18.763±0.890	*This study*
Sevinçler volcanites	Demirci basin	19.057±0.045	*This study*
		19.748±0.047	*This study*
Eğreltidağ volcanites	Selendi basin	20.35±0.55–18.90±0.10	(2), (4) and (5)
Akdağ volcanites	Emet basin	20.30±0.60–19.00±0.20	(2) and (6)
Asitepe volcanites	Demirci basin	17.580±0.094	*This study*
Yağcıdağ volcanites	Selendi basin	16.61±0.14–14.90±0.60	(2) and (3)
		16.43±0.32	*This study*
Karabacaklar volcanites	Güre basin	15.90±0.40–15.10±0.40	(2)
Köprücek volcanites	Emet basin	16.80±0.20	(6)
Early-middle Miocene mafic volcani units			
Gölcük basalt	Bigadiç basin	20.50±0.10–19.70±0.40	(1)
Kuzayır lamproite	Selendi basin	18.60±0.20–17.59±0.85	(4) and (5)
Naşa basalt	Demirci basin	15.80±0.30–15.20±0.30	(7)
Güre lamproite	Güre basin	14.20±0.12	(8)
Kestel volcanites	Emet basin	15.914±0.074	*This study*
		15.730±0.110	*This study*
Dereköy basalt	Emet basin	15.40±0.20–14.90±0.30	(2) and (6)
Kıran-Zahman basalts	Güre basin	15.50±0.40	(2)
Ilıcasu lamproite	North of Selendi basin	15.87±0.13–15.83±0.13	(8)
Late Miocene mafic volcanic units			
Taşokçular basalt	Demirci basin	10.46±0.034	*This study*
Kabaklar basalt	Selendi basin	8.50±0.20–8.37±0.07	(7) and (8)

2.1.2 Demirci Basin

Demirci basin (Figure 2.6) was first studied by İnci (1984), who suggests that the basin fill is composed of two main stratigraphic units separated by an angular unconformity (Figure 2.2b). According to İnci (1984), the basin-fill starts with early-middle Miocene conglomerates of the Kürtköyü Formation that pass upwards into the sandstone-mudstone alternations of the Yeniköy Formation. These units are unconformably overlain, in ascending order, by the Mahmutlar Formation (composed of conglomerate and sandstone with pyroclastic intercalations), the Demirci Formation (composed of sandstone, mudstone, bituminous shale, marl and limestones), and the Sevinçler Volcanites (composed of andesitic-dacitic lavas and pyroclastics) that outcrop in the northeastern part of the basin.

Yılmaz et al. (2000) revised the stratigraphy of Demirci basin and proposed that the basin fill started with boulder conglomerates of the Borlu Formation that pass into the sandstones and mudstones of the Köprübaşı Formation. The Köprübaşı Formation is intercalated with andesitic lavas and pyroclastics rocks of the Okçular volcanites that outcrop in the western-central part of the basin. According to Yılmaz et al. (2000), these units are conformably overlain by the marls and shales of the Demirci Formation (Figure 2.2b). Yılmaz et al. (2000) also proposed that all these units are early-middle Miocene in age and are unconformably overlain by the late Miocene-early Pliocene Adala Formation composed of limestones cropping out around Demirci town.

The infill of Demirci basin is cut into two sectors by the Pliocene-Quaternary Simav half-graben. The northern sector was named as the Akdere basin by Seyitoğlu (1997b) (Figures 2.1 and 2.7). The Neogene stratigraphy of this part of Demirci basin rests on the metamorphic rocks of the Menderes Massif that were intruded by the Oligocene-Miocene Eğrigöz and Koyunoba granitoids. New field evidence from this study shows that the stratigraphy of the Demirci basin is different from that previously suggested, and that the lithological, stratigraphic and structural features of

the Neogene volcano-sedimentary infill of Demirci basin are very similar to those of the Selendi and Uşak-Güre basins.
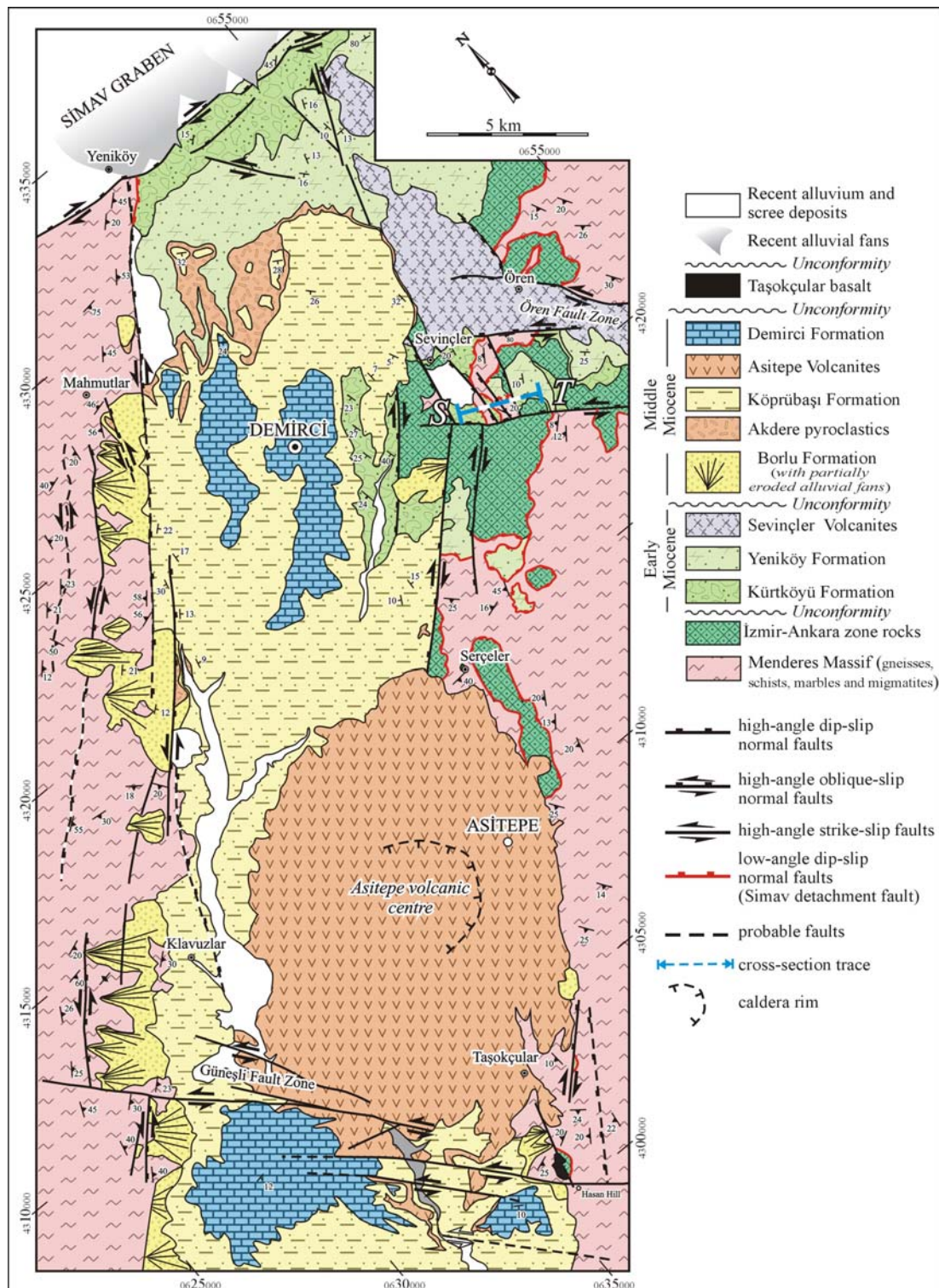
Figure 2.6 Geological map of the southern sector of Demirci basin. Also shown is the location of the S-T section which is illustrated in Figure 2.11. See Figure 2.1 for location.

The stratigraphy of the Demirci basin contains two distinct units separated by a basin-wide angular unconformity (İnci, 1984). The older one is correlated with the Hacıbekir Group in the adjacent Selendi and Uşak-Güre basins (Ercan et al., 1978), whereas data from this study indicates that the younger volcano-sedimentary unit unconformably overlies the Hacıbekir Group and can be correlated with the İnay Group in the adjacent Selendi basin.

The Hacıbekir Group in Demirci basin is composed of the Kürtköyü and Yeniköy formations and the rhyolitic volcanic rocks of Sevinçler Volcanites. The İnay Group comprises the Akdere pyroclastics, sedimentary rocks of the Borlu, Köprübaşı, and Demirci formations which are interfingered by andesitic-dacitic Asitepe Volcanites and the Naşa basalt to the north of the basin (Figures 2.2b, 2.5 and 2.7).
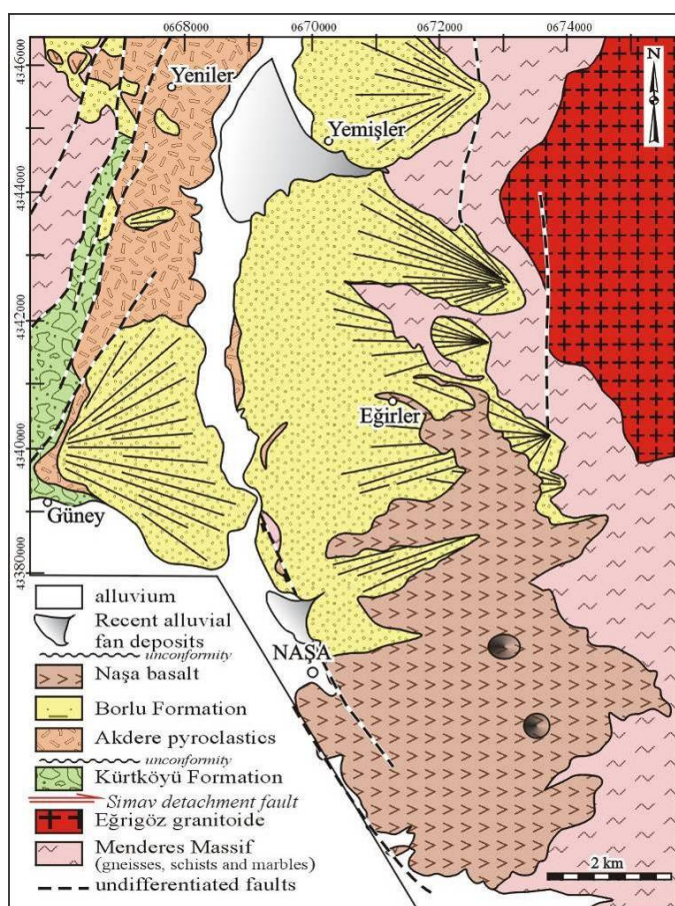
Figure 2.7 Geological map of the northern sector of Demirci basin (also known as Akdere basin). See Figure 2.2 for location.

The Kürtköyü Formation crops out in the northern part of Demirci basin, with the largest exposures on the southern flank of the Simav half-graben (Figure 2.6). The unit is composed of reddish brown to pale yellow boulder conglomerates (with blocks of up to 1m), pebblestones, cobblestones and sandstones. The conglomerates are mainly derived from the Menderes Massif metamorphics and the Eğrigöz granitoid. The basal contact of the unit can only be traced in limited areas, but there is no evidence for an unconformity between the unit and the Menderes Massif (i.e. there is no distinctive basal conglomerate or erosional surface); instead, in the western and eastern margin of the Demirci basin, the conglomerates overlie the metamorphic rocks along a low-angle tectonic contact, similar to that observed in Selendi basin (Ersoy et al., 2010a) (Figure 2.6). On the other hand, the conglomerates unconformably overlie the ophiolitic mélange units of the İzmir-Ankara zone. The Kürtköyü Formation is conformably overlain by rhyolitic pyroclastic rocks and lava flows of the Sevinçler Volcanites and the Yeniköy Formation (Figure 2.8a and b).

The Yeniköy Formation is composed of yellowish sandstones and mudstones with local laminated limestone and marls, and mainly outcrops in the north of Demirci basin. The contact relationship between the Yeniköy and Kürtköyü formations is best traced along the Demirci-Simav road section. The Yeniköy Formation is cut by dacitic-rhyolitic dykes and volcanic necks and is also conformably overlain by rhyolitic pyroclastics and lava flows of the Sevinçler Volcanites. Stratigraphic and geochemical data from the dacitic-rhyolitic lavas of the Sevinçler Volcanites indicate that they are correlated with the Lower Miocene Eğreltidağ Volcanites that crops out in the northern part of the Selendi basin (Ersoy & Helvacı, 2007; Ersoy et al., 2010a). Confirming this, in this study, 19.057±0.045 (MSWD = 1.80) plagioclase and 19.748±0.047 (MSWD = 2.10) biotite Ar/Ar ages have been obtained from the Sevinçler Volcanites.

In Demirci basin, the İnay Group is composed of Akdere pyroclastics, conglomerates of the Borlu Formation, sandstone-siltstone alternations of the Köprübaşı Formation, and shales, marls and limestones of the Demirci Formation. These sedimentary rocks are interfingered with the andesitic-dacitic lava flows and

pyroclastics of the Asitepe Volcanites (Figure 2.2b and 2.4c). In the northern flank of the Simav half-graben, the İnay Group consists of Akdere pyroclastics, conglomerates and sandstones of the Borlu and Köprübaşı formations, and the Naşa basalt (Figure 2.7).

The Akdere pyroclastics mainly crop out in the northern part of Demirci basin and west of Naşa (Figures 2.6 and 2.7). In some locations, the pyroclastic rocks overlie the older units of the metamorphic rocks and the Hacıbekir Group, either directly or along a basal conglomerate (Figure 2.8c), and they also interfinger with the Borlu Formation. The Akdere pyroclastics are a key marker horizon linking the stratigraphy of the Demirci basin either side of the Simav half-graben. The thickness of the Akdere pyroclastics decreases from the north (~50 m) to the south (~1 m) within the Demirci basin, implying that they originated from a volcanic centre located further north (Figure 2.6). However, this proposed centre is obscured by the normal to oblique slip faults of the Plio-Quaternary Simav half-graben which cut and displaced the infill of Demirci basin.

The Borlu Formation of the İnay Group is composed of boulder conglomerates (mainly derived from the Menderes Massif) with sandstone intercalations of alluvial fan origin. The unit has well-preserved outcrops at the eastern and western margin of Demirci basin (Figures 2.6 and 2.7). In the northern sector of Demirci basin (so-called Akdere basin) the total thickness of the unit can reach up to 250 m. The İnay Group unconformably overlies the Menderes Massif along an erosional surface in both sectors of Demirci basin (Figure 2.8d). Towards the centre of the basin, the conglomerates pass laterally into grey to green colored semi-lithified sandstone-claystone alternations of the Köprübaşı Formation (see also Yılmaz et al., 2000) that also includes locally developed marl and limestone lenses. The unit show well-developed syn-depositional deformation structures, especially along the western margin of Demirci basin (Figure 2.8c).
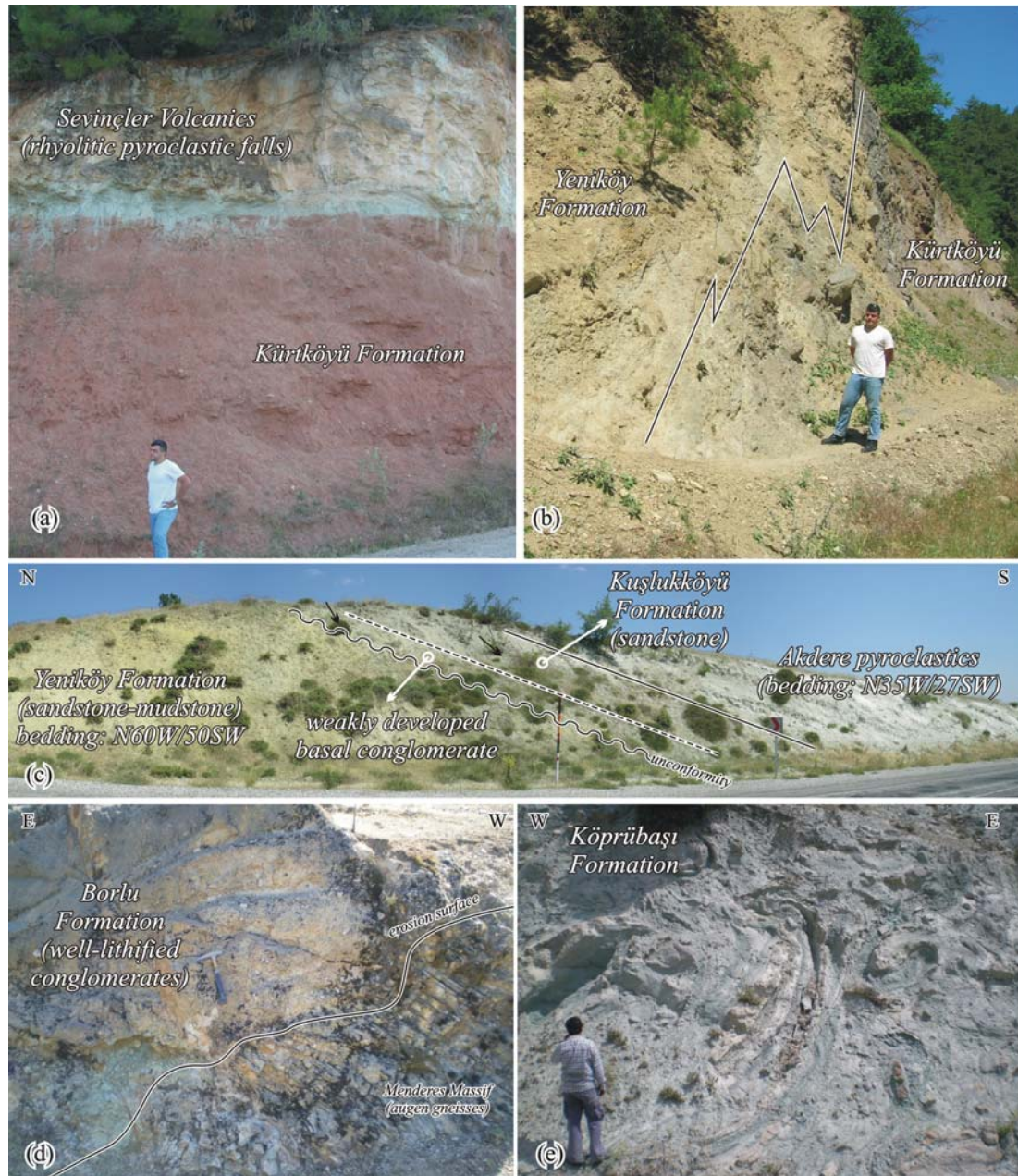
Figure 2.8 Field photographs from Demirci basin. (a) conformable contact between the reddish conglomerates of the Kürtköyü Formation and the pyroclastic deposits of the Sevinçler Volcanites of the Lower Miocene Hacıbekir Group, (b) transitional contact relation between the boulder conglomerates of the Kürtköyü Formation and the sandstones of the Yeniköy Formation, (c) unconformity between the Lower Miocene Yeniköy Formation of the Hacıbekir Group and the Middle Miocene İnay Group, (d) unconformity between the well-lithified conglomerates of the Borlu Formation of the Middle Miocene İnay Group and the metamorphic rocks of the Menderes Massif (note that the foliation planes of the metamorphics were perpendicularly cut by the erosional surface), and (e) syn-depositional deformation structures (slumps) in the Köprübaşı Formation of the Middle Miocene İnay Group, which were developed close to the basin bounding faults.

The Köprübaşı Formation is conformably overlain by the Asitepe Volcanites in the eastern margin of Demirci basin. These volcanic rocks are composed of pyroclastic rocks and andesitic lava flows, originating from a volcanic center located at the eastern margin of the basin, with field observations showing that the pyroclastic rock intercalations (ignimbrites) flowed southward. The ignimbrites are overlain by block-and-ash fall and finally andesitic-dacitic pink-colored plagioclase-phyric lavas. The Asitepe Volcanites can be correlated with the middle Miocene Yağcıdağ Volcanites in the Selendi basin (Ersoy et al., 2008) on the basis of their stratigraphic positions, lithology and geochemistry. In this study, 17.580 ± 0.094 Ma (MSWD = 0.52) plagioclase Ar/Ar age is obtained from the lavas of the Asitepe Volcanites. The Naşa basalt (15.8 ± 0.3 and 15.2 ± 0.3 Ma K-Ar ages of Ercan et al., 1996; Table 2.1) is composed mainly of syn-sedimentary basaltic lava flows that flowed over the sedimentary rocks of the Borlu Formation.

In Demirci basin, the Köprübaşı Formation passes transitionally into the marls, bituminous shales and limestones (with claystone and sandstone intercalations) of the Demirci Formation (İnci, 1984; Figures 2.2b and 2.4), which can be correlated with the Ulubey Formation in Selendi basin (Seyitoğlu, 1997a; Ersoy et al., 2010a). Small basaltic outcrops mapped on the eastern margin of Demirci basin (named here as the Taşokçular basalt) have similar geochemical features to the late Miocene basalts in Selendi basin. The youngest unit in Demirci basin is the basaltic lavas and pyroclastics with cinder cones of the Quaternary Kula volcanites that crop out to the south of the basin, on the northern shoulder of the Pliocene-Quaternary Gediz graben (Figure 2.1).

2.1.3 Emet Basin

Emet basin (Akdeniz & Konak, 1979; Helvacı, 1986; Figure 2.2c), is located between the Eğrigöz granitoid intruded into the Menderes Massif metamorphic rocks to the west, and the Afyon zone metamorphic rocks to the east (Figures 2.1 and 2.9). The stratigraphy of Emet basin comprises two Neogene volcano-sedimentary units separated by a regional unconformity (Figure 2.2c). These units can be correlated

with similar rocks from other basins on the basis of their age, lithology and deformational features, hence they are named here as the Hacıbekir and İnay groups. In this basin, the İnay Group hosts the world's biggest colemanite and probertite borate deposits (Helvacı, 1984, 1986; Helvacı & Alonso, 2000).
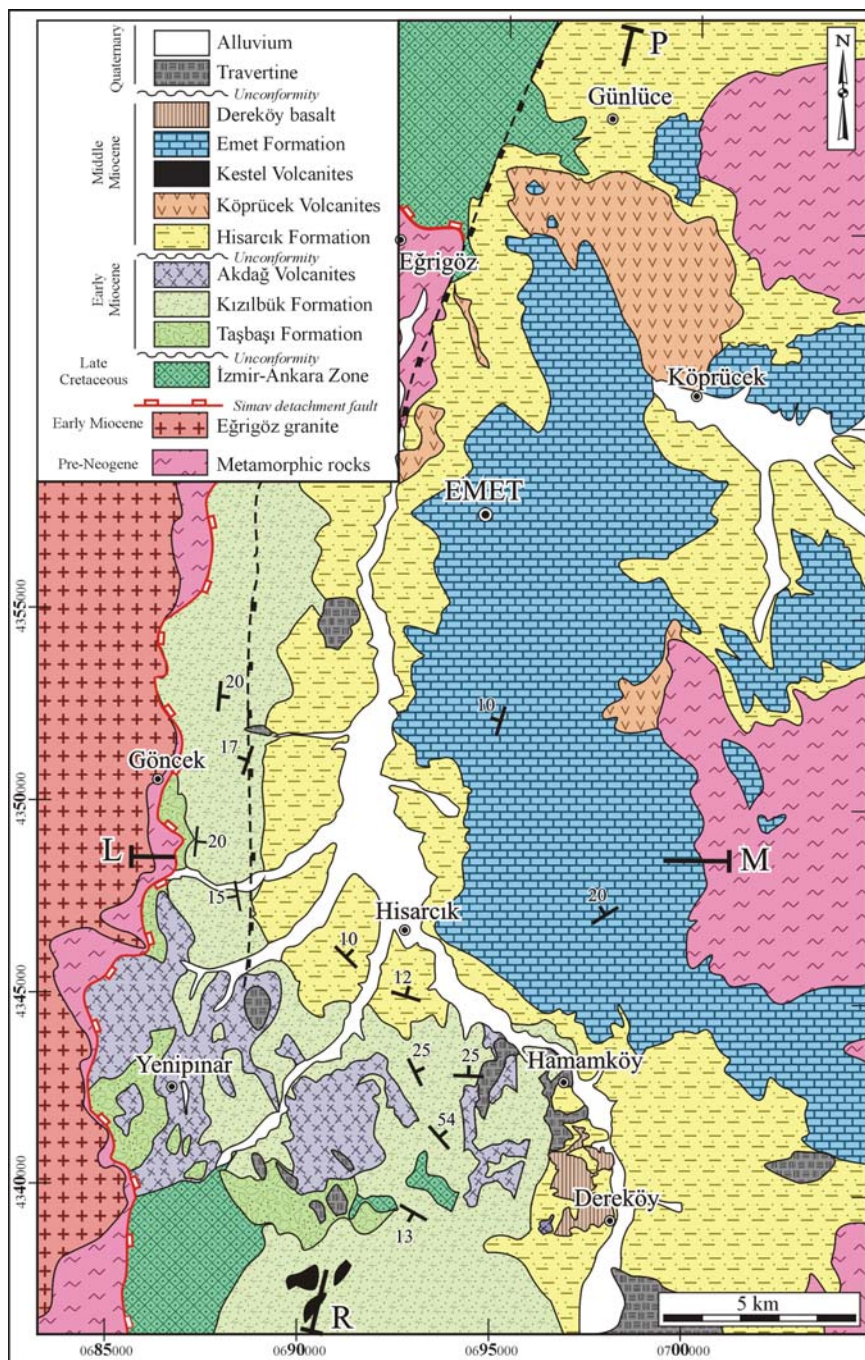
Figure 2.9 Geological map of Emet basin (modified from Helvacı, 1984 and 1986). See Figure 2.1 for location.

According to field data, the Hacıbekir Group consists of the Taşbaşı and Kızılbük formations and the Akdağ Volcanites (Figure 2.2c). The Taşbaşı Formation crops out to the western and southwestern parts of the Emet basin (Figure 2.9), and is made up of reddish-brown colored conglomerates with grayish sandstone intercalations deposited in alluvial fan facies. The conglomerates include unsorted and angular clasts derived from schists, marbles and granites. The basal contact of the unit is represented by a low-angle fault with the Menderes Massif, while the unit unconformably overlies the rocks of the İzmir-Ankara zone (Figure 2.4f). The Taşbaşı Formation is locally interfingered by rhyolitic pyroclastic rocks of the Akdağ Volcanites, and is conformably overlain by the Kızılbük Formation. The age of the unit is interpreted to be early Miocene on the basis of radiometric age data from the volcanic rock intercalations.

The Kızılbük Formation crops out in a large area to the western and southwestern parts of the Emet basin and composed of coal-bearing yellowish sandstone-siltstone-mudstone alternations and laminated limestone of fluvio-lacustrine origin. The Kızılbük Formation is interfingered by pyroclastic rocks of the Akdağ Volcanites, which are composed of rhyolitic lava flows, domes and pyroclastics with epiclastics. The Akdağ Volcanites have yielded 20.3±0.6 (Seyitoglu et al., 1997) and 19.0±0.2 Ma (Helvacı & Alonso, 2000) K-Ar ages (Table 2.1).

The İnay Group in Emet basin is made up of the Hisarcık and Emet formations that interfinger with the Köprücek volcanites, Kestel volcanites and the Dereköy basalt (Figure 2.2c). The Hisarcık Formation (Akdeniz & Konak, 1979) crops out in a large area in the Emet basin and is composed of conglomerates, pebblestones and sandstone intercalations. The age of the Hisarcık Formation is accepted to be middle Miocene on the basis of volcanic intercalations in the İnay Group. Towards the centre of the basin, the Hisarcık Formation passes laterally into the Emet Formation that is composed of sandstone-claystone-mudstone alternations of fluvio-lacustrine origin. The fine-grained parts of the unit, especially the mudstone-claystone levels contain large borate deposits which are mined for colemanite and ulexite.

The Kestel volcanites emplaced in a NE-SW-direction to the southwest of the basin. These volumetrically small volcanic rocks overlie the Kızılbük Formation. The age of the Kestel volcanites was stratigraphically accepted to be early Miocene, but the radiometric age data show that this volcanic units is middle Miocene in age (15.914±0.074, MSWD = 1.30 and 15.730±0.110, MSWD = 1.60; biotite Ar/Ar ages) (Table 2.1).

The Köprücek Volcanites crop out to the northern part of Emet basin (Figure 2.9). The unit is composed of andesitic to rhyolitic lava flows, dykes and associated pyroclastics which interfinger with the Hisarcık Formation. The thickness of the pyroclastic intercalations in the Hisarcık Formation increases towards the north of the basin, which suggests that the Köprücek Volcanites originated from this area (Figures 2.4g and 2.9). The Köprücek Volcanites are overlain by the limestones of the Emet Fomation. The pyroclastic intercalations yield 16.8±0.2 Ma K-Ar age (Helvacı & Alonso, 2000; Table 2.1). In the southern part of the basin, the Hisarcık Formation is also conformably overlain by basaltic lava flows of the Dereköy basalt. Along the basal contact of the Dereköy basalt several pepperitic textures are developed, indicating a syn-sedimentary emplacement of the lavas. The Dereköy basalt has been dated as 15.4±0.2 and 14.9±0.3 Ma (K-Ar ages, Helvacı & Alonso, 2000; Seyitoğlu et al., 1997).

2.2 Structural Data

2.2.1 Early Miocene Events

Both the western and eastern margins of Gördes basin are bounded by NNE–SSW-trending right-lateral strike-slip faults, along which the early Miocene sedimentary rocks (the Kızıldam Formation) were deposited (see Figures 2.3, 2.4a and 2.10a). In the eastern margin of Gördes basin several fault planes of the Kızıldam fault zone (Figure 2.3) have been measured with a strike of 18–35°, a dip of 62–70° to the NW, and a rake of 17–27°N (Figure 2.10c). The metamorphic rocks

were observed to be intensely deformed along the Kızıldam fault zone, such that in some places, the foliation planes of the metamorphic rocks became vertical along the eastern faulted margin (Figure 2.3). The boulder conglomerates of the Kızıldam Formation was also deposited on an E–W-trending dip-slip normal fault zone (Börez fault Zone) in the Börez-Salur districts (Figures 2.3 and 2.10b) where a fault plane strikes nearly E–W and dips ~85–89°S with a rake of ~90°. In the western margin of Gördes basin, N–S- to NE–SW-trending right-lateral strike-slip faults (the Göcek fault zone, Figures 2.3 and 2.10a) controlled the deposition of the Kızıldam Formation. Here, a right-lateral strike-slip fault plane of the Göcek fault zone is defined by strikes between 05–20° and dips ~85°SE with a rake of ~0°. Structural data from Gördes basin are shown on a stereographic plot (Figure 2.10d). These data indicate that Gördes basin formed under the control of NE–SW-trending strike-slip faults and E–W-trending dip-slip normal faults where the N–S extension is slightly oblique to the margins that bounded the basin.

In the northeastern part of Demirci basin, to the southeast of Sevinçler village (Figure 2.6), the contact relationship between the Lower Miocene Hacıbekir Group (the Kürtköyü and Yeniköy formations) and the tectonically underlying Menderes Massif is well-exposed (S-T cross section in Figure 2.11). The reddish conglomerates of the Kürtköyü Formation are underlain by metamorphic rocks and separated by a low-angle fault, along which the metamorphic rocks were progressively deformed in a ~70 m shear zone which is characterized by ductile deformation overprinted by cataclastites. The transition from ductile to brittle deformation, with top to the N-NE sense of shear, indicates that the low-angle fault is normal in character. The low-angle normal fault between the Hacıbekir Group and the metamorphic basement along the eastern margin of the Demirci basin also outcrops in a small area in the southeast of the study area (~1.5 km southeast of Taşokçular village; Figure 2.6).
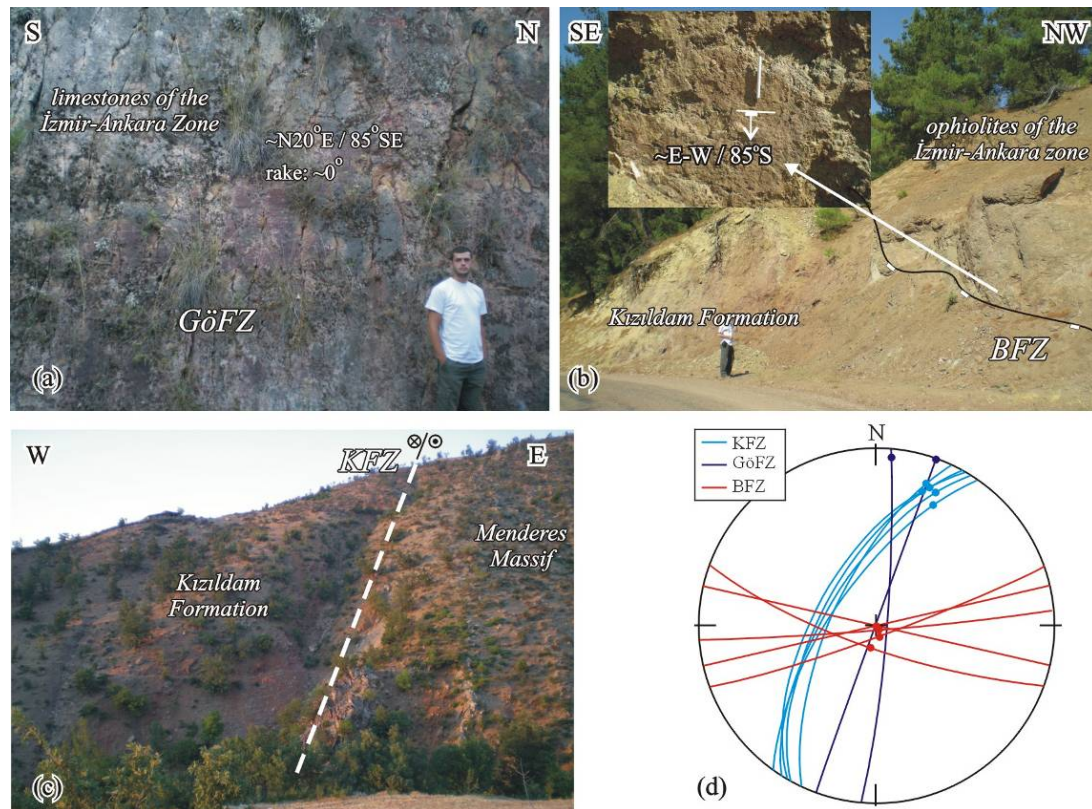
Figure 2.10 (a) A right-lateral strike-slip fault plane of the Göcek fault zone (GöFZ) developed in the limestones of the İzmir-Anakara zone rocks at the western margin of Gördes basin (UTM: 35S 05928983/4312823), (b) A normal fault plane of the Börez fault zone (BFZ) (UTM: 35S 0610169/4321133), (c) field view of the right-lateral strike-slip Kızıldam fault zone (KFZ) between the metamorphic rocks of the Menderes Massif and the conglomerates of the Kızıldam Formation at Kızıldam village, (d) Lower hemisphere equal-area stereographic plots of poles for the fault planes from the KFZ, GöFZ and BFZ.

The low-angle normal-faulted contact relationship between the Kürtköyü Formation and the metamorphic basement is also observed in the northwestern part of Demirci basin, where conglomerates of the Kürtköyü Formation are separated from the augen gneisses of the Menderes Massif by a low-angle (~30°) fault plane (Figure 2.6). Mylonitic augen gneisses show progressive deformational features towards the fault plane, as they become cataclastized (Figure 2.12). The fault surface is marked by brownish and reddish fine-grained cataclastics which are very hard and also brittle in hand specimen. The deformational textures of the metamorphic rocks shown in Figure 2.12 clearly indicate that the ductile deformed mylonitic rocks were also overprinted by a brittle deformation that is characterized by micro-scale faults

and fragmented crystals of quartz and feldspar. The deformational textures also indicate a top to N-NE sense of shear (Figure 2.12).
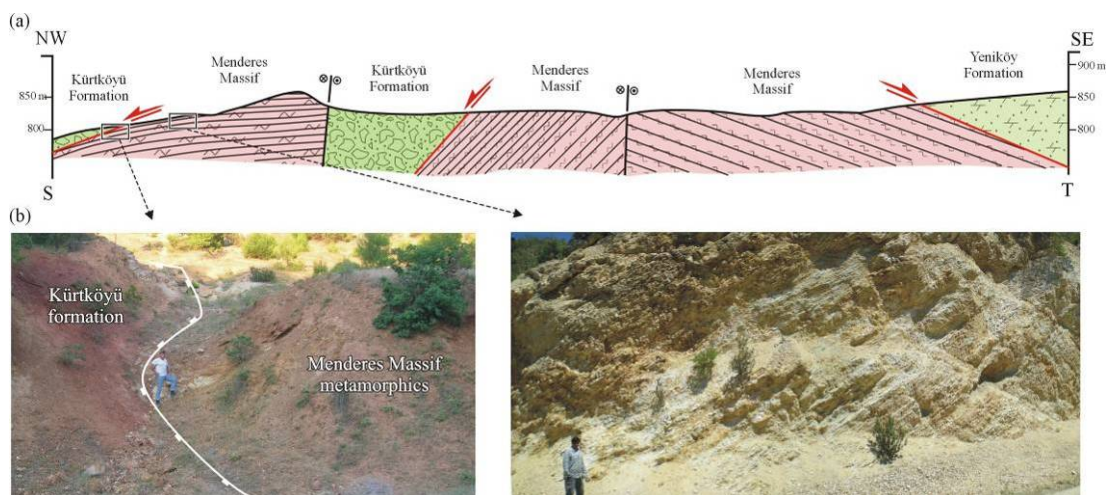
Figure 2.11 (a) S-T geological cross section in the northeastern area of Demirci basin (see Figure 2.7 for location), and (b) related field photos.
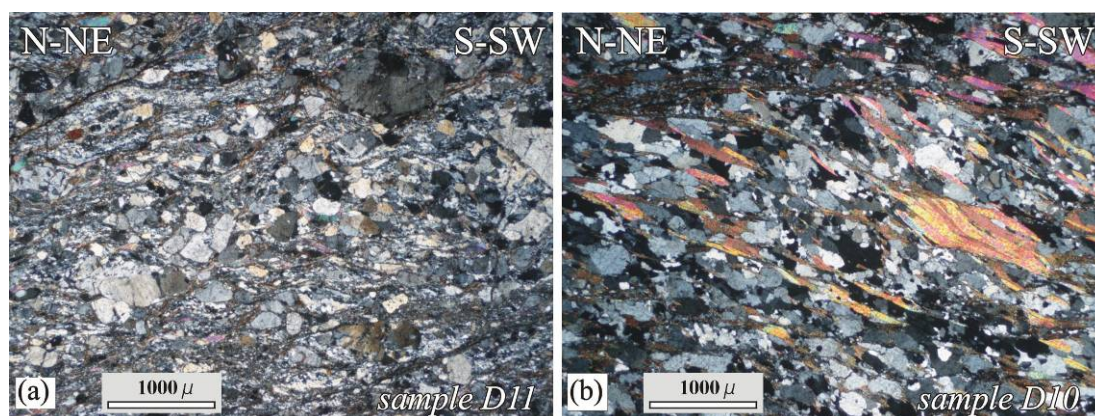
Figure 2.12 Microscope view of (a) cataclastic gneisses just below the low-angle normal fault, and (b) ductilely deformed gneisses.

A similar low-angle normal faulted contact between the metamorphic rocks of the Menderes Massif and the Hacıbekir Group (Taşbaşı and Kızılbük formations) is also recognized at the western part of Emet basin (Figures 2.4f and 2.9). The metamorphic rocks were intruded by the Eğrigöz granitoid, causing development of a 3–20 m thick chilled-margin. Away from the intrusive contact, the metamorphics are tectonically overlain by the conglomerates of the Lower Miocene Taşbaşı Formation (Figure 2.4f). In Emet basin, the metamorphic rocks also tectonically underlie

sandstones of the Lower Miocene Kızılbük Formation in the vicinity of Kestel village. Deformational features of the sheared metamorphic rocks beneath the tectonic contact are very similar to those observed in Demirci basin.

2.2.2 Middle Miocene Events

NE-SW-trending high-angle strike- to oblique-slip faulting in the region is observed in Demirci and adjacent basins. The eastern margins of Demirci basin were deformed by nearly NE–SW-trending right-lateral strike- to oblique-slip faults with a normal component (Figure 2.6). The middle Miocene volcano-sediments partially overlap onto these faults. The Middle Miocene Asitepe Volcanites and the Naşa basalt are also located on these NE–SW-trending faults. In contrast, the western margin of these basins was deformed by left-lateral strike- to oblique-slip faults with a normal component (Figures 2.6 and 2.13a). The sedimentary facies of the İnay Group show a gradual change from coarse- to fine-grained the clasts, from the margins of the basin to the centre, as well as from bottom to top. These features indicate that facies development of these middle Miocene units was controlled by the NE-SW-trending faults that were active during sediment transport and deposition.

In the eastern margin of Demirci basin, a NE–SW-trending fault zone is interpreted to have controlled the deposition of the Middle Miocene Borlu Formation, because the coarser-grained sediments of the unit are located on the hanging-wall of this fault and the sediment becomes finer-grained further away from the fault. Several planes have been measured, which strike 16–55° and dip 48–90°NW, with two distinct rakes of 45–72°S and 70–86°N. In the western margin of Demirci basin, a dextral fault plane is recognized striking at 25° and dipping at 55°SE, with a rake of 14–22°NE (Figure 2.13a and b). These faults juxtapose the Borlu Formation on the hanging wall with the Menderes Massif on the footwall. All these data indicate that the Middle Miocene İnay Group was deposited in the Demirci basin which was bounded by NE–SW-trending strike- to oblique-slip high-angle faults with a normal component.
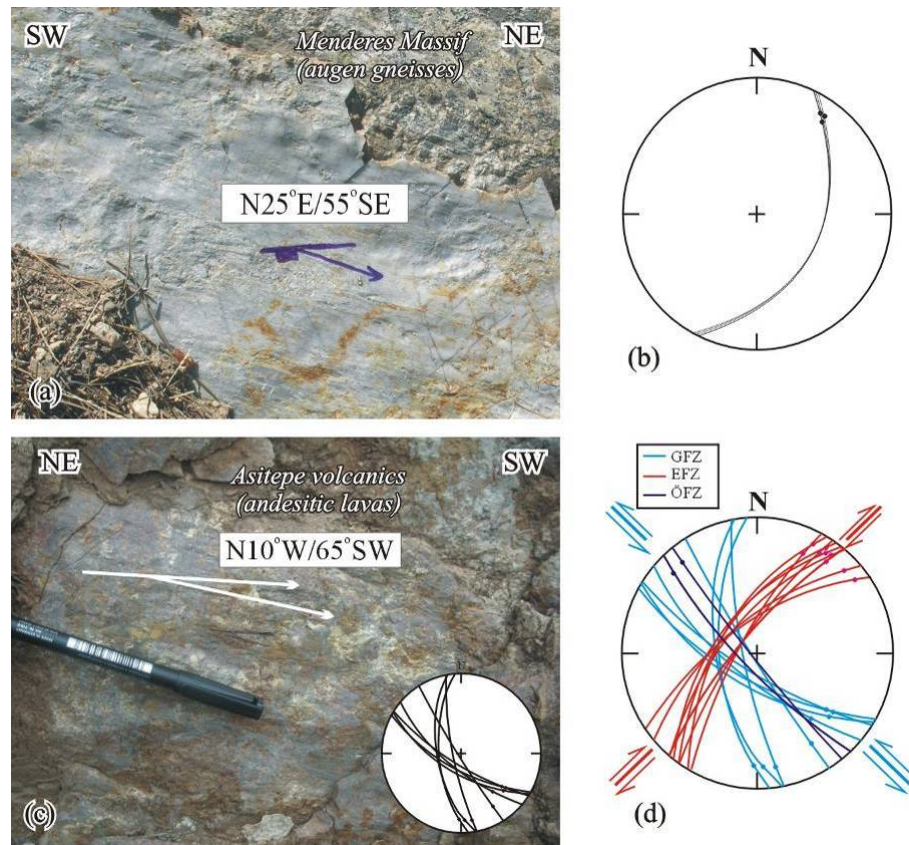
Figure 2.13 (a) a left-lateral oblique-slip normal fault developed in the gneisses of the Menderes Massif, which controlled the deposition of the Middle Miocene İnay Group at the western margin of Demirci basin (UTM: 35S 0642236/4329700), (b) Lower hemisphere equal-area stereographic plot of poles for the fault in (a); (c) a fault plane from the left-lateral strike-slip Güneşli fault zone developed in the andesitic lavas of the Middle Miocene Asitepe Volcanites (UTM: 35S 0631540/4307598). (d) Lower hemisphere equal-area stereographic plot of poles for the late Miocene faults: left-lateral strike-slip Güneşli fault zone (GFZ), right-lateral strike-slip Eskin fault zone (EFZ), left-lateral strike-slip Ören fault zone (ÖFZ).

Deposition of the Middle Miocene İnay Group in Emet basin (the Hisarcık and Emet formations) was also controlled by a nearly N–S-trending fault located on the western margin of the basin, similar to that observed in Demirci basin, with coarse-grained alluvial fans of the Hisarcık Formation located along the N–S-trending fault. However, there is no evidence for middle Miocene faulting on the eastern margin of the basin where the Emet Formation overlaps onto the metamorphic rocks of the

Afyon zone (Figures 2.4f and 2.9). The İnay Group was also controlled by NE–SW-
trending faults in the Selendi and Güre basins.

2.2.3 Late Miocene Events

In Demirci basin, the NW-SE-trending left-lateral fault zone cuts the Middle
Miocene Asitepe Volcanites and the Köprübaşı Formation, and the basement rocks
(Güneşli fault zone; Figure 2.6). Well-exposed fault planes show a dominant strike-
slip component (Figure 2.13c). The fault zone can be traced outside Demirci basin,
where it also cuts the metamorphic highs between the Demirci and Gördes basins
(Figure 2.1), and into the Güneşli district in the northern part of Gördes basin (Figure
2.3). NW–SE-trending left-lateral faulting is also seen in the Ören fault zone (Figures
2.6, 2.13d), which cuts the metamorphic high between the Demirci and Selendi
basins, and the early Miocene volcano-sedimentary units in both basins (Figure 2.1).
The right-lateral strike-slip Eskin fault zone deformed the eastern part of the Selendi
basin (Figures 2.1 and 2.13d) and controlled the emplacement of the late Miocene
basalts and associated sediments (Ersoy et al., 2010a).

2.2.4 Plio-Quaternary Events

The youngest structural element in the region is the high-angle dip- to oblique-slip
normal faults that form the southern margin of the Pliocene–Quaternary Simav half-
graben (see also Seyitoğlu, 1997b). The high angle normal faults cut the
metamorphic basement, the early Miocene Kürtköyü and Yeniköy formations, the
Güneşli volcanites and the rocks of the İzmir-Ankara zone in Demirci basin. ~2 km
south of Yeniköy village a fault plane strikes 80–85° and dips ~65–84°NE, with a
rake of 43–65°E, indicating that the fault has right-lateral strike-slip component. The
early-middle Miocene strata show a southwestward decrease in inclination that
indicates that the northern part of Demirci basin back-tilted to the south due to
vertical movement along the Simav fault (Figures 2.4e and 2.6).

2.3 Comparison with the Adjacent Basins

2.3.1 Stratigraphic Correlation

The Neogene volcano-sedimentary succession in Bigadiç basin contains the Kocaiskan volcanites (23.6±0.6 to 23.0±2.8 Ma, Table 2.1) that are composed of andesitic volcanites and the unconformably overlying Bigadiç volcano-sedimentary succession (Figure 2.14a). The later consists of borate-bearing lacustrine sediments and coeval felsic (Kayırlar, Sındırgı and Şahinkaya volcanites; 20.8±0.7 to 17.8±0.4 Ma K-Ar and Ar/Ar ages) and mafic (Gölcük basalt, 19.7±0.4 Ma K-Ar and 20.5±0.1 Ma Ar/Ar ages) volcanic rocks (Helvacı, 1995; Helvacı & Alonso, 2000; Erkül et al., 2005a,b). These rock units are also unconformably overlain by late Miocene-Pliocene continental detritus and alluvium. The radiometric ages and the stratigraphic relations clearly indicate that the borate-bearing succession was deposited during early Miocene and is very similar to that of Gördes basin (Figure 2.14b).
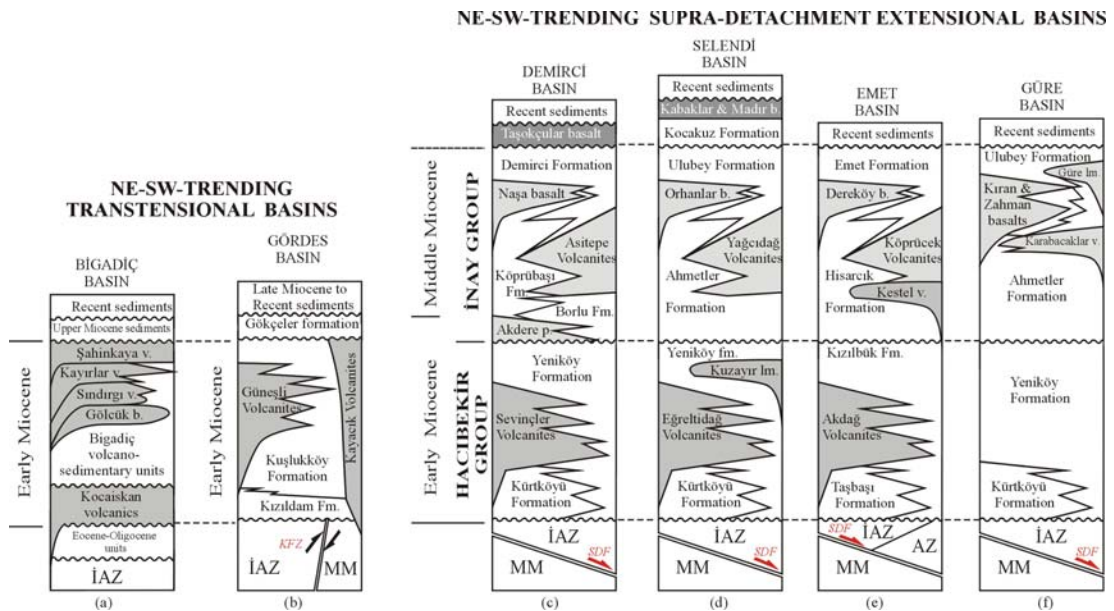
Figure 2.14 Correlative stratigraphic sections of the NE–SW-trending basins in Western Anatolia. (a) from Erkül et al. (2005a), (b-e) this study, (f) from Karaoğlu et al. (2010). MM-metamorphic rocks of the Menderes Massif, İAZ-İzmir-Ankara zone rocks, AZ-metamorphic rocks of the Afyon zone, KFZ-Kızıldam fault zone, SDF-Simav detachment fault, v–volcanites, fm–formation, p–pyroclastics, b–basalt.

Both the Selendi and Güre basins are characterized by two major volcano-sedimentary units: the Hacıbekir and İnay groups (Figure 2.14; Ercan et al., 1978, Seyitoğlu, 1997a; Westaway et al., 2004; Ersoy & Helvacı, 2007; Ersoy et al., 2010; Karaoğlu et al., 2010), whereas these middle Miocene volcano-sedimentary units are absent from the Bigadiç and Gördes basins. Rather, the stratigraphy of the Selendi and Güre basins is comparable with that of the Demirci and Emet basins (Figure 2.14c and e). The Lower Miocene Hacıbekir Group in these basins overlies the metamorphic basement with a tectonic contact, but the ophiolitic mélange rocks with an unconformity (see also Ersoy & Helvacı, 2007; Ersoy et al., 2010a). The Hacıbekir Group consists of conglomerates of the Kürtköyü Formation and sandstone-mudstone alternations of the Yeniköy Formation in the Demirci, Selendi and Güre basins and Taşbaşı and Kızılbük formations in the Emet basin. These fluvio-lacustrine units are interfingered with the felsic volcanic products of the Eğreltidağ volcanites (20.35±0.55 to 18.9±0.1 Ma Ar/Ar and K-Ar ages Seyitoğlu et al., 1997; Ersoy et al., 2008, 2010a) and the lamproitic lavas of the Kuzayır lamproite (18.6±0.2 to 17.59±0.85 Ma Ar/Ar ages; Ersoy et al., 2008, 2010a) in Selendi basin, the Sevinçler Volcanites in Demirci basin and the Akdağ and Kestel Volcanites in Emet basin. The unconformably overlying İnay Group is mainly composed of detrital units of fluvio-lacustrine origin (the Ahmetler and Hisarcık formations) and fresh-water limestones and marls (the Ulubey and Emet formations).

The İnay Group is intercalated with several syn-sedimentary volcanic products in the Demirci, Selendi, Emet and Gördes basins. These volcanites comprise; (1) the andesitic lava flows and pyroclastics of the Yağcıdağ Volcanites (16.61±0.14 to 14.9±0.6 Ma K-Ar and Ar/Ar ages; Seyitoğlu et al., 1997; Purvis et al., 2005) and basaltic lava flows of the Orhanlar basalt in Selendi basin, (2) the Asitepe Volcanites and Naşa basalt (15.8±0.3 to 15.2±0.3 Ma K-Ar ages; Ercan et al., 1996) in Demirci basin, (3) the Kıran and Zahman basalts (15.5±0.4 Ma K-Ar age; Seyitoğlu et al., 1997), Karabacaklar volcanites (15.9±0.4 to 15.1±0.4 Ma K-Ar and 16.02±0.13 to 15.93±0.08 Ma Ar/Ar ages; Seyitoğlu et al., 1997; Karaoğlu et al., 2010) and Güre lamproite (14.20±0.12 Ma Ar/Ar age; Innocenti et al., 2005) in Güre basin, and (4)

the Köprücek volcanites (16.8±0.2 Ma K-Ar age; Helvacı & Alonso, 2000) and Dereköy basalt (15.4±0.2 and 14.9±0.3 Ma K-Ar ages; Helvacı & Alonso, 2000; Seyitoglu et al., 1997) in Emet basin. The Ilıcasu lamproite (15.87±0.13 to 15.83±0.13 Ma Ar/Ar ages; Innocenti et al., 2005) also interfingers with the İnay Group and outcrops in the footwall rocks of the Simav half-graben. Karaoğlu et al. (2010) also present 17.29±0.13 to 12.15±0.15 Ma Ar/Ar ages from the Beydağ volcanic unit interfingers with the İnay Group in the Uşak basin. The Hacıbekir and İnay groups are in turn unconformably overlain by the Upper Miocene Kocakuz Formation (Ersoy & Helvacı, 2007, Seyitoğlu et al., 2009, Ersoy et al., 2010a) and Kabaklar basalt (8.50±0.20 to 8.37±0.07 Ma K-Ar and Ar/Ar ages; Ercan et al., 1996; Innocenti et al., 2005).

2.3.2 Structural Correlation

The strike-slip faults, which were active during the early Miocene, are recognized in the Bigadiç and Gördes basins. In Bigadiç basin, Erkül et al., (2005b) recognized; (1) NE–SW- and NW–SE-trending mainly strike- to oblique-slip faults, (2) NE–SW-trending thrust faults which are reactivated as dip-slip normal faults, and (3) NE–SW-trending folds which are interpreted to be related to compressional deformation developed between the NE–SW- and NW–SE-trending oblique-slip faults after deposition of the Neogene succession. These authors indicated that Bigadiç basin was deformed under NW–SE directed compression and NE–SW directed extension developed in a NE–SW-trending strike-slip deformational zone. Similarly, the early Miocene volcano-sedimentary succession in Gördes basin was deposited along right-lateral strike-slip faults (~N–S-trending Göcek fault zone to the west and ~NE–SW-trending Kızıldam fault zone to the east; Figure 2.3). In Gördes basin, the early Miocene sediments were also controlled by ~E–W-trending normal faults (Börez fault zone). The NE–SW-trending right-lateral strike- to oblique-slip Kızıldam and Göcek fault zones, together with the E–W-trending normal Börez fault zone were likely developed during N–S-trending extension in the early Miocene, hence Gördes basin (and Bigadiç basin) are interpreted to be transtensional basins (Figure 2.14) controlled by strike-slip and normal faults.

Early Miocene extensional detachment faulting which is correlated with the Simav detachment fault (SDF; Işık & Tekeli, 2001), developed in the Demirci, Selendi and Güre basins, where the Lower Miocene Hacıbekir Group tectonically overlies the metamorphic rocks (Ersoy et al., 2010a). The conglomerates of the Middle Miocene İnay Group (the Ahmetler and Borlu formations) directly overlie the metamorphic rocks of the Menderes Massif along an erosional surface, indicating that the detachment faulting (SDF) in the region ceased before deposition of these sediments.

The Middle Miocene İnay Group in the Demirci, Selendi, Emet and Güre basins was deposited along the NE–SW-trending strike- to oblique-slip faults (Seyitoğlu, 1997a, Ersoy et al., 2010a). In the western margin of Güre basin, the alluvial fans of the İnay Group also developed on the hanging walls of these NE–SW-trending faults, which also served as the sites for emplacement of the Kıran-Zahman basalts (Ersoy et al., 2010a; Karaoğlu et al., 2010; Figure 2.1). The western margin of Emet basin is marked by a ~N–S-trending fault along which the Middle Miocene Hisarcık Formation of the İnay Group was deposited. This fault can be correlated with the NE–SW-trending left-lateral oblique-slip faults bounding the western margin of the Selendi basin, along which the Middle Miocene Ahmetler Formation of the İnay Group was deposited (see also Seyitoğlu, 1997a; Ersoy et al., 2010a). Faults with similar directions and ages can be seen in the west of Demirci basin, but the eastern part of this basin is marked by NE–SW-trending right-lateral oblique-slip faults along which the İnay Group deposited and which are overlain by the Asitepe Volcanites and the Naşa basalt that erupted along the fault (Figures 2.7 and 2.8). These data show that the eastern margins of the Demirci, Selendi and Güre basins were controlled by NE–SW-trending right-lateral strike- to oblique slip faults while western margins by NE–SW-trending left-lateral strike- to oblique slip faults (see also Ersoy et al., 2010a).

In Selendi basin, late Miocene NE–SW-trending right-lateral strike-slip and related normal faults (the Eskin fault zone, Figure 2.1) controlled the deposition of the Upper Miocene Kocakuz Formation and emplacement of the late Miocene

Kabaklar basalt (Ersoy & Helvacı, 2007; Ersoy et al., 2008, 2010a). In Demirci basin, there are several NW–SE-trending left-lateral strike-slip fault zones (the Güneşli and Ören fault zones, Figures 2.1 and 2.6) which cut and displace the middle Miocene volcano-sedimentary units. On the basis of their stratigraphic relations, it has been suggested that the NW–SE-trending left-lateral and the NE–SW-trending right-lateral strike-slip faults that cut the metamorphic highs between the Gördes, Demirci, Selendi and Güre basin can be correlated with similarly trending faults that cut the early-middle Miocene basin fill.

The nearly E–W-trending Pliocene-Quaternary high-angle normal faults bounding the Gediz graben and the Simav half-graben can be similarly correlated with the Küçük and Büyük Menderes grabens, located further south (Cohen et al., 1995; Emre, 1996; Hakyemez et al., 1999; Bozkurt, 2000; Sarıca, 2000; Gessner et al., 2001b; Bozkurt & Sözbilir, 2004).

2.3.3 Geochemical Correlation

Volcanic intercalations in the NE-SW-trending Neogene volcano-sedimentary basins can be grouped as; (1) early Miocene high-K calc-alkaline andesite, dacite and rhyolite, (2) early Miocene ultrapotassic-shoshonitic mafic volcanic rocks, (3) middle Miocene high-K calc-alkaline andesite and dacite, (4) middle Miocene ultrapotassic-shoshonitic mafic volcanites, (5) late Miocene mafic lavas, and (6) Quaternary alkali basaltic volcanism.

Among group (1), the Sındırgı Kayacık, Güneşli, Sevinçler, Eğreltidağ, Akdağ Volcanites have similar geochemical compositions which plot in the dacite and rhyolite fields on a total alkalis (K_2O+Na_2O) versus silica (SiO_2) (TAS-IUGS) diagram (LeMaitre, 2002), on which the alkaline-sub-alkaline discrimination line of Irvine & Barragar (1971) is also shown (Figure 15a). These rocks show medium- to high-K calc-alkaline affinity. Note also that the Eğreltidağ Volcanites from Selendi basin and the Sevinçler Volcanites from Demirci basin have nearly identical geochemical features.

The Kayırlar volcanites from Bigadiç basin have lower SiO_2 contents and form intermediate compositions between the group (1) dacitic-rhyolitic samples and the group (2) early Miocene mafic volcanic units in Bigadiç basin. These comprise the Gölcük basalt (calc-alkaline shoshonite), which differs from the other early Miocene mafic samples of the Selendi and Emet basins that have higher K contents (shoshonitic to ultrapotassic Kuzayır lamproite). These data indicate that the early Miocene volcanism in all the NE–SW-trending basins is characterized by a bimodal volcanic association, dominated by calc-alkaline dacitic-rhyolitic members. For comparison the early Miocene Eğrigöz granitoid is also shown in Figure 2.15a, from which it can be seen that it has a nearly identical composition to the coeval volcanites.

The middle Miocene volcanism in the region is characterized by a second-stage bimodal volcanic association, including the group (3) high-K calc-alkaline to andesites and dacites, and the group (4) shoshonitic to ultrapotassic mafic products such as lamproites, ultrapotassic shoshonites, ultrapotassic latites (Figure 2.15b). These volcanic rocks interfinger with the Middle Miocene İnay Group in the Demirci, Selendi, Güre and Emet basins. However, there was no coeval volcanic activity in the Bigadiç and Gördes basins. The middle Miocene mafic volcanic rocks of the Naşa, Orhanlar, Dereköy, and Kıran-Zahman basalts, and the Güre and Ilıcasu lamproites are geochemically well-correlated, as are the middle Miocene Asitepe, Yağcıdağ and Köprücek felsic volcanites. It should be noted that the potassium contents of both the mafic and felsic members increase from west to east. When compared with the early Miocene bimodal activity, it is clear that more mafic volcanic rocks were produced during the middle Miocene, and that the felsic members have lower SiO_2 contents than the early Miocene felsic units. The composition of the middle Miocene Salihli and Turgutlu granitoids are also shown for comparison, and again they have lower silica and potassium contents than the early Miocene Eğrigöz granitoid.

During the late Miocene the group (5) volcanic rocks (mildly alkaline basalts, K-trachybasalt and shoshonites) were produced which are more mafic than the early-

middle Miocene volcanites (Figure 2.15c). This pulse of volcanic activity is characterized by the absence of the felsic magmas. These rocks occur only in the Demirci and Selendi basins. Finally, the Quaternary is represented by the strongly alkali group (6) basaltic (tephrite, basanite, phonotephrite) volcanic activity emplaced on the northern flank of the Gediz graben (Kula volcanites, Figure 2.15d).
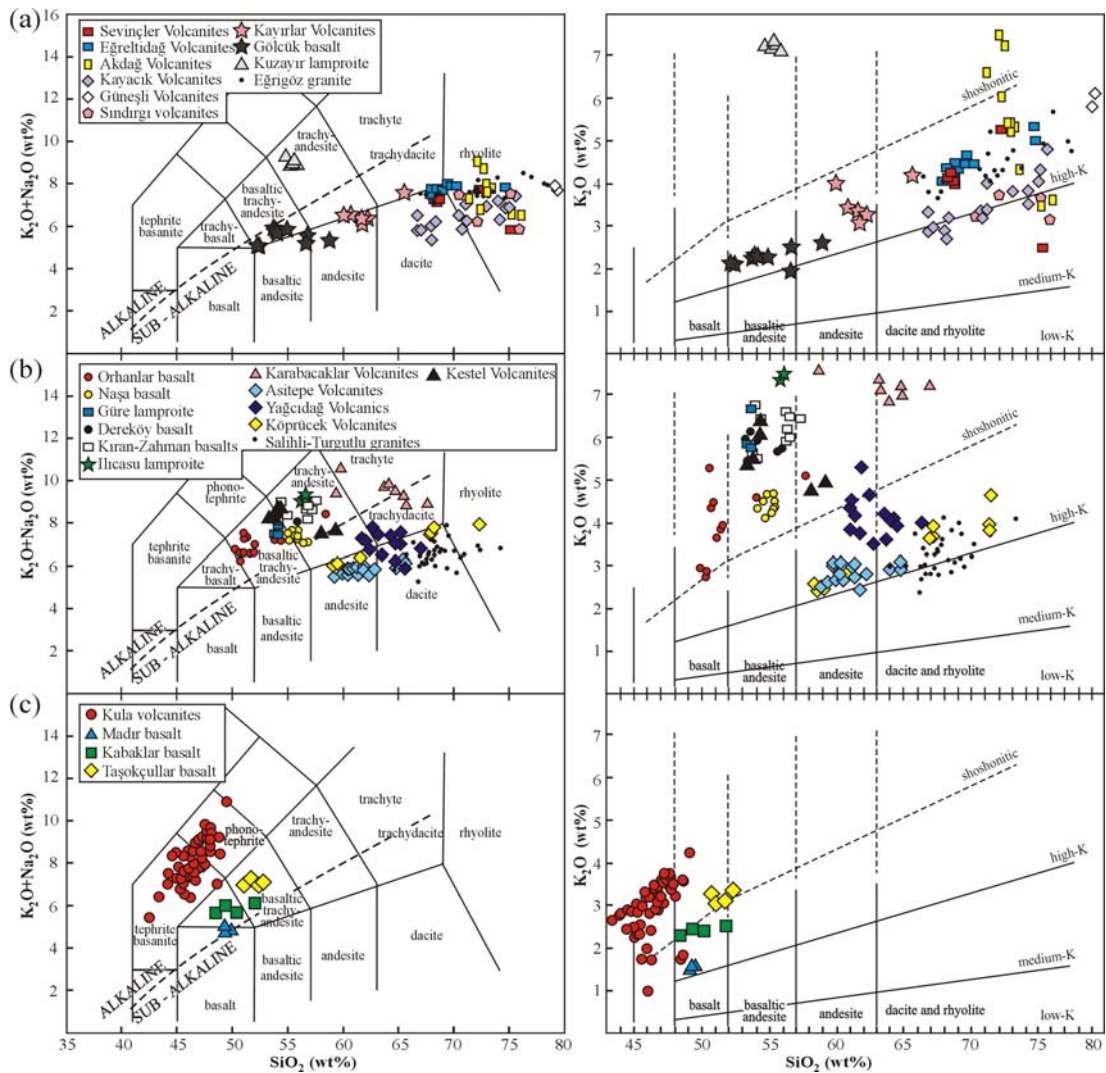
Figure 2.15 Total alkali-silica (TAS) plot (LeMaitre, 2002) for volcanic rocks in the NE-SW-trending basins in western Anatolia. The alkaline-subalkaline line is according to Irvine & Baragar (1971). The samples are plotted as water-free oxide contents normalized to 100%. Data are from Ercan et al. (1985), Güleç (1991), Ercan et al. (1996), Seyitoğlu et al. (1997), Alıcı et al. (2002), Innocenti et al. (2005), Erkül et al. (2005b), Ersoy & Helvacı (2007), Özgenç & Ilbeyli (2008), Ersoy et al. (2008), Öner et al. (2009), and this study. (a) early Miocene Group (1) and (2) volcanites, (b) middle Miocene Group (3) and (4) volcanites, and (c) late Miocene and Quaternary Group (5) and (6) volcanites.

CHAPTER THREE

PETROGRAPHY, GEOCHEMISTRY AND PETROLOGY OF THE VOLCANIC ROCKS IN THE NE–SW-TRENDING NEOGENE BASINS

In this chapter detailed petrographic and geochemical features of the Miocene volcanic units of which stratigraphic positions are described in Chapter II will be given. The data from this study are compiled with the previosly published chemical data, and then are evaluated together in order to present petrological models for mafic and felsic volcanic units. The studied volcanic units are Güneşli and Kayacık volcanites from the Gördes basin, Sevinçler and Asitepe volcanites, Naşa and Taşokçular basalts from the Demirci basin, Eğreltidağ and Yağcıdağ volcanites, Kuzayır and Ilıcasu lamproites, Orhanlar and Kabaklar basalts from the Selendi basin, Akdağ, Kestel and Köprücek volcanites, Dereköy basalt from the Emet basin and Karabacaklar volcanites, Kıran and Zahman basalts and Güre lamproite from the Güre basin (Figures 3.1).
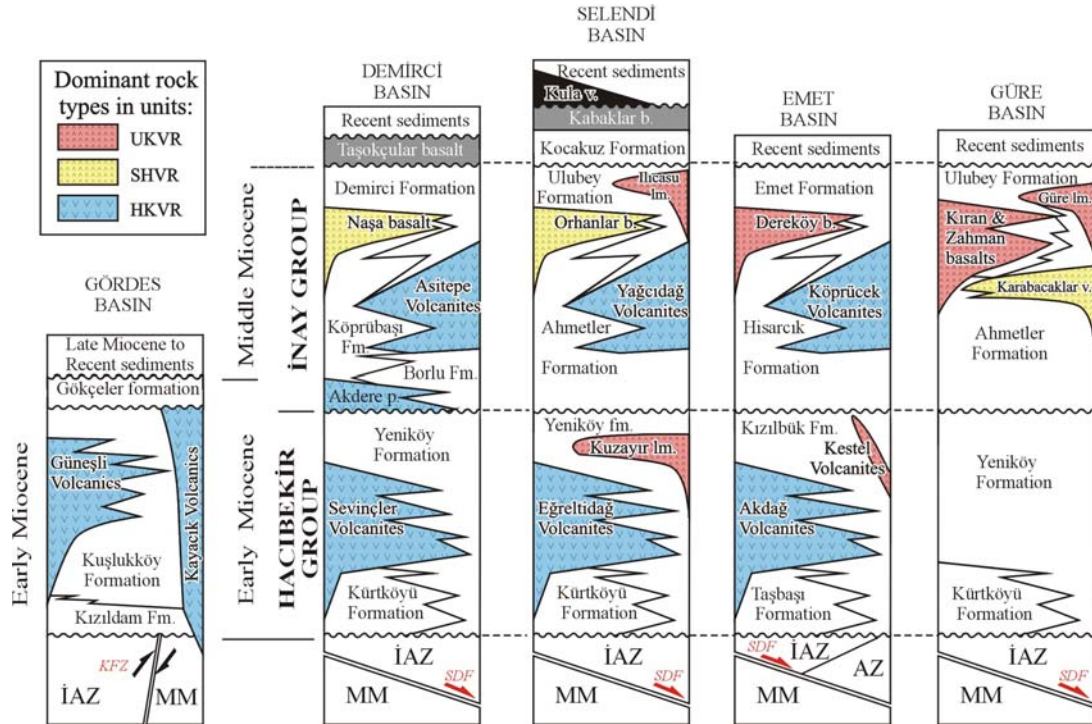
Figure 3.1 Stratigraphy of the late Cenozoic volcanic units in the NE–SW-trending basins.

3.1 Petrography

The lava flows and domes of the early Miocene Kayacık Volcanites include a phenocryst assemblage of $Qz_{0.05-0.20}$ + $Pl_{0.10-0.25}$ + $Bt_{0.05-0.10}$ + $Cpx_{0-0.02}$ in a groundmass of plagioclase laths and quartz (See Table 3.1 for mineral abbreverations). The early Miocene Güneşli Volcanites contain $Qz_{0.15-0.20}$ + $Pl_{0.05-0.10}$ + $Sa_{0.05-0.15}$ phenocrysts in a reddish brown to pink glassy matrix that shows flow textures. The lavas from the early Miocene Eğreltidağ Volcanites include phenocrysts of $Qz_{0.10-0.15}$ + $Pl_{0.15-0.20}$ + $Bt_{0.10-0.15}$ + $Hbl_{0.02-0.10}$ + $Sa_{0-0.05}$ in a glassy matrix with perlitic structures. Hornblende cumulates with lesser amounts of plagioclase exist in some samples. The early Miocene Sevinçler and Akdağ volcanites show similar petrographic features to the Eğreltidağ Volcanites, but with lesser amounts of amphibole and quartz. In these early Miocene felsic volcanic units, many of the quartz crystals are embayed, and the plagioclases are unzoned and generally euhedral to subhedral.

The middle Miocene volcanites have the following phenocryst assemblages; (1) Köprücek - $Pl_{0.20-0.30}$ + $Bt_{0.10-0.20}$ + $Amp_{0-0.03}$ + $Opx_{0-0.05}$, (2) Yağcıdağ - $Pl_{0.20-0.30}$ + $Bt_{0.10-0.20}$ + $Amp_{0.05-0.10}$ + $Cpx_{0-0.05}$ + $Qz_{0-0.10}$, (3) Asitepe - $Pl_{0.15-0.30}$ + $Opx_{0.10-0.20}$ + $Amp_{0-0.05}$ + $Cpx_{0-0.05}$ + $Bt_{0-0.05}$. Two types of plagioclase are present; those that are generally unzoned and smaller amounts of crystals that show a clear centre with sieve textured rims. Orthopyroxenes in the Asitepe Volcanites are generally seen in the early stage lavas, whereas in the late stage lavas the orthopyroxenes are generally resorbed by clinopyroxene, with biotite as the only phenocryst phase remaining in late stage lavas.

The Kuzayır, Güre and Ilıcasu lamproites contain zoned $Phl_{0.10-0.20}$ and partly altered $Ol_{0.05-0.10}$ and $Cpx_{0.10-0.20}$ in a feldspar matrix with lesser amounts of apatite. The Kestel volcanites have a similar mineralogy to the lamproites, but their phlogopites are unzoned and they contain fewer quartz xenocrysts. The middle Miocene Naşa basalt is characterized by $Ol_{0.10-0.20}$ + $Cpx_{0.10-0.30}$ phenocrysts with

plagioclase microlites. The Dereköy basalt has similar petrographic features to the Naşa basalt, but with some partly oxidized phlogopites.

Table 3.1 Petrographic data from the volcanic rocks. Amp: (brown) amphibole, Bt: biotite, Cpx: clinopyroxene, Hbl: hornblende, Lct: leucite, Opx: orthopyroxene, Phl: phlogopite, Pl: plagioclase, Qz: quartz, Sa: sanidine, WR: whole rock. Minerals in paranthesis forms groundmass.

Gördes Basin	Main Phenocryst assemblages (in descending order)
Kayacık volcanites	Qz + Pl + Bt+ Cpx
Güneşli volcanites	Qz + Pl + Sa
Demirci Basin	
Sevinçler volcanites	Pl + Bt + Qz ± Hbl
Naşa basalt	Ol + Cpx + (Pl)
Asitepe volcanites	Pl + Opx ± Bt ± Amp ± Cpx
Taşokçular basalt	Ol + Cpx + (Pl)
Selendi Basin	
Eğreltidağ volcanites	Pl + Qz + Bt + Hbl ± Sa
Kuzayır lamproite	Phl + Cpx + Ol + (Sa)
Yağcıdağ volcanites	Pl + Bt + Amp ± Cpx ± Qz
Orhanlar basalt	Ol + Cpx ± Phl/Bt ± Lct ± (Pl/Sa)
Kabaklar basalt	Ol + Cpx + (Pl)
Ilıcasu lamproite	Phl + Cpx + Ol + (Sa)
Emet Basin	
Akdağ volcanites	Pl + Bt + Qz ± Hbl
Kestel volcanites	Cpx + Phl+ Ol
Köprücek volcanites	Pl + Bt ± Amp± Opx
Dereköy basalt	Ol + Cpx ± Phl + (Pl)
Güre Basin	
Karabacaklar volcanites	Phl + Ol + Cpx ± (Sa)
Kıran-Zahman basalt	Ol + Cpx ± Sa
Güre lamproite	Phl + Cpx + Ol + (Sa)

The Kıran-Zahman basalt consists of euhedral $Ol_{0.10-0.20}$ and $Cpx_{0.05}$ phenocrysts in a groundmass of either plagioclase microlites or a sanidine matrix. The Karabacaklar

volcanites include $Ol_{0-0.10} + Cpx_{0.10-0.15} + Phl$(or Bt)$_{0.10-0.20} + Pl_{0-0.05}$ phenocrysts with abundant quartz xenocrysts and xenoliths. The Orhanlar basalt is characterized by $Ol_{0.15-0.25} + Cpx_{0.10-0.15} + Phl$(or Bt)$_{0.05-0.10} + Lct_{0-0.02} + Pl_{0-0.05} + Sa_{0-0.20}$ minerals. The late Miocene Taşokçular and Kabaklar basalts are characterized by $Ol_{0.10-0.15} + Cpx_{0.02-0.10}$ in a groundmass containing plagioclase microlites.

3.2 Major and Trace Elements

Detailed classification of the volcanic units, using major element contents is shown in Figure 3.1. The sub-alkaline rocks in Figure 3.1a show a calc-alkaline trend on the AFM diagram of Irvine & Barragar (1971) (Figure 3.1b). The chemical affinities of the volcanites are also illustrated in the MgO vs K_2O/Na_2O diagram, which is constructed for the ultrapotassic rocks on the basis of the criteria proposed by Foley et al. (1987) (Figure 3.1c). The volcanic rocks in this study span a large range on the classification diagrams (Figure 3.2), and can be grouped as; (1) high-potassic calc-alkaline volcanic rocks (**HKVR**) (with a few samples of medium-K affinity), including andesites, dacites, latites, trachytes and rhyolites, (2) shoshonitic volcanic rocks (**SHVR**) comprising latites, trachytes, trachydacites and shoshonites, and (3) ultrapotassic volcanic rocks (**UKVR**) comprising latites and shoshonites. The SHVR have SiO_2 and MgO contents in the range 50.3–67.5 wt.% and 1.4–10.6 wt.%, respectively, allowing them to be subdivided into high-Mg (MgO>8 wt.%) and low-Mg (MgO<7wt.%) SHVR. Among the UKVR, the early Miocene Kuzayır and the middle Miocene Güre and Ilıcasu lamproites also show lamproitic affinity.

Late Miocene volcanism in the region is represented by low-SiO_2 (47.9-51.3 wt.%) and high MgO (3.9-8.3 wt.%) lavas, classified as K-trachybasalts and shoshonites. The Kula volcanites are the most recent volcanic activity in the region and are classified as Na-alkali basalts, including tephrites, basanites and phonotephrites.
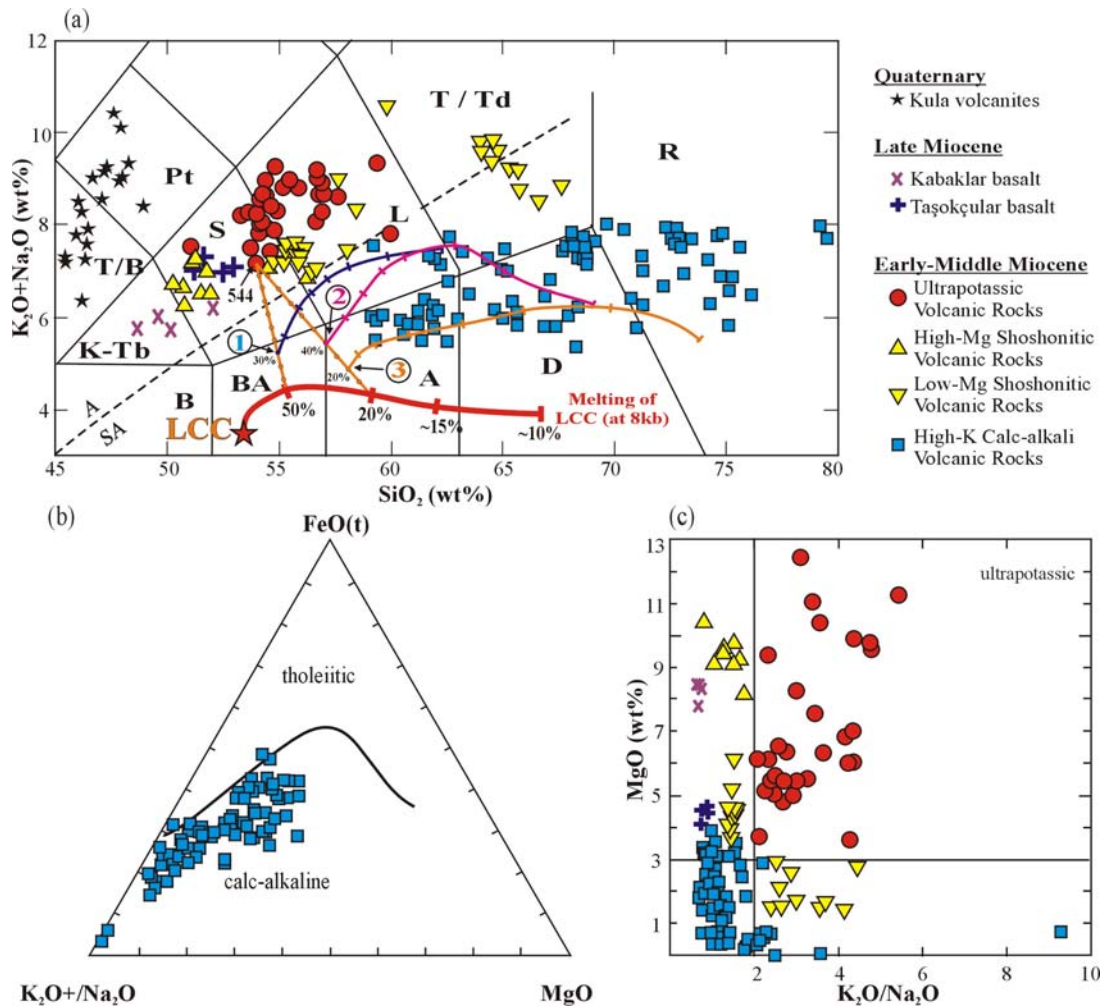
Figure 3.2 Classification and discrimination diagrams for the late Cenozoic volcanic units in the NE-SW-trending basins: (a) Total alkali–silica (TAS) plot with IUGS fields after LeMaitre (2002) for the early-middle Miocene mafic volcanic rocks in Western Anatolia. The alkaline (A)-subalkaline (SA) line is according to Irvine & Baragar (1971). Also shown are partial melting trend of lower continental crust (LCC, Taylor & McLennan, 1995), mixing trends between sample 544, and 20% and 50% partial melts from the LCC, and fractional crystallization (FC) trends of mixed magmas (points 1, 2 and 3). Melting and FC trends are derived from the MELTS program for 8 and 3 kbars, respectively (Ghiorso & Sack, 1995). Ticks on the FC trends represent 10% increments. T/B: tephrite/basanite, Pt: phonotephrite, K-Tb: K-trachybasalt, S: Shoshonite, B: basalt, BA: basaltic andesite, A: andesite, D. dacite, R: rhyoltie, T/Td: trachyte/trachydacite, L: latite. (b) Subdivision of the sub-alkaline samples as tholeiitic and calc-alkaline according to AFM diagram of Irvine & Baragar (1971); (c) MgO vs K_2O/Na_2O (Foley et al., 1987) diagrams.

The trace element compositions of the HKVR are similar to those of other calc-alkaline volcanic rocks in Western Anatolia (Aldanmaz et al., 2000), but the SHVR and UKVR have higher incompatible trace element compositions than those of the

HKVR. The high-Mg SHVR and the UKVR have the highest compatible trace element contents (e.g., Ni = 177-444 ppm).

On primitive mantle (PM)-normalized multi-element diagrams (Figure 3.3), all the early-middle Miocene volcanites are characterized by Ta, Nb and Ti negative anomalies. Some of the dacitic-rhyolitic high-K CA volcanic rocks are also characterized by strong Ba, Sr, Eu and Ti negative anomalies. The trace element patterns of the HKVR, SHVR and UKVR are all very similar to one another. The early-middle Miocene HKVR have similar trace element abundances to that of the gneiss sample from the Menderes Massif. On the other hand, the SHVR and UKVR show elevated light- and middle-rare earth element (LREE and MREE) contents. The late Miocene basalts show transitional trace element patterns between the early-middle Miocene volcanic rocks (characterized by LILE enrichments) and the Quaternary Kula volcanites (QKV), which show no depletion in HFSE with respect to LILE.
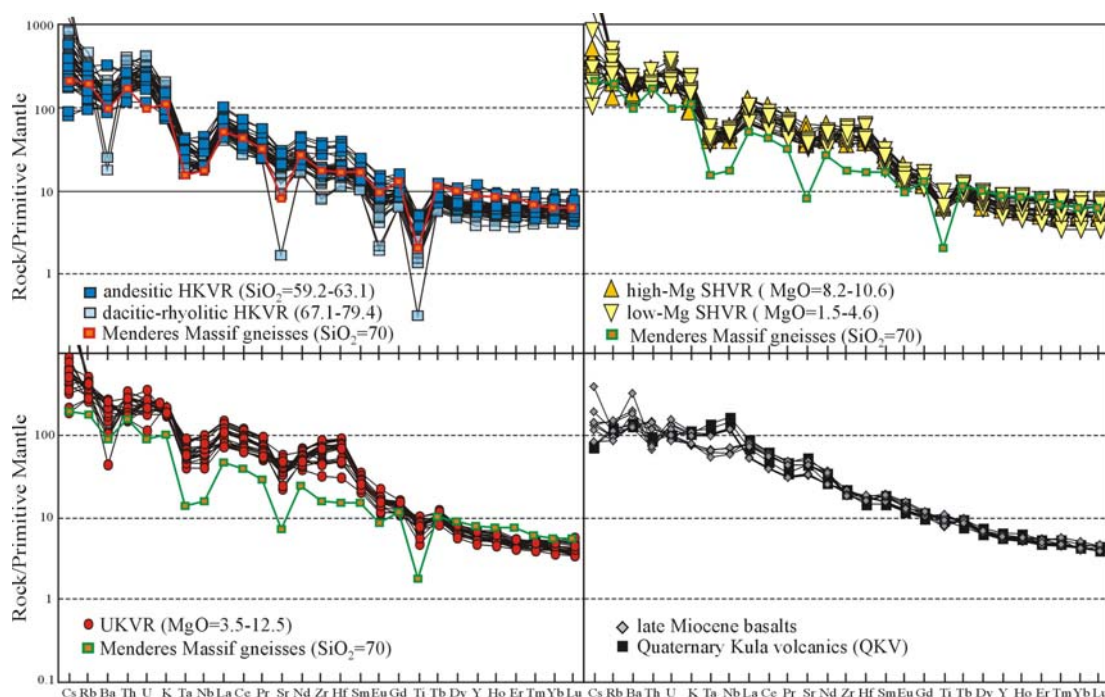
Figure 3.3 Primitive mantle normalized multi-element patterns of the volcanic units (primitive mantle values from Palme & O'Neil, 2004).

3.3 Isotopes

All the early-middle Miocene volcanic rocks in the region plot on the enriched part of $^{143}Nd/^{144}Nd_{(i)}$ versus $^{87}Sr/^{86}Sr_{(i)}$ diagram (Table 3.2; Figure 3.4a). The late Miocene basalts are characterized by depleted Sr-Nd isotopic ratios similar to those of the Quaternary Kula volcanites (QKV), the South Aegean volcanic arc (SAVA), the Northwest Anatolia Eocene volcanic rocks (NAEV), Eskişehir-Afyon-Isparta volcanic rocks (EAIV) and Galatian volcanic Province (GVP).
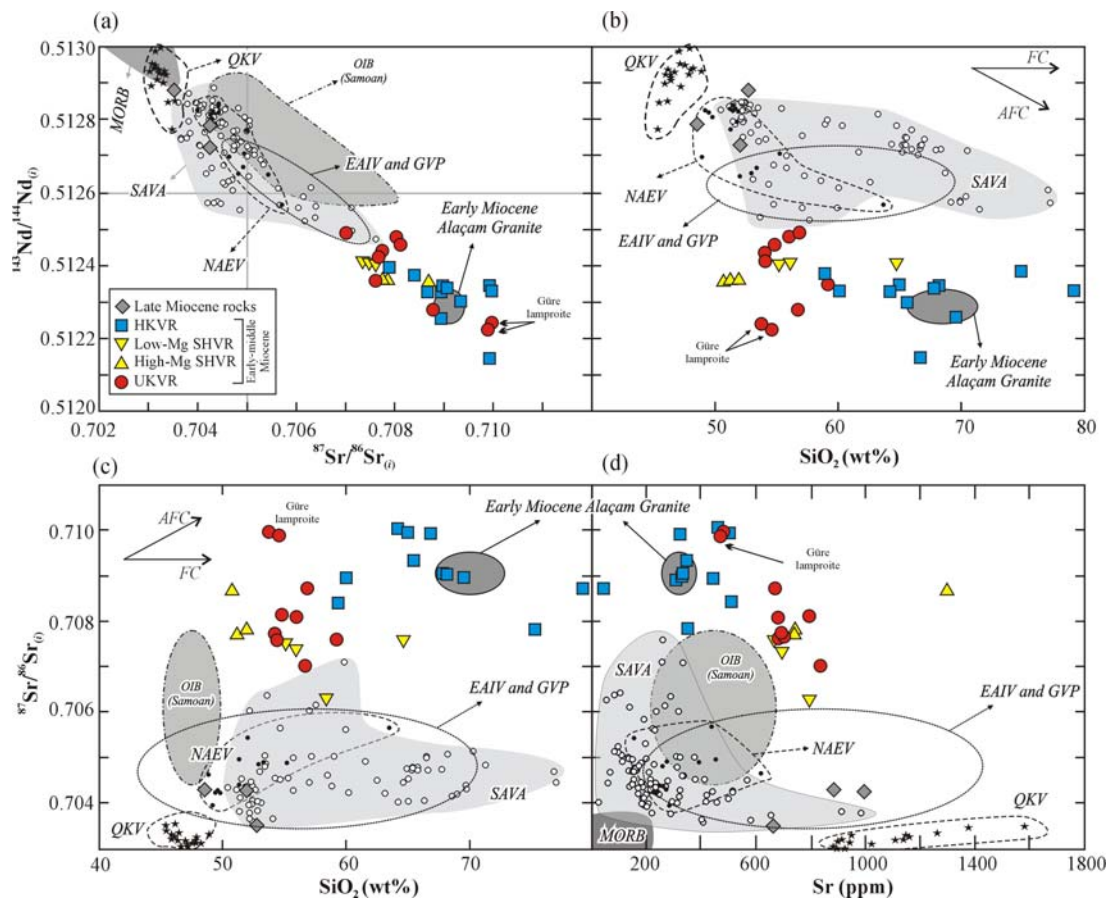
Figure 3.4 (*a*) $^{143}Nd/^{144}Nd_{(i)}$ vs $^{87}Sr/^{86}Sr_{(i)}$, (*b*) $^{143}Nd/^{144}Nd_{(i)}$ vs SiO_2, (*c*) $^{87}Sr/^{86}Sr_{(i)}$ vs SiO_2 and (*d*) $^{87}Sr/^{86}Sr_{(i)}$ vs Sr diagrams for the late Cenozoic volcanic rocks from the NE–SW-trending basins. Data for Quaternary Kula volcanites (QKV) are from Güleç (1991), Alıcı et al. (2002) and Innocenti et al. (2005), South Aegean volcanic Arc (SAVA) lavas are from Buettner et al. (2005) and Pe-Piper and Hatzipanagioto (1997), Northwest Anatolian Eocene volcanic rocks (NAEV) are from Altunkaynak & Genç (2008) and Kürkçüoğlu et al. (2008), Eskişehir-Afyon-Isparta volcanites (EAIV) and Galatian volcanic province (GVP) are from Wilson et al. (1997). Early Miocene Alaçam Granite compositions are from Hasözbek et al. (2011).

There is no clear correlation between SiO_2-$^{143}Nd/^{144}Nd_{(i)}$ and SiO_2-$^{87}Sr/^{86}Sr_{(i)}$, but the HKVR with high SiO_2 tend to have slightly high $^{87}Sr/^{86}Sr_{(i)}$ and slightly low $^{143}Nd/^{144}Nd_{(i)}$ ratios (Figures 3.4b and 3.4c). Sr contents of the early-middle Miocene volcanic rocks are negatively correlated with $^{87}Sr/^{86}Sr_{(i)}$ (Figure 3.4d). It is noteworthy that the early-middle Miocene volcanic rocks in the NE–SW-trending basins have higher $^{87}Sr/^{86}Sr_{(i)}$ and lower $^{143}Nd/^{144}Nd_{(i)}$ ratios than any of the QKV, NAEV, SAVA, EAIV and GVP (Figure 3.4a). This is also true for isotopic ratios at a given SiO_2 value (Figures 3.4b and 3.4c). The gneisses and granitic rocks of the Menderes Massif, representing the middle to upper crustal rocks of Western Anatolia, have high $^{87}Sr/^{86}Sr$ ratios (0.7115-1.2974; Satır & Friedrichsen 1986), as do the augen gneisses measured by Ersoy et al. (2010b) ($^{87}Sr/^{86}Sr$ = 0.7269 and 0.7768). The Early Miocene Alaçam Granite, which is interpreted to have been derived from a crustal source (Hasözbek et al., 2011), has a similar Sr-Nd isotopic composition to the HKVR. Depleted mantle Nd model ages (T_{DM}) of the volcanic rocks in the region increase from the UKVR and SHVR (~915–1090 Ma) to the HKVR (~1150–1300 Ma) (Table 3.2). The Eocene plutons in Northwestern Anatolia yield Nd model ages of ~920–1061 Ma (Altunkaynak, 2007). Neogene volcanic rocks from the Limnos (Greece) yield similar Nd model ages ranging generally between 937 and 1200 Ma (Pe-Piper et al., 2009). Except for volcanic rocks from Ios, the SAVA volcanic rocks yield Nd model ages ranging from 696 to 939 Ma (Buettner et al., 2005).

SMOW-normalized whole-rock $\delta^{18}O$ values of the volcanic rocks in the area (Table 3.3) are positively correlated with their SiO_2 and Th contents. There is negative correlation between $\delta^{18}O$ and $^{87}Sr/^{86}Sr_{(i)}$ of the HKVR, while no clear correlation appear for the SHVR and UKVR. The data set is limited, but the $\delta^{18}O$ values of the late Miocene mafic lavas are more similar to those of the SHVR and UKVR than the HKVR. The volcanic rocks have $^{206}Pb/^{204}Pb$, $^{207}Pb/^{204}Pb$ and $^{208}Pb/^{204}Pb$ isotopic ratios of 18.838–19.148, 15.672–15.725 and 38.904–39.172, respectively (Table 3.3). The $^{207}Pb/^{204}Pb$ and $^{208}Pb/^{204}Pb$ ratios of the volcanic rocks in this study are nearly identical, while the $^{206}Pb/^{204}Pb$ ratios of the volcanic rocks increase from the HKVR to the UKVR (Figure 3.6).

Table 3.2 Sr-Nd and Sm-Nd isotopic data obtained from the Miocene volcanic rocks in NE–SW-trending basins in western Anatolia.

Sample	classification	Rock Group	age	Rb	Sr	Nd	Sm	87Sr/86Sr	±2σ	$^{143}Nd/^{144}Nd$	±2σ	$^{147}Sm/^{144}Nd$	±2σ	$^{87}Sr/^{86}Sr_{(i)}$	$^{143}Nd/^{144}Nd_{(i)}$	σ_{DM} (Ma)
861	rhyolite	HKVR	EM	191,40	31,80	21,80	4,20	0,713644	5	0,512345	4			0,708703	0,512330	
756	dacite	HKVR	EM	114,70	327,60	24,50	4,66	0,710200	5	0,512160	4			0,709913	0,512145	
718	dacite	HKVR	EM	138,80	331,20	23,60	4,58	0,709342	5	0,512358	3	0,1198	5	0,709007	0,512343	1308,4
521	dacite	HKVR	EM	133,80	335,50	25,00	5,40	0,709357	10	0,512354	5			0,709038	0,512337	
529	rhyolite	HKVR	EM	165,70	319,20	27,70	5,30	0,709372	4	0,512270	4			0,708957	0,512255	
815	rhyolite	HKVR	EM	102,90	346,40	25,50	3,83	0,708117	5	0,512402	6			0,707873	0,512390	
717	andesite	HKVR	MM	82,80	444,00	42,20	8,07	0,709070	5	0,512342	3	0,1174	5	0,708951	0,512330	1296,0
754	dacite	HKVR	MM	101,90	350,80	23,10	4,62	0,709529	5	0,512313	4			0,709350	0,512301	
510	trachyte	HKVR	MM	156,40	471,60	41,50	7,30	0,710209	10	0,512337	5			0,710005	0,512327	
YF2	dacite	HKVR	MM	162,50	483,80	43,10	7,80	0,710153	5	0,512359	3	0,1073	5	0,709946	0,512348	1147,8
31207	dacite	HKVR	MM	163,90	491,00	36,50	6,60	0,710172	4					0,709966		
846	andesite	HKVR	MM	214,60	505,10	36,90	6,49	0,708701	5	0,512381	3			0,708422	0,512369	
746[*]	shoshonite	SHVR	MM	163,40	684,50	62,30	10,82	0,707651	5	0,512419	2	0,1062	5	0,707504	0,512409	1050,8
543[*]	shoshonite	SHVR	MM	189,80	743,70	63,50	11,90	0,707914	5	0,512376	2	0,1040	5	0,707741	0,512364	1092,0
541[*]	shoshonite	SHVR	MM	151,30	1300,00	81,40	15,00	0,708798	14	0,512371	11			0,708719	0,512359	
821[*]	latite	UKVR	EM	292,30	695,30	62,20	9,97	0,707979	5	0,512425	2	0,1031	5	0,707668	0,512414	1014,7
528[*]	latite	UKVR	EM	229,30	800,70	72,10	10,90	0,708346	5	0,512467(1)	2	0,0981	5	0,708136	0,512456	914,8
810[*]	shoshonite	UKVR	MM	220,10	547,30	58,60	9,50	0,707953	5	0,512438	2	0,1033	5	0,707639	0,512428	996,7
728	shoshonite		LM	91,60	665,50	33,90	6,77	0,703561	5	0,512889	2	0,1234	5	0,703516	0,512883	452,0
520-1	K-trachybasalt		LM	51,60	993,90	49,50	8,40	0,704290	10	0,512795	5			0,704272	0,512789	

[*]Trace elements and Sr-Nd isotope analyses of these samples are from Ersoy et al. (2010b). Ages: EM: early Miocene, MM: middle Miocene, LM: late Miocene.

Table 3.3 Oxygen and Pb isotopic data obtained from the Miocene volcanic rocks in NE–SW-trending basins in western Anatolia. EM: early Miocene, MM: middle Miocene, LM: late Miocene.

				Oxygen isotopic data			Lead isotopic data		
sample	classification	Group	age	measured	$\delta^{18}O$	$\pm 1\sigma$	$^{206}Pb/^{204}Pb$	$^{207}Pb/^{204}Pb$	$^{208}Pb/^{204}Pb$
861	rhyolite	HKVR	EM	14,30	12,60	0.19‰			
756	dacite	HKVR	EM	13,40	10,10	0.19‰			
718	dacite	HKVR	EM	13,30	11,80	0.19‰	18,8380	15,6890	38,9750
521	dacite	HKVR	EM	13,20	10,30	0.19‰	18,8558	15,7089	39,0308
815	rhyolite	HKVR	EM	13,70	13,80	0.19‰			
717	andesite	HKVR	MM	13,90	8,60	0.19‰	18,9690	15,7190	39,1290
510	trachyte	HKVR	MM				18,9033	15,7250	39,1689
YF2	dacite	HKVR	MM	13,80	10,80	0.19‰	18,9140	15,7220	39,1720
846	andesite	HKVR	MM	13,40	11,70	0.19‰			
746	shoshonite	SHVR	MM	11,10	7,70	0.19‰	18,9370	15,7020	39,0700
543	shoshonite	SHVR	MM	12,40	8,60	0.19‰	18,9930	15,6980	39,1030
536	shoshonite	SHVR	MM				19,0096	15,7198	39,1569
541	shoshonite	SHVR	MM				19,0350	15,7131	39,1651
821	latite	UKVR	EM	13,00	8,50	0.19‰	19,0500	15,7180	39,1560
732	latite	UKVR	MM	12,20	11,60	0.19‰			
839	shoshonite	UKVR	MM	12,60	8,90	0.19‰			
822	shoshonite	UKVR	MM	11,40	11,00	0.19‰			
736	latite	UKVR	MM	11,60	9,40	0.19‰			
518	latite	UKVR	EM				19,1482	15,7030	39,0483
528	latite	UKVR	EM	12,20	8,60	0.19‰	18,9850	15,6720	38,9040
810	shoshonite	UKVR	MM				19,0450	15,7140	39,1620
728	shoshonite		LM	12,60	8,30	0.19‰	18,8730	15,7010	39,0980
520-1	K-trachybasalt		LM	11,60	7,90	0.19‰	19,0314	15,6769	39,0490

The Neogene volcanic rocks in this study are characterized by higher $^{207}Pb/^{204}Pb$ ratios with respect to N- and E-MORBs, Samoan-OIB lavas, SAVA and QKV, and have higher $^{206}Pb/^{204}Pb$ ratios than the Neogene volcanic rocks of Lesvos, which lie further NW of the study area. The volcanic rocks in this study have similar $^{207}Pb/^{204}Pb$ and $^{208}Pb/^{204}Pb$ ratios to those of Samos and Chios islands located west of the study area, but their $^{208}Pb/^{204}Pb$ ratios partly overlap with those of the SAVA and Samoan-OIB lavas (Figures 3.5a and 3.5b). As with other Miocene volcanic rocks in the Aegean region, such as those from Lesvos, Chios and Limnos (Wyers & Barton, 1987; Pe-Piper, 1994; Pe-Piper & Piper, 2001), the $^{207}Pb/^{204}Pb$ and $^{208}Pb/^{204}Pb$ ratios

of the volcanic rocks from this study plot nearly horizontal against their SiO_2 contents (Figures 3.5c and 3.5d).
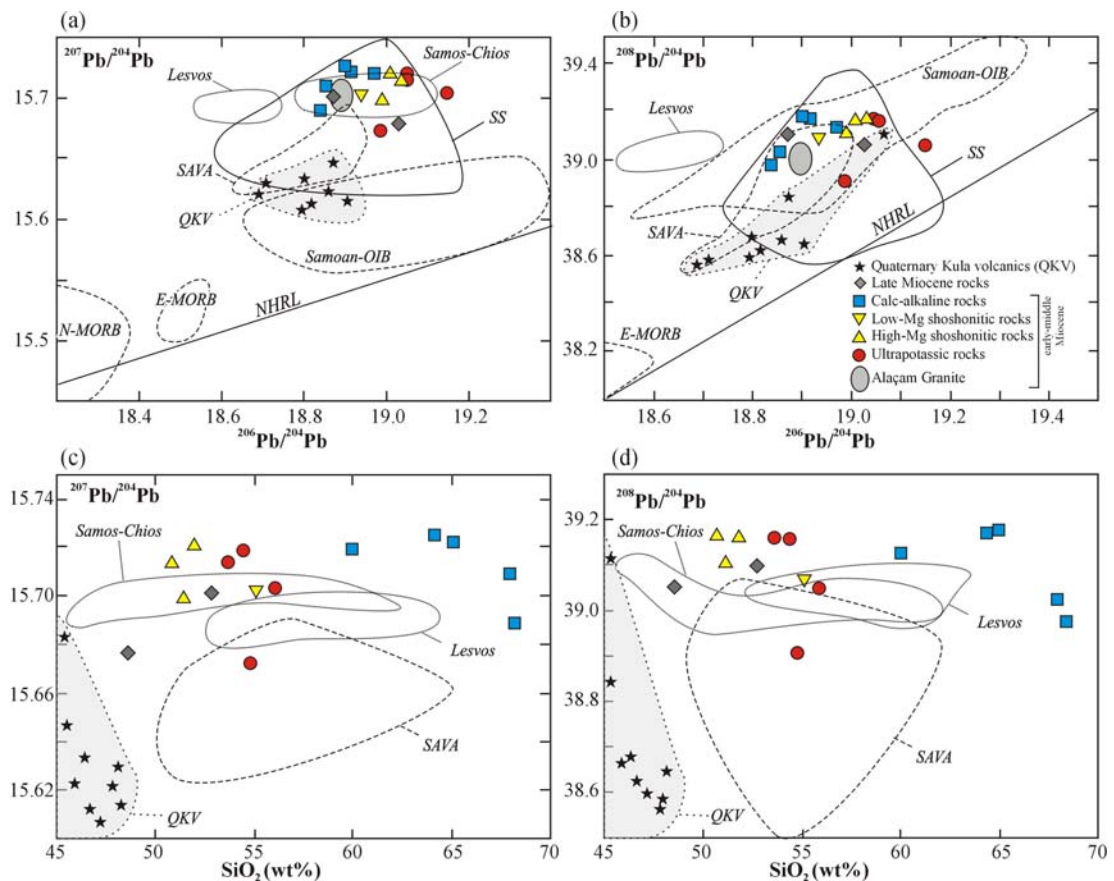
Figure 3.5 (*a–d*) $^{207}Pb/^{204}Pb$ and $^{208}Pb/^{204}Pb$ plots versus $^{206}Pb/^{204}Pb$ and SiO_2. Data for Miocene volcanic rocks from Lesvos, Samos and Chios islands are from Wyers & Barton (1987), Pe-Piper (1994), Pe-Piper et al. (1995); Pe-Piper & Piper (2001). Early Miocene Alaçam Granite data are from Hasözbek et al. (2011). South Aegean volcanic arc data (SAVA) from Buettner et al. (2005) and Bailey et al. (2009). Quaternary Kula volcanites (QKV) are from Alıcı et al. (2002). Data for E-MORB and N-MORB are from Klein (2004), Hart et al. (1999), and Donnelly et al. (2004). Subducted sediments (SS) are from Plank & Langimur (1998). Northern Hemisphere Reference Line (NHRL) is after Hart (1984).

3.4 Source characteristics of the SHVR and UKVR

It is generally accepted that the early-middle Miocene volcanism in Western Anatolia originated from lithospheric mantle sources (Aldanmaz et al., 2000; Innocenti et al., 2005; Dilek & Altunkaynak, 2007, 2009; Altunkaynak, 2007;

Altunkaynak & Genç, 2008; Helvacı et al., 2009; Ersoy et al., 2008, 2010b). However, the precise nature of the mantle source has been subject to debate. Numerical modelling of trace element compositions (Helvacı et al., 2009; Ersoy et al., 2008, 2010b) suggest that the Miocene mafic lavas originated from a lherzolitic mantle source in equilibrium with amphibole and garnet.

The HFSE ratios indicate that the mantle source composition of the early-middle Miocene volcanic rocks had a PM-like composition prior to any subduction-related enrichment process (Figures 3.6a, b and c; Ersoy et al., 2010b). Alternatively, Prelević et al. (2010) suggest that, on the basis of olivine compositions of the high-Mg ultrapotassic rocks, the volcanic rocks in the region originated from an ultra-depleted harzburgitic source that had been enriched by subduction-related metasomatism. Although, this model is not compatible with the HFSE ratios of the Miocene rocks, which are not altered during subduction-related processes (e.g., Pearce & Parkinson 1993), the mantle may have had an ultra-depleted chemical composition prior to the refertilization events, especially as a result of the multi-stage melting and melt-percolation processes that occurred in the lithosphere (*in-situ enrichment*).

Ersoy et al. (2010b) numerically modeled the mantle enrichment processes of the early-middle Miocene high-Mg ultrapotassic-shoshonitic lavas in the region, and concluded that the PM-like sources were altered by a 7–15% sediment contribution that included both sediment fluid and sediment melt components. Low degree partial melts (L1 in Figure 3.7) from this enriched (metasomatized) mantle (M0 in Figure 3.7) then underwent multi-stage melting and melt percolation processes to produce the early-middle Miocene SHVR and UKVR in the NE–SW-trending basins. This model requires that low-degree partial melts are continually produced from the starting mantle composition M0 and then react (mix) with the overlying original mantle to produce a more enriched and refertilized mantle source. The trace element enrichment produced by this process is summarized in Figure 3.7, using the model parameters given in Ersoy et al. (2010b).
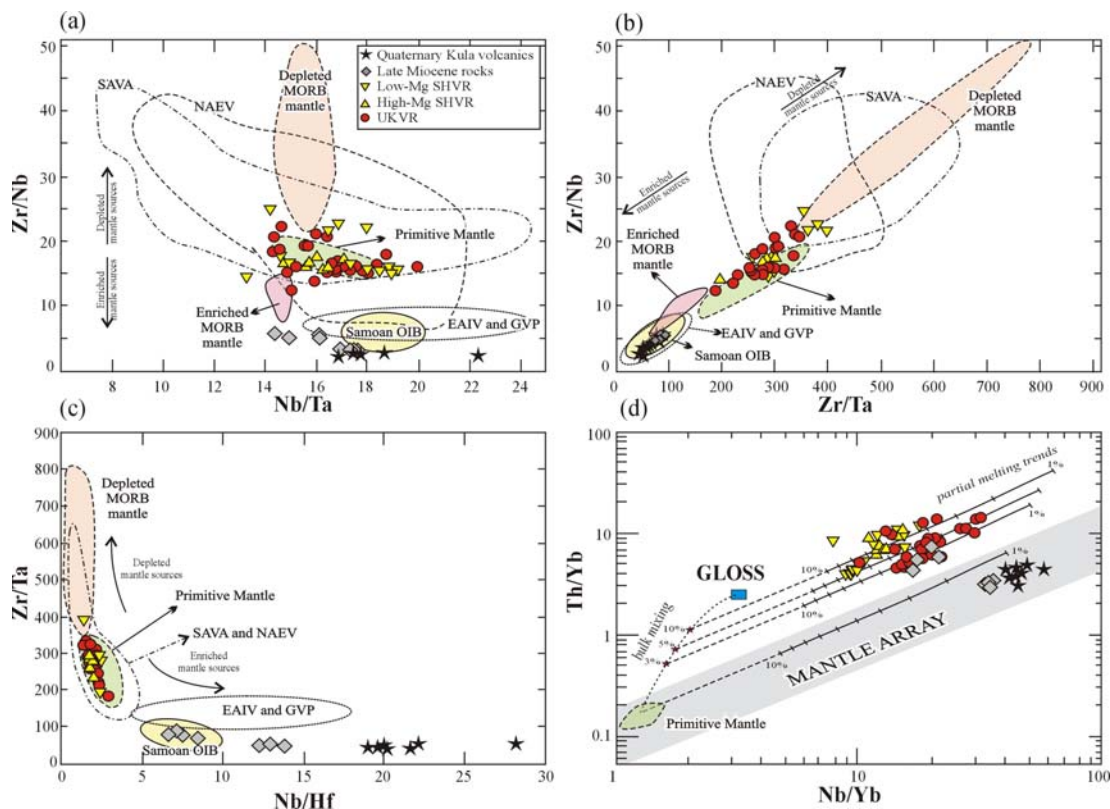
Figure 3.6 (*a–c*) HFSE/HFSE ratios of the volcanic rocks. Primitive mantle: Hofmann (1988), McDonough & Sun (1995), Palme & O'Neil (2004); enriched and depleted MORB mantles: Hart et al. (1999), Klein (2004), Workman & Hart (2005); Samoan Ocean Island Basalts (Samoan OIB): Workman et al. (2004). South Aegean volcanic arc data are from Buettner et al. (2005), Zellmer & Turner (2007), Bailey et al. (2009), Zellmer et al. (2000). (*d*) Th/Yb vs Nb/Yb plot for the volcanic rocks (after Pearce, 1983), on which non-modal partial melting trends (with partial melting ratios of 1% to 10%) of contaminated mantle source compositions are also shown. Contaminated mantle sources are represented by 3%, 5% and 10% bulk mixing between primitive mantle (Palme & O'Neil 2004) and Global Subducted Sediments (GLOSS, Plank & Langimur, 1998).

On a Th/Yb vs Nb/Yb log-log plot, elevated Th/Yb ratios with respect to the mantle array are interpreted to be due to source enrichment by subduction-related processes (Figure 3.6d). We used Nb instead of Ta (cf. Pearce, 1983), as both HFSE elements have similar chemical affinities and our Nb data is of higher quality. Except for some late Miocene lavas (the Taşokçular basalt) and the QKV, all the Miocene rocks show subduction-related enrichments. Bulk mixing lines between primitive mantle (PM) and GLOSS compositions on Figure 3.6d show that 1–8% non-modal partial batch melt trends, calculated from 3%, 5% and 10% mixing points can reproduce the Th/Yb vs Nb/Yb ratios measured in the volcanic rocks. However,

sediment addition to the mantle wedge in subduction zones likely occurs as sediment fluid or sediment partial melts accompanied by melt/fluid from subducted altered oceanic crust (MORB), rather than bulk sediment mixing.
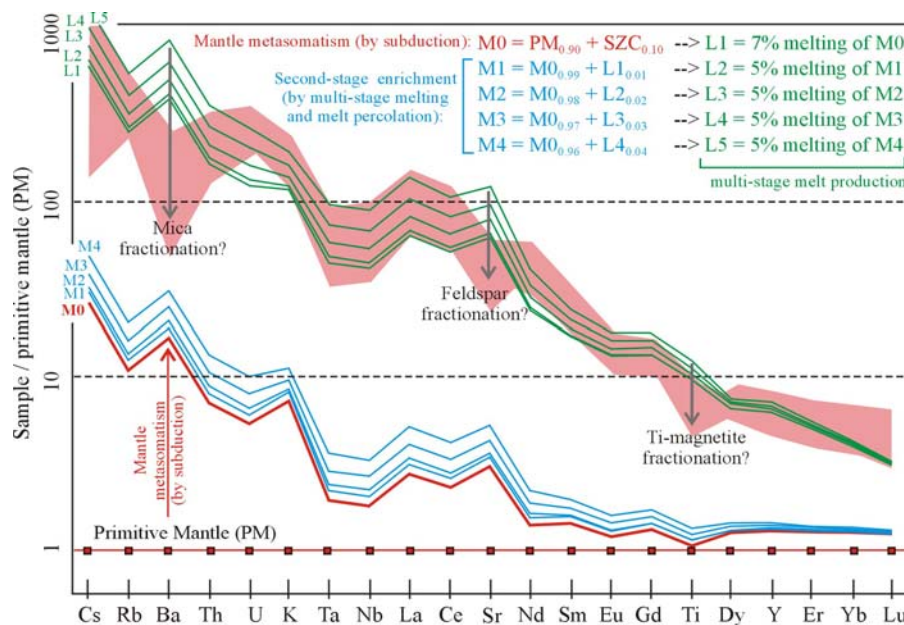
Figure 3.7 Primitive mantle (PM)-normalized multi-element spider-diagram for the mantle metasomatism and multi-stage melting and melt percolation model for trace element enrichments of the UKVR and SHVR (red-shaded area). See Ersoy et al. (2010b) for model parameters and detailed description. M0 to M5 refer to mantle compositions which are altered first by subduction enrichment (M0) and later by multi-stage melting and melt percolation process (M1–M6). L1 to L5 refer to melt compositions which are obtained from factional melting of M0 to M5.

HFSE ratios (Figures 3.6a, b and c) of the late Cenozoic lavas in the region indicate that the mantle sources of the volcanic rocks gradually changed from PM-like (before subduction-related metasomatism) to OIB-like mantle geochemistry after the late Miocene, suggesting that asthenospheric sources played a role in the origin of the late Miocene to Quaternary volcanism. Production of the late Miocene mafic lavas with transitional geochemistry between the lithospheric and asthenospheric sources (Innocenti et al., 2005), and finally the OIB-type volcanism represented by QKV (Güleç, 1991; Alıcı et al., 2002) also indicate that the asthenospheric contribution increased with time.

3.5 Origin of the HKVR

The early-middle Miocene voluminous HKVR are temporally and spatially associated with the less-voluminous SHVR and UKVR. In addition, both are characterized by K-increasing from west to east (see below), suggesting that a genetic link may exist between them. On SiO_2-dependent Sr, Nd and Pb isotopic variation plots (Figs. 3.4b, 3.4c, 3.5c and 3.5d), the volcanic rocks show an evolutionary trend from SHVR and UKVR to HKVR with a small radiogenic isotope enrichment. This rules out contamination of the SHVR and UKVR magmas by upper continental crust as the latter has Sr ratios that are too high and Nd isotope ratios that are too low (see also Ersoy et al., 2010b) that are too high to produce the HKVR. Furthermore, as the UKVR and SHVR have elevated incompatible trace element contents relative to the HKVR (Figure 3.3), they could not be parental magmas of the HKVR in a fractional crystallization (FC) scenario.

Mixing of the primitive lavas in the region with crustal melts derived from a source which had; (a) relatively high SiO_2, (b) lower trace element contents with respect to the mafic lavas, and (c) lower radiogenic Sr and Pb, and more radiogenic Nd isotopes with respect to the metamorphic rocks of the Menderes Massif (mid to upper crust of the region), can explain the origin of the HKVR. In this context, we use the Lower Continental Crust (LCC) values of Taylor & McLennan (1995) to model a mixing scenario with mantle derived magmas (sample 544 or model melts obtained from Figure 3.8).

As a first approximation, HFSE and HREE ratios (Hf/Yb and Zr/Nb) are used in this modeling exercise as these ratios are less affected by crystal fractionation (Figure 3.8a). The Hf/Yb and Zr/Nb ratios of the mean HKVR and the most primitive HKVR can be reproduced by ~40% and ~20% mixing between partial melts from the LCC with the relatively primitive lavas of the UKVR (as represented by sample 544). On the basis of these results, the trace element contents are also modeled on Figure 3.8b. Most of the elemental concentrations and patterns of the mixed magma (*l*1 on Figure 3.8b) obtained from mixing between sample 544 and

partial melts from LCC (50% batch melt) are identical to those observed in the most primitive HKVR. These scenarios are also modeled on Figure 3.2a using the MELTS program (Ghiorso & Sack 1995). 20% and 50% batch melts from the LCC (calculated for 8 kbars and representing lower crustal depths) are mixed with sample 544. The resultant compositions (points 1, 2 and 3), which are andesitic and basaltic andesitic, then undergo crystallization (up to 70%) at 3 kbars, representing the upper crustal depths. The trends obtained from this modeling are very similar to the major element concentrations observed in the HKVR. The involvement in a high degree crustal component in the genesis of the HKVR is also supported by the Sr-Nd, Pb and O isotope data, which are comparable to those observed in the early Miocene Alaçam Granite (Figures 3.4 and 3.5).
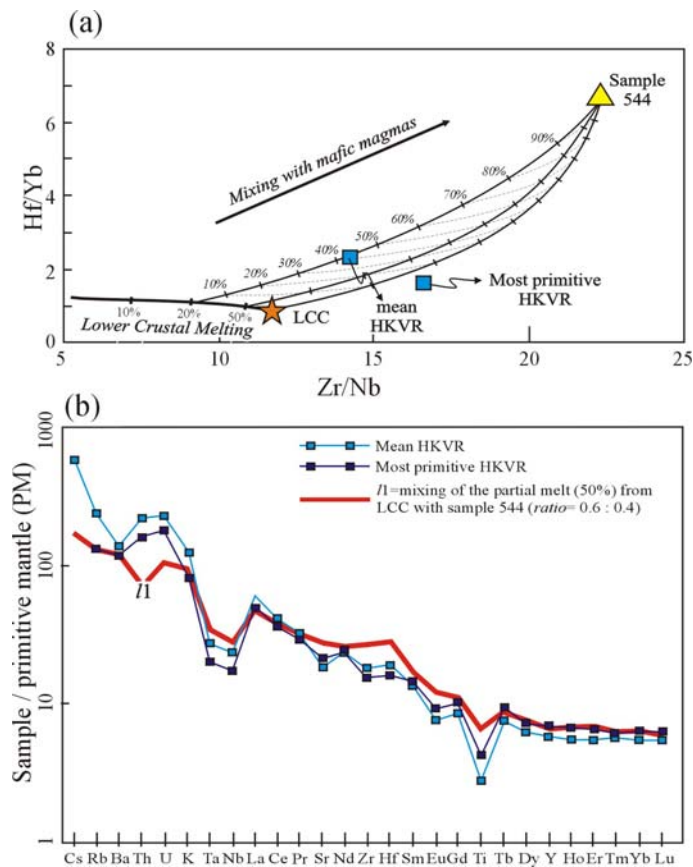
Figure 3.8 Hf/Yb vs. Zr/Nb and primitive mantle-normalized multi-element patterns for the evolution of the HKVR. Mineral fractionation is negligible on Hf/Yb vs. Zr/Nb. Melting models assume a mineral assemblage of $Cpx_{0.50} + Pl_{0.50}$ that obtained from MELTS algorithm (Ghiorso & Sack 1995). Partition coefficients are from Adam & Green (2006). See text for details of the models.

In conclusion, the high trace element contents of the SHVR and UKVR should have been lowered by mixing with lower crustal melts to produce those observed in the HKVR. This interpretation is also supported by petrographic data as the most primitive HKVR in the region (the Asitepe volcanites) show evidence for magma mixing, such as the presence of both sieve-textured and clear plagioclase. Lower crustal melting is also be evidenced by presence of orthopyroxene in the most primitive HKVR (Astipe volcancis), as shown by the MELTS calculations (up to 15% crystallization of point 2 on Figure 3.2a). Hammersley & DePaolo (2006) suggested a two-stage petrogenetic model for the Clear Lake volcanic system (California), involving assimilation and fractional crystallization in lower crust, followed by fractional crystallization in the upper crust. In a similar manner, the petrogenetic evolution of the HKVR can also be considered as having occurred in two-stages: (1) lower continental crustal melting (likely initiated by basaltic underplating) and mixing of these magmas with lithospheric mantle-derived melts, and (2) nearly pure fractional crystallization in the upper crust.

3.6 Fractional Crystallization and Assimilation (FC-AFC) Processes

Mass balance calculations for the SHVR (Table 3.4) as a single unit suggest an average fractionating assemblage of $Ol_{0.15} + Cpx_{0.25} + Pl_{0.35} + Sa_{0-010} + Phl_{0.15} + Mag/Ilm_{0.05}$ with F = ~75%. Better constrained results were obtained using the UKVR (e.g., sample 544 from the Kuzayır lamproite) as the starting magma and samples from the SHVR as the final magma compositions. The mineral phases obtained from these calculations are $Ol_{\sim 0.20} + Cpx_{\sim 0.24} + Sa_{\sim 0.45} + Phl_{\sim 0.10} \pm Mag/Ilm_{\sim 0.01}$, which more closely match the petrographic observations. However, the results of the mass balance calculations for the SHVR and UKVR are questionable as; (1) the Σr^2 values are too high, (2) a large number of small mafic volcanic units were investigated, and (3) each volcanic unit shows variable petrographic features. Hence, the geochemical variations among these rocks may be indicative of a more complex petrogenetic evolution involving different degrees of melting or source enrichment, rather than a simple fractional crystallization history (see also Innocenti et al., 2005; Ersoy et al., 2008, 2010b).

Table 3.4 Least squares major element modeling results for SHVR and UKVR. The compositions of the minerals used in the calculations are from Aldanmaz (2006).

Starting magma	Final magma	*Ol*	*Cpx*	*Pl*	*Sa*	*Phl*	*Mag/Ilm*	*Cryst,%*	*Σr²*
Kıran-Zahman basalts									
733	*Z-1*	38.2	30.1	-	-	31.7	-	*24*	*3.28*
733	*Z-1*	38.9	30.4	28.8	-	-	1.9	*23.5*	*3.13*
733	*Z-1*	7.8	27.1	-	45.5	16.4	3.3	*71*	*0.8*
Orhanlar basalt									
539	*535*	19.5	29.3	32.4	-	16.4	2.7	*59.8*	*2.52*
539	*545*	23.9	28.9	42.7	-	-	4.5	*39.7*	*2.77*
539	*545*	17.5	30.1	38	-	10.5	3.9	*42.9*	*2.51*
Karabacaklar volcanites									
IZ-187	*UG-74*	13.2	47.8	20.1	-	18.9	-	*55.5*	*6.33*
IZ-187	*UG-74*	13.4	48.5	20.4	-	15.6	2	*54.2*	*5.5*
IZ-187	*UG-74*	5.7	50.5	-	22.8	18.6	2.4	*63.5*	*8.79*
Naşa basalt									
ÖD-50	*SM-15*	54.9	-	45.1	-	-	-	*12.7*	*1.09*
ÖD-50	*SM-15*	53.4	-	45.4	-	-	1.2	*12.8*	*1.08*
ÖD-50	*SM-15*	24.9	-	27.2	-	47.8	-	*14.7*	*0.16*
SHVR as a whole									
539	*UG-74*	24	25.5	45.9	-	-	4.6	*74.8*	*6.8*
539	*UG-74*	14.3	26.4	33.1	11.2	11.3	3.7	*85.8*	*4.15*
539	*UG-58*	13.8	26.4	37.9	-	17.9	4	*75.8*	*3.89*
539	*UG-58*	14	25.9	35.7	5.5	15.1	3.9	*79.8*	*3.86*
UKVR → SHVR									
544	*UG-74*	16.2	29.4	-	36.2	16.8	1.4	83.8	1.47
544	*UG-145*	24.6	25.4	-	37.3	12.7	-	61.5	0.85
544	*IZ-061*	24.7	24.6	-	32	18.8	-	63	1.23
544	*539*	19.5	23.6	-	50.3	5.4	1.1	83.4	1.35
544	*IZ-045*	22.2	24.8	-	43.9	8.6	0.5	77.3	1.14
544	*IZ-187*	18.9	22.5	-	45.6	11.9	1.3	72.5	1.18

The Menderes Massif, which is typical of middle to upper crustal rocks of Western Anatolia, has high $^{87}Sr/^{86}Sr$ ratios. Interaction of relatively primitive magmas with wall-rocks of the Menderes Massif would, therefore, result in a sharp increase in $^{87}Sr/^{86}Sr$ in the contaminated magma. To test this, the AFC model of DePaolo (1981) has been applied to the $^{87}Sr/^{86}Sr_{(i)}$ of the volcanic rocks (Figure 3.9).
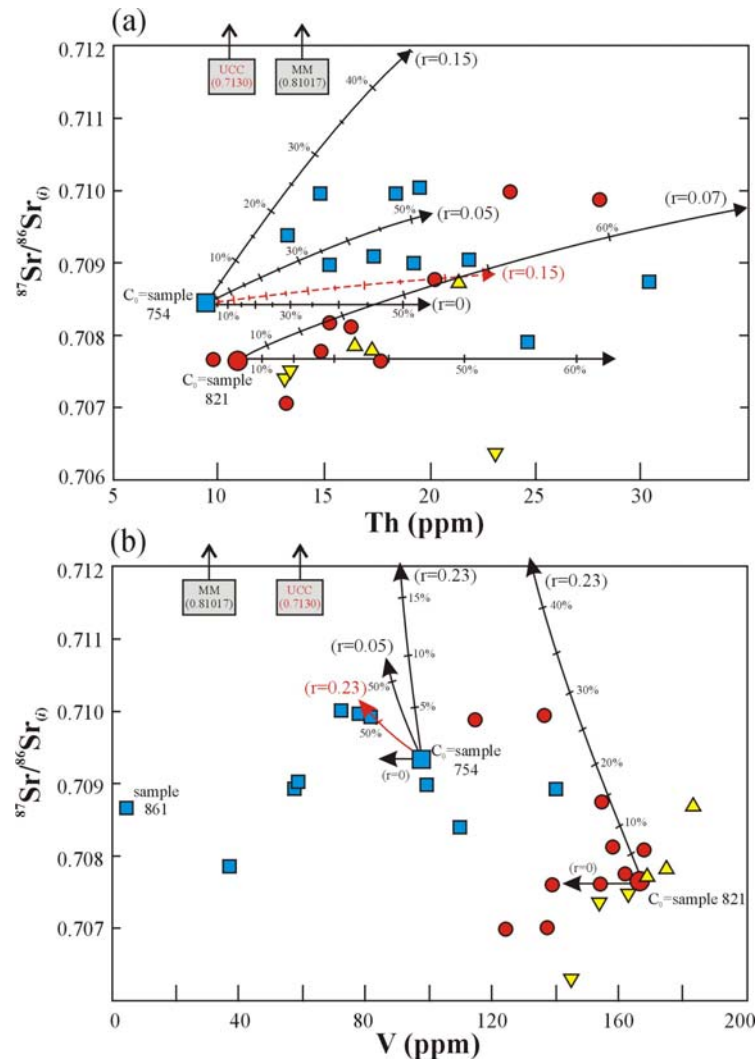
Figure 3.9 Fractional crystallization and combined assimilation (FC and AFC) models using equations of DePaolo (1981) "C_0" is the starting magma composition; "r": the ratio of assimilated to crystallized material. AFC trajectories from sample 754 use plagioclase-dominated (ol$_{0.05}$ + opx$_{0.05}$ + cpx$_{0.20}$ + pl$_{0.50}$ + amp$_{0.10}$ + bio$_{0.10}$) mineral assemblage with intermediate melt composition. AFC trajectories from sample 821 use $Ol_{0.20}$ + $Cpx_{0.24}$ + $Sa_{0.45}$ + $Phl_{0.10}$ + $Mag_{0.01}$. Black solid and red dashed trajectories use the Menderes Massif metamorphics (MM; Th: 13.9 ppm; Sr=158.8 ppm, ^{87}Sr/^{86}Sr=0.81017) and Upper Continental Crust (UCC; Th: 10.7 ppm; Sr=350.0 ppm, ^{87}Sr/^{86}Sr=0.71300; Taylor & McLennan, 1995) compositions, respectively. Partition coefficients are given in Table 3.5.

Many of the UKVR and SHVR plot parallel to the theoretical AFC trend from sample 821 (Kestel volcanites) (Figure 3.9a), suggesting that small degrees of assimilation and fractional crystallization may have played a role in their genesis (see also Ersoy et al., 2010b). Petrographic observations of resorbed quartz xenocrysts

and wall-rock xenoliths in some mafic lavas in the region also supports this interpretation. In addition, even the most mafic SHVR/UKVR samples have $\delta^{18}O$ values (~8.5‰) that suggest they were affected by lower to upper crustal contamination during their petrogenesis.

Table 3.5 Mineral/liquid partition coefficients used in the fractional crystallization models (from Adam & Green, 2006 and compilation of Ersoy & Helvacı, 2010).

	Ol	Opx	Cpx	Amp	Pl	Sa	Bt	Mg/Ilm
Th (intermediate)	0.1000	0.1500	0.1000	0.1500	0.0150	-	0.1500	-
Th (basic)	0.0002	0.0005	0.0070	-	-	≈0	-	≈0
Cs (intermediate)	0.0100	0.0100	0.0100	0.0100	0.0300	-	0.1900	-
Sr (intermediate)	0.0200	0.0300	0.0900	0.6000	26,000	-	0.1500	-
Sr (basic)	≈0	0.0019	0.1020	-	-	≈0	-	≈0
K (intermediate)	0.0056	0.0091	0.0034	-	0.1510	-	-	-
Rb (intermediate)	0.0350	0.0250	0.0600	0.1300	0.1300	0.1800	32,000	≈0
Nb (intermediate)	0.0100	0.2000	0.2000	10,000	0.0250	-	14,000	-
V (intermediate)	0.0800	11,000	11,000	320,000	0.0100	-	-	-
V (basic)	0.1500	16,500	26,700	34,000	≈0	≈0	25,000	260,000

In order to study the possible effects of upper crustal contamination and fractional crystallization (AFC) process on HKVR samples (from andesites to rhyolites), the graphical method of Aitcheson & Forrest (1994) has been applied (Figure 3.10). In this method, the AFC equations for elements Cs, K, Th, U and Nb are evaluated together, as they are highly incompatible. The starting composition is represented by sample 716 (SiO_2 = 58.4; andesite from the Asitepe volcanites), and the contaminated magma composition is given by sample 861 (SiO_2 = 77.8; rhyolite from the Güneşli volcanites). A gneiss sample from the Menderes Massif (MMG) and upper continental crust (UCC) values from Taylor & McLennan (1995) are both used as possible contaminant phases.
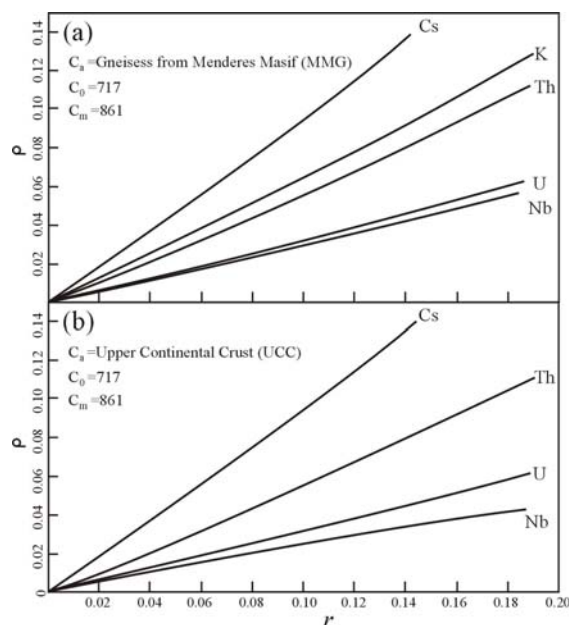
Figure 3.10 Graphical solution of AFC models for several trace elements using Eq. 6 of Aitcheson & Forrest (1994). Contaminant material is the Menderes Massif gneisses in (a) and average Upper Continental Crust in (b). C0, Ca and Cm are compositions of starting material, contaminant and contaminated magma, respectively. The parameters used are given in Table 3.6. See text for details.

Table 3.6 Model parameters for the graphical method of Aitcheson & Forrest (1994) shown on Figure 3.11.

Elements:	Bulk Partition Coefficients (intermediate composition)	Assimilant-1 (C_a) Menderes Massif gneiss (ppm)	Assimilant-2 (C_a) Upper continental crust (ppm)	Initial magma composition (C_0) Sample-717 (ppm)	Final magma composition (C_m) Sample-861 (ppm)
Cs	0.038	3.8	3.7	3.2	21.7
K	0.077	27560.3		20919.3	49642.8
Th	0.07	13.9	10.7	15.3	30.4
U	0.022	2.1	2.8	3.7	5.2
Nb	0.303	9.8	25	10.6	13.4
$^{87}Sr/^{86}Sr$		0.810017	0.713	0.708951	0.708703

Following the method of Aitcheson & Forrest (1994) (based on their Equation 6, in which only the elemental concentrations are used), the variables "r" (ratio of

assimilation to crystallization) and "ρ" (proportion of assimilated material relative to the original magma mass) appear to be very small (the vectors for each element converge close to zero; Figure 3.10). This suggests that upper crustal assimilation did not play a major role in the genesis of the HKVR. Instead, FC processes (or AFC with very low "r" values) are most compatible with the measured chemical variations. This is also supported by the absence of a positive correlation between $^{87}Sr/^{86}Sr_{(i)}$ and SiO_2 plus Sr contents (Figures 3.4c and 3.4d), and between Pb isotopes and SiO_2 contents (Figures 3.5c and 3.5d) of the HKVR.

To test the role of contamination processes by the Menderes Massif in the genesis of HKVR, $^{87}Sr/^{86}Sr_{(i)}$ compositions of the volcanic rocks are also modeled against Th and V contents (Figure 3.9). The results show that small degrees of contamination (r = 0.05–0.15) of sample 754 (andesite) by gneisses of the Menderes Massif (MM) would result in an unfeasibly large increase in the $^{87}Sr/^{86}Sr$ of the contaminated magma (Figure 3.9). Hence, the compositional variations of the HKVR can only accommodate very low "r" values (0–0.05). Contamination with average upper continental crust (UCC, Taylor & McLennan 1995; dashed red line on Figure 3.9a) with r = 0.15 would result in a smaller increase in the $^{87}Sr/^{86}Sr$ ratio of the contaminated magma, but the HKVR show horizontal trends, which are most compatible with FC. This modeling again strongly suggests that upper crustal contamination was not significantly involved in genesis of the HKVR, and again, this hypothesis is supported by petrographic observations, such as the absence of zoned or sieve textured plagioclase crystals in the evolved (dacitic and rhyolitic lavas) samples of the HKVR.

$\delta^{18}O$ values of the HKVR are positively correlated with their SiO_2 contents, which may be an indicative for extensive upper crustal contamination processes (Figure 3.11a), but the $\delta^{18}O$ values are negatively correlated with their $^{87}Sr/^{86}Sr_{(i)}$ compositions (Figure 3.11d). Two AFC models have been constructed using $\delta^{18}O$ values of 9‰ and 14‰ (min and max values) for the Menderes Massif (Figures 3.11c and 3.11d). The results show that high degrees of contamination (r = ~0.50) by crustal rocks with very high $\delta^{18}O$ values (~14‰) are needed to explain the $\delta^{18}O$ data

of the HKVR, but (as noted above) high degrees of contamination are not supported by other isotope and trace element data (e.g., Figure 3.9). In the light of these relationships, it appears unlikely that the high $\delta^{18}O$ values of the volcanic rocks can be explained by upper crustal contamination. Instead, these values were more likely inherited during early stages of differentiation of HKVR from more mafic magmas.
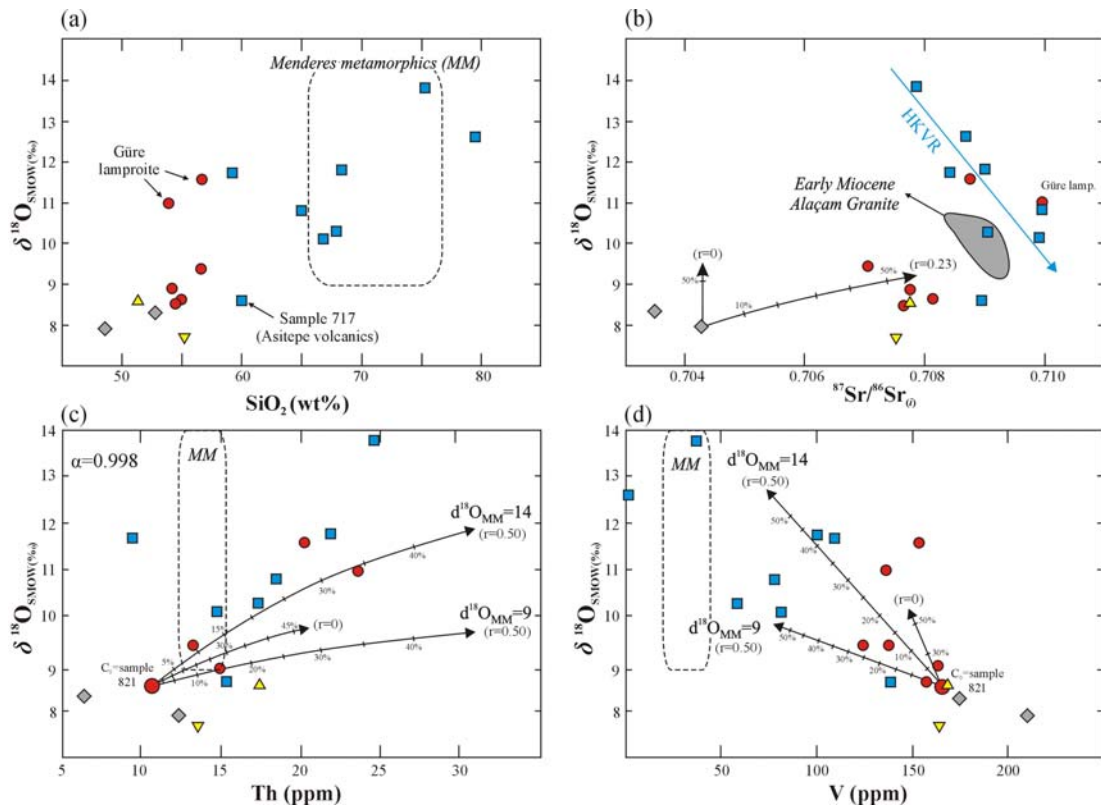
Figure 3.11 (a) $\delta^{18}O$ vs SiO$_2$ systematics for the volcanic rocks. (b–d) Fractional crystallization and combined assimilation (FC and AFC) models for $\delta^{18}O$ vs $^{87}Sr/^{86}Sr_{(i)}$, Th and V. AFC trajectories from sample 821 use $Ol_{0.20} + Cpx_{0.24} + Sa_{0.45} + Phl_{0.10} + Mag_{0.01}$. The partition coefficients used are given in Table 3.5. See Figure 3.6 for symbols. Oxygen fractionation factor (α) for silicate minerals is given as 0.998. Early Miocene Alaçam Granite data are from Hasözbek et al. (2011).

In order to study the effects of fractional crystallization (FC) process on the HKVR (from andesites to rhyolites), mass balance calculations (Stormer & Nicholls, 1978) have been performed (Table 3.7). The best results were obtained from the Asitepe volcanites ($\Sigma r^2 = 0.01\text{-}0.25$), and show that the HKVR was affected by *pl*- and *amp*-dominated fractionation. The other fractionating phases are pyroxenes,

biotite and Fe-Ti oxides; in agreement with the petrographic observations. Mass fractions of the crystallized materials in the models are between 20-35%.

Table 3.7 Least squares major element modeling results for individual HKVR. The compositions of the minerals used in the calculations are from Aldanmaz (2006).

Starting magma	Final magma	Ol	Opx	Cpx	Amp	Pl	Bt	Mag/Ilm	Cryst,%	Σr^2
Kayacık volcanites										
GÖ-1	GÖ-3	16.7	-	11.3	27.4	44.6	-	-	30.3	0.4
GÖ-1	GÖ-3	-	31.3	13.5	5.9	49.3	-	-	35.2	0.59
GÖ-1	GÖ-3	-	33.9	14.9	-	51.2	-	-	35.7	0.61
Eğreltidağ-Sevinçler volcanites										
522	506	-	-	-	18.7	72.9	-	8.4	21.2	0.17
522	506	-	-	-		81.5	7.5	11	20.3	0.57
522	506	-	-	-	32.4	61.3	6.3	-	23.1	1.45
Asitepe volcanites										
716	755	-	10.7	17.8	-	52.7	11	7.7	32.9	0.01
716	755	-	2.4	-	44.7	43.4	4.6	5	31.5	0.02
716	755	-	19	13.9	-	58.8	-	8.3	34.5	0.25
Yağcıdağ volcanites										
KD-3	YF-1	-	-	38.7	-	36	17.5	7.8	20.7	0.45
KD-3	YF-1	-	-	15.7	46.8	32.2	-	5.4	20.8	0.6
KD-3	YF-1	6.7	-	37.4	-	45.1	-	10.1	20	0.73

An average fractionating mineral assemblage ($Ol_{0.05} + Opx_{0.05} + Cpx_{0.20} + Pl_{0.50} + Amp_{0.10} Bt_{0.10}$), obtained from the least squares major element model has been applied to trace element Rayleigh fractionation modeling (Figure 3.12). Nearly 50% fractional crystallization from sample 716 closely matches the measured trace element variations of the HKVR, but while this FC process may have slightly increased the $\delta^{18}O$ values of the HKVR, it can not account for all the data.
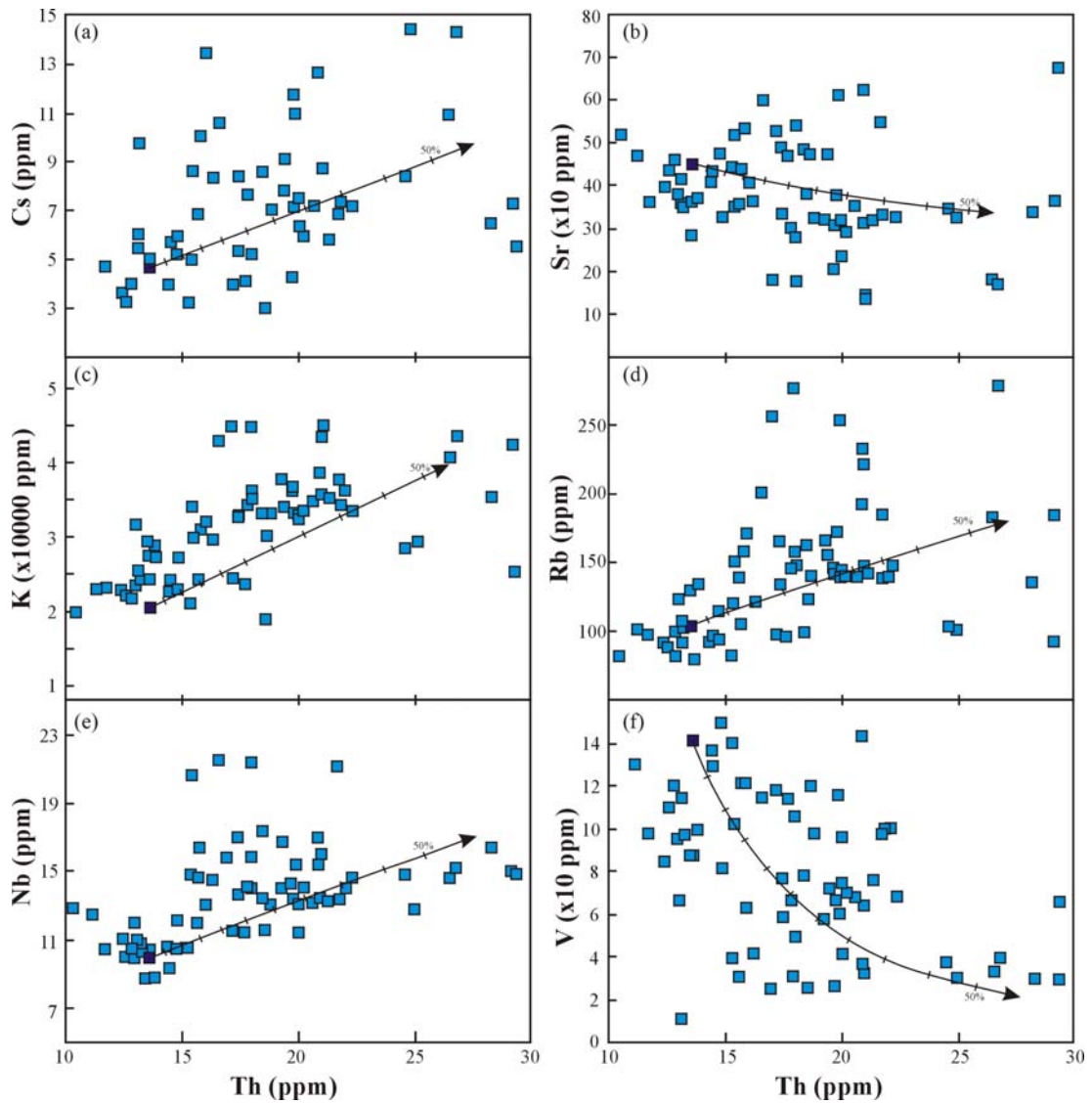
Figure 3.13 (a–f) Trace element fractional crystallization (FC) models for the HKVR. Theoretical FC curves are calculated using mineral assemblage of $Ol_{0.05} + Opx_{0.05} + Cpx_{0.20} + Pl_{0.50} + Amp_{0.10} + Bt_{0.10}$ and partition coefficients given in Table 3.5. Tick marks on the FC curves represent the ratio of the final to the initial mass of magma with 5% increments. The starting composition is sample 716 (SiO_2=58.4) from the Asitepe volcanites.

CHAPTER FOUR
MANTLE SOURCE CHARACTERISTICS OF THE EARLY-MIDDLE
MIOCENE MAFIC VOLCANIC ROCKS

4.1 Introduction to Mafic Volcanism in the Western Anatolia

In the eastern Mediterranean, Tertiary volcanic activity related to subduction or to post-collisional extension is commonly represented by K-rich, high-Mg orogenic magmatic rocks derived from heterogeneously enriched mantle lithosphere (e.g., Cvetković et al., 2004a, b; Prelević & Foley, 2007; Prelević et. al., 2004, 2005, 2008; Conticelli et al., 2009a,b). It has been suggested that partial melting of clinopyroxene-amphibole-phlogopite veins in metasomatized mantle produces high-Mg, K-rich magmas with different degrees of silica saturation/under-saturation (e.g., Conticelli et al., 2009a, and references therein).

The origin of the early-middle Miocene age volcanism in Western Anatolia has been unclear, largely because of the limited outcrops of the mafic lavas. However, the recent discovery of new outcrops of early-middle Miocene mafic lavas in the region has allowed their source compositions to be characterized (e.g., Innocenti et al., 2005; Ersoy & Helvacı, 2007; Agostini et al., 2007; Ersoy et al., 2008). In this chapter, a new set of major and trace element and Sr-Nd isotopic data from the early-middle Miocene mafic volcanic rocks in NE–SW-trending basins are combined with published data from the volcanic rocks located further west. The data is evaluated in order to reveal the geochemical characteristics and enrichment processes of the mantle sources of this volcanism in the region. These observations are then coupled with other geological data to construct a geodynamic model of the region during the early-middle Miocene and to suggest a petrological model for the origin of post-collisional magmatism which lead to enrichments in K and other incompatible trace elements.
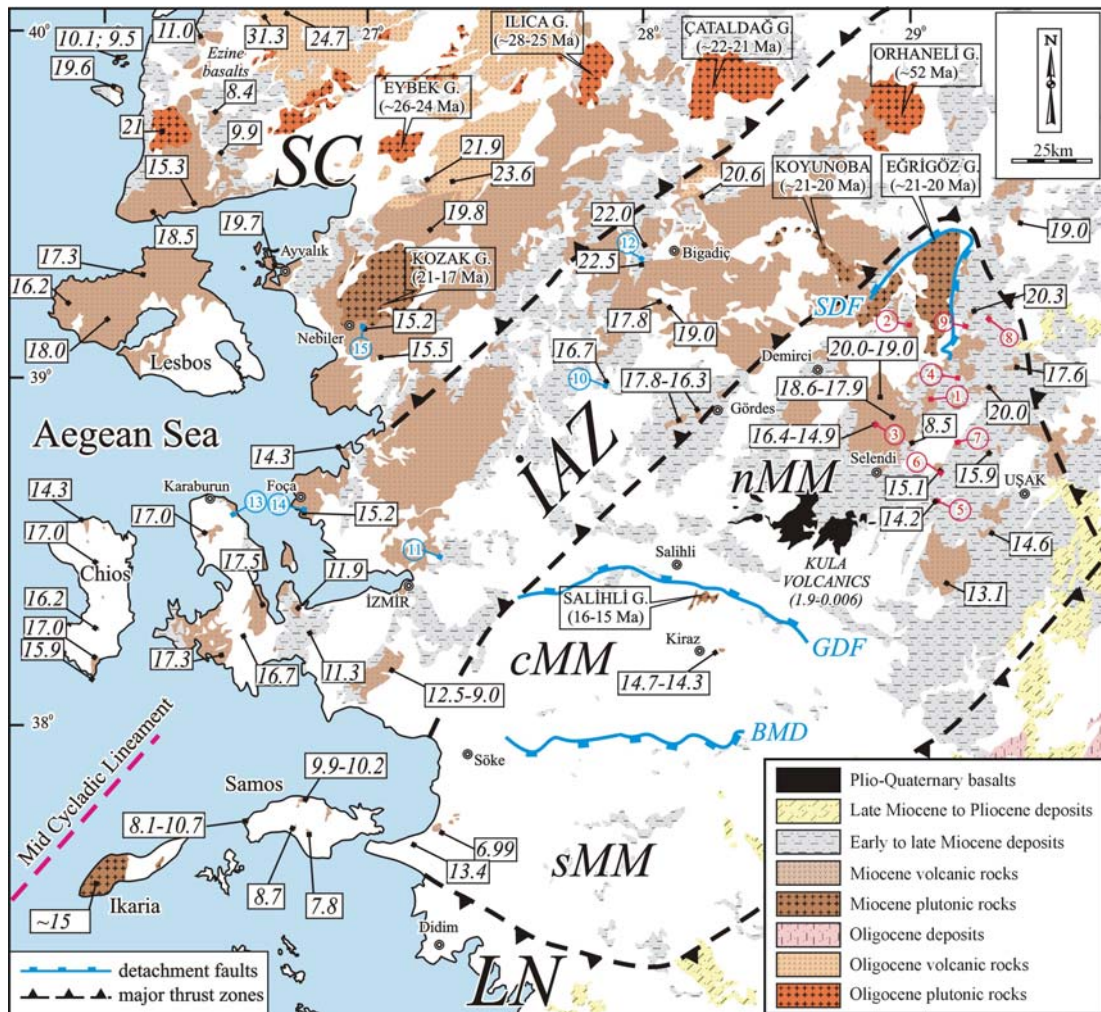
Figure 4.1 Geological sketch map of the Neogene magmatic rocks and lacustrine deposits in Western Anatolia (modified from Geological Map of Turkey (1:500000), 2002). The numbers in rectangles indicate the ages of the volcanites in Ma. The age data are from Borsi et al. (1972); Ercan et al. (1986, 1995); Helvacı (1995); Pe-Piper et al. (1995, 2009); Delaloye & Bingöl (2000); Aldanmaz et al. (2000); Emre & Sözbilir (2005); Innocenti et al. (2005); Erkül et al. (2005a); Purvis et al. (2005); Pe-Piper & Piper (2007); Altunkaynak & Genç (2008); Ersoy et al. (2008); Boztuğ et al. (2009); Helvacı et al. (2009). The numbers in circles indicate the volcanic units investigated in this study: UKVR and SHVR (red circles): (1) Orhanlar basalt, (2) Naşa basalt, (3) Kuzayır lamproite, (4) Ilıcasu lamproite, (5) Güre lamproite, (6) Kıran basalt; (7) Zahman basalt, (8) Dereköy basalt, (9) Kestel volcanites; HKMVR (blue circles): (10) Akhisar basalt, (11) Beşyol basalt, (12) Gölcük basalt, (13) Karaburun volcanites, (14) Foça mafic lavas, (15) Nebiler mafic lavas. The tectono-stratigraphic units are: SC: Sakarya Continent; İAZ: İzmir-Ankara Zone; MM: Menderes Massif (separated as northern (n-), central (c-) and southern (s-) MM), LN: Lycian Nappes. Detachment faults are Simav (SDF), Gediz (GDF), Büyük Menderes (BMD) detachment faults, from north to the south.

The early Miocene high-Mg potassic mafic lava flows in western Anatolia are the Karaburun volcanites of the Karaburun Peninsula (Helvacı et al., 2009), the Gölcük basalt in Bigadiç basin (Erkül et al., 2005a), the Kuzayır lamproite in Selendi basin (Ersoy & Helvacı, 2007) and the Kestel volcanites in Emet basin. Potassic mafic volcanism intensified during the middle Miocene, with production of the Beşyol and Akhisar basalts, Nebiler volcanites, and Foça mafic volcanites to the west, and the Dereköy, Naşa, Kıran and Zahman basalts, and Ilıcaksu and Güre lamproites to the east (e.g., Aldanmaz et al., 2000; Innocenti et al., 2005; Agostini et al., 2007; Ersoy et al., 2008) (Figure 4.1). These mafic volcanic units comprise (1) high-K products in the western part, and (2) shoshonitic and/or ultrapotassic products in the eastern part.

The early-middle Miocene high-K mafic volcanic rocks were emplaced along a corridor lying to the west of the Menderes Massif, and continued southwestward with respect to the eastern volcanites produced on the Menderes Massif. This corridor is interpreted as a "crustal-scale transfer zone" (cf. the İzmir-Balıkesir Transfer Zone in west Turkey: Uzel & Sözbilir, 2008; and the mid-Cycladic Lineament in Mykonos: Pe-Piper et al., 2002), and the late Cenozoic volcanic activity in this NE–SW-trending zone was controlled by strike-slip faults (Erkül et al., 2005a; Uzel & Sözbilir, 2008). The early-middle Miocene shoshonitic and/or ultrapotassic volcanic rocks which are located in the eastern part of the region, developed mainly in the northern part of the Menderes Massif synchronously with exhumation of the massif in an extensional tectonic regime.

In this chapter geochemical characteristics of the volcanic units from the northern part of the Menderes Massif (the main scope of this thesis) and from the İzmir Balıkesir Transfer Zone is compared. The differences between them allow to further develop the presumed geodynamic and petrologic evolution of the region and late Cenozoic magmatic activity.

4.2 Major and Trace Element Geochemistry

The ultrapotassic rocks (K_2O and $MgO > 3\%$wt. and $K_2O/Na_2O>2$; Foley et al., 1987) plot in shoshonite and latite fields on a total alkalis (Na_2O+K_2O) versus SiO_2 (TAS) diagram (LeMaitre, 2002) (Figure 4.2a), and are referred to as Ultra-K Volcanic Rocks (UKVR). Some UKVR samples also possess a lamproitic affinity, and are classified as Mediterranean lamproites which are characterized by higher SiO_2 and Al_2O_3 contents with respect to those of "normal" lamproites (Group 1 lamproites; e.g., Foley et al., 1987; Prelević et al., 2008). The details of the lamproitic rocks have been discussed by Innocenti et al. (2005), Ersoy & Helvacı (2007), and Ersoy et al. (2008).

The volcanic rocks, which do not show ultrapotassic affinity, have been classified as shoshonitic and high-K according to the SiO_2-K_2O diagram (Figure 4.2b). The shoshonitic rocks include both latites and shoshonites, and are referred to as Shoshonitic Volcanic Rocks (SHVR, Mg# = 49.1-72.4). The UKVR and SHVR are generally CIPW nepheline- or quartz-normative (ne- or qt-normative). These rocks are mainly located to the east of Western Anatolia (Figure 4.1). The high-K mafic rocks, located mainly to the west of Western Anatolia, include a wide range of rock types, such as high-K calc-alkaline basalt and basaltic andesite, calc-alkali shoshonite and latite, and potassic trachybasalt (Figure 4.2a). These rocks are referred to as High-K Mafic Volcanic Rocks (HKMVR, Mg# = 35.2-73.4). Three HKMVR samples possess a weak shoshonitic affinity, but they have been included with the HKMVR on the basis of their locations and similar trace element contents to other HKMVR samples. Overall, the K contents (and other incompatible trace elements) of the volcanites increase from west to east.

The chemical trends of the volcanic rocks show non-systematic increases in Al_2O_3 and Na_2O and decrease in Fe_2O_3 with decreasing MgO (not shown). K_2O and Na_2O contents are nearly constant. CaO contents of the SHVR increase, while those of the HKMVR and SHVR decrease. The HKMVR have lower contents of high field strength elements (HFSE such as Zr, Hf and Nb) and light to medium rare earth

elements (LREE to MREE, such as La, Gd) than those of the shoshonitic and ultrapotassic rocks. Compatible element contents, such as Ni, Co and V, and large ion lithophile element (LILE) contents, except for Rb, are also similar for the three groups.
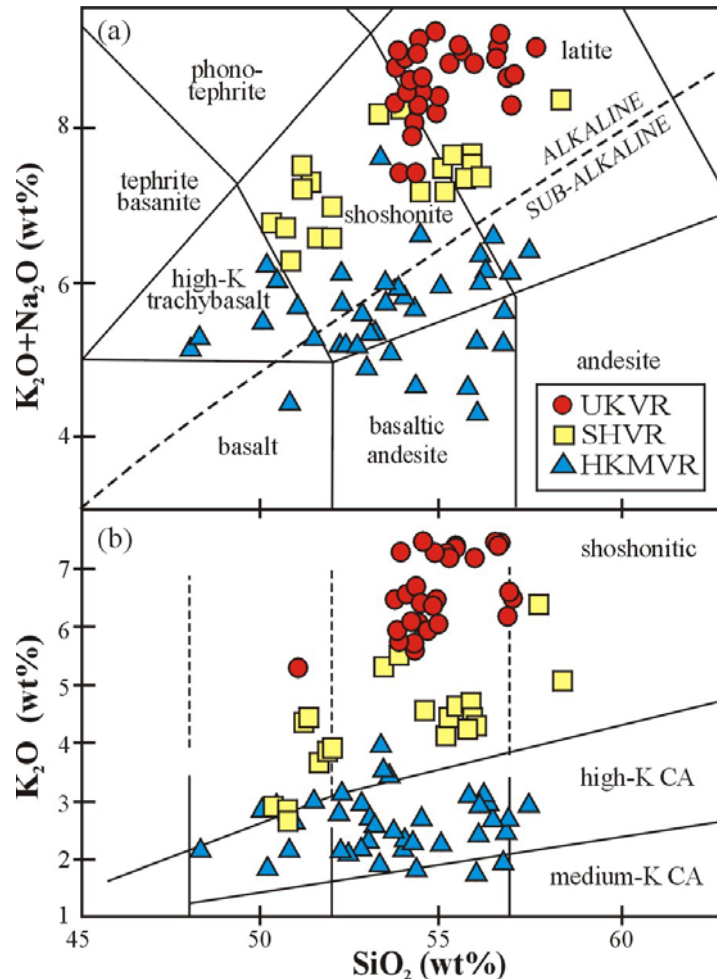
Figure 4.2 Total alkali–silica (TAS) plot (LeMaitre, 2002) for the early-middle Miocene mafic volcanic rocks in Western Anatolia. Alkaline–subalkaline (calc-alkaline) line is according to Irvine & Baragar (1971). The samples have been plotted on a water-free oxide contents normalized to 100%.

For simplicity, only the most mafic samples of each group have been shown on a Primitive mantle-normalized multi-element, but the patterns of these samples are representative of their groups (Figure 4.3). The volcanic rocks show enrichments in LILE and LREE over HFSE and heavy-REE (HREE), producing negative anomalies

in Ta, Nb and Ti. The UKVR and SHVR show similar trace element abundances, but the HKMVR is characterized by distinctly lower abundances of HFSE and REE. The volcanic samples in this study do not show large Eu negative anomalies (Eu/Eu* values are in the range of 0.69–0.99).
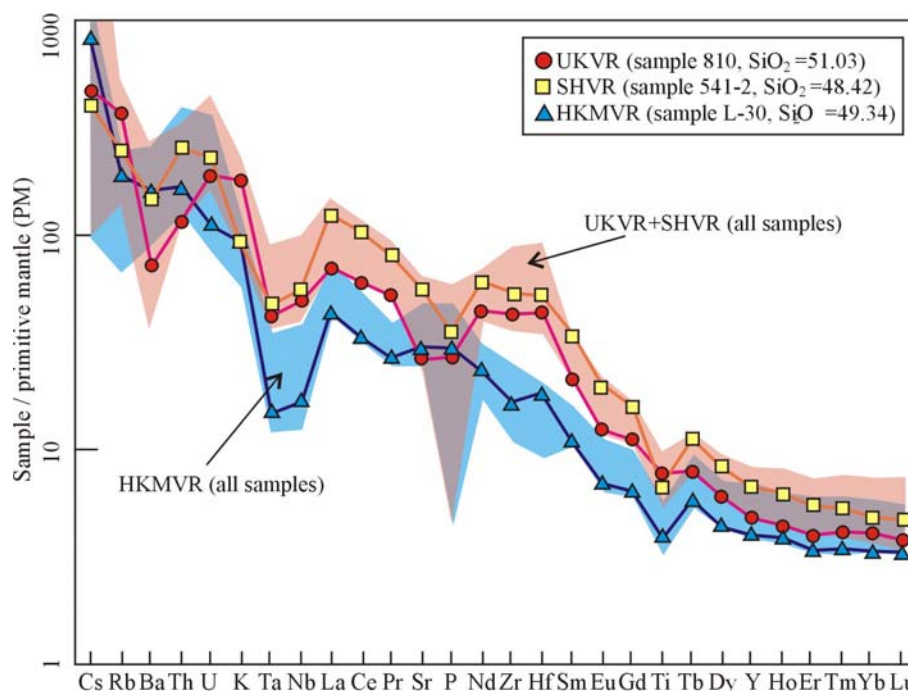
Figure 4.3 Primitive mantle (PM)-normalized incompatible element diagram for representative early-middle Miocene mafic rocks from Western Anatolia. Normalizing values are from Palme & O'Neil (2004).

4.3 Sr-Nd Isotopic Data

Initial $^{87}Sr/^{86}Sr$ and $^{143}Nd/^{144}Nd$ ratios of Western Anatolian early-middle Miocene mafic rocks, investigated in this study, range from 0.706312-0.709958 and 0.512165-0.512488, respectively (Table 3.2), and they plot in the enriched segment of the $^{87}Sr/^{86}Sr$-$^{143}Nd/^{144}Nd$ diagram (Figure 3.5a). The samples have a distinctly more continental signature than MORB, Quaternary Kula basalts and South Aegean volcanic arc lavas. Except for the Güre lamproite and Kıran basalt, the UKVR show relatively uniform isotope compositions, while the HKMVR and SHVR show a wider range, with no correlation between alkalinity and Sr-Nd isotopic ratios of the lavas.
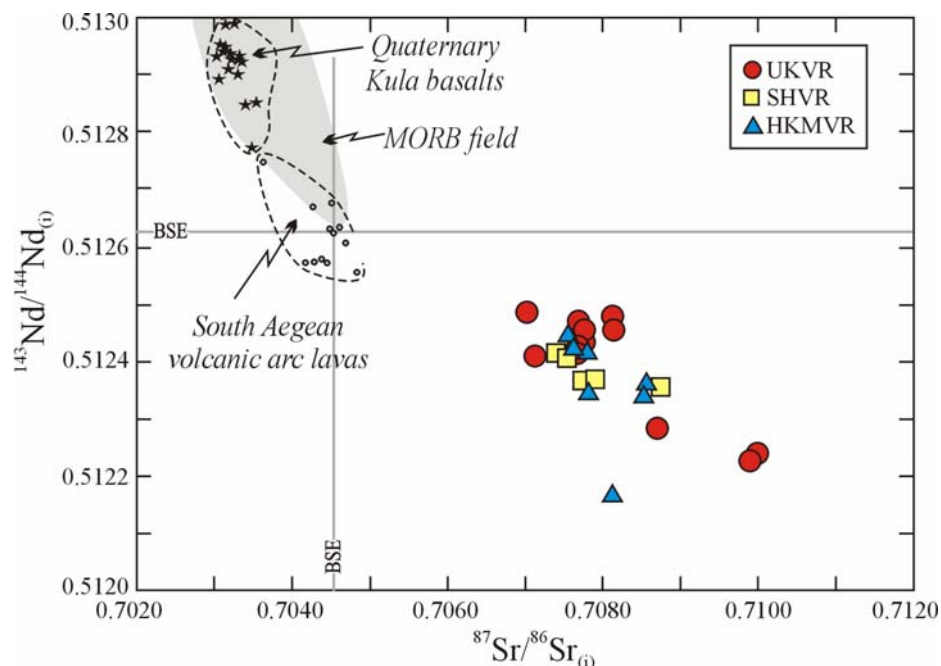
Figure 4.4 Initial $^{143}Nd/^{144}Nd$ versus initial $^{87}Sr/^{86}Sr$ for the early-middle Miocene mafic volcanic rocks from Western Anatolia. Data for Quaternary Kula basalts are from Alıcı et al. (2002) and Buettner et al. (2005). MORB field is from GEOROCK database (Sarbas et al., 2006). Bulk Silicate Earth composition (BSE) is from Workman & Hart (2005). The 2σ errors are less than symbol sizes.

4.4 Petrogenesis of the Early-Middle Miocene High-Mg Mafic Volcanites

4.4.1 Fractional Crystallisation and Contamination Effects

The SHVR and UKVR groups, which are characterized petrographically by olv + cpx + plg/snd ± phl (Table 4.1), are spatially and temporally associated, and hence have been evaluated together. The samples having highest MgO and lowest SiO_2 (least evolved) are assumed to represent the starting magma composition. Major element compositions of the fractionating mineral phases are calculated from mineral analyses, given by Aldanmaz (2006). Mass balance calculations are performed using the several mineral assemblages contain either plagioclase or sanidine and phlogopite (Table 4.2). The results show that evolved samples may be produced by ~43-50%

fractionation of $olv_{(\sim22-34\%)}$ + $cpx_{(\sim21-26\%)}$ + $plg_{(\sim36-51\%)}$ + $mg_{(\sim2-4\%)}$ (Σr^2 =2.1–4.7) or ~65-83% fractionation of $olv_{(\sim8-22\%)}$ + $cpx_{(\sim24-35\%)}$ + $sa_{(\sim39-50\%)}$ + $phl_{(\sim5-16\%)}$ + $mg_{(\sim1-3\%)}$ (Σr^2 = 0.5–1.1) from the least evolved samples. For the HKMVR group, ~44-52% fractionation of $olv_{(\sim33-37\%)}$ + $cpx_{(\sim17-30\%)}$ + $plg_{(\sim33-50\%)}$ (Σr^2 = 3.1–4.7) or $olv_{(\sim17-21\%)}$ + $cpx_{(\sim22-34\%)}$ + $plg_{(\sim14-23\%)}$ + $phl_{(\sim24-27\%)}$ (Σr^2 = 0.7–1.7) is needed. Although these least-squares analyses do not produce particularly high Σr^2 values, but they do indicate that this style of fractionation can account for a significant proportion of the major element variations.

Initial $^{87}Sr/^{86}Sr$ isotopic contents of the volcanic rocks are plotted against their Mg# values (Figure 4.5a). On this diagram, slight negative correlation for the UKVR samples indicates that a small degree of crustal assimilation accompanied the fractional crystallization. In order to evaluate the crustal contamination processes in the genesis of the studied rock units, AFC equation of DePaolo (1981) was also used. An average fractionating compositions of $olv_{(35\%)}$ + $cpx_{(25\%)}$ + $plg_{(40\%)}$ is used. The metamorphic rocks of the Menderes Massif, representing the middle crustal rocks of Western Anatolia, have high $^{87}Sr/^{86}Sr$ ratios. Satır & Friedrichsen (1986) obtained $^{87}Sr/^{86}Sr$ ratios of 0.71154-1.29740 from the gneisses and granites, and $^{87}Sr/^{86}Sr$ ratios of 0.72691 and 0.77680 were obtained for augengneisses in this study (Table 3.1). Interaction of basaltic melts with the rocks of the Menderes Massif would, therefore, result in a sharp increase in $^{87}Sr/^{86}Sr$ ratios in the contaminated magma. As a test of this process $^{87}Sr/^{86}Sr_{(i)}$ ratios of the volcanic rocks have been modeled against compatible (Ni) and incompatible trace elements (Th and Nd) (Figure 4.5). Sample IZ-041 (Innocenti et al., 2005) is the starting melt composition as it has the lowest $^{87}Sr/^{86}Sr_{(i)}$ and highest Mg# in the area. The Menderes Massif metamorphics (MM) and average upper continental crust (UCC) compiled by Cribb & Barton (1996) have been used as the contaminant phase in the AFC-1 and AFC-2 models, respectively. $^{87}Sr/^{86}Sr_{(i)}$ against Ni contents of the volcanic rocks are only partially explained by the AFC-1 model (Figure 4.5b).
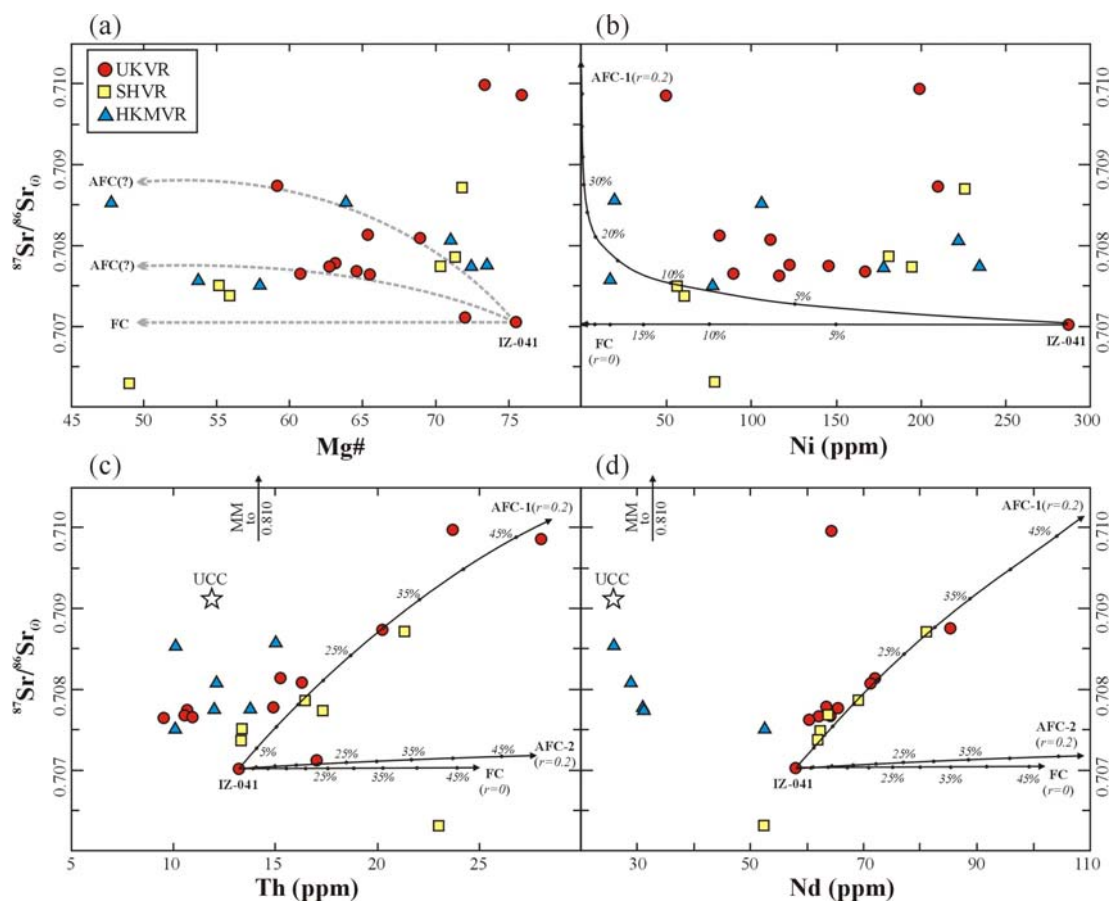
Table 4.2 Results of mass balance calculations (The calculations are carried out by using the software Petrograph software, Petrelli et al., 2005)

starting magma	final magma	Ol	Cpx	Pl	Sa	Phl	Mg	Cryst.%	Σr^2
UKVR+SHVR									
539	703	30.2	21.8	46.2	-	-	1.8	50.2	4.71
539	B-1	23.5	22.0	50.1	-	-	4.3	48.3	4.16
539	IZ-057	29.3	20.8	46.9	-	-	3.0	47.0	3.25
539	733	22.6	23.0	50.7	-	-	3.7	49.6	2.77
539	746	34.4	25.8	36.4	-	-	3.4	42.7	2.11
539	535	19.5	29.3	32.4	-	16.4	2.7	59.8	2.52
IZ-169	736	8.2	35.5	-	39.3	15.0	2.1	64.9	0.49
733	Z-1	7.8	27.1	-	45.5	16.4	3.3	71.0	0.80
544	539	19.5	23.6	-	50.3	5.4	1.1	83.4	1.35
544	IZ-045	22.2	24.8	-	43.9	8.6	0.5	77.3	1.14
HKMVR									
L-30	EA-407	37.1	20.7	42.2	-	-	-	47.0	4.71
L-30	853	36.9	29.9	33.2	-	-	-	43.7	4.62
IZ-147	EA-407	33.5	16.7	49.8	-	-	-	52.0	4.53
IZ-147	853	33.2	23.7	43.1	-	-	-	46.0	3.13
L-30	EA-407	21.4	26.2	26.9	-	25.5	-	52.9	0.83
L-30	853	17.2	33.6	22.5	-	26.7	-	50.2	1.71
IZ-147	EA-407	21.0	21.7	33.6	-	23.7	-	55.9	0.66

The AFC-2 model trajectory on this diagram is similar to the pure fractional crystallization (FC) trend. $^{87}Sr/^{86}Sr_{(i)}$ ratios of the volcanites largely show a positive correlation with the incompatible element Th (Figure 4.5c). The strongest positive correlation is achieved by the AFC-2 model (with $r = 0.2$; the ratio of assimilation to crystallization). The AFC-2 model trend also best explains the $^{87}Sr/^{86}Sr_{(i)}$ vs. Nd compositions of the UKVR and SHVR (Figure 4.5d). As indicated by these relationships, the AFC-1 model, using the MM shows that low degrees of assimilation ($r = 0.2$) of the MM would result in a rapid increase in the $^{87}Sr/^{86}Sr$ ratios of the contaminated magma.

Some of large ion lithophile elements (LILE), such as Sr, Ba, K and Rb, of the evolved samples cannot be well reproduced by using the less evolved samples and the fractionating mineral phases obtained from major element least-squares analysis. This arises mainly from the fact that the most primitive samples have higher LILE contents with respect to the evolved samples, and hence trace element fractional crystallization models using the most primitive lavas as starting composition result in unrealistic incompatible trace element contents. Moreover, the UKVR have higher Rb/Sr ratios with respect to the HKMVR and SHVR, requiring higher degrees of plagioclase fractionation. However, the UKVR group includes plagioclase-free lamproites (e.g., Ilıcasu lamproite) and ultrapotassic latites with very small amounts of plagioclase.

Taking into accounts the petrographic and geochemical features as a whole, it is apparent that neither FC nor AFC models can explain the whole range of trace element and $^{87}Sr/^{86}Sr_{(i)}$ compositions of the mafic rocks. Hence, there is no strong evidence from a wide spectrum of trace element and isotopic data to suggest that FC and AFC played a significant role in the petrogenesis of the early-middle Miocene mafic potassic to ultrapotassic volcanic rocks. Rather, it is most likely that the high $^{87}Sr/^{86}Sr_{(i)}$, LILE and LREE contents of the mafic lavas were likely inherited from the melt source, which had been modified by metasomatic processes in the subduction zone, as these elements can easily be transported from the descending slab to the overlying mantle wedge (Pearce, 1982, 1983). In the light of these data,

the wide compositional features of the mafic lavas are attributed primarily to source characteristics, such as source heterogeneity due to metasomatic events and/or different degrees of partial melting of the heterogeneously metasomatised source (see also Pe-Piper & Piper, 2001, 2007; Innocenti et al., 2005; Ersoy et al., 2008; Dilek & Altunkaynak, 2007; Altunkaynak & Genç, 2008).
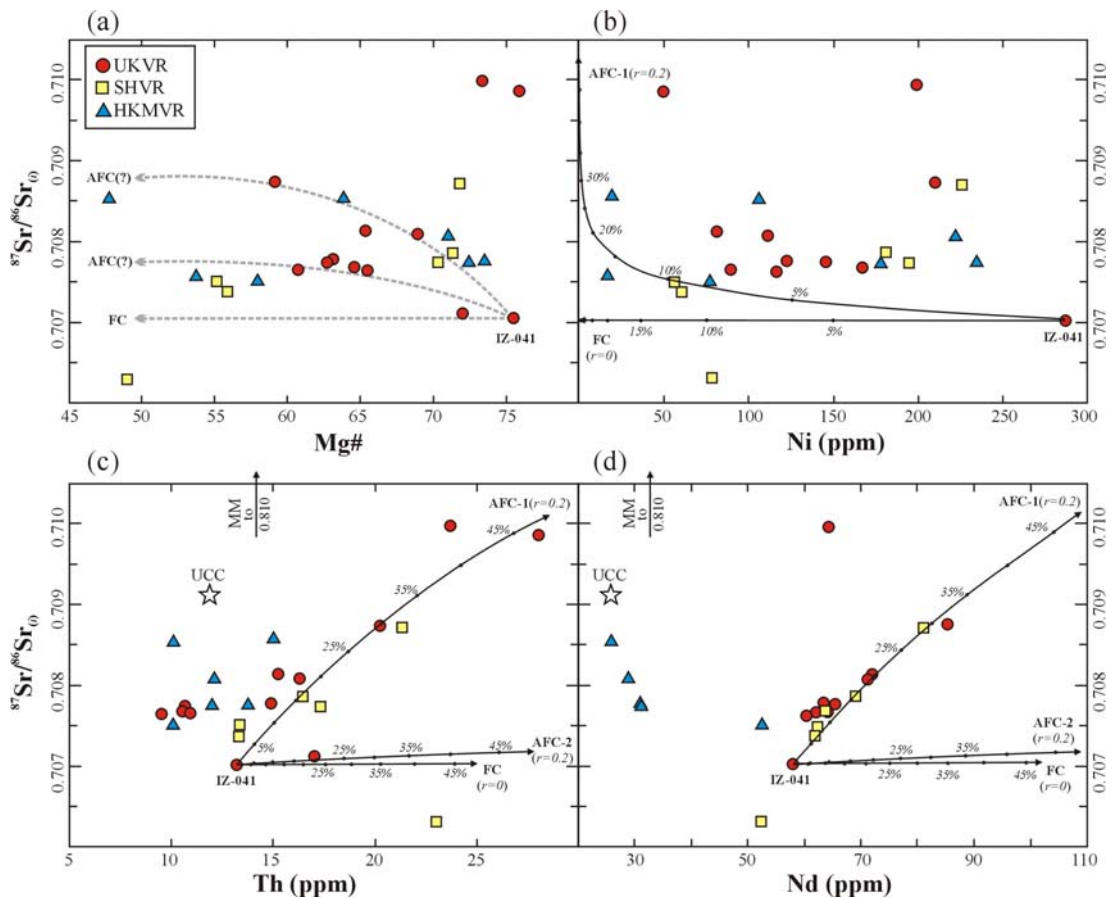
Figure 4.5 Initial $^{87}Sr/^{86}Sr$ versus Mg# values (a) and Ni, Th and Nd (b–d) contents for the early-middle Miocene mafic volcanic rocks from Western Anatolia. Fractional crystallization (FC) and coupled assimilation (AFC; after the equation of DePaolo, 1981) models use sample IZ-041 as the starting melt composition (C0). Mineral assemblage is $ol_{0.35}+cpx_{0.25}+plg_{0.40}$. "$r$" value (rate of crystallization to assimilation) is 0.2 for AFC-1 and AFC-2 models which use the Menderes Massif (MM; Ni=7.6 ppm, Th=13.9 ppm, Nd=33.8; $^{87}Sr/^{86}Sr$=0.810169) and the average Upper Continental Crust (UCC; Ni=20.0 ppm, Th=10.7 ppm; Nd=26.0 ppm, $^{87}Sr/^{86}Sr$=0.708983; from Taylor & McLennan, 1995; Cribb & Barton, 1996) as the contaminant (Ca), respectively. Partition coefficients for the respective minerals are given in Table 4.3. The 2σ errors are less than symbol sizes.

4.4.2 Source Characteristics

The objective of this section is to pose a number of hypotheses for the characteristics of the source area to the volcanic rocks and the processes that might have modified these initial compositions. Then, it has been considered that which of these hypotheses best explains the observed data, in order to arrive at a most probable petrogenetic model that can then be used to evaluate the geodynamic implications. The volcanic rocks with Mg# values higher than 65.0 (Green, 1971), $FeO_{(t)}/MgO$ ratios between 0.4-0.8 (Albaréde, 1992), and MgO contents higher than 6.0 wt.% (Luhr, 1997) are considered to be primitive magmas generated from a peridotitic source. In this study, the samples matching these characteristics and having SiO_2 contents lower than 55 wt.% are used to model the mantle source characteristics, thus avoiding even small AFC and FC effects.

4.4.2.1 Mantle Background

Several authors have suggested that the early-middle Miocene Western Anatolia volcanic rocks originated from a metasomatized mantle source (e.g., Yılmaz, 1989; Pe-Piper & Piper, 2001, 2007; Innocenti et al., 2005; Pe-Piper et al., 2009). Ersoy et al. (2008) and Helvacı et al. (2009) hypothesized the presence of minor amphibole in the mantle source region. As there is no direct evidence from mantle xenoliths embedded in the early-middle Miocene mafic volcanic rocks, some approximations are required in order to reveal the geochemical characteristics and mineralogy of their mantle source region.

As discussed above, radiogenic Sr, LILE and LREE contents of the mafic lavas in this study indicate a heterogeneous source enriched by subduction-related metasomatic components. The mantle source composition prior to such enrichment can be examined using the concentrations or ratios of HFSE and HREE in the lavas. For example, Zr, Hf, Ta, Nb, Y and Yb are immobile in fluids and not enriched in the mantle wedge during subduction-related metasomatism (Pearce, 1982, 1983; Pearce

& Parkinson, 1993; Hawkesworth et al., 1995, 1997; Eiler et al., 2007). The Nb/Ta and Zr/Nb ratios of the most primitive lavas are compared with several mantle sources in Figure 4.6 (see also Figure 3.10). The Zr/Nb and Nb/Ta ratios of the volcanites from this study overlap with each other, and lie close to those of primitive mantle, and are distinctly lower than those of MORB-like mantle, suggesting that they were derived from a primitive mantle-like source that had not been significantly depleted by previous melting event(s). Hence, we have numerically modeled the melting of a mantle source with primitive mantle (PM) composition using trace element data for the inferred PM source taken from Palme & O'Neil (2004).
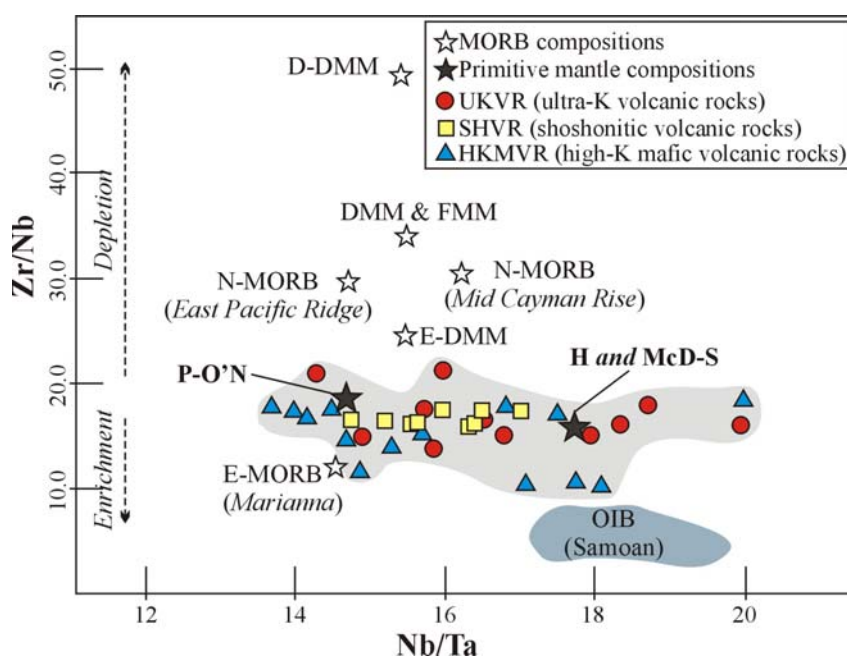
Figure 4.6 Zr/Nb versus Nb/Ta ratios of the most primitive volcanic rocks (SiO_2 < 55%; MgO > 6% and Mg# > 65). DMM: depleted MORB mantle, D-DDM: extremely depleted-DMM, E-DMM: enriched-DMM (Workman & Hart, 2005), FMM: fertile MORB mantle (Bédard, 1999). E-MORB (Marianna) and N-MORB (both East Pacific Ridge and Mid Cayman Rise) values are from Klein (2004). Primitive mantle compositions are from: H and McD-S: Hofmann (1988) and McDonough & Sun (1995) and P-O'N: Palme & O'Neil (2004). Samoan Ocean Island Basalts (OIB) are from Workman et al. (2004).

4.4.2.2 Batch Melting of Primitive Mantle-like Source

The mineralogical composition of the mantle source from which the volcanic rocks originated can be inferred using trace element ratios. For example, the presence of residual garnet in the mantle would deplete the Y and HREE abundances of the resulting partial melts (as long as garnet remains a restite phase). In a similar way, the presence of amphibole and phlogopite in the mantle source can be inferred by using trace elements with different partition coefficients in these phases. For example, Y and MREE are more compatible in amphibole and garnet with respect to phlogopite (Adam & Green, 2006). Ba and Rb, on the other hand, are highly compatible in phlogopite (e.g., Foley et al., 1996), so the ratios of these elements can be used to investigate the relative roles of amphibole and phlogopite during partial melting.

The melting of a primitive mantle source is modeled using Tb/Yb vs. Y/Rb ratios for three different mantle assemblages: (A) garnet lherzolite, (B) amphibole-bearing garnet lherzolite and (C) phlogopite-bearing garnet lherzolite (Figure 4.7). The garnet contents in model sources B and C are set at the same value. Hence, the partial melting trends for the Tb/Yb-Y/Rb ratios are independent of the garnet amount for these two model sources; instead, they depend on the amount of amphibole. The partition coefficients used in the model are given in Table 4.1 and the other melting parameters are in Table 4.4.

The model results indicate that Tb/Yb ratios of the lavas tend to lower values during partial melting of the mantle source. The presence of phlogopite in the source cannot explain the trace element compositions of the volcanic rocks, as Y/Rb ratios of the melts from such a source would be much higher than those observed in the volcanites (Figure 4.7). However, the presence of residual amphibole in the source during partial melting provides the closest fit to the observed Y/Rb ratios for very low degrees of partial melting. It is worthy to note that effects of the fractional crystallization of $ol_{(0.35)}+cpx_{(0.25)}+plg_{(0.40)}$ are negligible on this plot. The Y/Rb ratios of the volcanic rocks are still lower than those generated by even very low-degree

partial melts of the PM. Hence, an additional enrichment of Rb, possibly from subduction-related metasomatism, is required to fit the model to the volcanic rocks.

Table 4.3 Partition coefficients used in FC, AFC and melting models in this study. Partition coefficients are from a compilation of [1]Adam & Gren (2006), [2]Hart & Brooks (1974), [3]Kelemen & Dunn (1992), [4]Hart & Dunn (1993), [5]Dalpe & Backer (1994), [6]Philpotts & Schnetzler (1970), [7]McKenzie & O'Nions (1991), [8]Kennedy et al. (1993), [9]Green et al. (2000), [10]Jones & Layne (1997), [11]Villemant (1988), [12]Matsui et al. (1977), [13]Rollinson (1993)

	ol	opx	cpx	gt	amph	phl	plg
Cs	0.00020[1]	0.00090[1]	0.00070[1]	0.00100[1]	0.06000[1]	3.20000[1]	0.13000[11]
Rb	0.00010[1]	0.00380[1]	0.00140[1]	0.00200[1]	0.26000[1]	7.50000[1]	0.10000[7]
Ba	0.00010[1]	0.00360[1]	0.00110[1]	0.00200[1]	0.19000[1]	4.10000[1]	0.30000[12]
Th	0.00017[1]	0.00050[1]	0.00700[1]	0.00140[1]	0.00350[1]	0.00020[1]	0.01000[13]
U	0.00026[1]	0.00070[1]	0.00700[1]	0.00350[1]	0.00390[1]	0.00020[1]	0.01000[13]
K	0.00018[2]	0.00030[3]	0.00720[4]	0.00070[3]	1.36000[5]	2.65000[6]	0.15600[6]
Ta	0.00020[1]	0.00080[1]	0.01100[1]	0.00220[1]	0.08300[1]	0.07800[1]	0.04000[11]
Nb	0.00001[1]	0.00070[1]	0.00350[1]	0.00200[1]	0.06900[1]	0.07000[1]	0.01000[13]
La	0.00005[1]	0.00060[1]	0.04700[1]	0.00200[1]	0.05000[1]	0.00040[1]	0.27000[7]
Ce	0.00050[1]	0.00170[1]	0.08300[1]	0.00300[1]	0.09000[1]	0.00030[1]	0.20000[7]
Pr	0.00080[7]	0.00027[8]	0.15000[7]	0.00830[9]	0.35000[7]	n.a	0.17000[7]
Sr	0.00001[1]	0.00190[1]	0.10200[1]	0.00200[1]	0.24000[1]	0.17800[1]	2.00000[7]
P	0.03800[1]	0.00700[1]	0.01000[1]	0.03000[1]	0.01900[1]	0.00410[1]	n.a
Nd	0.00300[1]	0.00400[1]	0.19000[1]	0.02000[1]	0.20000[1]	0.00020[1]	0.14000[7]
Zr	0.00100[1]	0.00990[1]	0.11000[1]	0.09000[1]	0.13000[1]	0.01100[1]	0.04800[13]
Hf	0.00080[1]	0.01700[1]	0.25000[1]	0.06000[1]	0.27000[1]	0.01600[1]	0.05100[7]
Sm	0.00200[1]	0.01100[1]	0.35000[1]	0.12000[1]	0.30000[1]	0.00010[1]	0.11000[7]
Eu	0.00160[7]	0.01300[7]	0.23000[9]	0.32000[7]	0.88000[7]	n.a	0.73000[7]
Gd	0.00150[7]	0.01600[7]	0.24000[7]	0.49800[7]	0.86000[7]	n.a	0.06600[7]
Ti	0.01100[7]	0.10000[7]	0.28000[7]	0.15000[7]	0.72000[7]	1.02000[7]	0.04000[7]
Tb	0.00100[7]	0.03000[7]	0.51000[7]	1.00000[7]	0.40000[7]	0.00010[7]	0.06000[7]
Dy	0.00140[8]	0.03300[10]	0.52000[1]	2.40000[8]	0.40600[5]	n.a	0.05500[7]
Y	0.00300[1]	0.04600[1]	0.53000[1]	2.64000[1]	0.38000[1]	0.00200[1]	0.03000[7]
Ho	0.00310[1]	0.04800[1]	0.56000[1]	2.75000[1]	0.41000[1]	0.00010[1]	0.04800[7]
Er	0.00870[8]	0.06500[10]	0.38700[4]	4.40000[8]	0.36200[5]	n.a	0.04100[7]
Tm	0.00910[1]	0.07100[1]	0.54000[1]	5.26000[1]	0.36000[1]	0.00050[1]	0.03600[7]
Yb	0.01000[1]	0.07700[1]	0.39000[1]	6.25000[1]	0.27000[1]	0.00500[1]	0.03100[7]
Lu	0.02400[1]	0.09000[1]	0.49000[1]	8.03000[1]	0.30000[1]	0.00170[1]	0.02500[7]
Ni	32.00000[1]	11.30000[1]	10.00000[1]	8.78000[1]	n.a	n.a	n.a

Table 4.4 Non-modal batch melting model parameters used in melting models

	ol	opx	cpx	gt	amp	phl
garnet lherzolite						
source mode	0.55	0.22	0.15	0.08	-	-
melt mode	0.05	0.05	0.81	0.09	-	-
garnet-amphibole lherzolite						
source mode	0.55	0.22	0.15	0.03	0.05	-
melt mode	0.05	0.05	0.40	0.05	0.45	-
garnet-phlogopite lherzolite						
source mode	0.55	0.22	0.15	0.03	-	0.05
melt mode	0.05	0.05	0.65	0.05	-	0.20

melt fraction (F)	Rb (ppm)	Y (ppm)	Tb (ppm)	Yb (ppm)	Tb/Yb	Y/Rb
	garnet lherzolite					
0.01	54.25	13.20	0.65	0.67	0.97	0.24
0.05	11.83	12.73	0.58	0.67	0.87	1.08
0.10	5.99	12.20	0.51	0.66	0.77	2.04
	garnet-amphibole lherzolite					
0.01	29.47	20.45	0.73	1.37	0.53	0.69
0.05	10.74	19.86	0.64	1.45	0.44	1.85
0.10	5.99	19.17	0.56	1.57	0.36	3.20
	garnet-phlogopite lherzolite					
0.01	2.04	22.08	0.81	1.43	0.57	10.82
0.05	2.19	21.65	0.70	1.57	0.45	9.89
0.10	2.41	21.13	0.60	1.80	0.33	8.77

Non-modal batch melting of a garnet-amphibole lherzolite with PM composition is also modeled on a multi-element diagram (Figure 4.8). Even very low-degree batch melts are unable to explain overall trace element patterns of the volcanic rocks. Fractional crystallization (F=0.55) of $ol_{0.35}+cpx_{0.25}+plg_{0.40}$ from a low-degree (1%) non-modal batch melt yields LILE abundances that are broadly similar to those of the HKMVR (Figure 4.8).
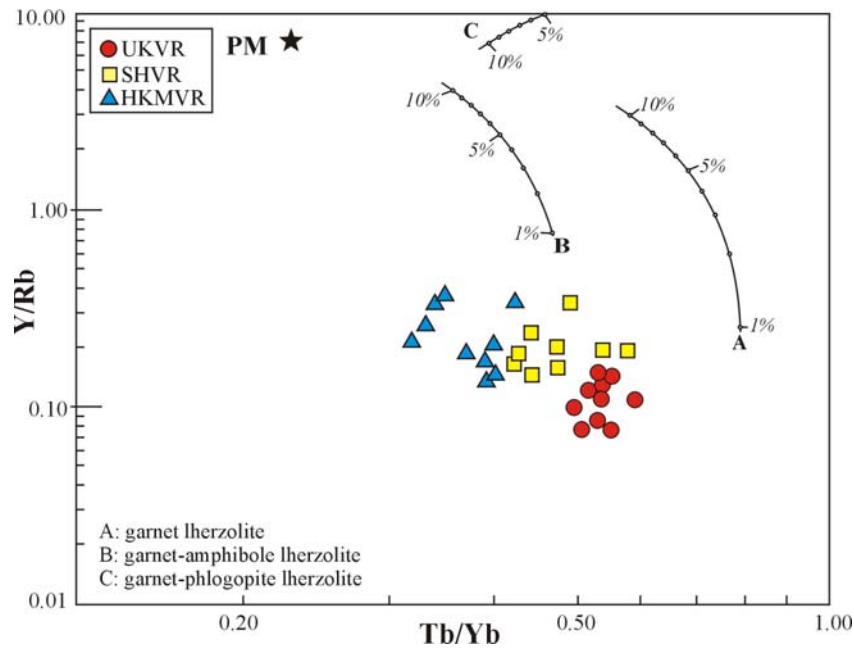
Figure 4.7 Tb/Yb versus Y/Rb ratios of the most primitive volcanic rocks. Non-modal batch melting curve for the primitive mantle (PM, Palme & O'Neil, 2004) is also shown. The partition coefficients are given in Table 3. Melting parameters are given in Table 4.4. Note that extension of fractional crystallization $(ol_{(0.35)}+cpx_{(0.25)}+plg_{(0.40)})$ is smaller than the symbols, and hence is negligible.

However, the models are less successful if describing the incompatible trace element contents of the mafic volcanites. Moreover, the melt composition obtained from this model yields a strong negative K anomaly, and the absence of Ta-Nb negative anomalies that are not supported by the data. Hence, another process must be invoked to explain the trace element compositions of the mafic volcanic rocks, particularly those of the UKVR and SHVR, with LILE and LREE metasomatism of the mantle source by subduction-related processes being the most likely. These models also strongly indicate that ~4-5% garnet was included in the mantle source region of the volcanites in order to produce the HREE abundances of the volcanites.
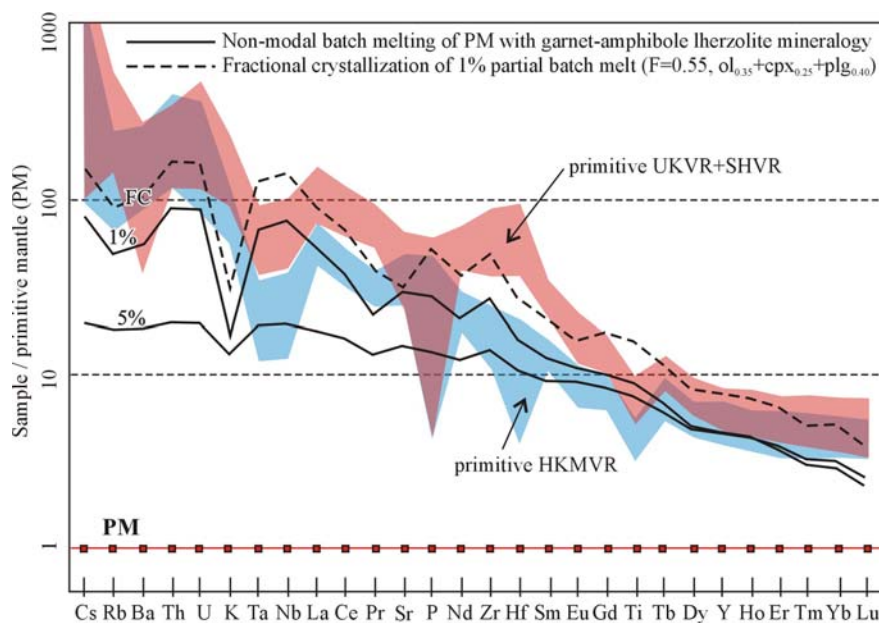
Figure 4.8 Trace element abundances obtained from 1% and 5% non-modal batch melting of a primitive mantle (PM) source with garnet-amphibole lherzolite mineral composition, and obtained from 30% fractional crystallization (FC) of $ol_{(0.35)}+cpx_{(0.25)}+plg_{(0.40)}$ from the 1% partial melt. Melting parameters are given in Tables 4.3 and 4.4. Normalizing values are from Palme & O'Neil (2004).

4.4.2.3 Mantle Metasomatism and Melting of Metasomatized Source

It is apparent from the discussion above, that low degree batch melting of a PM-like source with residual garnet can reproduce the HFSE and HREE content of the mafic lavas in the region, but it fails to explain their LILE and LREE contents. The high Sr and low Nd isotope ratios and high LILE and LREE contents of even the most primitive volcanic rocks require a crustal component in their mantle source, which may be supplied by subduction-related processes. In convergent plate margins, the original composition of the mantle wedge can be altered by the addition of several subduction related components, such as melts or fluids released from subducted sediments or MORB, or their combination. (e.g., McCulloch & Gamble, 1991; Edwards et al., 1993; Elliot et al., 1997; Hawkesworth et al., 1997; Turner et al., 1997; Class et al., 2000; Münker, 2000; Hochstaedter et al., 2001; Nakamura & Iwamori, 2009). Thorium and LREE (such as La, Ce, Pr and Nd) are not highly

mobile in fluids, but they are enriched in sediments (e.g., Elliot et al., 1997). These features allow them (and also $^{143}Nd/^{144}Nd$) to be used in identifying the sediment contributions either as partial melt, or as bulk sediment without fluid. LILE elements, such as Sr, Ba, Cs, Pb and U, together with Sr and Pb isotopes are fluid mobile elements and they can be used as tracers of slab-derived fluids (from subducted sediments or oceanic crust, or both). In this way, LILE/HFSE and LREE/HFSE ratios such as Th/Nb vs Ba/Nb, Th/Yb vs Ba/Yb, Ce/Zr vs Sr/Zr, and , Ce/Yb vs Sr/Yb are useful in identifying possible subduction components.

The HKMVR lavas, which are mainly from the western part of the area, are characterized by elevated Ba/Nb vs Th/Nb and Sr/Zr vs Ce/Zr with respect to the SHVR and UKVR (Figures 4.9a, b). Although this could be interpreted as evidence for higher degrees of subduction components (both sediment melts and fluids) in their genesis, all the rock groups plot closely on Th/Yb vs Ba/Nb and Ce/Yb vs Sr/Yb diagrams (Figures 4.9c, d). These relations yield further insights, as the Ba/Nb and Th/Nb ratios are sensitive to the presence of residual rutile (e.g., $Nb^{(rutile/melt)}$=102–540, Foley et al., 2000; $Nb^{(rutile/fluid)}$=38–484, Brenan et al., 1994) in the source during partial melting or source enrichment, but are independent of garnet. Sr/Zr and Ce/Zr ratios, however, are sensitive to the presence of both rutile (e.g., $Zr^{(rutile/melt)}$=3.07–4.24, Foley et al., 2000; $Zr^{(rutile/fluid)}$=206, Brenan et al., 1994) and zircon (e.g., Hermann & Rubatto, 2009) in the source. In this case, these relationships may suggest that the role of the residual rutile (during partial melting of the mantle source or its subduction related metasomatism) was more important for the HKMVR than for the UKVR and SHVR. The Th/Yb-Ba/Yb and Ce/Yb-Sr/Yb ratios are affected by the presence of residual garnet instead of rutile, as Yb is highly compatible in garnet (e.g., $Yb^{(garnet/melt)}$=6.25, Adam & Green, 2006).

Amounts of residual garnet in the mantle source of the volcanic rocks are nearly identical, therefore it is more appropriate to use Th/Yb vs Ba/Nb and Ce/Yb vs Sr/Yb plots. The HKMVR lavas have generally lower Th/Yb and Ce/Yb ratios than for the UKVR and SHVR, but the Ba/Yb and Sr/Yb ratios of the volcanic rocks are nearly identical. In the light of these data, it is concluded that the role of the sediment-melt

contributions in the genesis of the UKVR and SHVR was more important than for the HKMVR, but the fluid-related contributions to the mantle source of all the volcanites was nearly identical. Quantitative modeling of the subduction-related components on these plots is difficult, as the effects of residual garnet, rutile and zircon during partial melting or source enrichment processes of the volcanites complicate the interpretation.
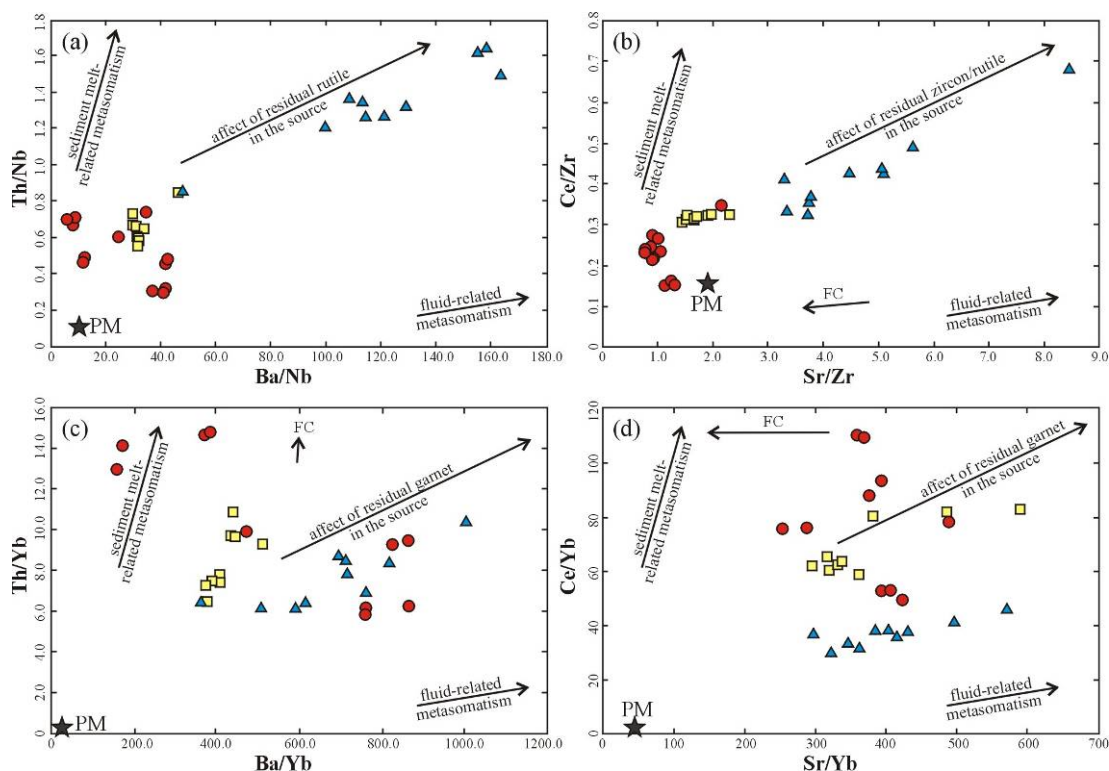
Figure 4.9 (a–d) Incompatible trace element ratios for the most primitive lavas in Western Anatolia. See Figure 4.8 for symbols. Primitive mantle (PM) compositions are from Palme & O'Neil (2004). Small affects of fractional crystallization (FC; F=0.50 with the parameters used in Figure 4.7) are also indicated.

In order to estimate the amount of the subducted sediment contribution to the source of the volcanic rocks, their Sr-Nd isotopic ratios may be compared with several end-member compositions, including the original mantle composition and subduction components. On a Sr-Nd isotopic diagram, the most primitive volcanic rocks are plot on a binary mixing curve (Figure 4.10a) that may represent mixing between the original mantle and subducted sediment components, including both sediment melt (SM) and sediment fluid (SF). Published Sr-Nd isotope data from the

Levantine Basin (Krom et al., 1999 and Freydier et al., 2001) and Global Subducted Sediments (GLOSS, Plank & Langimur, 1998) are also shown on Figure 4.10a. The Levantine basin is located to the north of the Nile delta and its sedimentary infill may be representative of the subducted sediments along the Aegean subduction system, which have played a role in the origin of the Neogene volcanic rocks in Western Anatolia. It is apparent that the GLOSS isotopic composition cannot explain the bulk sediment component in the origin of the volcanites. However, the composition of the sediments from a site in the Levantine Basin (BC-19) may represent the required composition. The Sr-Nd isotopic composition of BC-19a is from Freydier et al. (2001), while those of BC-19b is a compilation of Krom et al. (1999) and Freydier et al. (2001), and the latter appear most compatible with the volcanic rock data (see Table 4.5).

The chemical effects of SM and SF addition to the PM-like mantle source are nearly identical. Except for a few samples (two samples from the Güre lamproite and one HKMVR sample), the volcanic rocks have similar Sr-Nd isotopic ratios that can be explained by ~5–15% mixing between PM and SM/SF (Figure 4.10b). Fluids or melt from Altered Oceanic Crust (AOC) have high Nd and low Sr isotopic ratios (e.g., $^{87}Sr/^{86}Sr$=0.704750 (Staudigel et al., 1999); Sr=558ppm, Nd=0.13, $^{143}Nd/^{144}Nd$=0.513077 (Hochstaedter et al., 2001)), and hence, tend to increase the Nd isotopic ratios of the mixed material. On $^{87}Sr/^{86}Sr_{(i)}$ vs Sr and $^{143}Nd/^{144}Nd_{(i)}$ vs Nd plots, the volcanic rocks plot on nearly horizontal trends, such that extensions to the SM and SF mixing lines may correspond to mixing ratios between PM and sediment components (Figures 4.10c, d). Therefore, the Sr and Nd isotopic ratios of the volcanites may be explained by 7–15% SM or SF addition to their original mantle source. However, Sr and Nd elemental concentrations of the volcanic rocks still require an additional enrichment processes. Such a process will be discussed below.

Table 4.5 The parameters used in mixing and melting models.

	Primitive Mantle	bulk subducted sediment	D_{melt}	D_{fluid}	sediment melt (SM)	sediment fluid (SF)	sediment component (SM+SF)	mixed mantle source (MMS)
Cs	0.018	3.480	0.340	1.600	6.76	2.18	4.47	0.46
Rb	0.605	57.200	0.520	2.000	89.46	28.67	59.06	6.45
Ba	6.750	776.000	0.550	0.840	1173.63	922.93	1048.28	110.90
Sr	20.300	219.000	0.320	0.530	436.56	411.37	423.96	60.67
Th	0.083	6.910	0.730	4.810	8.69	1.44	5.07	0.58
U	0.022	1.680	0.930	1.370	0.70	1.23	0.96	0.12
Ta	0.040	0.630	1.350	2.000	0.50	0.32	0.41	0.08
Y	4.370	29.800	4.340	1.160	8.27	25.71	16.99	5.63
Nb	0.588	8.940	1.360	2.650	7.00	3.38	5.19	1.05
La	0.686	28.800	1.790	4.000	17.88	7.23	12.55	1.87
Ce	1.786	57.300	1.840	4.010	34.73	14.34	24.53	4.06
Nd	1.327	17.360	1.530	3.260	12.32	5.34	6.35	1.83
Sm	0.431	5.780	3.300	2.410	2.07	2.41	2.24	0.61
Eu	0.162	1.310	4.220	2.270	0.37	0.58	0.48	0.19
Gd	0.571	5.260	3.890	1.760	1.62	3.00	2.31	0.74
Dy	0.711	4.990	4.290	1.340	1.40	3.73	2.56	0.90
Er	0.465	2.920	4.330	1.140	0.81	2.56	1.69	0.59
Yb	0.462	2.760	4.280	1.060	0.78	2.60	1.69	0.58
Lu	0.071	0.413	4.790	1.050	0.10	0.39	0.25	0.09
K	257.30	16934.70	0.500	2.600	25897.26	6508.49	16202.87	1851.89
Ti	1275.20	3694.60	1.700	2.200	2409.39	1676.36	2042.87	1351.99
P	87.30	829.30	2.900	2.500	331.69	328.77	330.23	111.59
$^{87}Sr/^{86}Sr$	0.704500	0.710120			0.710116	0.710116	0.710116	0.708425
$^{143}Nd/^{144}Nd$	0.512640	0.512150			0.512150	0.512150	0.512150	0.512469

Primitive Mantle (PM) trace element and isotopic compositions are from Palme & O'Neil (2004) and Workmann & Hart (2005), respectively; bulk subducted sediment composition (GLOSS) is from Plank & Langimur (1998) except for Sr and Nd elements and their isotopes which are Krom et al. (1999) and Freydier et al. (2001); sediment melt (SM) is calculated from 40% fractional melting of bulk subducted sediments using bulk sediment melt partition coefficients (D_{melt}) of Johnson & Plank (1999); sediment fluid (SF) is calculated as 1% fluid in equilibrium with sediments using bulk sediment fluid partition coefficients (D_{fluid}) of Johnson & Plank (1999); sediment component (SM+SF) is assumed to be $SM_{0.50}+SF_{0.50}$; mixed mantle source composition is calculated from 10% mixing of PM with SM+SF. Elemental abundances are in ppm
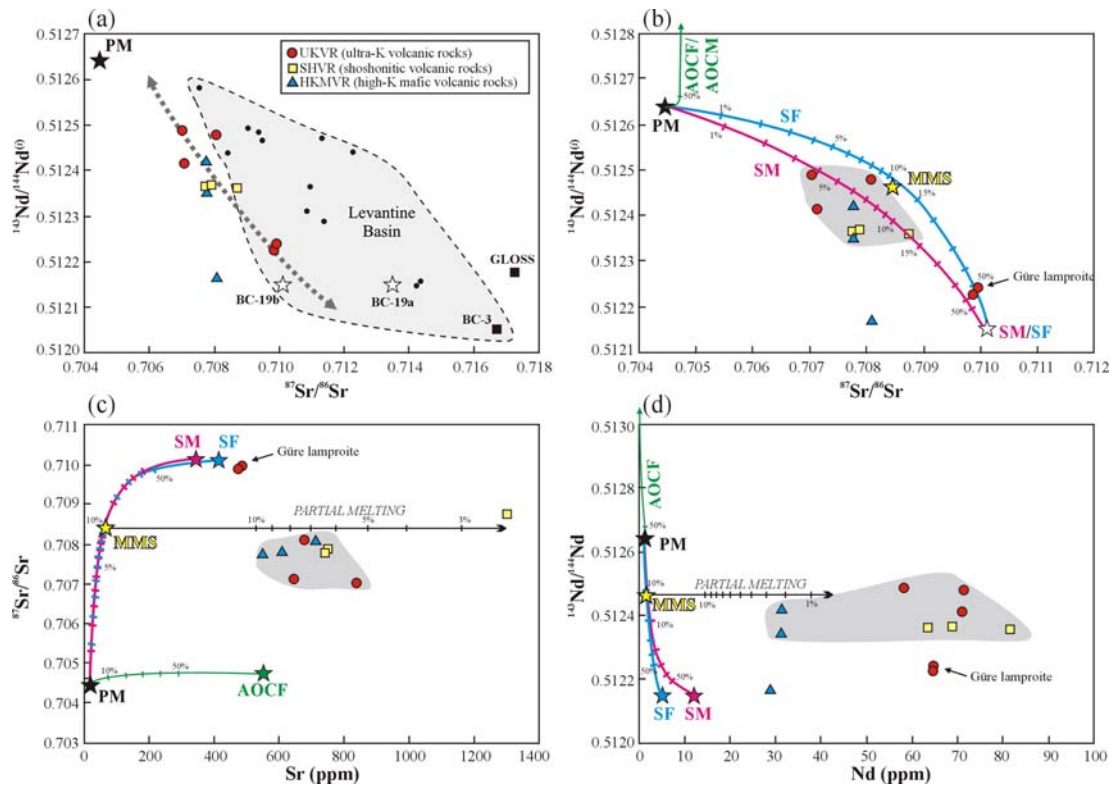
Figure 4.10 (a) Sr-Nd isotope diagram showing relationship between the most primitive volcanic rocks in the area, the original mantle composition and subducted sediment compositions. (b–d) Isotopic mixing models between primitive mantle (PM) and subduction zone components (sediment fluid–SF; sediment melt–SM and altered oceanic crust fluid–AOCF). Mixed Mantle Source MMS represent the mantle composition contaminated by SF and SM. The compositions of the end-members are given in Table 4.5.

On the basis of the relationships illustrated in Figure 4.10 it is hypothesized that the inferred PM-like source of the mafic lavas was enriched by addition of ~7–15% sediment melt or sediment fluid (SM/SF) and a less constrained proportion of fluid/or melts from Altered Oceanic Crust (AOC). A sedimentary component in late Cenozoic volcanic rocks from the Aegean region is also reported by Pe-Piper & Piper (2001) on the basis of Pb isotope data of the lavas. If the mantle source region of the volcanites is contaminated by subducted sediments, the trace element contents of the volcanites can be modeled by batch melting, using Mixed Mantle Source (MMS) where PM-like compositions are contaminated by later addition of subducted sediments (Figure 4.11). In this model, the MMS is obtained from 10% mixing of PM with a subducted sediment component. The subducted sediment composition is calculated from 50% SM (40% melt in equilibrium with bulk sediments) and 50% SF

(1% fluid in equilibrium with bulk sediments) (Table 4.5). Trace element abundances of the 5–10% partial batch melts of the MMS are similar to those of the HKMVR. Although the pattern of the 5% batch melt shows great similarities to the HKMVR, it fails to explain the compositions of the SHVR and HKMVR. When compared with the patterns of the HKMVR, the absence of Ti and lesser extent of Ta-Nb negative anomalies of the 5% model batch melt again indicate the presence of rutile in their source, as discussed above. Non-modal batch melting of the MMS composition is also shown on Figures 4.10c and d. Although 5–10% partial melting can account for the Sr compositions of the volcanites, it is important to note that the volcanic rocks, especially the HKMVR, may be affected by feldspar-bearing fractionation that would result in decreased Sr contents (Figure 4.10c). In contrast, the Nd contents of the volcanic rocks, especially those of the UKVR and SHVR, require a further enrichment process (Figure 4.10d).
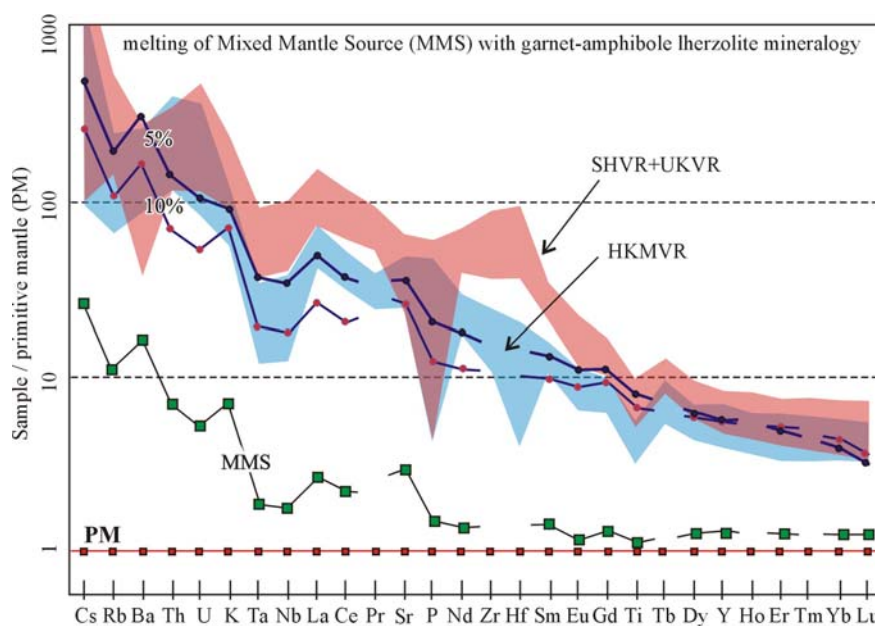
Figure 4.11 Trace element abundances obtained from 5% and 10% non-modal batch melting of mixed mantle source MMS. The composition of the MMS is calculated by 10% mixing of PM with sediment components that including 50% sediment fluid and 50% sediment melt. The parameters are given in Tables 4.3, 4.4 and 4.5. Normalizing values are from Palme & O'Neil (2004).

4.4.2.4 Multi-stage Melting and Melt Percolation

The batch melting models described above only simulate single-stage melting and subduction-related enrichment events in the inferred mantle source. The models (Figures 4.10 and 4.11) indicate that the trace element concentrations of the especially UKVR and SHVR require a further enrichment process in addition to subduction-related metasomatic events. For example, multi-stage percolation of low-degree melts in the mantle lithosphere can result in additional enrichment of incompatible trace elements, especially LILE and LREE. Hence, a multi-stage enrichment and melt percolation process have been modeled (Figure 4.12). In this model, a low-degree partial melt (L_1) from the mantle percolates into the overlying unmodified mantle (M_0) to yield a new composition in the overlying mantle (M_1). In the next stage, a new low-degree partial melt (L_2) from the metasomatized mantle (M_1), percolates into the overlying mantle with an original M0 composition, resulting in a new mantle composition (M_2), and so on. This model is similar to the re-enrichment model proposed by Barry et al. (2003) for the late Cenozoic Mongolian basalts. In the case of the Western Anatolian mafic lavas, there is an additional process of subduction-related enrichment plus the partial melting-related re-enrichment events. In this way, we used a mixed mantle source MMS as the starting mantle composition (M_0), which obtained in previous sections. This mantle composition represents the PM-like source that had been metasomatized during a subduction event. On the basis of isotopic mixing model results in Figure 4.10, further enrichment of the Western Anatolian mantle is assumed to be related to melt percolation (representing the second-stage enrichment during lithospheric extension). The composition of the partial melts is assumed to result from fractional melting, as this produces higher incompatible trace element abundances than batch melting. The steps of the last multi-stage melting and melt percolation model mentioned above can be summarized as:

M_0 = MMS (10% mixing of PM with subduction components)
L_1 = 7% non-modal fractional melt from M_0
M_1 = 1% mixing of M_0 with L_1
L_2 = 5% non-modal fractional melt from M_1

M_2 = 1% mixing of M_1 with L_2
L_3 = 5% non-modal fractional melt from M_2
M_3 = 2% mixing of M_2 with L_3
L_4 = 5% non-modal fractional melt from M_3
M_4 = 3% mixing of M_3 with L_4
L_5 = 5% non-modal fractional melt from M_4
M_5 = 4% mixing of M_4 with L_5
L_6 = 5% non-modal fractional melt from M_5

The results of the multi-stage melting and melt percolation model are summarized in Figure 4.12, and provide the best fit to the observed data for the SHVR and UKVR. According to this model, the trace element composition of the SHVR and UKVR can be reproduced by extra steps of multi-stage melting and melt percolation relative to the HKMVR, whose composition is obtained previously.
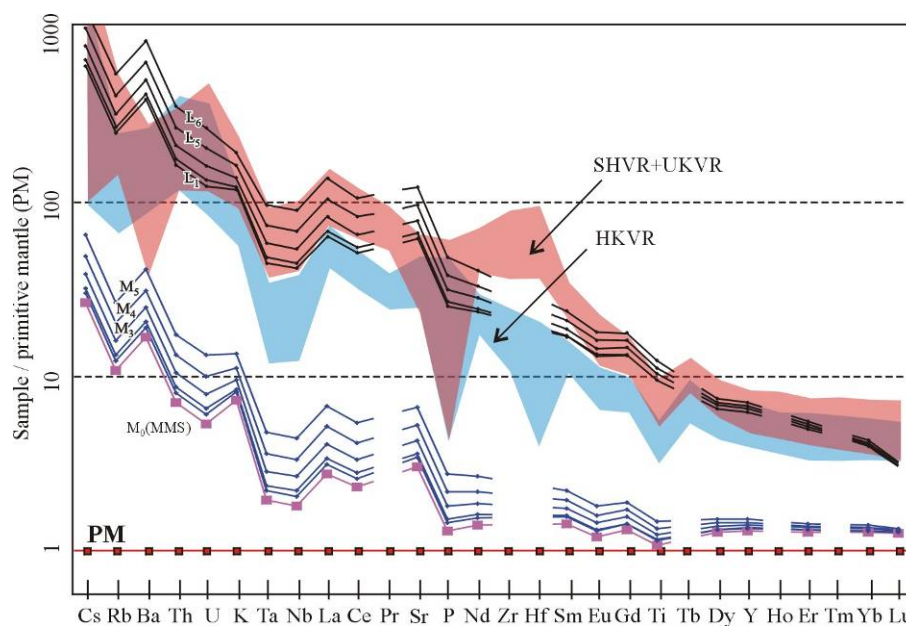
Figure 4.12 Trace element abundances obtained from multi-stage melting and enrichment model. L_1 represents melt composition calculated from 7% melting of Mixed Mantle Source MMS. L_2–L_6 represents melt compositions are from 5% non-modal batch melting of mantle sources M_1–M_5. See text for model description. Melting parameters are given in Tables 4.3, 4.4 and 4.5. Normalizing values are from Palme & O'Neil (2004).

The greater enrichment of trace elements in the mantle by such a process may result from a thick lithosphere undergoing extension (as discussed below). In this context it is noteworthy that the samples of the HKMVR group are mainly from the

west of Western Anatolia, where the lithosphere is thinner, while the samples of the SHVR and UKVR groups are from eastern parts where orogenic collapse occurred on the thicker lithosphere. Hence, the east-west variations in the trace element enrichments of the volcanic rocks is interpreted as resulting from variations in the number of multi-stage melting and melt percolation events in response to variations in the lithospheric thickness.

CHAPTER FIVE
DISCUSSION AND GEODYNAMIC IMPLICATIONS

5.1 Tectonic Evolution of the NE–SW-trending Basins

It is concluded that the NE–SW-trending Demirci, Selendi, Güre and Emet basins have similar stratigraphic, tectonic and geochemical features in the Chapter II. The basin fill of these Neogene basins are characterized by; (a) Lower Miocene Hacıbekir Group, (b) Middle Miocene İnay Group, (c) locally developed late Miocene sedimentary and basaltic volcanic rocks, (d) Quaternary sediments and basaltic volcanites, which are separated by regional-scale major unconformities (Figure 2.15; see also Ercan et al., 1978; Seyitoğlu, 1997a,b; İnci, 1984; Yılmaz et al., 2000; Ersoy & Helvacı, 2007; Ersoy et al., 2010a). The contact between the Hacıbekir Group and the Menderes Massif in these basins is characterized by a low-angle detachment fault, while the İnay Group unconformably overlies the metamorphic basement. On the other hand, the Bigadiç and Gördes basins have distinct stratigraphic and tectonic features from the other NE–SW-trending basins. Instead, the Bigadiç and Gördes basins are characterized by early Miocene volcano-sedimentary successions which were deposited along early Miocene strike-slip and related normal faults.

Işık & Tekeli (2001) described the Simav detachment fault (SDF) to the north of the study area. They concluded that the gneisses, migmatites and high-grade schists of the Menderes Massif are tectonically overlain by low-grade schists, marbles and non-metamorphosed ophiolitic mélange rocks along the SDF. The footwall rocks of the SDF were intruded by the late Oligocene-early Miocene Eğrigöz granitoid that yielded 20.4±0.6 and 20.0±0.7 Ma K/Ar biotite (Bingöl et al., 1982); 20.41±0.53 Ma Ar-Ar biotite (Işık et al., 2004); and 20.7±0.6 Ma SIMS U-Pb zircon (Ring & Collins, 2005) ages. Similarly, the Koyunoba granitoid yielded a 21.0±0.2 Ma SIMS U-Pb zircon age (Ring & Collins, 2005).

Syn-tectonic white micas from the mylonitized gneisses in the footwall of the SDF are also dated as 23.0±1.0 Ma (Ar/Ar) by Işık et al., (2004). Textural features of the deformed rocks describe a top-to-northeast movement along the shear zone of the Simav detachment fault. These data show that extension in the region began during the late Oligocene with the commencement of activity along the SDF that exhumed the high-grade metamorphic rocks of the Menderes Massif.

Ersoy et al., (2010a) revealed that the SDF in Selendi basin juxtaposes the high-grade metamorphic rocks of the Menderes Massif in the footwall with the ophiolitic mélange rocks of the İzmir-Ankara Zone and the early Miocene volcano-sedimentary units of the Hacıbekir Group in the hanging-wall of the SDF. This study demonstrates that similar relationships are also seen in the Demirci and Emet basins. In the Demirci basin, low-degree schists of the Menderes Massif, ophiolitic mélange rocks of the İzmir Ankara zone and the Hacıbekir Group tectonically overlie the metamorphic rocks along the SDF that is SE-inclined in the western margin and NW-inclined in the eastern margin of the basin (Figures 2.5 and 2.7). In the western margin of Demirci basin, the eastward grading in the Kürtköyü formation implies that the sedimentation was fed from this margin. The deformation characteristics of the faults show top-to N-NE movement with ductile-brittle transition (see also Işık & Tekeli, 2001; Işık et al., 2004; Ersoy et al., 2010a). This indicates that the Lower Miocene Hacıbekir Group in the Demirci, Selendi and Emet basins was deposited on an early Miocene supra-detachment basin that formed on the regional-scale corrugated fault plane of the SDF (Figure 5.1a; see also Purvis & Robertson, 2004; Ersoy et al., 2010a). The corrugated fault plane is evidenced by the presence of NE–SW-trending antiformal corrugations developed on the metamorphic highs between the Neogene basins. Ersoy et al. (2010a) presented field evidence showing that such folding in the massif must have occurred before deposition of the Middle Miocene İnay Group, as the İnay Group does not show folded strata in Selendi basin. In Demirci basin, there is also no evidence for NE–SW-trending folding in the sedimentary rocks of the Middle Miocene İnay Group. Moreover, the absence of NE–SW-trending folds in the early Miocene volcano-sedimentary units in Gördes basin strongly indicates that the NE–SW-trending anticlines in the footwall rocks of

the SDF were developed during the low-angle normal faulting as the massif was exhumed in an extensional setting (Figure 5.1a). The middle Miocene volcano-sedimentary units of the İnay Group in these basins unconformably overlie the Menderes Massif and the SDF, indicating that the activity of the SDF ceased by the middle Miocene.

Purvis & Robertson (2004) suggest that the Neogene infill of Gördes basin (and the other basins) was deposited along an eroded detachment fault surface that formed during exhumation of the massif. However, the field data from this study clearly show the early Miocene sedimentation in Gördes basin developed under the control of the NE-SW-trending strike-slip (e.g., Göcek and Kızıldam fault zones) and E–W-trending normal faults (e.g., Börez fault zone), in contrast to the other basins where the early Miocene strata are juxtaposed with the metamorphic rocks along the low-angle normal faults. Strike-slip faulting during early Miocene has also been recorded in Bigadiç basin. In this respect, the eastern margin of Gördes basin is very important as it marks the western boundary of the Menderes Massif (Figures 2.1 and 2.2). Hence, the tectonic characteristics of this margin hold the key to solving the exhumation style of the Menderes Massif, and imply that there was a close association between the early Miocene strike-slip faulting and low-angle normal detachment faulting.

The relationship between low-angle normal faulting, which controls exhumation of mid-crustal rocks, and large-scale strike-slip faults has also been documented in South Carolina, where high-grade pelitic schist was exhumed by synchronous crustal-scale strike-slip and normal faulting (Snoke & Frost, 1990). Pe-piper et al. (2002) also showed that Miocene I-type granitoids at Delos (Cyclades, Greece) were emplaced by; (a) a steeply dipping dextral crustal-scale strike-slip zone and (b) low-angle normal shear zones in the Aegean. NE–SW-trending shear zones in this area extend into western Turkey, where NE–SW-trending İzmir-Balıkesir Transfer zone is described (İBTZ; Sözbilir et al., 2003; Erkül et al., 2005a; Uzel & Sözbilir, 2008).
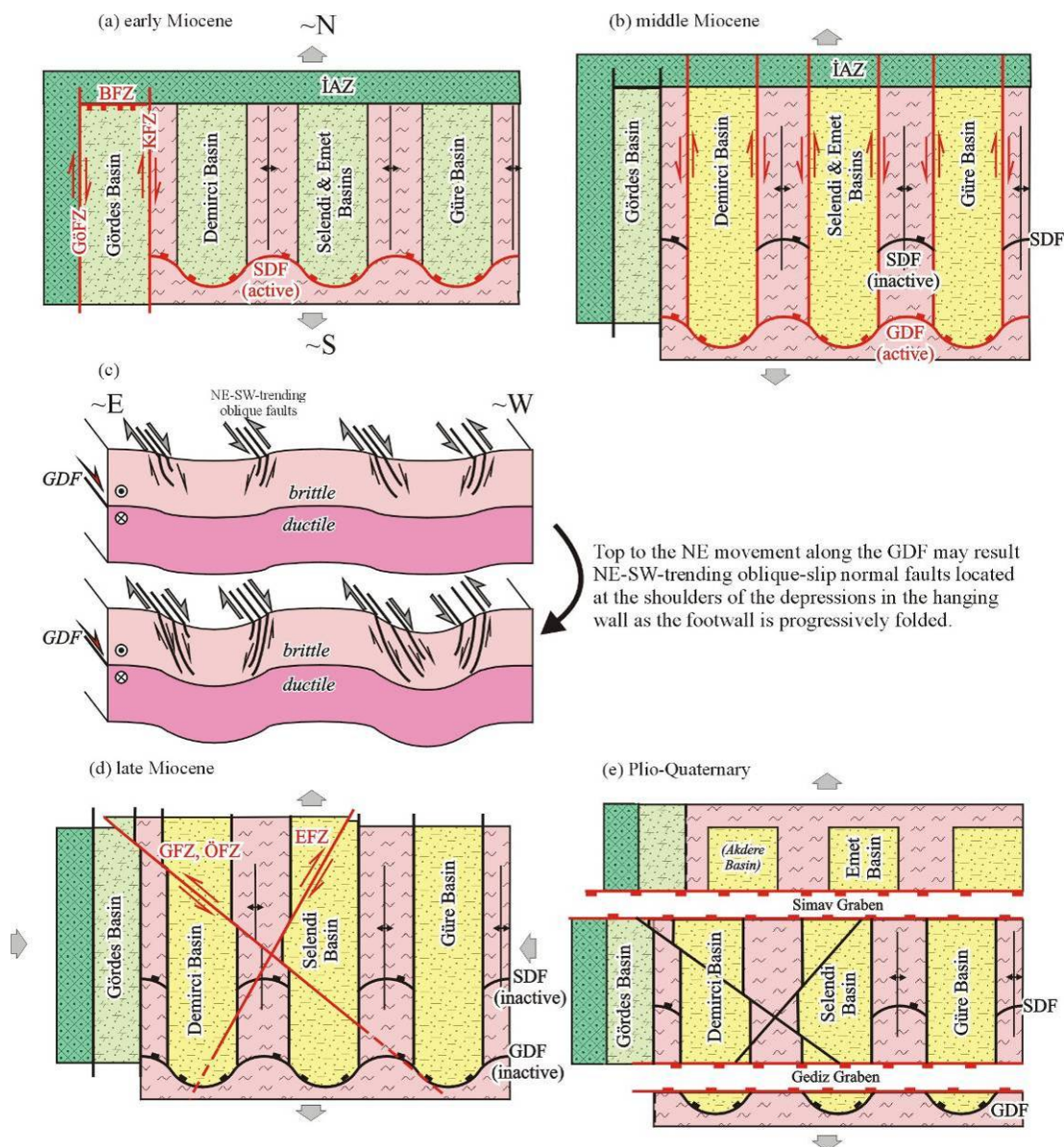
Figure 5.1 Cartoon showing the evolution of the NE–SW-trending Gördes, Demirci, Selendi, Emet and Güre basins from the early Miocene to Recent: (a) the early Miocene exhumation of the Menderes Massif along the Simav detachment fault (SDF) caused formation of synclines on the SDF in which early Miocene sedimentary units were deposited. (b) Second-stage collapse and formation of the Gediz detachment fault (GDF) during the middle Miocene. (c) Differential stretching in the hanging wall of the corrugated GDF formed a number of NE–SW-trending oblique-slip accommodation faults that controlled deposition of the middle Miocene İnay group. (d) Formation of late Miocene NE–SW-trending right-lateral (Eskin fault zone, EFZ) and NW–SE-trending left-lateral (Güneşli and Ören fault zones, GFZ and ÖFZ) strike-slip faults that locally deposited the late Miocene volcano-sedimentary units. (e) Last phase of the N–S extension (rift-mode) was responsible for formation of the E–W-trending grabens.

The İBTZ is thought to have been active during the upper Cretaceous (Okay & Siyako, 1991), and on the basis of paleomagnetically determined rotational differences in the region, Ring et al., (1999b) suggested that the zone was also active during the Miocene as a sinistral wrench corridor. Erkül (2010) also presented evidence for NE–SW-trending crustal-scale strike-slip deformation further to the northeast of this zone, along which early Miocene granitoids were emplaced at the NE of the Gördes basin (the Alaçamdağ granitoid). Moreover, Çemen et al. (2006) suggested that the first exhumation of the massif along the low-angle normal detachment faults may have been accommodated by steeply dipping oblique- to strike-slip faults in the eastern margin of the massif.

Taking into account the new field data and the geological observations in previous studies, it is suggested that exhumation of the northern flank of the Menderes Massif (controlling the deposition of the Hacıbekir group) was accommodated by strike-slip faulting on its western margin, along which Gördes basin is formed. In these respects, it is proposed that exhumation of the Menderes Massif occurred by; (a) low-angle normal detachment faults to the northeast, on which Neogene volcano sedimentary basins (Demirci, Selendi and Güre basins) developed, and (b) dextral strike-slip shear zones of the İBTZ to the west, along which Gördes basin was developed (Figure 5.1a).

In contrast to the Bigadiç and Gördes basins, the Demirci, Selendi, Emet and Güre basins are characterized by the presence of middle Miocene volcano-sedimentary successions, namely the İnay Group (Figure 2.15). Deposition of the İnay Group in these basins was controlled by NE–SW-trending left- or right-lateral strike- to oblique-slip faults which cut and displaced the older low-angle SDF. Cross-cutting relations between the early Miocene SDF and the middle Miocene NE-SW-trending strike- to oblique-slip faults are best observed in the northwestern and southern parts of Demirci basin (see Figures 2.2 and 2.7) and in the eastern margin of Selendi basin (Ersoy et al., 2010a). Note that these faults, as well as the İnay Group itself, are restricted to the north of the middle Miocene (Glodny & Hetzel, 2007) Gediz detachment fault (GDF) which is located further south (Figure 2.2). On the basis of

the model of Şengör (1987), Ersoy et al., (2010a) interpreted the formation of these faults in Selendi basin to have occured as a response to differential stretching on the hanging-wall of the southerly located GDF (see also Bozkurt (2003) for review). The hanging-wall and a part of footwall units of the early Miocene SDF likely remained on the hanging-wall of the middle Miocene GDF. From this perspective, the top to N-NE movement along the GDF may have caused formation of the NE–SW-trending strike- to oblique-slip faults that controlled deposition of the İnay Group in the hanging-wall, in response to differential stretching (Figure 5.1b). Hence, the NE–SW-trending strike- to oblique-slip faults that developed during the middle Miocene would have cut the footwall and hanging-wall units of the SDF, but would have been terminated in the hanging-wall of the GDF, thus restricting both the NE–SW-trending middle Miocene faults and the İnay Group to the north of the GDF (Figure 2.1). Note that, the NE–SW-trending middle Miocene faults developed at the shoulders of the previously formed NE–SW-trending folds (Figure 5.1a, b). This may be explained by extensional folding in ductile conditions, which is developed in the footwall of the GDF. Such folding causes the formation of brittle faults and resulting depressions above its synforms; as the synforms are formed, some faults would have developed in the hangingwall, where the antiforms changed into the synforms (Figure 5.1c). This is evidenced by field data from the Selendi, Demirci and Güre basins. The western margin of Demirci basin and the western margins of the Selendi and Güre basins are cut by middle Miocene oblique-slip faults developed along the edges of the antiformal metamorphic highs. Thus, the NE–SW-trending Demirci, Selendi, Emet and Güre basins are superimposed basins, in which, different volcano-sedimentary units developed in distinct stages of extension (see Ersoy et al., 2010a).

van Hinsbergen et al. (2010) concluded that the volcanic region from Lesbos to Uşak, including the NE–SW-trending basins on the northern Menderes Massif, underwent no rotation since middle Miocene, while the region to the south and southeast of the massif, including Beydağları and Lycian Nappes, rotated ~20° between 16 and 5 Ma. This causes a rotation difference between two regions, and such a difference accommodated the second-stage exhumation of the Menderes Massif along the Gediz and Büyük Menderes detachments during the middle

Miocene. On the basis of this rotation difference and presently linear boundary of the eastern edge of the Menderes Massif, van Hinsbergen et al. (2010) interpreted that the early-middle Miocene exhumation of the Menderes Massif may have been accommodated by a NE–SW-trending discrete transform fault along its eastern side. When the results of this study coupled with these interpretations, it may be concluded that two-stage successive exhumation of the Menderes Massif should be driven by (1) extensional detachments to the north and south and (2) contemporaneous transform faults to the west and east.

The late Miocene NE–SW-trending right-lateral (Eskin fault zone) and the NW–SE-trending left-lateral strike-slip faults (the Güneşli and Ören fault zones), which cut and displaced the early-middle Miocene volcano-sedimentary units, and were responsible for development of late Miocene volcanites (the Kabaklar basalt) and sedimentary units (the Kocakuz Formation in Selendi basin), are comparable and suggest that the region was deformed during the late Miocene under an N–S-directed extension and E–W-directed compression (Figure 5.1c; pure shear model; see also Ersoy et al., 2010a). As seen from Figure 2, cross-cutting relations between these faults and the older structures are best observed in the northern part of Gördes basin (in the Güneşli district, Figure 2.4), northeastern and southern parts of Demirci basin (in the Ören-Sevinçler and Kılavuzlar-Taşokçular districts, respectively, Figure 2.7), and in the eastern and northwestern parts of Selendi basin (in the Eskin-Kabaklar and Kuzayır districts, respectively) These faults also caused local dip-slip normal faults.

In Selendi basin, the Upper Miocene Kocakuz Formation was deposited on the hanging walls of NE–SW-trending right-lateral strike-slip and NW–SE-trending dip-slip normal faults. Late Miocene (Kabaklar) basalts in Selendi basin were also emplaced along the Eskin fault zone. The Taşokçular basalt in Demirci basin may also have been emplaced on the Güneşli fault zone (Figure 2.7). The nearly horizontal beds of the İnay Group were only deformed locally where late Miocene strike-slip faults developed. Note that Koçyiğit et al. (1999) proposed that the extensional tectonic regime in western Anatolia was interrupted by an N–S-directed compressional phase during the late Miocene-Pliocene. However, there is no

evidence of folding in the middle Miocene strata in the NE–SW-trending basins. Instead, these units were locally deformed by strike-slip faulting. The pattern of the late Miocene faults indicates that the region was deformed under N–S-directed extension and E–W-directed compression under pure shear during late Miocene, and the N–S-directed extension in the region was continuous.

Western Anatolia is also characterized by actively deforming nearly E–W-trending grabens controlled by high-angle dip-slip faults under rift-type N–S-directed extension. The reader is referred to Cohen et al. (1995), Emre (1996), Seyitoğlu (1997b), Bozkurt & Sözbilir (2004), Çiftçi & Bozkurt (2009) for further information on the E–W-trending grabens. Among these, the Simav half-graben also exhibits a right-lateral component causing dextral displacement of the older units. The southern faults of the Simav half-graben cut and displaced Demirci basin (Figure 5.1d), with its northern part termed as the Akdere basin (Seyitoğlu, 1997b). From this perspective, it is also suggested that Emet basin is the northward continuation of Selendi basin (Figure 2.2). Another E–W-trending graben in the region is the Gediz graben located further south of the area (Bozkurt & Sözbilir, 2004; Çiftçi & Bozkurt, 2009; Figures 2.1 and 2.2). Geophysical data clearly show that there are remnants of the NE–SW-trending basins on the southern margin of the Gediz graben (Çiftçi & Bozkurt, 2009; Figure 5.1d). A comparison of the stratigraphic, structural and geochemical features of the Neogene volcano-sedimentary successions in the NE-SW-trending basins is given in Table 5.1.

During the early Miocene, wide-spread dacitic-rhyolitic volcanism occurred in the region. This activity was also accompanied by local mafic occurrences such as the high-K calc-alkaline Gölcük basalt in Bigadiç basin (Erkül et al., 2005a) and the ultrapotassic Kuzayır lamproite in Selendi basin (Ersoy & Helvacı, 2007). This was followed in the middle Miocene by the high-K calc-alkaline andesitic and dacitic Asitepe, Yağcıdağ, Karabacaklar and Köprücek volcanites. These were accompanied by the shoshonitic to ultrapotassic mafic Orhanlar, Naşa, Dereköy, and Kıran-Zahman basalts, and the Güre-Ilıcasu lamproites. The geochemical data reveal that the late Cenozoic volcanism in the region became more mafic and alkaline with time,

indicating that the lithosphere thinned progressively from the early to middle Miocene (see also Ersoy et al., 2008).

Table 5.1 Comparison of the transtensional Gördes basin and supra-detachment extensional basins

		Transtensional NE–SW-trending Gördes basin	Supradetachment extensional NE–SW-trending basins
BASIN-BAUNDING FAULTS	Plio-Quaternary	E–W-trending oblique-to dip-slip graben-bounding normal faults which trancuted the older structures	
	Late Miocene	NE–SW-trending dextral & NW–SE-trending sinistral strike-slip faults	
	Middle Miocene	Reactivated NE–SW-trending dextral strike-slip faults (?)	NE–SW-trending oblique-slip accommodation faults developed in the hanging-wall of to-the-NE Gediz detachment fault
	Early Miocene	NE–SW-trending dextral strike-slip faults & E–W-trending dip-slip normal faults	Simav Detachment Fault with top-to-the-NE sense of shear
BASIN INFILL UNITS	Plio-Quaternary	Semi-lithified alluvial fan and alluvial plain deposits in E–W-trending grabens	
	Late Miocene	Locally developed continental units and basic volcanites (e.g., Kocakuz Formation)	
	Middle Miocene	Göcek Formation (?)	Volcano-sedimentary İnay Group
	Early Miocene	Early miocene volcano-sedimentary units (Kızıldam and Kuşlukköy formations with Kayacık and Güneşli volcanites)	Volcano-sedimentary Hacıbeklir Group
VOLCANIC INTERCALATIONS	Quaternary	alkali basalts with OIB type compositions (asthenospheric)	
	Late Miocene	Basic lavas with K-trachybasaltic and shoshonitic composition (traditional between lithospheric and asthenospheric (OIB) compositions)	
	Middle Miocene		andesites and dacites with High-K calc-alkaline affinity & mafic lavas with ultrapotassic/shoshonitic/lamproitic affinity (lithospheric)
	Early Miocene	High-K calc-alkaline dacites and rhyolites	dacites and rhyolites with High-K calc-alkaline affinity & Minor mafic lavas with ultrapotassic affinity (lithospheric)

Overall, this study provides new geological data, as well as synthesizing a large number of previously published geological investigations of western Anatolia. This has allowed for the development of a comprehensive model for the structural and sedimentary evolution of Miocene basins in the region. This model can thus serve as a template for the interpretation of the numerous geochemical, isotopic and structural data that has been gathered in this region, as well as providing an important guide for future studies of western Anatolia.

5.2 Neogene Volcanism in Western Anatolia

The origin and evolution of the early to middle Miocene volcanism and its geodynamics in the Western Anatolia is contentious. The geologic evidence summarized above clearly indicates that the magmatic activity in the region was closely related to post-collisional extensional tectonics, and that the Miocene volcanic rocks in the NE–SW-trending basins were emplaced during early-middle Miocene episodic exhumation of the Menderes Massif as a core-complex. Overall, it is apparent that the massif was asymmetrically uplifted and collapsed, beginning from the north and continuing to the south during the early to middle Miocene. The HKVR, SHVR and UKVR groups were produced in this interval. Geochemical data show that the origin of the HKVR includes crustal contributions to the mantle-derived magmas. While rhyolites dominated during the early Miocene, more primitive andesites are seen during the middle Miocene. At the same time, the amount of the UKVR and SHVR increased rapidly, compatible with lithospheric thinning.

Recently, Prelević et al. (2010) favored a model involving horizontal subduction, in order to explain the presence of ultra-depleted components in the genesis of the UKVR. Such a horizontal subduction is thought to have resulted in; (a) compressional tectonics in the overriding plate yielding a regional uplift, and (b) temporal cessation in volcanic activity, as observed in the Andes (Martinod et al., 2010). However, this model is supported by neither mantle tomographic data (Facenna et al., 2003; van Hinsbergen et al., 2005, 2010; Hafkenscheid et al., 2006; Ring et al., 2010), nor the fact that the Miocene tectonics of the western Anatolia is represented by post-collisional ~N–S extension with long-term volcanic activity.

5.2.1 N–S Geochemical Variation

In a regional scale, Western Anatolian late Cenozoic magmas show time-dependent compositional changes from north to south. Eocene volcanism in the

northern part of the western Anatolia (NAEV) is characterized by medium-K calc-alkaline, and tholeiitic volcanism with arc-like geochemical affinities (NAEV; Ercan et al., 1998; Altunkaynak & Genç, 2008; Kürkçüoğlu et al., 2008). During the Oligocene, volcanic activity migrated south, and was characterized by felsic products with a high-K, calc-alkaline affinity. The subsequent early Miocene felsic volcanism took place in a large area to the south, from Lesbos in the west to western central Anatolia in the east (Aldanmaz et al., 2000; Pe-Piper & Piper, 2001), and is generally characterized by felsic, shoshonitic products. The Miocene volcanism continued with increasing amounts of mafic products, especially on the northern part of the Menderes Massif. In the centre of western Anatolia, Quaternary Kula volcanism (QKV) occurs with OIB-like geochemical features (Güleç, 1991; Alıcı et al., 2002). To the south of the region, volcanism along the south Aegean volcanic arc (SAVA) marks the convergence between the African and Anatolian plates, with typical arc-type magmatism (Buettner et al., 2005).

Increasing $^{87}Sr/^{86}Sr$ ratios of the volcanic rocks from the Eocene to middle Miocene has been interpreted as due to increased crustal contamination in response to crustal thickening (Dilek & Altunkaynak, 2007; Altunkaynak & Genç, 2008). However, the most primitive early-middle Miocene mafic volcanites in this study (SiO$_2$ = ~50 and Mg# = ~75) also have considerably high $^{87}Sr/^{86}Sr$ ratios (~0.7063-0.7087) when compared to both mafic and evolved Eocene volcanites (SiO$_2$ = ~50 and 65, Mg# = ~50 and 36, $^{87}Sr/^{86}Sr$ = 0.7046 and 0.7057, respectively; Altunkaynak & Genç, 2008) to the north. Moreover, it is noteworthy that the early-middle Miocene volcanic rocks have higher $^{87}Sr/^{86}Sr_{(i)}$ and lower $^{143}Nd/^{144}Nd_{(i)}$ compositions at a given SiO$_2$ value than those of the NAEV and SAVA. The north-south Sr-Nd isotopic variations among the Eocene to Recent volcanic rocks is seen in Figure 3.4a, in which the NAEV have similar isotopic compositions to those of the SAVA (Figure 3.4a), whereas the early-middle Miocene volcanic rocks plot in the isotopically more enriched part of the diagram. HFSE ratios of the NAEV are also different from those of the Miocene volcanic rocks in this study, but similar to that of the SAVA (Figure 3.6). This suggests that the high $^{87}Sr/^{86}Sr$ ratios of the volcanic rocks from this study are not indicative of crustal contamination. Rather, the change in isotopic

compositions of the Eocene-early Oligocene volcanites and early-middle Miocene volcanites most likely reflects changes in the magma sources through space and time, and hence the older volcanism northernmost of the area should be evaluated separately.

These data suggest that the NAEV and SAVA have similar origin represented by depleted mantle sources (MORB-like) which also enriched by subduction processes, and that the enriched chemical nature of the early-middle Miocene volcanic rocks in the supra-detachment basins on the Menderes Massif was not produced via crustal contamination processes. Ustaömer et al. (2009) obtained a 47.6 Ma date for a calc-alkaline, metaluminous, Eocene granite in the Marmara region to the north. This granitoid occurs in north-dipping thrust sheets and has geochemical features indicating the presence of a mid-Eocene arc in the region. The compositional similarities between the NAEV and SAVA suggest that these volcanites should be evaluated separately from the Miocene volcanic rocks from this study.

In the eastern part of Western Anatolia, the early-middle Miocene volcanic activity and associated sedimentary basins are mainly restricted to the north of the Menderes Massif that is an uplifted and exhumed mid-crustal unit in the region (Figure 4.1). Exhumation of the Menderes Massif was synchronous with basin formation and volcanism (SHVR and UKVR), and occurred in several phases (e.g., Hetzel et al., 1995a,b; Lips et al., 2001; Sözbilir, 2002a; Ring et al., 2003; Ersoy et al., 2010a). It is important to note that exhumation of the massif along the detachment faults was asymmetrical, developing from north to the south as evidenced by; (1) basin formation and associated volcanism is restricted to the northern part of the region, (2) the emplacement and cooling ages of the syn-extensional granites decrease from the north to the centre (Thomson & Ring, 2006; Glodny & Hetzel, 2007, and references therein), (3) the ages of the volcanic rocks on the Menderes Massif mainly decrease to the southwest (Figure 4.1), and (4) the early Miocene volcano-sedimentary successions are mainly located to the north, while those of the middle Miocene lie to the south (e.g., Selendi basin, Ersoy et al., 2008).

5.2.2 E–W Geochemical Variation and Petrogenetic Model for K-rich volcanites

Incompatible trace element contents of the early-middle Miocene felsic and mafic volcanic rocks increase from west to east (Figure 5.2). These chemical variations were previously interpreted as the result of; (1) the presence of ancient eastward-subduction along the Aegean (Ercan et al., 1979), and (2) lithospheric thickening from the west to the east (McKenzie & Yılmaz, 1991). As the paleo-reconstruction of the region is now well-established, this first hypothesis can be eliminated.

Petrogenetic investigations of high-MgO potassic volcanic rocks and their geochemical variations from west to east in western Anatolia hold a key to propose a model for K-enrichment in the lavas.

It has been proposed that the high-Mg, K-rich mafic volcanic rocks were produced by melting of clinopyroxene/amphibole/phlogopite-rich metasomatic veins in the mantle lithosphere (e.g., Conticelli et al., 2009a and references therein). In this model, the first volcanic products (e.g., ultrapotassic, shoshonitic) were derived mainly from melting of the metasomatic veins, and are thus expected to be more potassic than later volcanic products (e.g., high-K, calc-alkaline) which resulted from melting of residual peridotites as lithospheric melting proceeds. In such a metasomatized lithospheric mantle domain, the potassium (and the other incompatible elements) content of a melt column would be expected to increase as the thickness of the lithosphere increases, due to greater melt production from metasomatic veins in a thicker lithosphere (Figure 5.3a). Such a model would account for the east-west variation in trace element contents in Western Anatolia where the high-MgO and -K volcanic rocks (HKMVR, with lower incompatible element contents) are located to the west, while the high-MgO shoshonitic to ultrapotassic rocks (SHVR and UKVR, with higher incompatible trace element contents) lie to the east.
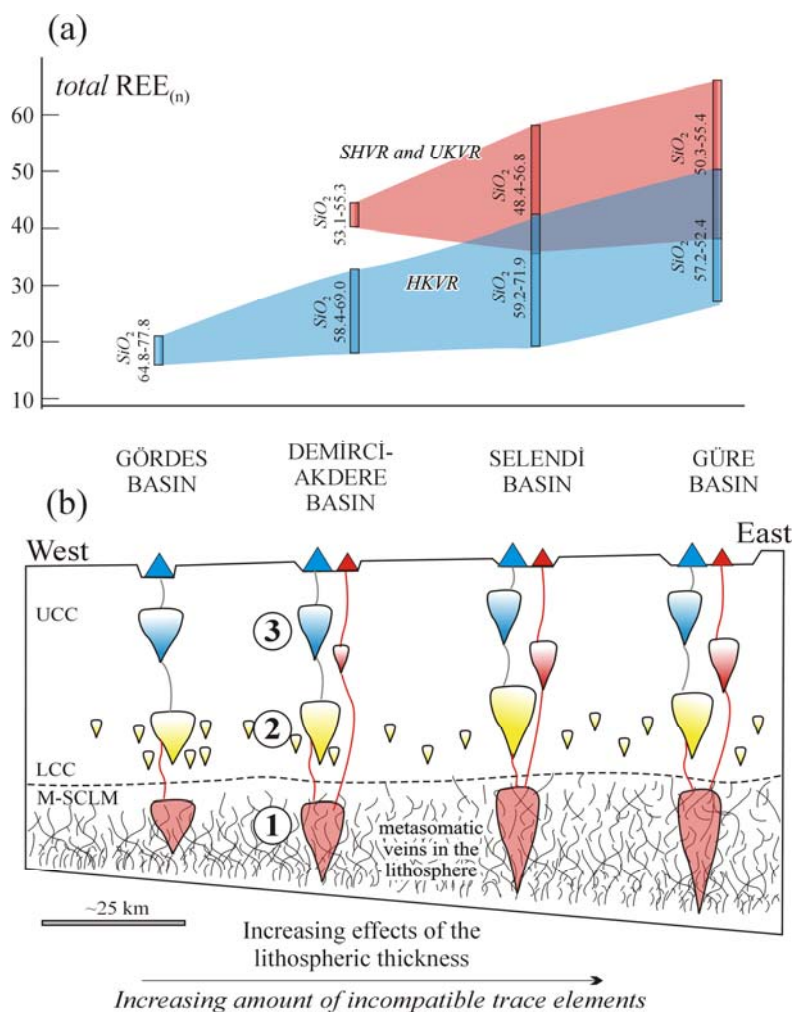
Figure 5.2 (*a*) Primitive Mantle-normalized total REE contents of the volcanic rocks with their geographic positions. (*b*) Schematic cross section showing the increasing effects of the mantle lithosphere on the incompatible trace element contents of the volcanic rocks during early-middle Miocene. UCC and LCC are upper and lower continental crust, respectively, and M-SCLM: metasomatized sub-continental lithospheric mantle. (1): melting in the M-SCLM and formation of the potassic mafic lavas with high trace element contents. Amounts of the trace elements increases from west to east resulted from increasing effects of the M-SCLM. (2): melting in the lower crust and mixing of mafic magmas with crustal melts with lower trace element contents to produce relatively primitive andesites of HKVR. (3): FC and low-degree crustal contamination in the magma chambers to produce the UKVR and SHVR from mantle-derived magmas, and the rhyolites from andesites. During late Miocene, the effects of the M-SCLM is decreased and finally disappeared in Quaternary to produce QKV which have mainly asthenospheric components (not shown).

However, in Western Anatolia there is no temporal pattern in the K content of the volcanic rocks under investigation; the SHVR and UKVR were either emplaced synchronously with, or after the high-K calc-alkaline (felsic) volcanites. In addition, the melting models in Chapter IV, demonstrate that the source rocks of the K-rich rocks (HKMVR, SHVR and UKVR) are amphibole- and ~4-5% garnet-bearing lherzolite, and cannot have had significant concentrations of phlogopite in the source – i.e. the rocks were not derived from melting of only metasomatic veins. Hence, when the fact that the SHVR and UKVR are located on the Menderes Massif (that exhumed along detachment faults during collapse of a thick lithosphere) is taken into account, it is suggested that the K (and other LILE and LREE) enrichment in the UKVR and SHVR may have resulted from multi-stage melting and melt percolation as the over-thickened lithosphere was thinning, and that this provides a consistent explanation for both the E-W-directed potassium variations of the volcanites (Figure 5.3b).

Detailed quantitative geochemical models for the high-MgO potassic rocks in Chapter IV indicate that eastward increasing of the trace element contents of the lavas should be resulted from eastward thickening in the lithosphere, allowing to multi-stage melting and melt percolation of mantle lithosphere. In this case, the volcanic rocks located to the west of the region have lower incompatible trace element contents with respect to those of the eastern lavas. As noted above, high trace element contents of the ultrapotassic and shoshonitic series should be depressed by crustal-derived magmas with lower trace element contents. In this case, the space-related geochemical features of the high-K calc-alkaline lavas may have been inherited from the more mafic magmas which also show increases in incompatible trace element contents from west to east (Figure 5.2a). Hence, the space-related geochemical variation in the early-middle Miocene volcanic rocks was likely inherited from their source regions.
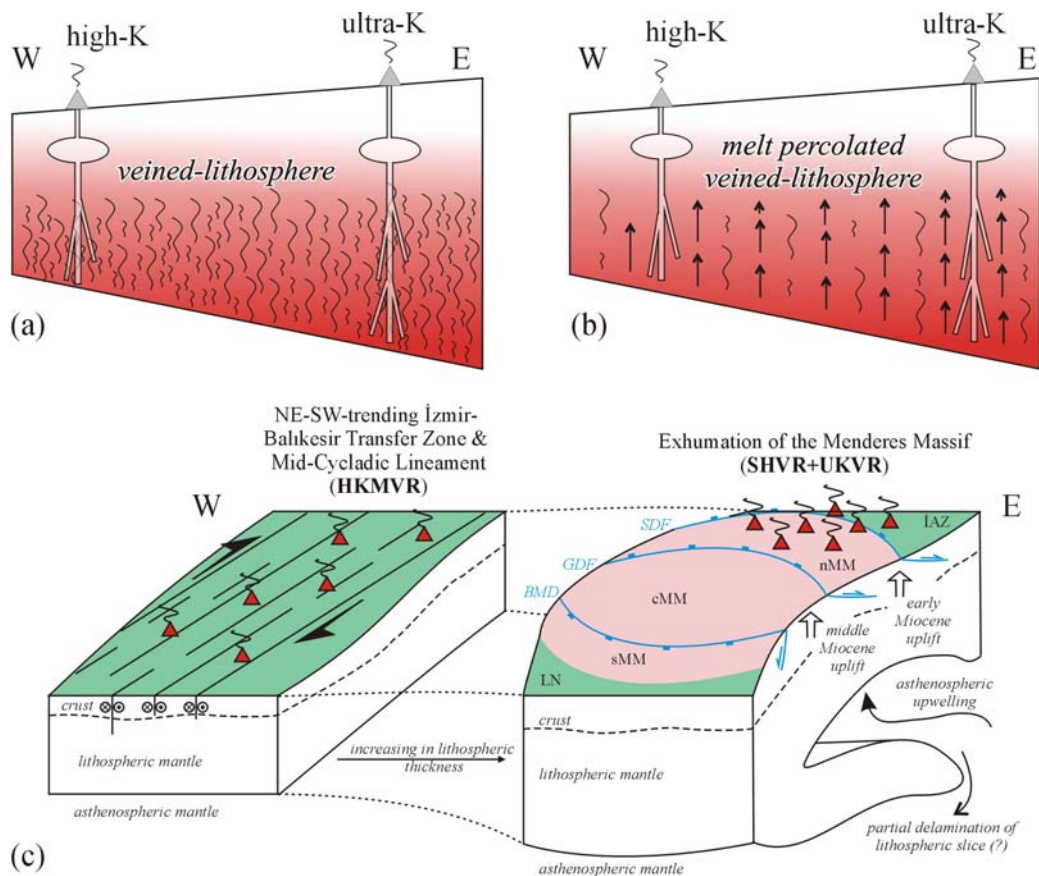
Figure 5.3 (a-b) Inferred petrogenetic models for K-rich magmatism in response to variations in lithospheric thickness in Western Anatolia. In a veined lithospheric mantle, potassium contents may increase in response to increasing amounts of metasomatic veins as the lithospheric thickness increases from west to the east. In a melt-percolated veined lithospheric mantle, the extent of the multi-stage melting and melt percolation increases as the lithosphere became thicker from west to east, allowing for production of more potassic partial melts. (c) Inferred geodynamic model for Western Anatolia. Strike-slip faulting dominates in the western part of the region where lithosphere is thin. HKMVR is produced along this corridor. Assymetrical exhumation of the Menderes Massif along successive early-middle Miocene detachment faults is accompanied by volcanic activity producing SHVR and UKVR in the east. Here, thick lithosphere allows more incompatible trace element enrichment via multi-stage melting and melt-percolation processes when compared to the western part.

5.2.3 Core Complex Formation and Volcanism on the Menderes Massif

Post-collisional extension in Western Anatolia led to exhumation of the Menderes Massif as a core complex that began along the Simav detachment fault (SDF) to the

north during the latest Oligocene-early Miocene (Bozkurt, 2007; Lips et al., 2001; Ring et al., 2003; Işık et al., 2004; Thomson & Ring, 2006; Catlos et al., 2008). The early Miocene volcano-sedimentary succession in the Demirci, Selendi and Güre basins (the Hacıbekir group) was deposited in a supra-detachment basin that was formed by a N-facing low-angle normal detachment fault (the SDF; Işık & Tekeli, 2001; Ersoy et al., 2010a). Syn-kinematic granitic intrusives (the Eğrigöz and Koyunoba granitoides) emplaced in the footwall of the Simav detachment fault, have been dated as ~20.2 Ma (Ar/Ar age; Işık et al., 2004) and 20.7 Ma (SHRIMP-U/Pb-zircon age; Ring & Collins, 2005). Volcanic units in the early Miocene volcano-sedimentary succession have also been dated as ~21-17 Ma (Ersoy et al., 2008). These data show that the early Miocene magmatic activity in the region was directly related to first-stage tectonic exhumation of the Menderes Massif. The early Miocene basins and synchronous volcanic activity is clearly restricted to the northern part of the massif (Figure 3.1) indicating that the exhumation was asymmetrical, producing volcano-sedimentary basins to the north.

The second stage exhumation of the massif in its inner part occurred along the Gediz detachment fault (GDF) to the north and Büyük Menderes Detachment (BMD) to the south during the middle Miocene (Hetzel et al., 1995b; Sözbilir, 2001). The syn-extensional granites (Salihli and Turgutlu granitoides), intruded into the footwall of the Gediz detachment fault, have been dated as ~16-15 Ma (U-Pb ages) (Glodny & Hetzel, 2007), and Catlos et al. (2008) obtained similar Th-Pb ion microprobe monazite ages from associated granodiorites. The volcanic units in the middle Miocene volcano-sedimentary successions in the NE–SW-trending basins, which post-date the early Miocene events, have also been dated as ~16–14 Ma (e.g., Ersoy et al., 2008, 2010a). These data indicate that the middle Miocene magmatic activity in the region was related to second-stage exhumation of the massif. The volcano-sediments deposited in the supra-detachment basins were also located asymmetrically to the northern part of the massif, but migrated slightly to the south of the main early Miocene basins. Overall, it is apparent that the massif was asymmetrically uplifted and collapsed, beginning from the north and continuing to the south during the early to middle Miocene.

The late Miocene basalts were emplaced along strike-slip faults in a transtensional tectonic regime (Ersoy et al., 2010a). They have intermediate isotopic (Sr-Nd and B) and trace element characteristics between the lithospheric mantle-derived early-middle Miocene lavas and the mainly asthenosphere-derived QKV (Innocenti et al., 2005; Tonarini et al., 2005). Hence, they represent a transition between two distinct magma sources of the volcanic rocks in the region. Finally, the QKV lies near the centre of the Menderes Massif, which was uplifted during the early-middle Miocene (Figure 3.1). The Kula volcanites have a mainly asthenospheric mantle origin (Güleç, 1991; Alıcı et al., 2002; Innocenti et al., 2005; Tonarini et al., 2005) that reflects the presence of asthenospheric upwelling from the Miocene onwards. This upwelling also likely contributed to uplift of the Menderes Massif.

The evidence presented above indicates that asthenospheric upwelling took place from north to south, possibly as a result of (a) subduction roll-back and/or (b) asymmetrical delamination of a lithospheric slice. It is unlikely that Neogene volcanism in Western Anatolia was directly linked to the Aegean subduction system as; (1) volcanism is restricted to the northern parts of the region, (2) volcanism is associated with basin formation in extensional areas, and (3) there is a large area south of the Menderes Massif between the Neogene volcanic zone and the Aegean subduction system. While this appears to rule out southward migration of the volcanism due to subduction-roll back processes, mantle topographic images show a steep slab that is interpreted in terms of roll-back of the Aegean subduction system, and that the subduction was single and continuous (Facenna et al., 2003; Hafkenscheid et al., 2006). When these observations are coupled with the geochemical arguments favoring a subduction-influenced metasomatized nature of the mantle source region of the Miocene volcanic rocks, it may be suggested that although the Miocene volcanism was not directly driven by Aegean subduction, fluids driven off the subducted slab created the metasomatized mantle geochemical signature. In Chapter IV, it is concluded concluded that the mantle source of the early-middle Miocene volcanic rocks was altered by ~7-15% subduction components that are too high with other observations from the world. These high amounts of metasomatic components may be added during different subduction events in the

course of geodynamic evolution of the region (as proposed by Pe-Piper & Piper, 2001).

As the Neogene volcanites were produced during extensional tectonics and exhumation of the metamorphic massifs, the cause of the extension likely arose from asymmetrical partial delamination from north to south and/or from southward retreating of the Aegean subduction system.

5.2.4 Delamination or Convective Removal?

Removal and thinning of the SCLM may have developed in two ways; (1) "convective removal" of the lithosphere roots, (2) "delamination" of a slice of mantle lithosphere, or (3) thermal perturbation along a slab tear (Bird, 1979; Houseman et al., 1981; Pe-Piper & Piper 2007; Göğüş & Pysklywec, 2008). According to the convective removal model, the lithospheric root symmetrically "drops" into the hot asthenosphere, and is replaced symmetrically by hot asthenosphere as it drops. This scenario might be expected to give rise to volcanic activity with an outward surface pattern, and symmetric regional uplift where the crustal rocks were exhumed progressively (see also Göğüş & Pysklywec, 2008 for computational models), as has been proposed for the Betic-Alboran region (Turner et al., 1999). In the "delamination" model, a dense lithospheric mantle slice peels off, and is replaced by underlying convective mantle. According to the delamination model, detachment of the lithospheric slice is asymmetric as it begins at one side and continues to detach towards opposite side. As the lithospheric keel detaches and sinks into the asthenosphere, it is replaced by hot asthenospheric flow. This process may account for the asymmetrical regional uplift and the southward propagating sedimentary basin formation and magmatism observed in Western Anatolia.

In the light of this discussion it is suggested that the volcanism in the east of the region were resulted from lithospheric extension probably due to partial delamination and assymetrical asthenospheric upwelling, and eventual exhumation of the mid-crustal units of the Menderes Massif along successive detachment faults. The

extension in this geodynamic regime may thus have allowed the multi-stage melting and melt percolation in the lithosphere that produced the ultrapotassic and shoshonitic magmas with high concentrations of incompatible trace elements during detachment faulting (Figure 5.3c).

5.2.5 Volcanism along İzmir-Balıkesir Transfer Zone

The geodynamics for the hig-K mafic volcanic rocks emplaced along the western margin of the Menderes Massif (HKMVR along the İzmir-Balıkesir Transfer Zone) should be considered separately, on the basis of; (1) the stratigraphic relationships, (2) surface distributions, and (3) geochemical features. The HKVR were emplaced along İzmir-Balıkesir Transfer Zone/mid-Cycladic Lineament (Pe-Piper et al., 2002; Uzel & Sözbilir, 2008) to the west of the Menderes Massif, so that the volcanic activity in this NE-SW-trending zone was controlled by strike-slip faults (Erkül et al., 2005a; Uzel & Sözbilir, 2008). In this region, the volcanism would have been produced in a thinner lithospheric domain than in the eastern part. The petrogenetic models in Chapter IV support this geodynamic interpretation, as the mafic volcanites (HKMVR) are less enriched than those from the shoshonitic and ultrapotassic volcanic rocks emplaced on the northern part of the Menderes Massif, and thus require lesser amounts of multi-stage melting and melt percolation process.

CHAPTER SIX
CONCLUSIONS

The results of this thesis are summarized as:

1. The NE–SW-trending Demirci, Selendi, Emet and Güre basins, which developed on the Menderes Core Complex, have similar stratigraphies that comprise two main volcano-sedimentary successions: the Lower Miocene Hacıbekir Group, and the unconformably overlying Middle Miocene İnay Group. These two groups are also locally overlain by late Miocene volcanic and sedimentary units and recent sediments.

2. The NE–SW-trending Gördes basin has a similar volcano-sedimentary sequence to that of Bigadiç basin. These basins are characterized by a main early Miocene volcano-sedimentary sequence.

3. The Lower Miocene Hacıbekir Group in the Demirci, Selendi, Emet and Güre basins was deposited in a supra-detachment basin formed on the Simav detachment fault (SDF). The SDF juxtapose the low-grade schists of the Menderes Massif (and Afyon zone?), ophiolitic mélange rocks of the İzmir Ankara zone, and Lower Miocene Hacıbekir Group in the hanging-wall against the high-grade metamorphic rocks of the Menderes Massif in the footwall. The gneisses of the Menderes Massif, i.e., footwall units of the SDF, are unconformably overlain by the middle Miocene volcano-sedimentary rocks of the İnay Group, implying that the activity of the SDF ceased by the middle Miocene. Hence, the NE-SW-trending Demirci, Selendi, Emet and Güre basins were supra-detachment basins during the early Miocene.

4. The early Miocene volcano-sediments of Gördes basin were controlled by NE-SW-trending dextral strike- to oblique-slip and E–W-trending dip-slip normal faults. Hence, Gördes and Bigadiç basins are transtensional basins that developed during the early Miocene.

5. During the early Miocene, the eastern margin of Gördes basin acted as a structural boundary between (a) the strike-slip dominated zone of deformation to the west (the İzmir-Balıkesir transfer zone) and (b) the top to N–NE directed low-angle detachment faulting (the SDF) that was tectonically exhuming various parts of Menderes Massif to the east.

6. Deposition of the Middle Miocene İnay Group in the Demirci, Selendi, Emet and Güre basins was controlled by NE–SW-trending strike- to oblique-slip faults that formed synchronously with the Gediz detachment fault (GDF) located to the south. Therefore, these basins are superimposed in character and have a complex evolutionary history. The NE–SW-trending faults terminate in the hanging-wall of the GDF and are interpreted to result from differential stretching in the hanging-wall.

7. In the light of the above observations, it is concluded that the massif was exhumed by a combination of strike-slip faulting to the west (and also to the east) and successive detachment faulting to the north and south. This may explains the overall ellipsoidal shape of the Menderes massif, whereby the western (and eastern) boundary (parallel to the long-axis) was controlled by strike-slip faulting.

8. The NE–SW-trending basins were also deformed by NW–SE-trending sinistral and NE–SW-trending dextral faults during late Miocene as a result of regional N–S-directed extension and E–W-directed compression.

9. In the last stage, all the NE–SW-trending basins were cut by nearly E–W-trending high-angle oblique- to dip-slip normal faults that caused formation of the E–W-trending Simav half-graben to the north, and the Gediz graben to the south under rift-type extensional tectonics. Overall, the different types of extensional to transtensional basins in this part of western Anatolia were superimposed and episodic, and they were all developed under ~N–S-directed extension.

10. Neogene volcanic rocks in the NE-SW-trending basins of Western Anatolia, developed on the northern part of the Menderes Massif, include early-middle

Miocene high-K calc-alkaline (HKVR), ultrapotassic (UKVR) and shoshonitic (SHVR) rocks, late Miocene basaltic lavas, and Quaternary Na-alkaline Kula volcanites (QKV). The HKVR, SHVR and UKVR have similar $^{87}Sr/^{86}Sr_{(i)}$ (0.70631–0.71001), $^{143}Nd/^{144}Nd_{(i)}$ (0.512145–0.512488) and Pb isotopes ($^{206}Pb/^{204}Pb$ 18.838–19.148; $^{207}Pb/^{204}Pb$ 15.672–15.725; $^{208}Pb/^{204}Pb$ 38.904–39.172). The late Miocene basalts have similar Pb isotopes to the early-middle Miocene lavas, but their Sr-Nd isotopes are more depleted and are similar to those of the QKV which have a mainly OIB-like mantle origin.

11. The high-Mg early-middle Miocene volcanic rocks in Western Anatolia comprise shoshonitic (SHVR), ultrapotassic (UKVR) and high-K mafic volcanic rocks (HKMVR). The SHVR and UKVR are mainly located in the east of the region, where the mid-crustal units of Menderes Massif were uplifted and exhumed along detachment faulting in an assymetrical core-complex mode. The HKMVR samples are located in the west of the region, where strike-slip tectonics dominates. The UKVR and SHVR are more potassic and are also more enriched in trace elements (LILE, LREE and HFSE) with respect to HKMVR.

12. Petrogenetic models show that the SHVR, HKMVR and UKVR originated from a lithospheric mantle source which originally had a primitive mantle-like geochemical composition. This mantle source was metasomatized by subduction related components, giving rise to enrichments in LILE, LREE and $^{87}Sr/^{86}Sr$ during Mesozoic-Cenozoic contractional events. Isotopic mixing and trace element melting models indicate that the original mantle composition was altered by 7-15% subduction-related components, including both sediment melt and sediment fluid. The sediment-melt contribution to the source of the UKVR and SHVR was more important than for the HKMVR, but the fluid-related contributions to their sources were nearly identical.

13. The higher trace element concentrations of the SHVR and UKVR in the east with respect to HKMVR in the west require an additional enrichment process. Trace element contents of the SHVR and UKVR have been modeled using a petrogenetic

approach involving multi-stage melting and melt percolation processes. High-degree enrichment via multi-stage melting and melt percolation processes during extension likely occurred in a thicker lithosphere, whereas such enrichment was more limited in a thinner lithosphere. This interpretation accords with geographical variations that show the more potassic rocks (SHVR and UKVR) formed in the east of the region, where post-orogenic collapse occurred, whereas less potassic rocks (HKMVR) were produced to the west, where strike-slip tectonics controlled the basin formation and volcanism.

14. The petrogenesis of the high-K calc-alkaline felsic units (HKVR) developed on the northern part of the Menderes Massif include high amounts of lower crustal contributions. The most primitive early-middle Miocene HKVR samples (Asitepe volcanites) formed by ~20-40% mixing of lower crustal melts with lithospheric mantle-derived potassic magmas. The HKVR then differentiated from andesites to rhyolites via nearly-pure fractional crystallization processes. The contemporaneous SHVR and UKV are only minimally affected by upper crustal contamination.

15. The early-middle Miocene volcanic rocks in the NE-SW-trending basins differ from the Northwest Anatolian Eocene volcanic rocks (NAEV), the South Aegean volcanic arc (SAVA), Eskişehir-Afyon-Isparta volcanic area (NAEV) and Galatian volcanic province (GVP) rocks. HFSE ratios of the NAEV and SAVA reveal that they were mainly derived from MORB-like depleted mantle sources and that they should be evaluated differently. Furthermore, the volcanic rocks from NAEV and GVP were mainly derived from enriched mantle sources.

REFERENCES

Adam, J. & Green, T. (2006). Trace element partitioning between mica- and amphibole-bearing garnet lherzolite and hydrous basanitic melt: 1. Experimental results and the investigation of controls on partitioning behaviour. *Contributions to Mineralogy and Petrology, 152*, 1–17.

Agostini, S., Doglioni, C., Innocenti, F., Manetti, P., Savaşçın, M.Y. & Tonarini, S. (2005). Tertiary high-Mg volcanic rocks from Western Anatolia and their geodynamic significance for the evolution of the Aegean area. In: Fytikas, M. & Vougioukalakis, G.E., (Eds.), The South Aegean Active Volcanic Arc: Present Knowledge and Future Perspectives: Amsterdam, *Elsevier book series Developments in Volcanology*, *7*, 345–362.

Agostini, S., Doglioni, C., Innocenti, F., Manetti, P., Tonarini, S. & Savaşçın, M.Y. (2007). The transition from subduction-related to intraplate Neogene magmatism in the Western Anatolia and Aegean area. In: Beccaluva, L., Bianchini, G. & Wilson, M., (Eds.), Cenozoic Volcanism in the Mediterranean Area. *Geological Society of America, Special Paper, 418*, 1–15.

Agostini, S., Ryan, J.G., Tonarini, S. & Innocenti, F. (2008). Drying and dying of a subducted slab: coupled Li and B isotope variations in Western Anatolia Cenozoic volcanism. *Earth Planet. Sci. Lett, 272*, 139–147.

Aitcheson, S.J. & Forrest, A.H. (1994) Quantification of crustal contamination in open magmatic systems. *Journal of Petrology*, *35*, 461–488.

Akal, C. (2008). K-richterite–olivine–phlogopite–diopside–sanidine lamproites from the Afyon volcanic province, Turkey. *Geological Magazine*, *145*, 570–585.

Akay, E. & Erdoğan, B. (2004). Evolution of Neogene calc-alkaline to alkaline volcanism in the Aliagˇa-Foc¸a region (Western Anatolia, Turkey). *Journal of Asian Earth Sciences, 24* 367–387.

Akdeniz, N. & Konak, N. (1979). Simav-Emet-Dursunbey-Demirci yörelerinin jeolojisi (Geology of the Simav-Emet-Dursunbey-Demirci areas). *Bulletin of*

Mineral Research and Exploration Institute of Turkey (unpublished) Report. No: 6547.

Akkök, R. (1983). Structural and metamorphic evolution of the northern part of the Menderes Massif: new data from the Derbent area and their implication for the tectonics of the massif. *Journal of Geology*, 91, 342–350.

Albaréde, F. (1992). How Deep Do Common Basaltic Magmas Form and Differentiate? *Journal of Geophysical Research, 97*(B7), 10997–11009.

Aldanmaz, E. (2006). Mineral-Chemical Constraints on the Miocene Calc-alkaline and Shoshonitic Volcanic Rocks of Western Turkey: Disequilibrium Phenocryst Assemblages as Indicators of Magma Storage and Mixing Conditions. *Turkish Journal of Earth Science, 15*, 47–73.

Aldanmaz, E., Pearce, J.A., Thirwall, M.F. & Mitchell, J.G. (2000). Petrogenetic evolution of late Cenozoic, post-collision volcanism in western Anatolia, Turkey. *Journal of Volcanology and Geothermal Research*, *102*, 67-95.

Alıcı, P., Temel, A. & Gourgaud, A. (2002). Pb-Nd-Sr isotope and trace element geochemistry of Quaternary extension-related alkaline volcanism: a case study of Kula region (western Anatolia, Turkey), *Journal of Volcanology and Geothermal Research*, *115*, 487-510.

Alıcı, P., Temel, A. Gourgaud, A., Kieffer, G., & Gündoğdu, M.N. (1998). Petrology and geochemistry of potassic rocks in the Gölcük area Isparta, SW Turkey/: genesis of enriched alkaline magmas. *Journal of Volcanology and Geothermal Research*, *85*, 423–446.

Alıcı-Şen, P., Temel, A. & Gourgaud, A. (2004). Petrogenetic modelling of Quaternary post-collisional volcanism: a case study of central and eastern Anatolia. *Geological Magazine*, *141*, 81–98.

Alpaslan, M. (2007). Early to Middle Miocene intra-continental basaltic volcanism in the northern part of the Arabian plate, SE Anatolia, Turkey: geochemistry and petrogenesis. *Geoogical Magazine*, *144*, 867–882.

Alpaslan, M., Boztuğ, D., Frei, R., Temel, A., Kurt, M.A. (2006). Geochemical and Pb–Sr–Nd isotopic composition of the ultrapotassic volcanic rocks from the extension-related Çamardı-Ulukışla basin, Niğde Province, Central Anatolia, Turkey. *Journal of Asian Earth Sciences*, *27*, 613–627.

Alpaslan, M., Ekici, T., Otlu, N., Boztuğ, D. & Temel, A. (2005). Magmatic processes and mixing origin of andesite: Miocene Karamağara volcanites, Central Anatolia, Turkey. *Geological Journal*, 193–214.

Altherr, R., Meyer, H.-P., Holl, A., Volker, F., Alibert, C., McCulloch, M.T. & Majer, V. (2004). Geochemical and Sr-Nd-Pb isotopic characteristics of Late Cenozoic leucite lamproites from the East European Alpine belt (Macedonia and Yugoslavia). *Contributions to Mineralogy and Petrology, 147*, 58–73.

Altunkaynak, Ş. (2007) Collision-driven slab breakoff magmatism in northwestern Anatolia, Turkey. *Journal Geol., 115*, 63–82.

Altunkaynak, Ş. & Genç, Ş.C. (2008). Petrogenesis and time-progressive evolution of the Cenozoic continental volcanism in the Biga Peninsula, NW Anatolia (Turkey). *Lithos 102*, 316–340.

Altunkaynak, Ş., Rogers, N.W. & Kelley, S.P. (2010) Causes and effects of geochemical variations in late Cenozoic volcanism of the Foça volcanic centre, NW Anatolia, Turkey. *Int. Geol. Rev., 52*, 579–607.

Asmerom, Y., Jacobsen, S.B. & Wernicke, B.P. (1994). Variations in magma source regions during large-scale continental extension, Death Valley region, western United States. *Earth and Planetary Science Letters 125*, 235–254.

Bailey, J.C., Jensen, E.S., Hansen, A., Kann, A.D.J., & Kann, K. (2009). Formation of Heterogeneous Magmatic Series Beneath North Santorini, South Aegean Island Arc. *Lithos, 110*, 20–36.

Barry, T.L., Saunders, A.D., Kempton, P.D., Windley, B.F., Pringle, M.S., Dorjnamjaa, D. & Saandar, S. (2003). Petrogenesis of Cenozoic basalts from

Mongolia: evidence for the role of asthenospheric versus metasomatized lithospheric mantle sources. *Journal of Petrology 44*, 5–91.

Bédard, J.H. (1999). Petrogenesis of Boninites from the Betts Cove Ophiolite, Newfoundland, Canada: Identification of Subducted Source Components. *Journal of Petrology, 40*, 1853–1889.

Benito, R., Lopez-Ruiz, J., Cebria, J.M., Hertogen, J., Doblas, M., Oyarzun, R. & Demaiffe, D. (1999). Sr and O isotope constraints on source and crustal contamination in the high-K calc-alkaline and shoshonitic Neogene volcanic rocks of SE Spain. *Lithos, 46*, 773–802.

Bingöl, E., Delaloye, M. & Ataman, G. (1982). Granitic intrusions in western Anatolia: a contribution to the geodynamic study of this area. *Eclogae geol. Helv., 75*, 437-446.

Bird, P. (1979). Continental delamination and the Colorado Plateau. *Journal of Geophysical Research*, 84, 7561-7571.

Boari, E., Tomassini, S., Laurenzi, M.A. & Conticelli, S. (2009). Transition from Ultrapotassic Kamafugitic to Sub-alkaline Magmas: Sr, Nd, and Pb Isotope, Trace Element and 40Ar-39Ar Age Data from the Middle Latin Valley Volcanic Field, Roman Magmatic Province, Central Italy. *Journal of Petrology, 50*, 1327–1357.

Borsi, J., Ferrara, G., Innocenti, F. & Mazzuoli, R. (1972). Geochronology and petrology of recent volcanites in the eastern Aegean Sea (West Anatolia and Lesvos Iceland). *Bullettin of Volcanology, 36*, 473-496.

Bozkurt, E. (2000). Timing of extension on the Büyük Menderes Graben, western Turkey, and its tectonic implications, in: E. Bozkurt, J.A. Winchester, J.D.A. Piper (Eds.), Tectonics and Magmatism in Turkey and the Surrounding Area, vol. 173, *Geological Society of London Special Publication, 73*, 385–403.

Bozkurt, E. (2003). Origin of NE-trending basins in western Turkey. *Geodinamica Acta, 16*, 61-81.

Bozkurt, E. & Oberhänsli, R. (2001). Menderes Massif (western Turkey): Structural, Metamorphic and Magmatic Evolution. *International Journal of Earth Sciences, Special Issue, 89*, 679-882.

Bozkurt, E. & Sözbilir, H. (2004). Geology of the Gediz Graben: new field evidence and tectonic significance. *Geological Magazine, 141*, 63-79.

Boztuğ, D., Harlavan, Y., Jonckheere, R., Can, İ. & Sarı, R. (2009). Geochemistry and K-Ar cooling ages of the Ilıca, Çataldağ (Balıkesir) and Kozak (İzmir) granitoids, west Anatolia, Turkey. *Geological Journal, 44*, 79–103.

Brenan, J.M., Shaw, H.F, Phinney, D.L. & Ryerson, F.J. (1994). Rutile-aqueous fluid partitioning of Nb, Ta, Hf, Zr, U and Th: implications for high field strength element depletions in island-arc basalts. *Earth and Planetary Science Letters, 128*, 327–339.

Buettner, A., Kleinhanns, I.C., Rufer, D., Hunziker, J.C. & Villa, I.M. (2005). Magma generation at the easternmost section of the Hellenic arc: Hf, Nd, Pb and Sr isotope geochemistry of Nisyros and Yali volcanoes (Greece). *Lithos, 83*, 29–46.

Buket, E. & Temel, A. (1998). Major-element, trace-element, and Sr–Nd isotopic geochemistry and genesis of Varto (Muş) volcanic rocks, Eastern Turkey. *Journal of Volcanology and Geothermal Research, 85*, 405–422.

Candan, O. (1995). Menderes Masifinde kalntı granulit fasiyesi metamorfizması (in Turkish with English Abstract). *Turkish Jornal of Earth Science, 4*, 35-55.

Candan, O. (1996). Çine asmasifindeki (Menderes Masifi) gabroların metamorfizması ve diğer asmasiflerle karşılatırılması [in Turkish with English Abstract]. *Turkish Jornal of Earth Science, 4*, 123-139.

Candan, O., Dora, O.Ö., Çetinkaplan, M., Oberhänsli, R., Partzsch, J.H., Warkus, F.C. & Dürr, S. (2001). Pan-African high-pressure metamorphism in the Precambrian basement of the Menderes Massif, western Anatolia, Turkey. *International Journal of Earth Sciences, 89*, 679–882.

Candan, O., Dora, O.Ö., Oberhänsli, R., Çetinkaplan, M., Oelsener, F.C. & Dürr, S. (1998). Two different high-pressure metamorphisms in the Menderes Massif: Pan-African and Tertiary events. *Geological Congress Turkey*, Abstracts, 52–54

Candan, O., Dora, O.Ö., Oberhansli, R., Oelsner, F. & Dürr, S. (1997). Blueschist relics in the Mesozoic cover series of the Menderes Massif and correlations with Samos Island, Cyclades. *Schweizerische Mineralogische Und Petrographische Mitteilungen, 77*, 95–99.

Carey, S.W. (1958). A tectonic approach to continental drift. in: S.W. Carey (Editor), Continental Drift: A Symposium.Geology Department, *University of Tasmania, Hobart*, pp. 177-355.

Castillo, P.R. (2006). An overview of adakite petrogenesis. *Chinese Science Bulletin, 51*, 257–268.

Catlos, E.J. & Çemen, İ. (2005). Monazite ages and the evolution of the Menderes Massif, western Turkey. *International Journal of Earth Sciences*, *94*, 204-217.

Catlos, E.J., Baker, C.B., Sorensen, S.S., Çemen, İ. & Hançer, M. (2008). Monazite geochronology, magmatism, and extensional dynamics within the Menderes Massif, Western Turkey. *IOP Conference Series: Earth and Environmental Sci. 2*, 012013.

Çemen, İ., Catlos, E.J., Göğüş, O. & Özerdem, C. (2006). Postcollisional extensional tectonics and exhumation of the Menderes Massif in Western Anatolia extended terrane, Turkey. *Geological Society of America Special Publication 409*, 353–379.

Çiftçi, B. & Bozkurt, E. (2009). Evolution of the Miocene sedimentary fill of the Gediz Graben, SW Turkey. *Sedimentary Geology, 216*, 49–79.

Class, C., Miller, D.M., Goldstein, S.L. & Langimur, H. (2000). Distinguishing melt and fluid subduction components in Umnak Volcanites, Aleutian Arc. *Geochemistry, Geophysics, Geosystems, 1*, 1004.

Clayton, R.N. & Mayeda, T. (1963). The use of bromine pentafluoride in the extraction of oxygen from oxides and silicates for isotopic analysis. *Geochim. Cosmochim. Acta 27*, 47–52.

Çoban, H. & Flower, M.F.J. (2006). Mineral phase compositions in silica-undersaturated 'leucite' lamproites from the Bucak area, Isparta, SW Turkey. *Lithos, 89*, 275–299

Cohen, H.A., Dart, C.J., Akyüz, H.S. & Barka, A. (1995). Syn-Rift Sedimentation and Structural Development of the Gediz and Büyük-Menderes Graben, Western Turkey. *Journal of Geological Society of London, 152*, 629–638.

Conticelli, S. (1998). The effect of crustal contamination on ultrapotassic magmas with lamproitic affinity: mineralogical, geochemical and isotope data from the Torre Alfina lavas and xenoliths, Central Italy. *Chemical Geology, 149*, 51–81.

Conticelli, S., D'Antonio, M., Pinarelli, L. & Civetta, L. (2002). Source contamination and mantle heterogeneity in the genesis of Italian potassic and ultrapotassic volcanic rocks: Sr-Nd-Pb isotope data from Roman Province and Southern Tuscany. *Mineralogy and Petrology, 74*, 189-222.

Conticelli, S., Guarnieri, L., Farinelli, A., Mattei, M., Avanzinelli, R., Bianchini, G., Boari, E., Tommasini, S., Tiepolo, M., Prelević, D. & Venturelli, G. (2009a). Trace elements and Sr-Nd-Pb isotopes of K-rich, shoshonitic, and calc-alkaline magmatism of the Western Mediterranean Region: Genesis of ultrapotassic to calc-alkaline magmatic associations in a post-collisional geodynamic setting. *Lithos, 107*, 68–92.

Conticelli, S., Marchionni, S., Rosa, D., Giordano, G., Boari, E. & Avanzinelli, R. (2009b). Shoshonite and sub-alkaline magmas from an ultrapotassic volcano: Sr–Nd–Pb isotope data on the Roccamonfina volcanic rocks, Roman Magmatic Province, Southern Italy. *Contrib. Mineral. Petrol. 157*, 41–63.

Coulon, C., Megartsi, M'hamed, Fourcade, S., Maury, R.C., Bellon, H., Louni-Hacini, A., Cotton, J., Coutelle, A. & Hermitte, D. (2002). Post-collisional

transition from calc-alkaline to alkaline volcanism during the Neogene in Oranie (Algeria): magmatic expression of a slab breakoff. *Lithos*, *62*, 87-110.

Cox, K.G., Bell, J.D. & Pankhurst, R.J. (1979). In: The Interpretation of Igneous Rocks. *George Allen & Unwin, London* 450. pp.

Cribb, J.W. & Barton, M. (1996). Geochemical effects of decoupled fractional crystallization and crustal assimilation. *Lithos, 37*, 293–307.

Cvetković, V., Downes, H., Prelević, D., Jovanović, M. & Lazarov, M. (2004a). Characteristics of the lithospheric mantle beneath East Serbia inferred from ultramafic xenoliths in Palaeogene basanites. *Contributions to Mineralogy and Petrology, 148*, 335–357.

Cvetković, V., Prelević, D., Downes, H., Jovanović, M., Vaselli, O. & Pecskay, Z. (2004b). Origin and geodynamic significance of Tertiary postcollisional basaltic magmatism in Serbia (central Balkan Peninsula). *Lithos, 73*, 161–186.

Dalpe, C. & Baker, D.R. (1994). Partition coefficients for rare-earth elements between calcic amphibole and Ti-rich basanitic glass at 1.5 Gpa, 1100 degrees C. *Mineralogical Magazine, 58*, 207–208.

Davis, G.H. & Coney, P.J. (1979). Geologic development of the Codilleran metamorphic core complex. *Geology, 7*, 120–124.

Delaloye, M. & Bingöl, E. (2000). Granitoids from western and northwestern Anatolia: geochemistry and modelling of geodynamic evolution. *International Geology Reviews, 42*, 241–268.

DePaolo, D.J. (1981). Trace element and isotopic effects of combined wall-rock assimilation and fractional crystallisation. *Earth and Planetary Science Letters, 53*, 189–202.

Di Battistini, G., Montanini, A., Vernia, L. Bargossi, G.M. & Castorina F. (1998). Petrology and geochemistry of ultrapotassic rocks from the

Montefiascone Volcanic Complex (Central Italy): magmatic evolution and petrogenesis. *Lithos, 43*, 169–195.

Di Battistini, G., Montanini, A., Vernia, L. Venturelli, G. & Tonarini, S. (2001). Petrology of melilite-bearing rocks from the Montefiascone Volcanic Complex (Roman Magmatic Province): new insights into the ultrapotassic volcanism of Central Italy. *Lithos, 59*, 1–24.

Dilek, Y. & Altunkaynak, Ş. (2007). Cenozoic crustal evolution and mantle dynamics of post-collisional magmatism in western Anatolia. *International Geology Reviews, 49*, 431–453.

Dilek, Y. & Altunkaynak, Ş. (2009) Geochemical and temporal evolution of Cenozoic magmatism in western Turkey: Mantle response to collision, slab breakoff, and lithospheric tearing in an orogenic belt. In: van Hinsbergen DJJ, Edwards MA, Govers R (eds) *Collision and Collapse at the Africa-Arabia-Eurasia Subduction Zone, Geol. Soc. London, Spec. Publ., 311*, 213–233.

Dilek, Y. & Altunkaynak, Ş. (2010). Geochemistry of Neogene-Quaternary alkaline volcanism in western Anatolia, Turkey, and implications for the Aegean mantle. *International Geology Review, 52*, 631-655.

Donnelly, K.E., Goldstein, S.L., Langmuir, C.H. & Spiegelman, M. (2004) Origin of enriched ocean ridge basalts and implications for mantle dynamics. *Earth Planet. Sci. Lett., 226*, 347–366.

Duggen, S., Hoernle, K., van den Bogaard, P. & Garbe-Schönberg, D. (2005). Post-Collisional Transition from Subduction to Intraplate-type Magmatism in the Westernmost Mediterranean: Evidence for Continental-Edge Delamination of Subcontinental Lithosphere. *Journal of Petrology, 46*, 1155–1201.

Duggen, S., Hoernle, K., van den Bogaard, P. & Harris C. (2004). Magmatic evolution of the Alboran region: The role of subduction in forming the western Mediterranean and causing the Messinian Salinity Crisis. *Earth and Planetary Science Letters, 218*, 91–108.

Dürr, S. (1975). Über Alter und geotektonische Stellung des Menderes Kristallins / SW – Anatolien und seine Äquivalente in der Mittleren Aegean. Habilitation Thesis, *University of Marburg.*

Edwards, C.M.H., Morris, J.D. & Thirlwall, M.F. (1993). Separating mantle from slab signatures in arc lavas using B/Be and radiogenic isotope systematics. *Nature, 362*, 530–533.

Eiler, J.M., Schiano, P., Valley, J.W., Kita, N.T. & Stolper, E.M. (2007). Oxygen-isotope and trace element constraints on the origins of silica-rich melts in the subarc mantle. *Geochemistry, Geophysics, Geosystems 8*, Q09012.

Elitok, Ö., Özgür, N., Drüppel, K., Dilek, Y., Platevoet, B., Guillou, H., Poisson, A., Scaillet, S., Satır, M., Siebel, W., Bardintzeff, J-M., Deniel, C. & Yılmaz, K. (2010). Origin and geodynamic evolution of late Cenozoic potassium-rich volcanism in the Isparta area, southwestern Turkey. *International Geology Review, 52*, 454–504.

Elliott, T., Plank, T., Zindler, A.,White,W. & Bourdon, B. (1997). Element transport from slab to volcanic front at the Mariana arc. *Journal of Geophysical Research, 102*, 14991–15019.

Emre, T. (1996). Gediz Grabeninin jeolojisi ve Tektoniği, *Turkish Jurnal of Earth Science, 5*, 171-185.

Emre, T. & Sözbilir, H. (1997). Field evidence for metamorphic core complex, detachment faulting and accommodation faults in the Gediz and Büyük Menderes Grabens (Western Turkey), in: Ö. Pişkin, M. Ergün, M.Y. Savaşçın, G. Tarcan (Eds.), *IESCA Proceedings*, 73-94.

Emre, T. & Sözbilir, H. (2005). Küçük menderes grabeni doğu ucundaki andezitlerin (Başova-Kiraz/İzmir) jeolojisi, petrografisi ve jeokimyası (Geology, petrography and geochemistry of the andesites in the eastern part of the Küçük Menderes graben). *Mineral Research and Exploration (MTA) Bulletin, Turkey, 131*, 1–19.

Emre, T. & Sözbilir, H. (2007). Tectonic Evolution of the Kiraz Basin, Küçük Menderes Graben: Evidence for Compression/Uplift-related Basin Formation Overprinted by Extensional Tectonics in West Anatolia. *Turkish Journal of Earth Science, 16*, 441–470.

Ercan, T., Akat, U., Günay, E. & Savaşçın, Y. (1986). Söke-Selçuk-Kuşadası dolaylarının jeolojisi ve volkanik kayaçların petrokimyasal özellikleri (Geology of the Söke-Selçuk-Kuşadası region and petrochemical features of the volcanic rocks). *Mineral Research and Exploration (MTA) Bulletin, Turkey, 105/106*, 15–38.

Ercan, T., Dinçel, A., Metin, S., Türkecan, A. & Günay, A. (1978). Uşak yöresindeki Neojen havzalarının jeolojisi (Geology of the Neogene basins in Uşak region). *Bulletin of the Geological Society of Turkey, 21*, 97-106.

Ercan, T., Satır T., Steinitz, G., Dora, A., Sarıfakıoğlu, E., Adis, C., Walter, H-J. & Yıldırım, T. (1995). Biga Yarimadası ile Gökçeada, Bozcaada ve Tavşan Adalarındaki (KB Anadolu) Tersiyer Volkanizmasının Özellikleri (Features of the Tertiary volcanites in the Biga Peninsula, Gökçeada, Bozcaada and Tavşan islands [NW Anatolia]). *Mineral Research and Exploration (MTA) Bulletin, Turkey, 177*, 55–86.

Ercan, T., Satır, M., Kreuzer, H., Türkecan, A., Günay E., Çevikbaş, A., Ateş, M. & Can, B. (1985). Batı Anadolu Senozoyik volkanitlerine ait yeni kimyasal, izotopik ve radyometrik verilerin yorumu. *Türkiye Jeoloji Kurumu Bülteni, 28*, 121–136.

Ercan, T., Satır, M., Steinitz, G., Dora, A., Sarifakioğlu, E., Adis, C., Walter, H-J. & Yıldırım,T. (1996). Features of the Tertiary volcanism in the Biga Peninsula and in the islands of Gökçeada, Bozcaada and Tavan adasi (in Turkish). *Bulletin of the Mineral Research and Exploration,* Ankara, *117*, 55–86.

Ercan, T., Türkecan, A., Dinçel, A. & Günay, E. (1983). Kula – Selendi (Manisa) dolaylarının jeolojisi (Geology of Kula – Selendi (Manisa) area). *Jeoloji Mühendisliği, 17*, 3-28.

Ercan, T., Türkecan, A., Guillou, H., Satır, M., Sevin, D. & Şaroğlu, F. (1998). Marmara Denizi Çevresindeki Tersiyer Volkanizmasinin Özellikleri. *MTA Dergisi, 120*, 199–221.

Erdoğan, B. (1990). İzmir-Ankara Zonu'nun, İzmir ile Seferihisar Arasındaki Bölgede Stratigrafik Özellikleri ve Tektonik Evrimi. *TPJD Bülteni*, *2*, 1–20.

Erdoğan, B., Altiner, D., Güngör, T. & Özer, S. (1990). Stratigraphy of Karaburun Peninsula. *Bulletin of the Mineral Research and Exploration,* Ankara, *111*, 1–20.

Erkül, F. (2010). Tectonic significance of synextensional ductile shear zones within the Early Miocene Alaçamdağ granites, northwestern Turkey. *Geological Magazine, 147,* 611–637.

Erkül, F., Helvacı, C. & Sözbilir, H. (2005a). Stratigraphy and Geochronology of the Early Miocene Volcanic Units in the Bigadiç Borate Basin, Western Turkey. *Turkish Journal of Earth Science, 14*, 227–253.

Erkül, F., Helvacı, C. & Sözbilir, H. (2005b). Evidence for two episodes of volcanism in the Bigadic borate basin and tectonic implications for Western Turkey. *Geological Journal, 40,* 545–570.

Ersoy, E.Y. & Helvacı, C. (2007). Stratigraphy and Geochemical Features of the Early Miocene Bimodal (Ultrapotassic and Calc-alkaline) Volcanic Activity within the NE-trending Selendi basin, Western Anatolia, Turkey. *Turkish Journal of Earth Science, 16,* 117–139.

Ersoy, E.Y. & Helvacı, C. (2010). FC-AFC-FCA and mixing modeler: a Microsoft[®] Excel[©] spreadsheet program for modeling geochemical differentiations of magma by crystal fractionations, crustal assimilation and mixing. *Computers and Geosciences, 36*, 383–390.

Ersoy, E.Y., Helvacı, C. & Palmer, M.R. (2010b). Mantle source characteristics and melting models for the early-middle Miocene mafic volcanism in Western Anatolia: implications for enrichment processes of mantle lithosphere and origin

of K-rich volcanism in post-collisional settings. *J. Volcanol. Geotherm. Res.,* *198*, 112–128.

Ersoy, E.Y., Helvacı, C. & Palmer, M.R. (2011a). Stratigraphic, structural and geochemical features of the NE-SW trending Neogene volcano-sedimentary basins in western Anatolia: implications for associations of supradetachment and transtensional strike-slip basin formation in extensional tectonic setting, *J Asian Earth Sci. 41,* 159–183.

Ersoy, E.Y., Helvacı, C. & Palmer, M.R. (2011b). Petrogenesis of the Neogene volcanic units in the NE-SW-trending basins in western Anatolia, Turkey. *Contributions to Mineralogy and Petrology.* (In press).

Ersoy, E.Y., Helvacı, C. & Sözbilir, H. (2010a). Tectono-stratigraphic evolution of the NE-SW-trending superimposed Selendi basin: implications for late Cenozoic crustal extension in Western Anatolia, Turkey. *Tectonophysics, 488,* 210–232.

Ersoy, E.Y., Helvacı, C., Sözbilir, H., Erkül, F. & Bozkurt, E. (2008). A geochemical approach to Neogene–Quaternary volcanic activity of Western Anatolia: An example of episodic bimodal volcanism within the Selendi Basin, Turkey. *Chemical Geology, 255*, 265–282.

Faccenna, C., Jolivet, L., Piromallo, C. & Morelli, A. (2003). Subduction and the depth of convection of the Mediterranean mantle. *Journal of Geophysical Research, 108*, 2099.

Floyd, P.A., Helvacı, C. & Mittwede, S.K. (1998). Geochemical discrimination of volcanic rocks associated with borate deposits: an exploration tool? *Journal of Geochemical Exploration*, *60*, 185–205.

Foley, S.F., Barth, M.G. & Jenner, G.A. (2000). Rutile/melt partition coefficients for trace elements and an assessment of the influence of rutile on the trace element characteristics of subduction zone magmas. *Geochimica et Cosmochimica Acta 64*, 933–938.

Foley, S.F., Jackson, S.E., Fryer, B.J., Greenough, J.D. & Jenner, G.A. (1996). Trace element partition coefficients for clinopyroxene and phlogopite in an alkaline lamprophyre from Newfoundland by LAM-ICP-MS. *Geochimica Cosmochimica Acta, 60*, 629–638.

Foley, S.F., Venturelli, G., Green, D.H. & Toscani, L. (1987). The ultrapotassic rocks: characteristics, classification, and constraints for petrogenetic models. *Earth-Science Reviews*, 24, 81–134.

Francalanci, L., Innocenti, F., Manetti, P. & Savaşçın, M.Y. (2000). Neogene alkaline volcanism of the Afyon-Isparta area, Turkey: petrogenesis and geodynamic implications. *Mineralogy and Petrology*, 70, 285–312.

Freydier, R., Michard, A., De Lange, G. & Thomson, J. (2001). Nd isotopic compositions of Eastern Mediterranean sediments: tracers of the Nile influence during sapropel S1 formation? *Marine Geology, 177,* 45–62.

Friedmann, S.J. & Burbank, D.W. (1995). Rift basins and supradetachment basins: intracontinental extensional end-members. *Basin Research, 7*, 109–127.

Fytikas, M., Innocenti, F., Manetti, P., Mazzuoli, R., Peccerillo, A. & Villari, L. (1984). Tertiary to Quaternary evolution of volcanism in the Aegean region. In: J.E. Dixon, and A. H. F. Robertson, (eds). The Geological evolution of the Eastern Mediterranean. *Geological Society Special Publication*, *17*, 687-699.

Genç, Ş.C. & Yılmaz, Y. (1997). An example of postcollisional magmatim in northwestern Anatolia: the Kizderbent Volcanites (Armutlu Peninsula, Turkey). *Turkish J. Earth Sci., 6,* 33–42.

Geological Map of Turkey; 1:500000 (2002). Publication of Mineral Research and Exploration Institute of Turkey.

Gessner, K., Piazolo, S., Güngör, T., Ring, U., Kröner, A. & Passchier, C.W. (2001a). Tectonic significance of deformation patterns in granitoid rocks of the Menderes nappes, Anatolide belt, southwest Turkey, *International Journal of Earth Science*, *89*, 766–780.

Gessner, K., Ring, U., Chrıstopher, J., Hetzel, R., Passchıer, C. W. & Güngör, T. (2001b). An active bivergent rolling-hinge detachment system: central Menderes metamorphic core complex in western Turkey. *Geology*, *29*, 611–14.

Ghiorso, M.S. & Sack, R.O. (1995) Chemical Mass Transfer in Magmatic Processes. IV. A Revised and Internally Consistent Thermodynamic Model for the Interpolation and Extrapolation of Liquid-Solid Equilibria in Magmatic Systems at Elevated Temperatures and Pressures. *Contrib. Mineral. Petrol. 119*, 197–212.

Glodny, J. & Hetzel, R. (2007). Precise U-Pb ages of syn-extensional Miocene intrusions in the central Menderes Massif, Western Turkey. *Geological Magazine, 144*, 235–246.

Göğüş, O.H. & Pysklywec, R.N. (2008). Near-surface diagnostics of dripping or delaminating lithosphere. *Journal of Geophysical Research, 113,* B11404.

Göncüoğlu, M.C., Özcan., A., Turhan., N. & Işık, A. (1992). Stratigraphy of the Kütahya region. *In Field Guide Book for the Symposium on the Geology of the Black See Region*, Ankara, 3-11.

Görür, N., Oktay, F.Y., Seymen, I. & Şengör, A.M.C. (1984). Palaeotectonic evolution of the Tuzgölü basin complex, Central Turkey: sedimentary record of a Neo-Tethyan closure. In: The Geological Evolution of the Eastern Mediterranean (J.E. Dixon & A.H.F. Robertson, eds), pp. 467–482. *Geological Society Special Publication*, 17, Blackwell Scientific, Oxford.

Görür, N., Şengör, A.M.C., Akkök, R. & Yılmaz, Y. (1983). Sedimentological data regarding the opening of the northern branch of Neo-Tethys in the Pontides. *Geological Society of Turkey Bulletin*, *26*, 11-20.

Green, D.H. (1971). Composition of basaltic magmas as indicators of origin: application to oceanic volcanism. *Philosophical Transactions Royal Society London, A268*, 707–725.

Green, T., Blundy, J., Adam, J. & Yaxley, G. (2000). SIMS determination of trace element partition coefficients between garnet, clinopyroxene and hydrous basaltic liquids at 2-7.5 Gpa and 1080-1200C. *Lithos, 53*, 165–187.

Güleç, N. (1991). Crust-mantle interaction in western Turkey: implications from Sr and Nd isotope geochemistry of Tertiary and Quaternary volcanites. *Geological Magazine*, *23*, 417-435.

Hafkenscheid, E., Wortel, M.J.R. & Spakman, W. (2006). Subduction history of the Tethyan region derived from seismic tomography and tectonic reconstructions. *Journal of Geophysical Research, 111*, B08401.

Hakyemez, H.Y., Erkal, T. & Göktaş, F. (1999). Late Quaternary evolution of the Gediz and Büyük Menderes grabens, Western Anatolia, Turkey. *Quaternary Science Review, 18*, 549–554.

Hammersley, L. & DePaolo, D.J. (2006) Isotopic and geophysical constraints on the structure and evolution of the Clear Lake volcanic system. *J. Volcanol. Geotherm. Res., 153*, 331–356.

Harangi, S., Downes, H., Thirlwall, M. & Gmeling, K. (2007). Geochemistry, Petrogenesis and Geodynamic Relationships of Miocene Calc-alkaline Volcanic Rocks in the Western Carpathian Arc, Eastern Central Europe. *Journal of Petrology, 48*, 2261–2287.

Hart, S.R. (1984). The Dupal anomaly: a large-scale isotope anomaly in the southern hemisphere mantle. *Nature, 309*, 753–757.

Hart, S.R. & Brooks, C. (1974). Clinopyroxene-matrix partitioning of K, Rb, Cs, Sr and Ba. *Geochimica et Cosmochimica Acta, 38,* 1799–1806.

Hart, S.R. & Dunn, T. (1993). Experimental cpx/melt partitioning of 24 trace elements. *Contributions to Mineralogy and Petrology, 113*, 1–8.

Hart, S.R., Blusztajn, J., Dick, H.J.B., Meyer, P.S. & Muehlenbachs, K. (1999). The fingerprint of seawater circulation in a 500-meter section of ocean crust gabbros. *Geochim. Cosmochim. Acta, 63,* 4059–4080.

Hasözbek, A., Erdoğan, B., Satır, M., Siebel, W., Akay, E., Doğan, G.D. & Taubald, H. (2011). Al-in-Hornblende Thermobarometry and Sr-Nd-O-Pb Isotopic Compositions of the Early Miocene Alacam Granite in NW Anatolia (Turkey). *Turkish J. Earth Sci*. (in press).

Hawkesworth, C.J., Hergt, J.M., Ellam, R.M. & McDermott, F. (1991). Element Fluxes Associated with Subduction Related Magmatism. *Philosophical Transactions Royal Society London, 335*, 393–405.

Hawkesworth, C.J., Turner, S., Gallagher, K., Hunter, A., Bradshaw, T. & Rogers, N. (1995). Calc-alkaline magmatism, lithospheric thinning and extension in the Basin and Range. *Journal of Geophysical Research, 100*, 10271–10286.

Hawkesworth, C.J., Turner, S.P., McDermott, F., Peate, D.W. & van Calsteren, P. (1997). U-Th isotopes in arc magmas; implications for element transfer from the subducted crust. *Science, 276,* 551–555.

Helvacı, C. (1984). Occurrence of rare borate minerals: Veatchite-A, tunellite, teruggite and cahnite in the Emet borate deposit, Turkey. *Mineral Deposita, 19*, 217–226.

Helvacı, C. (1986), Stratigraphic and structural evolution of the Emet borate deposits, Western Anatolia. Dokuz Eylül University, Faculty of Engineering and Architecture, Research Papers, No: MM/JEO-86 AR 008.

Helvacı, C. (1995). Stratigraphy, mineralogy, and genesis of the Bigadiç borate deposits, Western Turkey. *Economic Geology, 90,* 1237–1260.

Helvacı, C. & Alonso, R.N. (2000). Borate deposits of Turkey and Argentina; a summary and geological comparison. *Turkish Journal of Earth Sciences, 24,* 1-27.

Helvacı, C. & Yağmurlu, F. (1995). Geological setting and economic potential of the lignite and evaporite-bearing Neogene basins of Western Anatolia, Turkey. *Israel Journal of Earth Science, 44*, 91–105.

Helvacı, C., Ersoy, E.Y., Sözbilir, H., Erkül, F., Sümer, Ö. & Uzel, B. (2009). Geochemistry and 40Ar/39Ar Geochronology of Miocene volcanic rocks from the Karaburun Peninsula: implications for amphibole-bearing lithospheric mantle source, Western Anatolia. *Journal of Volcanology and Geothermal Research, 185,* 181–202.

Hermann, J. & Rubatto, D. (2009). Accessory phase control on the trace element signature of sediment melts in subduction zones. *Chemical Geology, 265,* 512–526.

Hetzel, R., Passchier, C.W., Ring, U. & Dora, O.Ö. (1995a). Bivergent extension in orogenic belts: The Menderes Massif (southwestern Turkey). *Geology*, 23, 455–458.

Hetzel, R., Ring, U., Akal, C. & Troesch, M. (1995b). Miocene NNE-directed extensional unroofing in the Menderes Massif, southwestern Turkey. *Journal of Geological Society*, *London, 152*, 639–654.

Hetzel, R., Romer, R.L., Candan, O. & Passchier, C.W. (1998). Geology of the Bozdağ area, central Menderes Massif, SW Turkey: Pan-African basement and Alpine deformation. *Geologische Rundschau, 87*, 394–406.

Hochstaedter, A., Gill, J., Peters, R., Broughton, P., Holden, P. & Taylor, B. (2001). Across-arc geochemical trends in the Izu-Bonin arc: Contributions from the subducting slab. *Geochemistry, Geophysics, Geosystems 2*, 2000GC000105.

Hofmann, A.W. (1988). Chemical differentiation of the Earth: the relationship between mantle, continental crust, and oceanic crust. *Earth and Planetary Science Letters, 90*, 297–314.

Houseman, G.A., McKenzie, D.P. & Molnar, P. (1981). Convective instability of a thickened boundary layer and its relevance for the thermal evolution of continental convergent belts. *Journal of Geophysical Research, 86*, 6115–6132.

İnci, U. (1984). Neogene oil shale deposits of Demirci and Burhaniye regions. 27th *International Geological Congress*, Abs. Vol. VII, 13–16, 57.

İnci, U. (1998). Miocene synvolcanic alluvial sedimentation in lignite-bearing Soma Basin, Western Turkey. *Turkish Journal of Earth Science, 7,* 63–78.

Innocenti, F., Agostini, S., Di Vincenzo, G., Doglioni, C., Manetti, P., Savaşçın, M.Y. & Tonarini, S. (2005). Neogene and Quaternary volcanism in Western Anatolia: magma sources and geodynamic evolution. *Marine Geology, 221*, 397–421.

Irvine, N. & Baragar, W.R.A. (1971). A guide to chemical classification of the common volcanic rocks. *Canadian Journal of Earth Science*, 8, 523–548.

Ishizuka, O., Taylor, R.N., Yuasa, M., Milton, J.A., Nesbitt, R.W., Uto, K., & Sakamoto, I. (2007) Processes controlling along-arc isotopic variation of the southern Izu-Bonin arc. *Geochem. Geophys. Geosyst. 8:* Q06008.

Işık, V. & Tekeli, O. (2001). Late orogenic crustal extension in the northern Menderes Massif (western Turkey): evidence for metamorphic core complex formation. *International Journal of Earth Sciences*, 89, 757–65.

Işık, V., Seyitoğlu, G. & Çemen, İ. (2003). Ductile-brittle transition along the Alasehir shear zone and its structural relationship with the Simav detachment, Menderes massif, western Turkey. *Tectonophysics*, 374, 1–18.

Işık, V., Tekeli, O. & Seyitoğlu, G. (2004). The $^{40}Ar/^{39}Ar$ age of extensional ductile deformation and granitoid intrusions in the northern Menderes core complex: Implications for the initiation of extensional tectonics in western Turkey. *Journal of Asian Earth Science, 23*, 555–566.

Johnson, M.C. & Plank, T. (1999). Dehydration and Melting Experiments Constrain the Fate of Subducted Sediments. *Geochemistry, Geophysics, Geosystems, 1,* 1999GC000014.

Jolivet, L. & Patriat, M. (1999). Ductile extension and the formation of the Aegean Sea. In The Mediterranean basins: Tertiary Extension within the Alpine Orogen (eds B. Durand, L. Jolivet, F. Horvath and M. Seranne), *Geological Society of London*, *156*, 427–56.

Jones, R.H. & Layne, G.D. (1997). Minor and trace element partitioning between pyroxene and melt in rapidly cooled chondrules. *American Mineralogist, 8,* 534–545.

Karacık, Z., Yılmaz, Y. & Pearce, J.A. (2007) The Dikili-Çandarlı Volcanites, Western Turkey: Magmatic Interactions as Recorded by Petrographic and Geochemical Features. *Turkish J. Earth Sci., 16,* 493–522.

Karaoğlu, Ö., Helvacı, C. & Ersoy, E.Y. (2010). Petrogenesis and 40Ar/39Ar geochronology of the volcanic rocks of the Uşak-Güre basin, western Türkiye. *Lithos, 119*, 193-210.

Keleman, P.B. & Dunn, J.T. (1992). Depletion of Nb relative to other highly incompatible elements by melt/rock reaction in the upper mantle. EOS, *Transactions of the American Geophysical Union, 73*, 656–657.

Kelemen, P.B., Hanghoj, K. & Greene, A.R. (2004). One View of the Geochemistry of Subduction-related Magmatic Arcs, with an Emphasis on Primitive Andesite and Lower Crust. In: Holland, H.D., Turekian, K.K., (Eds), Treatise on Geochemistry. Elsevier, Amsterdam. *3*, 593–659.

Kennedy, A.K., Lofgren, G.E. & Wasserburg, G.J. (1993). An Experimental-Study of Trace-Element Partitioning between Olivine, Ortho-Pyroxene and Melt in Chondrules - Equilibrium Values and Kinetic Effects. *Earth and Planetary Science Letters, 115*, 177–195.

Keskin, M. (2002). FC-modeler: a Microsofts Excel& spreadsheet program for modeling Rayleigh fractionation vectors in closed magmatic systems. *Computers & Geosciences, 28,* 919–928.

Keskin, M. (2003). Magma generation by slab steepening and breakoff beneath a subduction-accretion complex: an alternative model for collision-related volcanism in eastern Anatolia, Turkey. *Geophysical Research Letters*, *30*, 8045.

Keskin, M., Genç, Ş.C. & Tüysüz, O. (2008). Petrology and geochemistry of post-collisional Middle Eocene volcanic units in North-Central Turkey: Evidence for magma generation by slab breakoff following the closure of the Northern Neotethys Ocean. *Lithos, 104*, 267–305.

Keskin, M., Pearce, JA. & Mitchell, J.G. (1998). Volcano-stratigraphy and geochemistry of collision-related volcanism on the Erzurum–Kars Plateau, northeastern Turkey. *Journal of Volcanology and Geothermal Research, 85*, 355–404.

Klein, E.M. (2004). Geochemistry of the Igneous Oceanic Crust. In: Treatise on Geochemistry. Holland, H.D., Turekian, K.K., (Eds.), Elsevier, Amsterdam. 3, 433–463.

Koçyiğit, A., Winchester, J.A., Bozkurt, E. & Holland, G. (2003). Saraçköy Volcanic Suite: implications for the subductional phase of arc evolution in the Galatean Arc Complex, Ankara, Turkey. *Geological Journal, 38,* 1–14.

Koçyiğit, A., Yusufoğlu, H. & Bozkurt, E. (1999). Evidence from the Gediz Graben for episodic two-stage extension in western Turkey. *Journal of the Geological Society, London, 156*, 605–616.

Konak, N., Akdeniz, N. & Öztürk, E.N. (1987). Geology of the South ofMenderes Massif. IGCP Proj. 5: Guide Book field excursionWestern Anatolia, Turkey. *Mineral Research and Exploration Institute of Turkey Publication,* 42–53.

Krom, M.D., Michard, A., Cliff, R.A. & Strohle, K. (1999). Sources of sediment to the Ionian Sea and western Levantine basin of the Eastern Mediterranean during S-1 sapropel times. *Marine Geology, 160*, 45–61.

Kürkçüoğlu, B. (2010). Geochemistry and petrogenesis of basaltic rocks from the Develidağ volcanic complex, Central Anatolia, Turkey. *Journal of Asian Earth Sciences, 37*, 42–51.

Kürkçüoğlu, B, Furman, T. & Hanan, B. (2008) Geochemistry of post-collisional mafic lavas from the North Anatolian Fault zone, Northwestern Turkey. *Lithos, 101*, 416–434.

Le Bas, M.J., Le Maitre, R.W., Streckeisen, A. & Zanettin, B. (1986). A chemical classification of volcanic rocks based on the total alkali–silica diagram. *Journal of Petrology, 27*, 745–750.

LeMaitre, R.W. (2002). Igneous rocks: a classification and glossary of terms: recommendations of the International Union of Geological Sciences, Subcommission on the Systematics of Igneous Rocks, Cambridge University Press.

Lips, A.L.W. (1998). Temporal constraints on the kinematics of the destabilization of an orogen; syn- to post-orogenic collapse of the Northern Aegean region, PhD. Thesis, *Geol. Ultraiect., 166*, 223.

Lips, A.L.W., Cassard, D., Sözbilir, H., Yılmaz, H. & Wijbrans, J. (2001). Multistage exhumation of the Menderes Massif, western Anatolia (Turkey), *International Journal of Earth Science, 89*, 781-92.

Lister, G.S. & Davis, G.A. (1989). The origin of metamorphic core complexes and detachment faulting formed during continental extension in the Colorado River region, U.S.A. *Journal of Structural Geology, 11*, 65–94.

Loos, S. & Reischmann, T. (1999). The evolution of the southern Menderes Massif in SW Turkey as revealed by zircon dating. *Journal of the Geological Society, London, 156,* 1021-1030.

Luhr, J.F. (1997). Extensional tectonics and the diverse primitive volcanic rocks in the Western Mexican Volcanic Belt. *The Canadian Mineralogist, 35*, 473–500.

Marchev, P., Raicheva, R., Downes, H., Vaselli, O., Chiaradia, M. & Moritz, R. (2004). Compositional diversity of Eocene–Oligocene basaltic magmatism in the Eastern Rhodopes, SE Bulgaria: implications for genesis and tectonic setting. *Tectonophysics, 393*, 301–328.

Martinod, J., Husson, L., Roperch, P., Guillaume, B. & Espurt, N. (2010) Horizontal subduction zones, convergence velocity and the building of the Andes. *Earth Planet. Sci. Lett., 299,* 299–309.

Matsui, Y., Onuma, N., Nagasawa, H., Higuchi, H. & Banno, S. (1977). Crystal structure control in trace element partition between crystal and magma. *Tectonics, 100*, 315–324.

McCulloch, M.T. & Gamble, J.A. (1991). Geochemical and geodynamical constraints on subduction zone magmatism, *Earth Planetary Science Letters, 102,* 358–374.

McDonough, W.F. & Sun, S.-S. (1995). Composition of the Earth. *Chemical Geology, 120*, 223–253.

McKenzie, D.P. & O'Nions, R.K. (1991). Partial melting distributions from inversion of rare earth elementconcentrations. *Journal of Petrology*, *32*, 1021-1091.

Münker, C. (2000). The Isotope and Trace Element Budget of the Cambrian Devil River Arc System, New Zealand: Identification of Four Source Components. *Journal of Petrology, 6,* 759–788.

Nakamura, H. & Iwamori, H. (2009). Contribution of slab-fluid in arc magmas beneath the Japan arcs, *Gondwana Research, 16*, 431–445.

Nebert, K. (1961). Gördes (Batı Anadolu) bölgesindeki Neojen volkanizması hakkında bazı bilgiler [Some information on Neogene volcanism in Gördes

(Western Anatolia) region]. *Mineral Research and Exploration Bulletin (Turkey), 57,* 50–54.

Oberhänsli, R., Candan, O., Dora O.Ö. & Dürr, H. (1997). Eclogites within the Menderes Massif, western Turkey. *Lithos*, *41*, 135–150.

Oberhänsli, R., Monie, P., Candan, O., Warkus, F.C., Partzsch, J.H. & Dora, O.Ö. (1998). The age of blueschist metamorphism in the Mesozoic cover series of the Menderes Massif. *Swiss Bulletin of Mineralogy and Petrology*, *8*, 309–316.

Okay, A.İ. & Kelley, S.P. (1994). Tectonic setting, petrology and geochronology of jadeite glaucophane and chloritoid glaucophane schists from north-west Turkey. *Journal of Metamorphic Geology*, *12*, 455–466.

Okay, A.İ. & Siyako, M. (1991). The new position of the İzmir-Ankara Neo-Tethyan Suture between İzmir and Balıkesir. In: *Proceedings of the Ozan Sungurlu Symp.,* 333–355.

Okay, A.İ. & Siyako, M. (1993). The New Position of the İzmir-Ankara Neo-Tethyan Suture Between İzmir and Balıkesir (in Turkish). In Tectonic and Hydrocarbon Potential of Anatolia and Surraunding Regions, *Preceedings of the Ozan Sungurlu Symposium*, Ankara, ed., S. Turgut, 333–55.

Okay, A.İ. & Tüysüz, O. (1999). Tethyan sutures of northern Turkey. In The Mediterranean Basins: Tertiary extension within the Alpine orogen (eds B. Durand, L. Jolivet, F. Horváth and M. Séranne), pp. 475–515. *Geological Society of London*, Special Publication no. 156.

Okay, A.İ., Satır, M., Maluski, H., Siyako, M., Monie, P., Metzger, R. & Akyüz, S. (1996). Paleo- and Neo-Tethyan events in northwestern Turkey: Geologic and geochronologic contraints. *The Tectonic Evolution of Asia*, 420–441.

Okay, A.İ., Satır, M., Tüysüz, O., Akyüz, S. & Chen, F. (2001). The tectonics of the Strandja Massif: late Variscan and mid-Mesozoicdeformation and metamorphism in the northern Aegean. *International Journal of Earth Sciences*, *90*, 217–233.

Okay, A.İ., Şengör, A.M.C. & Görür, N. (1994). Kinematic history of the opening of the Black Sea and its effect on the surrounding regions. *Geology*, *22,* 267–70.

Öner, Z., Dilek, Y. & Kadıoğlu, Y.K. (2009). Geology and geochemistry of the synextensional Salihli granitoid in the Menderes core complex, western Anatolia, Turkey. *International Geological Review, 52*, 336–368.

Özdemir, Y., Karaoğlu, Ö., Tolluoğlu, A.Ü. & Güleç, N. (2006). Volcanostratigraphy and petrogenesis of the Nemrut stratovolcano (East Anatolian High Plateau): The most recent post-collisional volcanism in Turkey. *Chemical Geology*, *226,* 189– 211.

Özer, S. & Sözbilir, H. (2003). Presence and tectonic significance of Cretaceous rudist species in the so-called Permo-Carboniferous Göktepe Formation, central Menderes Massif, western Turkey. *International Journal of Earth Sciences*, *92*, 397–404.

Özer, S. (1998). Rudist bearing Upper Cretaceous metamorphic sequences of the Menderes Massif (western Turkey). *Geobios, 22,* 235–249.

Özgenç, İ. & Ilbeyli, N. (2008). Petrogenesis of the Late Cenozoic Eğrigöz Pluton in Western Anatolia, Turkey: Implications for Magma Genesis and Crustal Processes. *International Geological Review, 50,* 375–391.

Palme, H. & O'Neill, H.St.C. (2004). Cosmochemical estimates of Mantle Composition. In: Treatise on Geochemistry. In: Holland, H.D., Turrekian, K.K., (Eds), Elsevier, Amsterdam 2, 1–38.

Parlak, O., Delaloye, M., Demirkol, C. & Ünlügenç., U.C. (2001). Geochemistry of Pliocene/Pleistocene basalts along the Central Anatolian Fault Zone (CAFZ), Turkey. *Geodinamica Acta, 14*, 159–167.

Pearce, J.A. (1982). Trace element characteristics of lava from destructive plate boundaries. Andesites, 525–548. Ed: R.S. Thorpe, *Wiley*, New York.

Pearce, J.A. (1983). Role of the sub-continental lithosphere in magma genesis at active continental margins. In: Hawkesworth, C.J., Norry, M.J. (Eds.), Continental basalts and mantle xenoliths. *Shiva Publishing*, Nantwich, pp. 230–249.

Pearce, J.A. & Parkinson, I.J. (1993). Trace element models for mantle melting: application to volcanic arc petrogenesis, in: H.M. Prichard, T. Alabaster, N.B. Harris, C.R. Neary (Eds.), Magmatic Processes and Plate Tectonics, *Geological Society Special Publications*, *76,* 373–403.

Peccerillo, A. & Taylor, S.R. (1976). Geochemistry of eocene calc-alkaline volcanic rocks from the Kastamonu area. Northern Turkey. *Contributions to Mineralogy and Petrology, 58*, 63–81.

Peccerillo, A. (1998). Relationships between ultrapotassic and carbonate-rich volcanic rocks in central Italy: petrogenetic and geodynamic implications. *Lithos, 43*, 67–279.

Pe-Piper, G. & Piper, D.J.W. (2001). Late Cenozoic, post-collisional Aegean igneous rocks: Nd, Pb and Sr isotopic constraints on petrogenetic and tectonic models. *Geological Magazine, 138*, 653–668.

Pe-Piper, G. & Piper, D.J.W. (2007). Late Miocene igneous rocks of Samos: the role of tectonism in petrogenesis in the southeastern Aegean. In: Taymaz, T., Yılmaz, Y., Dilek, Y. (Eds.), The Geodynamics of the Aegean and Anatolia. *Geological Society of London, Special Publications, 291*, 75–97.

Pe-Piper, G. (1994) Lead isotopic compositions of Neogene volcanic rocks from the Aegean extensional area. *Chem. Geol., 118*, 27–41.

Pe-Piper, G., Piper, D.J.W. & Matarangas, D. (2002). Regional implications of geochemistry and style of emplacement of Miocene I-type diorite and granite, Delos, Cyclades. Greece. *Lithos, 60*, 47–66.

Pe-Piper, G., Piper, D.J.W., Kotopouli, C.N. & Panagos, A.G. (1995). Neogene volcanoes of Chios, Greece: The relative importance of subduction and back-arc extension. *Geological Society of London, Special Publications, 81*, 213–232.

Pe-Piper, G., Piper, D.J.W., Koukouvelas, I., Dolansky, L.M. & Kokkalas, S. (2009) Postorogenic shoshonitic rocks and their origin by melting underplated basalts: The Miocene of Limnos, Greece. *Bull. Geol. Soc. Am., 121*, 39–54.

Pe-Piper, G., Piper, D.J.W., Koukouvelas, I., Dolansky, L.M. & Kokkalas, S. (2009). Postorogenic shoshonitic rocks and their origin by melting underplated basalts: The Miocene of Limnos, Greece. *Geological Society of America Bulletin, 121*, 39–54.

Petrelli, M., Poli, G., Perugini, D. & Peccerillo, A. (2005). Petrograph: a New Software to Visualize, Model, and Present Geochemical Data in Igneous Petrology. *Geochemistry, Geophysics, Geosystems 6*, Q07011.

Philpotts, J.A. & Schnetzler, C.C. (1970). Phenocryst-matrix partition coefficients for K, Rb, Sr and Ba, with applications to anorthosite and basalt genesis. *Geochimica et Cosmochimica Acta, 34*, 307–322.

Plank, T. & Langmuir, C.H. (1998). The chemical composition of subducting sediment and its consequences for the crust and mantle. *Chemical Geology, 145*, 325–394.

Powell, R. (1984). Inversion of the assimilation and fractional crystallization (AFC) equations; characterization of contaminants from isotope and trace element relationships in volcanic suites. *Journal of the Geological Society, 141*, 447–452.

Prelević, D. & Foley, S.F. (2007). Accretion of arc-oceanic lithospheric mantle in the Mediterranean: evidence from extremely high-Mg olivines and Cr-rich spinelinclusions from lamproites. *Earth and Planetary Science Letters, 256*, 120–135.

Prelević, D., Akal, C., Romer, R.L. & Foley, S.F. (2010a) Lamproites as indicators of accretion and∕or shallow subduction in the assembly of south-western Anatolia, Turkey. *Terra Nova, 22,* 443–452.

Prelević, D., Foley, S.F., Cvetković, V. & Romer, R.L. (2004). Origin of minette by mixing of lamproite and dacitemagmas in VelikiMajdan Serbia. *Journal of Petrology, 45,* 759–792.

Prelević, D., Foley, S.F., Romer, R. & Conticelli, S. (2008). Mediterranean Tertiary lamproites derived from multiple source components in postcollisional geodynamics. *Geochimica et Cosmochimica Acta, 72*, 2125–2156.

Prelević, D., Foley, S.F., Romer, R.,L., Cvetković, V. & Downes, H. (2005). Tertiary Ultrapotassic Volcanism in Serbia: Constraints on Petrogenesis and Mantle Source Characteristics. *Journal of Petrology*, *46*, 1443–1487.

Prelević, D., Stracke, A., Foley, S.F., Romer, R.L. & Conticelli, S. (2010b). Hf isotope compositions of Mediterranean lamproites: Mixing of melts from asthenosphere and crustally contaminated mantle lithosphere. *Lithos, 119*, 297–312.

Purvis, M. & Robertson, A.H.F. (2004). A pulsed extension model for the Neogene–Recent E–W-trending Alaşehir Graben and the NE–SW-trending Selendi and Gördes Basins, western Turkey, *Tectonophysics*, *391*, 171–201.

Purvis, M., Robertson, A. & Pringle, M. (2005). Ar-40-Ar-39 dating of biotite and sanidine in tuffaceous sediments and related intrusive rocks: Implications for the Early Miocene evolution of the Gördes and Selendi basins, W Turkey. *Geodinamica Acta 18,* 239–253.

Rayleigh, J.W.S. (1896). Theoretical considerations respecting the separation of gases by diffusion and similar processes. *Philosophical Magazine 42,* 77–107.

Régnier, J.I., Ring, U., Passchier, C.W., Gessner, K. & Güngör, T. (2003). Contrasting Metamorphic Evolution of Metasedimentary Rocks From The Çine

and Selimiye Nappes In The Anatolide Belt, Western Turkey. *Journal of Metamorphic Geology, 21*, 699–721.

Régnier, J.L., Mezger, J.E. & Passchier, C.W. (2007). Metamorphism of Precambrian–Palaeozoic schists of the Menderes core series and contact relationships with Proterozoic orthogneisses of the Western Çine Massif, Anatolide belt, Western Turkey. *Geological Magazine, 144,* 67–104.

Ring, U. & Collins, A.S. (2005). U-Pb SIMS dating of synkinematic granites: timing of core-complex formation in the northern Anatolide belt of western Turkey. *Journal of Geological Society*, London, *162*, 289–298.

Ring, U., Gessner, Güngör, T. & Passchier, C. (1999a). The Menderes Massif of Turkey and the Cycladic Massif in Aegean- do they really corralte? *Journal of Geological Society*, London, *156*, 3-6.

Ring, U., Glodny, J., Will, T. & Thomson, S. (2010) The Hellenic Subduction System: High-Pressure Metamorphism, Exhumation, Normal Faulting, and Large-Scale Extension. *Annual Rev. Earth Planet. Sci., 38*, 45–76.

Ring, U., Johnson, C., Hetzel, R. & Gessner, K. (2003). Tectonic denudation of a Late Cretaceous-Tertiary collisional belt: regionally symmetric cooling patterns and their relation to extensional faults in the Anatolide belt of western Turkey. *Geological Magazine, 140*, 421-441.

Ring, U., Susanne, L. & Matthias, B. (1999b). Structural analysis of a complex nappe sequence and late orogenic basins from the Aegean Island of Samos, Greece. *Journal of Structural Geology, 21*, 1575–1601.

Rojay, B., Toprake, V., Demirci, C. & Süzen, L. (2005). Plio-Quaternary evolution of the Küçük Menderes Graben southwestern Anatolia, Turkey. *Geodinamica Acta, 18*, 317–331.

Rollinson, H. (1993). Using Geochemical Data: Evaluation, Presentation, Interpretation, Longman Geochemistry Series, *Prentice Hall*, London, 352 p.

Romer, R.L., Forster, H-J. & Breitkreuz, C. (2001) Intracontinental extensional magmatism with a subduction fingerprint: the late Carboniferous Halle Volcanic Complex (Germany). *Contributions to Mineral. Petrol. 141*, 201–221.

Sarbas, B., Nohl, U., Busch, U., Kalbskopf, B. Schäfer, H. & Schramm, B. (2006). The geochemical database GEOROC - what's the news. *Geophysical Research, Abs*. 8, 03905.

Sarıca, N. (2000). The Plio-Pleistocene age of Büyük Menderes and Gediz grabens and their tectonic significance on N-S extensional tectonics in West Anatolia: mammalian evidence from the continental deposits. *Geological Journal, 35*, 1–24.

Satır, M. & Friedrichsen, H. (1986). The origin and evolution of the Menderes Massif, W-Turkey: A rubidium/strontium and oxygen isotope study. *Geologische Rundschau 75/3*, 703–714.

Saunders, A.D., Norry, M.J. & Tarney, J. (1991). Fluid influence on the trace element compositions of subduction zone magmas. *Philosophical Transactions Royal Society London, 335*, 377–392.

Seghedi, I, Downes, H, Pecskay, Z, Thirlwall, MF, Szakacs, A., Prychodko, M. & Mattey, D., (2001). Magmagenesis in a subduction-related post-collisional volcanic arc segment: the Ukrainian Carpathians. *Lithos, 57*, 237– 262.

Seghedi, I., Bojar, A-V., Downes, H., Roşu, E., Tonarini, S. & Mason, P. (2007). Generation of normal and adakite-like calc-alkaline magmas in a non-subductional environment: An Sr–O–H isotopic study of the Apuseni Mountains neogene magmatic province, Romania. *Chemical Geology, 245*, 70–88.

Şengör, A.M.C. (1987). Cross-faults and differential stretching of hanging walls in regions of low-angle normal faulting: examples from western Turkey. From Coward, M.P., Dewey, J.F., Hancock, P.L. (eds.), 1987, Continental Extensional Tectonics. *Geological Society Special Publication*, 28, 575-589.

Şengör, A.M.C. & Yılmaz, Y. (1981). Tethyan Evolution of Turkey: A Plate Tectonic Approach. *Tectonophysics*, 75, 181-241.

Şengör, A.M.C., Satır, M. & Akkök, R. (1984). The timing of tectonic events in the Menderes Massif, western Turkey: implication for tectonic evolution and evidence for Pan-African basement in Turkey. *Tectonics*, 3, 693-707.

Seyitoğlu, G. (1997a). Late Cenozoic tectono-sedimentary development of the Selendi and Uşak-Güre basins: a contribution to the discussion on the development of east-west and north trending basins in western Anatolia. *Geological Magazine*, 134, 163-175.

Seyitoğlu, G. (1997b). The Simav graben: An example of young E-W trending structures in the late Cenozoic extensional system of Western Turkey. *Turkish Journal of Earth Science 6*, 135–141.

Seyitoğlu, G. & Scott, B.C. (1991). Late Cenozoic crustal extension and basin formation in west Turkey. *Geological Magazine*, 128, 155-166.

Seyitoğlu, G. & Scott, B.C. (1994a). Late Cenozoic basin development in west Turkey. Gördes basin: tectonics and sedimentation. *Geological Magazine*, 131, 631-637.

Seyitoğlu, G. & Scott, B.C. (1994b). Neogene palynological and isotopic age data from Gördes basin, West Turkey. *Newsletter Stratigraphy* 31, 133-142.

Seyitoğlu, G., Alçiçek, M.C., Işık, V., Alçiçek, H., Mayda, S., Varol, B., Yılmaz, İ. & Esat, K. (2009). The stratigraphical position of Kemiklitepe fossil locality (Uşak-Eşme) revisited: Implications for the Late Cenozoic sedimentary basin development and extensional tectonics in Western Turkey. *Neues Jahrbuch für Geologie und Paläontologie, 251*, 1–15.

Seyitoğlu, G., Anderson, D., Nowell, G. & Scott, B.C. (1997). The evolution from Miocene potassic to Quaternary sodic magmatism in western Turkey: implications for enrichment processes in the lithospheric mantle. *Journal of Volcanology and Geothermal Research, 76*, 127-147.

Seyitoğlu, G., Çemen, İ. & Tekeli, O. (2000). Extensional folding in the Alasehir (Gediz) graben, western Turkey. *Journal of the Geological Society, London, 157,* 1097-1100.

Seyitoğlu, G., Işık, V. & Çemen, İ. (2004). Complete Tertiary exhumation history of the Menderes massif, western Turkey: an alternative working hypothesis. *Terra Nova*, *16*, 358-364.

Seyitoğlu, G., Tekeli, O., Çemen, İ., Şen, S. & Işık, V. (2002). The role of flexural rotation/rolling hinge model in the tectonic evolution of the Alasehir graben, western Turkey. *Geological Magazine*, *139*, 15-26.

Snoke, A.W. & Frost, B.R. (1990). Exhumation of high pressure pelitic schist, Lake Murray Spillway, South Carolina: Evidence for crustal extension during Alleghanian strike-slip faulting. *American Journal of Science, 290*, 853–881.

Sözbilir, H. (2001). Extensional tectonics and the geometry of related macroscopic structures: field evidence from the Gediz Detachment, Western Turkey. *Turkish Journal of Earth Science, 10*, 51–67.

Sözbilir, H. (2002a). Geometry and origin of folding in the Neogene sediments of the Gediz Graben, western Anatolia, Turkey. *Geodinamica Acta*, *15*, 277–288.

Sözbilir, H. (2002b). Revised Stratigraphy and Facies Analysis of Palaeocene-Eocene Supra-allochthonous Sediments (Denizli, SW Turkey) and Their Tectonic Significance. *Turkish Journal of Earth Sciences, 11*, 87–112.

Sözbilir, H. (2005). Oligo–Miocene extension in the Lycian orogen: evidence from the Lycian molasse basin, SW Turkey. *Geodinamica Acta, 18*, 257–284.

Staudigel, H., Tauxe, L. & Gee, J.S. (1999). Geochemistry and Intrusive Directions In Sheeted Dikes in the Troodos Ophiolite: Implications for Mid-Ocean Ridge Spreading Centers. *Geochemistry, Geophysics, Geosystems 1,* 1999GC000001.

Stormer, J.C. & Jr, Nicholls, J. (1978). XLFRAC: A program for the interactive testing of magmatic differentiation models. *Computers & Geosciences, 4,* 143–159.

Tankut, A., Dilek, Y. & Önen, P. (1998). Petrology and geochemistry of the Neo-Tethyan volcanism as revealed in the Ankara mélange, Turkey. *Journal of Volcanology and Geothermal Research, 85,* 265–284.

Taylor, H.P. (1980). The effects of assimilation of country rocks by magmas on 18O/16O and 87Sr/86Sr systematics in igneous rocks. *Earth and Planetary Science Letters, 47*, 243–254.

Taylor, S.R. & McLennan, S.M. (1995). The geochemical evolution of the continental crust. *Reviews in Geophysics, 33*, 241–265.

Temeş, A., Gündoğdu, M.N. & Gourgaud, A. (1998). Petrological and geochemical characteristics of Cenozoic high-K calc-alkaline volcanism in Konya, Central Anatolia, Turkey. *Journal of Volcanology and Geothermal Research, 85*, 327–354.

Thomson, S.N. & Ring, U. (2006). Thermochronologic evaluation of postcollision extension in the Anatolide orogen, western Turkey, *Tectonics 25*, TC3005.

Tomassini, S., Avanzinelli, R. & Conticelli, S. (2011). The Th/La and Sm/La conundrum of the Tethyan realm lamproites. *Earth and Planetary Science Letters, 301*, 469–478.

Tonarini, S., Agostini, S., Innocenti, F. & Manetti, P. (2005). δ11B as tracer of slab dehydration and mantle evolution in Western Anatolia Cenozoic Magmatism. *Terra Nova 17*, 259–264.

Turner, S.P., Hawkesworth, C.J., Rogers, N., Bartlett, J., Worthington, T., Hergt, J., Pearce, J. & Smith, I. (1997). 238U/230Th disequilibria, magma petrogenesis, and flux rates beneath the depleted Tonga-Kermadec island arc. *Geochimica et Cosmochimica Acta, 61*, 4855–4884.

Turner, S.P., Platt, J.P., George, R.M.M., Kelley, S.P., Pearson, D.G. & Nowell, G.M. (1999). Magmatism associated with orogenic collapse of the Betic-Alboran domain, SE Spain: *Journal of Petrology*, *40*, 1011–1036.

Tüysüz, O. (1993). Stratigraphic and petrologic characteristics of two parallel magmatic belts in Central Anatolia and their significance in the tectonic evolution of Anatolian Neo-Tethys. EUG VII, *Terra Abstracts*, 5, 271.

Ustaömer, P.A., Ustaömer, T., Collins, A.S. & Reischpeitsch, J. (2009). Lutetian arc-type magmatism along the southern Eurasian margin: New U-Pb LA-ICPMS and whole-rock geochemical data from Marmara Island, NW Turkey. *Mineral. Petrol., 96*, 177–196.

Uzel, B. & Sözbilir, H. (2008). A First Record of a Strike-slip Basin in Western Anatolia and Its Tectonic Implication: The Cumaovası Basin. *Turkish Journal of Earth Science, 17*, 559–591.

van Hinsbergen, D.J.J., Dekkers, M.J., Bozkurt, E. & Koopman, M. (2010). Exhumation with a twist: Paleomagnetic constraints on the evolution of the Menderes metamorphic core complex, western Turkey. *Tectonics, 29*, TC3009.

van Hinsbergen, D.J.J., Hafkenscheid, E., Spakman, W., Meulenkamp, J.E. & Wortel, R. (2005) Nappe stacking resulting from subduction of oceanic and continental lithosphere below Greece. *Geology, 33*, 325–28.

Villemant, B. (1988). Trace-Element Evolution in the Phlegrean Fields (Central-Italy) - Fractional Crystallization and Selective Enrichment. *Contributions to Mineralogy and Petrology, 98*, 169–183.

Walcott C., R. & White S., H. (1998). Constraints on the kinematics of post-orogenic extension imposed by stretching lineations in the Aegean region. *Tectonophysics*, *298*, 155-175.

Wernicke, B.P. & Snow, J.K. (1998). Cenozoic tectonism in the central Basin and Range: Motion of the Sierran-Great Valley Block: *International Geology Review, 40*, 403–410.

Wernicke, B.P. (1995). Low-angle normal faults and seismicity: A review: *Journal of Geophysical Research, 100*, B10, 20159-20174.

Westaway, R., Pringle, M., Yurtmen, S., Demir, T., Bridgland, D., Rowbotham, G. & Maddy, D. (2004). Pliocene and Quaternary regional uplift in western Turkey: the Gediz River terrace staircase and the volcanism at Kula, *Tectonophysics*, 391, 121-169.

Workman, R.K. & Hart, S.R. (2005). Major and trace element composition of the depleted MORB mantle (DMM). *Earth and Planetary Science Letters, 231*, 53–72.

Workman, R.K., Hart, S.R., Jackson, M., Regelous, M., Farley, K.A., Blusztajn, J., Kurz, M. & Staudigel, H. (2004). Recycled metasomatized lithosphere as the origin of the Enriched Mantle II (EM2) end-member : evidence from the Samoan Volcanic Chain. *Geochemistry, Geophysics, Geosystems 5*, Q04008.

Yağmurlu, F. (1984). Akhisar doğusunda kömür içeren Miyosen tortulların stratigrafisi, depolanma ortamları ve tektonik özellikleri. *Bulletin of the Geological Society of Turkey 5*, 3–20.

Yılmaz, Y. (1989). An approach to the origin of young volcanic rocks of Western Turkey. In A. M. C. Şengör (Editor), Tectonic evolution of the Tethyan Region. *Kluwer Academic Publishers*, 159-189.

Yılmaz, Y., Genç, S.C., Gürer, O.F., Bozcu, M., Yılmaz, K., Karacık, Z., Altunkaynak, Ş. & Elmas, A. (2000). When did the western Anatolian grabens begin to develop? In: Bozkurt, E., Winchester, J. A. & Piper, J. D. A. (eds), Tectonics and Magmatism in Turkey and the Surrounding Area. *Geological Society, London*, Special Publications, *173*, 353.84.

Yılmaz, Y., Genç, Ş.C., Karacık, Z. & Altunkaynak, Ş. (2001). Two contrasting magmatic associations of NW Anatolia and their tectonic significance, *Journal of Geodynamics*, 31, 243-271.

Yurtmen, S., & Rowbotham, G. (2002). Geochemistry, mineralogy and petrogenesis of the northeast Niğde volcanites, central Anatolia, Turkey. *Geological Journal*, *37*, 189-215.

Zellmer, G.F. & Turner, S.P. (2007) Arc Dacite Genesis Pathways: Evidence from mafic enclaves and their hosts in Aegean lavas. *Lithos, 95,* 346–362.

Zellmer, G.F., Turner, S.P. & Hawkesworth, C.J. (2000) Timescales of destructive plate margin magmatism: new insights from Santorini, Aegean Volcanic Arc. *Earth Planet. Sci. Lett. 174*, 265–281.

Appendix 1
FC-AFC-FCA and Mixing Modeler

A1.1 Introduction

Magmatic rocks are differentiated by a range of petrological processes such as (a) different degrees of melting of the source rocks, (b) crystal fractionation in magma chambers (fractional crystallization, FC), (c) contamination of the magma via assimilation of the wall-rocks (assimilation), and (d) mixing of magmas of different compositions. Among these processes, FC and assimilation are generally combined and they may occur simultaneously (AFC; Taylor, 1980; DePaolo, 1981). Cribb & Barton (1996) have also suggested that FC and assimilation are not always related and that these two processes may be decoupled (FCA). The mixing of magmas having different compositions also resulted in changes to the original magma compositions.

A number of computer programs have been designed to theoretically graph the vectors of FC and AFC equations (see Keskin, 2002 for detail). As pointed out by Keskin (2002), the main advantage of spreadsheet programs is that they are easier and faster to use during data converting, storing, and evaluating. The FC–AFC–FCA and mixing program, presented in this study, has many advantages in data input, execution, and output. The data can easily be transferred to the FC–AFC–FCA and mixing program. The results of modeling in addition to several classification diagrams can be converted to a Graphics Interchange Format (GIF) file. Additionally, numerical results of the modeling can be derived as tables. Another main advantage of the program is that the modeling results of each magmatic process can be traced on the same diagram.

A1.2 Modeling the Magmatic Processes

In this section brief summary of calculations of magmatic processes and some parameters, used in FC-AFC-FCA and the mixing program will be presented. .

A1.2.1 Fractional Crystallization Process (FC)

Crystallization of magmas can occur by two main processes: (a) equilibrium crystallization (EC), and (b) fractional crystallization (FC; Rayleigh fractionation, Rayleigh (1896)). Equilibrium crystallization refers to the crystallization process throughout which the solid phases remain in the melt and stays in chemical equilibrium with the liquid phase. In Rayleigh fractionation, early formed phases are continuously removed from liquid during cooling and crystallization of the magma. Equilibrium crystallization is expressed by:

$$C_l^{EC} = C_0 / [F + D(1-F)] \qquad (1)$$

where C_l^{EC} is the concentration of a trace element in remaining melt during crystallization, C_0 is the concentration of the trace element in parental liquid (starting composition), D is the bulk partition coefficient of the elements for fractionating mineral phases, F is the fraction of melt remaining during crystallization. The partition coefficient (Kd) refers to the ratio of concentration an element in the solid mineral to the concentration in the melt phase. In the case of the presence of more than one mineral phase, bulk partition coefficient (D) is calculated by:

$$D = \sum_i^n x_i Kd_i = x_a K_d^{\min a} + x_b K_d^{\min b} .... x_n K_d^{\min n} \qquad (2)$$

where D is the bulk partition coefficient, x is the weight fraction of the mineral phase i, and Kd is the partition coefficient of any element in mineral phase i. F value in the Eq. (1) is in the range of 0 to 1.

On the other hand, fractional crystallization (FC) is expressed by:

$$C_l^{FC} = C_0 F^{(D-1)} \qquad (3)$$

where, C_l^{FC} is the concentration of an element in remaining melt during fractional crystallization. The other parameters are as described previously. In our program, only Rayleigh fractionation is considered. Isotopic ratios are assumed not to be affected by crystal fractionation, and remain constant.

A1.2.2 Combined Assimilation and Fractional Crystallization Process (AFC)

Fractional crystallization processes are generally combined with assimilation of the wall rocks surrounding the magma chamber (Taylor, 1989; DePaolo, 1981). During the AFC process there is a strict relationship between the amount of material assimilated and the amount of material crystallized during cooling of the magma. The AFC process is expressed by:

$$C_l{}^{AFC} = C_0[F^{-z} + (\frac{r}{r-1})\frac{C_a}{zC_0}(1-F^{-z})] \tag{4}$$

where, $C_l{}^{AFC}$, C_0, C_a are the concentration of an element in the resulting magma, parental magma, and assimilating material (wall rock), respectively. F is the fraction of melt during cooling of the magma. The "r" value describes the relative ratio of assimilated material to crystallized material, and it is expressed by:

$$r = \frac{m_a}{m_c} \tag{5}$$

where m_a is the amount of assimilated material and m_c is the amount of crystallized material. The z value in AFC equation is expressed by:

$$z = \frac{r+D-1}{r-1} \tag{6}$$

where D is the bulk partition coefficient as described above.

In the case of $r = 1$ ($m_a = m_c$), Eqs. (4) and (6) are not applicable. This case is described as zone refining. If $m_c = 0$, then this process represents simple mixing of

two phases (i.e., no crystallization). In the case of $r = 0$ and $m_a = 0$, then the equation represents pure fractional crystallization. For the case of $r + D = 1$, then the z value would be 0. For such cases Eq. (7) is used:

$$C_l^{AFC} = C_0[(1 + (\frac{r}{r-1})(\frac{C_a}{C_0})\ln(F^{-z})]$$ (7)

The isotopic ratio of a magma undergoing AFC process is also modeled by:

$$IC_l^{AFC} = \frac{(\frac{r}{r-1})(\frac{C_a}{z})(1 - F^{-z})Ic_a + C_0F^{-z}Ic_0}{(\frac{r}{r-1})(\frac{C_a}{z})(1 - F^{-z}) + C_0F^{-z}}$$ (8)

where Ic_l^{AFC}, Ic_a and Ic_0 are isotopic ratios in the magma that undergoing AFC process, isotopic ratios in the assimilating material and in the parental magma, respectively. The parameters of r, z, F, C_0, C_a are the same as in Eq. (4).

A1.2.3 Decoupled Assimilation and Fractional Crystallization Process (FCA)

Cribb & Barton (1996) have proposed that the assimilation and fractional crystallization in a magma system are not strictly related; the mass assimilated may be decoupled from mass crystallized, and therefore varies independently. This process is defined as FCA (decoupled assimilation and fractional crystallization). For a given element it is expressed by:

$$C_l^{FCA} = \frac{C_0RM_c + C_f(1 - M_c)}{F}$$ (9)

where R is the ratio of assimilated material (M_a) to crystallized material (M_c), C_0 and C_f are the concentrations of the element in the original magma and resulting from fractional crystallization, respectively. The other parameters are the same as previously described.

A1.2.4 Mixing Process

Simple mixing of two magmas (e.g., Powell, 1984) is expressed by:

$$C_m = X(C_a - C_b) + C_b \qquad (10)$$

where C_a, C_b and C_m are the concentration of an element in magma *a*, in magma *b*, and in mixed magma resulted from mixing of magmas *a* and *b*, respectively. *X* is the degree of mixing. For the isotopic concentrations, the equation is expressed by:

$$Ic_m = Ic_a \left(\frac{C_a X}{C_m} \right) + Ic_b \left(\frac{C_b (1 - X)}{C_m} \right) \qquad (11)$$

where Ic_a, Ic_b and Ic_m are the isotopic ratio of any element in magma *a*, magma *b* and in mixed magma resulting from mixing of magmas *a* and *b*, respectively. *X, C_a, C_b* and *C_m* have been described previously.

When the "*r*" value in the AFC equations (Eqs. (4) and (7)) is 0, and then the equations will be identical to mixing equations (Eqs. (8) and (9)).

A1.2.5 Other Parameters

In the FC-AFC-FCA and mixing modeler, several parameters are automatically calculated by the program. This will help the user to see and evaluate the parameters together on a single worksheet. These parameters are (1) *Eu/Eu** values, (2) Mg# values, (3) εSr and εNd values, and (4) Nd isotopic model ages of depleted mantle (τ_{DM}^{Nd}).

Eu/Eu* value of a rock sample indicates whether the sample shows a positive or negative Eu anomaly on a rare earth element (REE)-spider diagram, on which the REE concentrations of the rock are normalized to a standard. If Eu/Eu* value is

greater than 1, then the sample has a positive anomaly, and vice verse. The *Eu/Eu** value is expressed by:

$$Eu/Eu^* = Eu_N / \sqrt{(Sm_N) \times (Gd_N)} \tag{12}$$

where, Eu_N, Sm_N and Gd_N are normalized values of these elements.

Mg# value is a representation of the ratio of Mg to Mg+Fe contents of any sample, on a molar or an oxide value basis. It is expressed by:

$$Mg\# = MgO/(MgO + FeO_t) \tag{13}$$

The ε notation for Sr and Nd is simply the relative deviation of the $^{87}Sr/^{86}Sr$ and $^{143}Nd/^{144}Nd$ isotopic ratios of the sample from the chondritic or bulk earth isotopic ratios, respectively. These are expressed by:

$$\varepsilon Sr = \frac{(^{87}Sr/^{86}Sr)_{sample} - (^{87}Sr/^{86}Sr)_{chondrite}}{(^{87}Sr/^{86}Sr)_{chondrite}} \times 10^4 \tag{14}$$

$$\varepsilon Nd = \frac{(^{143}Nd/^{144}Nd)_{sample} - (^{143}Nd/^{144}Nd)_{chondrite}}{(^{143}Nd/^{144}Nd)_{chondrite}} \times 10^4 \tag{15}$$

Nd isotopic model ages of depleted mantle (τ_{DM}^{Nd}) is calculated by extrapolating the $^{143}Nd/^{144}Nd$ back to the intersection with the mantle growth curve on a $^{143}Nd/^{144}Nd$ vs. time diagram (White, 2003). It is expressed by:

$$\tau_{DM}^{Nd} = \frac{1}{\lambda} \times \ln\left(\frac{(^{143}Nd/^{144}Nd)_{sample} - (^{143}Nd/^{144}Nd)_{DM}}{(^{147}Sm/^{144}Nd)_{sample} - (^{147}Sm/^{144}Nd)_{DM}} + 1\right) \tag{16}$$

where, λ is decay constant of ^{147}Sm (6.54 x $10^{-12}y^{-1}$). Nd model ages of depleted mantle are given in Ma (Million years) by the program.

A1.3 Structure and working of the program

The FC-AFC-FCA and mixing modeler have been designed on several sheets which include data input and output sections. The data input section contains two sheets: (1) parameters and (2) samples. The output section is based on graphical and numerical sheets which consist of (1) modeling, (2) classification, (3) Harker1, (4) Harker2, (5) isotopes, and (6) numerical output sheets (Table A1.1).

Table A1.1. Summary of structural features of the program

	Sheets	ENTERING VALUES	CHOSEN PARAMETERS	GRAPHIC OUTPUT
DATA INPUT	PARAMETERS	* Element ordering * Name of fractionating minerals * Partition coefficients * Assimilant values * Normalizing values * Isotopic standards		
	SAMPLES	* Major element oxides (*wt.* %) * Trace element concentrations (ppm) * Isotope ratios		
DATA OUTPUT	MODELING		* Starting composition (C_0) * Assimilant (C_a) * Mixing with (C_b) * Melt composition * Axes of bivariate diagram * "r" value for AFC modeling * Increments of crystallisation * Normative values * Buttons to show any points and vectors on diagrams	* Bivariate diagram * REE-spider diagram * Multi-element spider diagram
	CLASSIFICATION		* Major element oxides can be shown on hydrous or anhydrous basis	* Bivariate diagrams
	HARKERS1			* Bivariate diagrams
	HARKERS2		* Buttons to show any group on diagrams	* Bivariate diagrams
	ISOTOPES		* Buttons to show any group on diagrams	* Bivariate diagrams
	NUMERICAL OUTPUT	Allows the user to get the tables of using parameters (FC, AFC and mixing results and bulk partition coefficients)		

The "parameters" sheet contain some tables that allow selection of (a) the elements (and isotopes) that will be used in modeling, (b) the fractionating minerals, (c) the partition coefficient (*Kd*) dataset that has been prepared for acidic, intermediate and basic melt compositions, (d) the assimilant rock compositions to be

used in AFC and FCA modeling, (e) the normalizing rock compositions to be used in rare earth element (REE)- and multi-element spider diagrams, and (f) the isotopic standard values (Table A1.1). In order to provide some useful facilities to the users, several elements, on the basis of their common utilization, have already been entered into the present program. Many published *Kd* values, assimilant [upper, bulk and lower continental crust values and normalizing rock compositions [Enriched type- and Normal type-Mid Oceanic Ridge Basalts (E-MORB and N-MORB), Primitive Mantle (PM) and C1-Chondrite values] which are frequently used, have also been entered on these tables. Users can only change these and other parameters which are only placed in uncolored cells.

The "samples" sheet contains 10 dataset tables each has 20 sample columns. In these tables, the element columns are filled with element symbols according to the order that are already entered in the "parameters" sheet. Names of datasets for each of the 20 samples and numbers of the samples are entered into the "dataset" and "sample#" lines, respectively. The names of the datasets and the sample numbers are linked to the related places in the other sheets. In these tables Fe_2O_3 values (as total) should be entered as $Fe_2O_{3(total)}$, the program will automatically calculate the FeO values (*FeO wt.% = Fe₂O₃ / 1.11*) for the each sample. In the same way, the Mg# values (Mg# = molar *MgO/[MgO+FeO]*) are automatically calculated. Among the trace elements, such as K, Ti, P (in ppm) values are also calculated using their major oxide values (in *wt*. %). The grey colored cells in which the automatically calculated values are placed, can not be changed by the users. The Eu/Eu* values and some isotopic parameters such as εSr, εNd, and τ_{DM}^{Nd} values are also calculated automatically by the program. These values can also be shown and modeled on the bivariate diagram located in the "modeling" sheet. The major element values are recalculated on the basis of water-free results in the tables placed just below each of the datasets. Each dataset table contains "min", "max" and "mean" columns in which the minimum, maximum and mean values of the samples are shown for each element, isotope and the other values.

The "modeling" sheet is the major panel of the program and contains two sections. The first models a bivariate diagram of which axes can be selected, whilst the second models the REE- and multi element-spider diagrams. In the first section, several parameters controlling the model curves (such as starting composition, assimilant material, the material mixing with the starting composition, fractionating phase, melt composition, "r" value for AFC and FCA models, increments for model curves and axes of the bivariate diagram) are changed and/or chosen. Firstly, the axes of the bivariate diagram are chosen by aid of three combo-boxes for each axis. For example, in order to set a Sr (on x-axis) versus Ba/Sr (on y-axis) diagram, "Sr" is selected from the first combo-box on the x-axis panel and the second combo-box remains blank; "Ba", "/" and "Sr" are correspondingly selected from the third combo-box on the y-axis panel. The axes can also be set as linear- or logarithmic-scales by aid of the buttons on the x- and y-axis panels. The sample groups (namely datasets on the "samples" sheet) which are needed to be shown on the diagram are clicked on the right-side of the diagram, so that the samples belonging to the selected groups will appear on the diagram.

The combo-box that is used to select the starting composition simultaneously lists the sample numbers already entered in the "sample" sheet. The program uses this selected sample as starting composition (C_0) in calculations of FC, AFC, FCA and mixing models [Eqs. (3), (4), (7), (8) and (9)]. The combo-box of assimilant lists the entered materials onto the assimilant table in the "parameters" sheet. Selected assimilant material is used in AFC and FCA equations as assimilant (C_a). Fractionating phases are entered as their mass ratios in the "fractionating phases" table. The sum of the ratios of the fractionating phases must be 100%. The bulk partition coefficient (Eq. 2) is calculated according these mineral ratios. The melt composition combo-box allows the user to select any melt composition, such as acidic, intermediate or basic for their partition coefficient data sets. This selection changes the partition coefficients (Kd) of an element in a mineral for different melt compositions. The "r-value" panel allows the users set the ratio of fractionating material to assimilated materials in the AFC and FCA models (r; Eq. 5). The r-value can be selected in a range of 0–0.9. In the AFC equations, a "0" value of "r" would

give raise to an AFC trajectory identical to the FC trajectory. The "increment" panel set the F values (fraction of melt remaining) in the FC, AFC and FCA equations. Increments can be in the range of 1%–11%. If it is set to 1%, then crystallization start at 1% and reaches up to 9% (namely, F= 0.99, 0.98 ... 0.91) with 1% increments. In the same way, if the increment button is 10%, then crystallization start at 10% and reaches up to 90% (F: 0.90, 0.80 ... 0.10) with 10% increments. Several buttons are designed to show (or hide) the trajectories of any modeling results, which are placed in the bottom of the right-side of the first section on the "modeling" sheet. The assimilant material (C_a), the minimum value of melt fraction (namely maximum value of crystallization) and the starting composition (C_0) are shown arbitrarily on the bivariate diagram. When needed, the bivariate diagram can be exported as a GIF file. The button of "export graphic" on the diagram allows the users to export the diagram; by clicking on this button a window appears on the screen, on which the name of the diagram can be entered. The GIF file is saved to the folder in which the program is located. A useful feature of the program is that the isotopic compositions of the rock samples can also be modeled on the basis of AFC, FCA and mixing equations.

The second section on the "modeling" sheet is used to construct the REE- and multi element-spider diagrams. These diagrams show the trace element compositions which are normalized to certain materials, such as Normal-type Mid Ocean Basalts (N-MORB) and Chondrites. The normalizing material can also be selected by a combo-box labeled as "normalizing factor". The user can also enter any normalizing factor to the "parameters" sheet. The element orders of the REE diagram on the x-axis begins with La and ends with Lu, which is the ordering of the lanthanides on the periodic table of the elements. On the other hand, the multi-element spider diagram is arranged according to the frequently used element orders of relative compatibility in the literature. The other factors and parameters can also be selected as summarized above. The users can also export these diagrams as GIF files.

The FC-AFC-FCA and mixing modeler can plot some classification and nomenclature diagrams that are frequently used in magmatic petrology. In the "classification" sheet some diagrams have been designed for classification and comparison of the magmatic groups: (1) total alkali–silica (TAS) plot of Le Bas et al. (1986), on which the alkaline–subalkaline line is shown according to Irvine & Baragar (1971); (2) K_2O versus SiO_2 plot with IUGS fields after LeMaitre (2002); (3) total alkali–silica (TAS) plot of Cox et al. (1979); (4) Na_2O versus K_2O plot of Peccerillo & Taylor (1976), Ta/Yb versus Th/Yb plot of Pearce (1983); and Y (ppm) versus Sr/Y plot of Castillo (2006). In this sheet, the rock groups can be selected to be shown on any diagram with the aid of the related buttons. These diagrams can use the water-free major element results which are already calculated on the "sample" sheet. Similarly, "Harkers1" and "Harkers2" sheets allow the users to plot the SiO_2-dependent major and trace element variations of the samples. The program also plots the diagrams using Sr, Nd and Pb isotopes on the "isotopes" sheet.

A1.4 Conclusions

The FC-AFC-FCA and mixing modeler is a Microsoft® Excel© spreadsheet program designed on the basis of already proposed magmatic differentiation equations for crystal fractionation, assimilation and mixing processes in magmatic systems. The results of geochemical analyses of magmatic rocks can easily be transferred to the program. The program also has the advantage that the user can output the graphical and/or numerical results of fractional crystallization (FC), combined assimilation and fractional crystallization (AFC), decoupled assimilation and fractional crystallization (FCA) and mixing processes in addition to several geochemical parameters. The program allows the users to change the several parameters and to see the different modeling results on the same diagram. The graphical results of any modeling can be exported and saved as a GIF file. The numerical results can also be taken into tables.

Appendix 2
Analytical Techniques

Seventy-eigth volcanic rock samples collected from the region were prepared by standard preparation techniques for major and trace element contents, and Sr, Sm-Nd, Pb and O isotope analyses at Dokuz Eylül University sample preparation laboratory. Rock powders of the selected fresh samples were prepared by removing the altered surfaces and powdering with a tungsten carbide shatter box. The $^{87}Sr/^{86}Sr$ and $^{143}Nd/^{144}Nd$ analyses were performed at Middle East Technical University Central Laboratory (METU, Ankara, Turkey) and at University of Southampton Isotope Geochemistry Laboratory (United Kingdom). The O and Sm-Nd isotope analyses were performed at Activation Laboratories Ltd. (Actlabs, Canada). Lead isotope analyses are performed at University of Southampton and Actlabs.

A2.1 Sr and Nd isotope analyses at METU and Southampton

Twenty-nine $^{87}Sr/^{86}Sr$ and twenty-seven $^{143}Nd/^{144}Nd$ isotope analyses were carried out at METU and Southampton. The samples were not leached before analysis, as they do not show any evidence of alteration or secondary minerals. Sr-Nd isotopic analyses from these samples are in close agreement with published data.

The analyses carried out at METU were conducted using procedures similar to those described by Romer et al. (2001). Isotope ratios were measured using a Triton Multi-Collector Thermal Ionization Mass Spectrometer (TIMS). Powdered samples (ca. 80 mg) were weighed and transferred into teflon perfluoroalkoxy vials. Samples were leached with 4 ml of 52% HF for four days at 160 °C on the hot plate. Digested samples were dried and then dissolved overnight in 4 mL of 6 N HCl at 160 °C on the hot plate. Leaching and drying were done on teflon hot plates within laminar flow hotboxes.

Sr was separated in 2.5 N HCl medium using 12 mL Bio Rad poly-propylene columns with 2 mL Bio Rad AG50 W-X12, 100–200 mesh resin. Sr was loaded on single Re-filaments with Ta-activator and 0.005 N H_3PO_4 and its isotopic composition was determined by using static multi-collection. Analytical uncertainties are given at 2δ level. During the course of the measurement Sr standard NIST SRM 987 was measured as 0.710247±10 (n= 3) that is within the error of the accepted value of this standard.

A REE fraction was collected from the cation exchange columns with 6 N HCl after Sr was separated. Nd was separated from the REE fraction in a 0.022 N HCl medium using 12 mL Bio Rad poly-propylene columns with 2 ml biobeads (Bio Rad) coated with HDEHP (bisethyexyl phosphate). Nd was loaded on double Re-filaments with 0.005 N H_3PO_4 and its isotopic composition was determined by using static multicollection. Measurement of the Nd La Jolla standard gave a value of 0.511846±5 (n=3) that is within the accepted error range for this standard. No corrections were applied to Nd and Sr isotopic compositions for instrumental bias.

At Southampton, Sr-Nd isotope ratios were determined using methods described in Ishizuka et al. (2007). Measured values for NBS SRM-987 and JNdi-1 were $^{87}Sr/^{86}Sr = 0.710246 \pm 14$ (n=4) and $^{143}Nd/^{144}Nd = 0.512110 \pm 11$ (n=18). In both labs, isotope ratios are normalized to $^{86}Sr/^{88}Sr$ of 0.1194 and $^{146}Nd/^{144}Nd$ of 0.7219.

A2.2 Sm-Nd isotope analyses at Actlabs

Nine ^{147}Sm-^{144}Nd isotope analyses were carried out by TIMS in ACTLABS (Canada). The analytical procedures for the Sm and Nd isotopic analyses of the rock samples by TIMS are as follows. Rock powders for Sm-Nd studies were dissolved in a mixture of HF, HNO_3 and $HClO_4$. Before the decomposition, all samples were totally spiked with ^{149}Sm-^{146}Nd mixed solution. REE were separated using conventional cation-exchange techniques. Sm and Nd were separated by extraction chromatography on HDEHP covered teflon powder. Total blank are 0.1-0.2 ng for

Sm and 0.1-0.5 ng for Nd. Accuracy of the measurements of Sm, Nd contents - ±0.5%, ^{147}Sm/^{144}Nd - ±0.5% (2s). ^{143}Nd/^{144}Nd ratios are relative to the value of 0.511860 for the La Jolla standard. During the period of work the weighted average of 10 La Jolla Nd-standard runs yielded 0.511874±10 (2s) for ^{143}Nd/^{144}Nd, using 0.7219 for ^{146}Nd/^{144}Nd to normalize. Analysis was performed on Triton-MC mass-spectrometer.

A2.3 O isotope analyses at Actlabs

Eighteen oxygen isotope analyses on the representative samples have been carried out at ACTLABS Laboratory, Canada. In order to measure the δ^{18}O compositions of the lavas, the pulped samples are reacted with BrF5 at ~650°C in nickel bombs following the procedures described in Clayton and Mayeda (1963). The fluorination reaction converts O in the mineral(s) to O_2 gas, which is subsequently converted to CO_2 gas using a hot C rod. All reaction steps are quantitative. Isotopic analyses are performed on a Finnigan MAT Delta, dual inlet, isotope ratio mass spectrometer. The data are reported in the standard delta notation as per mil deviations from V–SMOW. External reproducibility is ± 0.19‰ (1s) based on repeat analyses of our internal white crystal standard (WCS). The value for NBS 28 was 9.61 ±0.10‰ (1s).

A2.3 Pb isotope analyses at Actlabs and Southampton

Fifteen lead isotope analysis were carried out at ACTLABS (Canada) and University of Southampton. Pb was separated using the ion-exchange technique with Bio-Rad 1x8. Pb isotope compositions were analyzed on Finnigan MAT–261 multicollector mass spectrometer. The measured Pb isotope ratios were corrected for mass fractionation calculated from replicate measurements of Pb isotope composition in NBS SRM–982 standards. External reproducibility of Pb isotope ratios- ^{206}Pb/^{204}Pb=0.1%, ^{207}Pb/^{204}Pb=0.1%, ^{208}Pb/^{204}Pb=0.2% - on the 2σ level has been demonstrated through multiple analyses of standard BCR-1.

Appendix 3

Major and Trace Element Results

Major element oxides are in *wt.%* and trace elements are in *ppm*.

Sample	861	860	702	756	701	718	719	720
Unit	Güneşli volcanites	Güneşli volcanites	Kayacık volcanites	Kayacık volcanites	Kayacık volcanites	Sevinçler volcanites	Sevinçler volcanites	Sevinçler volcanites
Classification	rhyolite	rhyolite	rhyolite	dacite	dacite	dacite	rhyolite	dacite
Affinity	HK-CA	HK-CA	HK-CA	HK-CA	MK-CA	HK-CA	MK-CA	HK-CA
Basin	Gördes	Gördes	Gördes	Gördes	Gördes	Demirci	Demirci	Demirci
AGE	EM	EM	EM	EM	EM	EM	EM	EM
References	1	1	1	1	1	1	1	1
SiO_2	77.83	78.26	70.16	64.76	64.83	66.58	68.81	66.62
Al_2O_3	11.64	11.82	14.39	15.42	14.73	15.10	12.55	15.09
Fe_2O_3	0.53	0.32	2.92	3.78	4.03	3.69	1.47	3.70
MgO	0.02	0.03	1.13	2.32	2.62	1.24	0.61	1.01
CaO	0.32	0.40	2.62	3.71	4.12	3.17	2.32	3.04
Na_2O	1.65	2.26	2.97	3.05	2.72	2.97	3.09	3.11
K_2O	5.98	5.54	3.98	3.23	2.86	4.12	2.27	3.86
TiO_2	0.06	0.06	0.34	0.49	0.50	0.50	0.28	0.51
P_2O_5	0.01		0.07	0.10	0.11	0.15	0.12	0.13
MnO			0.06	0.08	0.06	0.06	0.05	0.06
LOI	1.90	1.30	1.10	3.00	3.20	2.20	8.00	2.60
Mg#	6.96	15.66	43.40	54.87	56.30	39.97	45.12	35.10
Cs	21.70	15.10	7.50	5.20	5.00	7.30	35.90	6.30
Rb	191.40	200.70	140.30	114.70	103.20	138.80	100.70	141.60
Ba	164.00	158.00	665.00	712.00	691.00	971.00	1224.00	1008.00
Sr	31.80	31.10	236.30	327.60	365.30	331.20	380.50	320.70
Pb	8.70	3.60	7.00	8.10	2.50	3.10	26.40	9.80
Th	30.40	33.00	20.00	14.80	13.60	21.80	18.50	20.00
U	5.20	6.90	5.30	5.00	4.30	6.80	6.70	4.60
Zr	80.40	82.30	129.60	140.70	135.80	303.10	141.30	196.00
Hf	3.20	3.30	4.30	4.00	4.20	7.20	4.10	5.70
Ta	1.20	1.40	0.50	1.10	0.10	0.30	1.30	0.20
Y	15.70	18.80	25.70	24.80	22.40	25.40	21.20	24.60
Nb	13.40	14.70	11.50	12.20	10.50	13.40	13.40	13.10
Sc	2.00	2.00	8.00	12.00	12.00	9.00	5.00	8.00
Cr			54.74	41.06	54.74			
Ni	0.70	1.00	4.80	10.90	16.20	3.20	2.00	3.00
Co	13.10	22.40	62.20	42.00	26.70	105.50	139.70	34.10
V			42.00	82.00	88.00	100.00	25.00	96.00
La	29.10	26.10	35.10	31.20	32.40	33.40	29.20	42.80
Ce	46.50	47.20	62.80	59.90	54.30	58.50	56.60	73.30
Pr	6.56	6.12	6.93	6.62	6.23	6.64	6.34	7.94
Nd	21.80	20.20	25.20	24.50	22.10	23.60	23.20	28.40
Sm	4.20	4.13	4.80	4.66	4.25	4.58	4.12	4.58
Eu	0.33	0.29	0.79	0.93	0.97	1.01	0.74	1.04
Gd	3.36	3.40	4.43	4.24	3.98	4.41	3.59	4.40
Tb	0.55	0.58	0.75	0.73	0.68	0.73	0.61	0.69
Dy	3.07	3.26	3.98	4.18	3.55	4.18	3.41	3.76
Ho	0.56	0.64	0.83	0.86	0.76	0.84	0.71	0.81
Er	1.55	1.85	2.33	2.33	2.11	2.43	2.06	2.33
Tm	0.26	0.30	0.40	0.37	0.35	0.41	0.34	0.40
Yb	1.75	2.03	2.47	2.53	2.23	2.54	2.04	2.39
Lu	0.26	0.31	0.40	0.37	0.34	0.42	0.33	0.40

Sample	721	744	745	815	816	817	704	705
Unit	Sevinçler volcanites	Sevinçler volcanites	Sevinçler volcanites	Akdağ volcanites	Akdağ volcanites	Akdağ volcanites	Asitepe volcanites	Asitepe volcanites
Classification	dacite	rhyolite	dacite	rhyolite	rhyolite	rhyolite	trachyte	andesite
Affinity	HK-CA	HK-CA	HK-CA	MK-CA	MK-CA	HK-CA	HK-CA	HK-CA
Basin	Demirci	Demirci	Demirci	Emet	Emet	Emet	Demirci	Demirci
AGE	EM	EM	EM	EM	EM	EM	MM	MM
References	1	1	1	1	1	1	1	1
SiO_2	66.58	69.03	66.41	73.62	74.15	72.19	60.79	60.23
Al_2O_3	15.08	13.77	15.07	12.77	12.17	13.82	16.94	16.75
Fe_2O_3	3.62	2.37	3.69	2.04	2.08	2.10	6.16	5.95
MgO	1.17	0.64	1.24	0.48	0.43	0.38	1.67	2.79
CaO	3.06	1.82	3.09	2.08	1.98	1.71	5.27	5.67
Na_2O	3.07	2.33	3.17	2.99	2.79	3.37	3.07	3.06
K_2O	3.98	5.01	4.02	3.43	3.53	4.25	2.96	2.94
TiO_2	0.50	0.34	0.51	0.32	0.30	0.31	0.86	0.80
P_2O_5	0.15	0.11	0.15	0.12	0.10	0.08	0.23	0.20
MnO	0.06	0.05	0.07	0.03	0.03	0.03	0.05	0.11
LOI	2.50	4.20	2.30	1.90	2.20	1.40	1.70	1.20
Mg#	39.04	34.85	39.97	31.80	29.06	26.39	34.94	48.16
Cs	7.00	7.30	7.10	8.30	14.40	6.40	4.00	6.80
Rb	139.50	182.70	147.10	102.90	101.70	134.60	98.20	104.60
Ba	1059.00	1402.00	1060.00	1139.00	1195.00	1753.00	989.00	868.00
Sr	324.10	364.20	328.60	346.40	322.50	337.40	526.00	439.60
Pb	2.40	6.40	2.70	4.20	4.50	7.90	8.00	2.80
Th	18.80	29.20	22.30	24.60	25.00	28.30	17.20	15.70
U	6.40	6.50	6.80	4.50	4.80	7.20	4.60	4.60
Zr	192.60	199.10	191.40	148.20	136.10	183.80	184.00	176.70
Hf	6.00	5.70	5.70	4.30	4.20	5.10	5.30	5.20
Ta	0.20	1.20	1.30	1.10	1.10	1.20	0.80	1.00
Y	23.30	24.00	26.60	13.70	14.10	19.80	35.90	26.40
Nb	13.10	15.00	14.60	14.60	12.70	16.30	11.60	12.00
Sc	8.00	5.00	9.00	3.00	2.00	3.00	17.00	17.00
Cr		191.59	177.91				13.69	27.37
Ni	3.20	1.20	3.20	0.90	1.30	1.30	3.60	2.30
Co	52.50	57.80	71.40	13.10	27.60	19.50	46.20	71.70
V	98.00	31.00	68.00	37.00	30.00	30.00	118.00	121.00
La	39.70	50.50	48.10	42.70	39.20	57.40	50.70	38.00
Ce	64.70	90.20	86.60	73.70	67.70	97.70	93.50	71.80
Pr	7.08	9.88	9.51	7.63	7.13	10.23	11.57	8.68
Nd	25.70	34.30	33.60	25.50	23.80	35.20	44.10	32.00
Sm	4.67	5.63	5.76	3.83	3.59	4.84	7.96	6.01
Eu	0.99	0.94	1.07	0.83	0.74	1.02	1.73	1.27
Gd	4.24	4.73	5.02	2.98	2.74	3.75	7.70	5.56
Tb	0.67	0.75	0.77	0.48	0.42	0.58	1.19	0.86
Dy	3.50	4.12	4.34	2.74	2.36	3.28	6.75	4.81
Ho	0.77	0.80	0.91	0.46	0.47	0.66	1.30	0.94
Er	2.14	2.28	2.51	1.44	1.37	1.90	3.43	2.77
Tm	0.41	0.36	0.43	0.23	0.25	0.34	0.56	0.45
Yb	2.34	2.40	2.71	1.47	1.63	2.28	3.57	2.76
Lu	0.39	0.36	0.41	0.23	0.25	0.36	0.50	0.42

Sample	706	709	712	713	714	715	716	717	722
Unit	Asitepe volcanites	Asitepe volcanites	Asitepe volcanites	Asitepe volcanites	Asitepe volcanites	Asitepe volcanites	Asitepe volcanites	Asitepe volcanites	Asitepe volcanites
Classification	andesite	andesite	andesite	andesite	andesite	andesite	andesite	andesite	andesite
Affinity	HK-CA	HK-CA	HK-CA	HK-CA	HK-CA	HK-CA	HK-CA	HK-CA	HK-CA
Basin	Demirci	Demirci	Demirci	Demirci	Demirci	Demirci	Demirci	Demirci	Demirci
AGE	MM	MM	MM	MM	MM	MM	MM	MM	MM
References	1	1	1	1	1	1	1	1	1
SiO_2	62.00	59.83	60.51	59.36	59.51	59.96	58.36	58.85	60.86
Al_2O_3	16.84	16.11	16.99	16.12	16.65	16.94	16.91	16.66	16.65
Fe_2O_3	5.81	6.40	6.12	6.22	6.00	6.33	6.96	6.72	6.25
MgO	1.98	2.64	1.89	3.50	3.10	2.55	3.31	2.92	2.16
CaO	4.95	6.23	5.30	6.49	6.24	5.98	6.38	6.18	5.62
Na_2O	3.13	2.84	3.11	2.62	2.81	3.08	2.96	3.00	2.98
K_2O	2.75	2.57	2.83	2.92	3.02	2.66	2.46	2.52	2.71
TiO_2	0.75	0.76	0.86	0.72	0.81	0.84	0.89	0.86	0.82
P_2O_5	0.20	0.20	0.24	0.19	0.18	0.21	0.20	0.20	0.21
MnO	0.07	0.08	0.06	0.08	0.10	0.10	0.08	0.07	0.07
LOI	1.30	2.10	1.90	1.50	1.30	1.10	1.10	1.70	1.50
Mg#	40.31	44.97	37.96	52.72	50.58	44.39	48.51	46.26	40.64
Cs	3.60	4.00	4.10	5.70	5.40	3.20	4.70	3.20	4.00
Rb	92.20	82.70	95.90	96.60	93.30	87.90	80.30	82.80	93.00
Ba	701.00	717.00	896.00	647.00	759.00	757.00	786.00	780.00	756.00
Sr	399.90	457.40	470.40	433.10	415.00	435.30	449.30	444.00	409.70
Pb	5.50	16.30	6.80	2.00	3.20	10.40	7.20	9.00	7.70
Th	12.40	12.80	17.70	14.50	13.10	12.60	13.60	15.30	14.40
U	3.50	3.90	4.50	4.00	4.00	3.80	3.90	3.70	3.80
Zr	167.10	146.90	187.60	154.20	159.70	163.20	164.90	169.30	183.50
Hf	5.00	4.30	6.10	4.90	4.60	4.80	4.80	5.10	5.00
Ta	0.90	0.90	0.80	0.80	0.80	0.80	0.80	0.80	
Y	26.80	24.80	25.50	26.00	25.30	28.60	30.10	46.50	28.80
Nb	11.10	10.50	11.50	9.40	10.30	10.10	10.00	10.60	10.60
Sc	16.00	23.00	17.00	19.00	19.00	20.00	22.00	20.00	19.00
Cr	27.37	102.64	13.69	68.43	61.58	47.90			
Ni	3.20	10.20	2.90	6.50	4.50	5.60	2.20	3.10	6.00
Co	56.90	46.20	43.70	87.90	68.90	66.00	86.00	62.60	40.70
V	85.00	120.00	114.00	129.00	115.00	110.00	142.00	140.00	137.00
La	37.30	32.60	40.40	31.50	34.80	35.20	33.60	48.10	35.40
Ce	61.60	56.00	72.40	61.70	64.30	62.40	65.40	68.60	60.20
Pr	8.44	7.63	9.54	7.50	7.89	7.99	8.10	10.71	7.25
Nd	30.40	29.50	37.00	27.40	30.10	30.50	31.70	42.20	27.50
Sm	5.67	5.55	6.43	5.24	5.43	5.65	6.18	8.07	5.53
Eu	1.31	1.23	1.47	1.26	1.22	1.28	1.46	1.92	1.31
Gd	5.16	5.16	5.83	4.78	4.87	5.18	5.67	7.97	5.24
Tb	0.86	0.83	0.91	0.80	0.78	0.84	0.95	1.27	0.85
Dy	4.88	4.61	5.00	4.20	4.51	4.86	5.00	6.98	4.45
Ho	0.99	0.91	1.01	0.93	0.93	1.02	1.07	1.54	0.93
Er	2.75	2.58	2.81	2.49	2.57	2.90	3.06	4.31	2.64
Tm	0.43	0.40	0.45	0.42	0.45	0.46	0.43	0.69	0.41
Yb	2.66	2.57	2.67	2.65	2.62	2.91	2.95	4.17	2.58
Lu	0.41	0.36	0.38	0.42	0.40	0.45	0.44	0.66	0.40

Sample	725	752	753	754	755	801	802	804
Unit	Asitepe volcanites	Asitepe volcanites	Asitepe volcanites	Asitepe volcanites	Asitepe volcanites	Köprücek volcanites	Köprücek volcanites	Köprücek volcanites
Classification	andesite	andesite	dacite	dacite	trachydacite	rhyolite	andesite	dacite
Affinity	HK-CA	MK-CA	HK-CA	HK-CA	HK-CA	HK-CA	HK-CA	HK-CA
Basin	Demirci	Demirci	Demirci	Demirci	Demirci	Emet	Emet	Emet
AGE	MM	MM	MM	MM	MM	MM	MM	MM
References	1	1	1	1	1	1	1	1
SiO_2	60.10	61.02	62.36	63.36	63.87	71.14	58.35	67.05
Al_2O_3	16.99	16.74	15.96	15.83	16.52	14.28	16.20	15.63
Fe_2O_3	5.97	6.03	4.87	4.67	4.26	2.54	7.84	4.05
MgO	2.63	1.90	1.56	1.59	1.41	0.39	1.78	0.63
CaO	5.78	5.50	4.80	4.40	4.42	1.77	5.95	3.11
Na_2O	3.03	2.95	2.93	3.04	3.14	3.20	3.49	3.86
K_2O	2.77	2.37	2.78	2.86	3.03	4.60	2.40	3.60
TiO_2	0.89	0.89	0.62	0.62	0.65	0.33	1.29	0.64
P_2O_5	0.21	0.18	0.16	0.16	0.18	0.13	0.37	0.23
MnO	0.09	0.10	0.04	0.07	0.07	0.02	0.11	0.09
LOI	1.30	2.20	3.80	3.30	2.30	1.40	1.90	0.90
Mg#	46.60	38.43	38.83	40.28	39.61	23.33	31.03	23.56
Cs	5.90	3.20	4.70	9.80	6.00	11.00	27.70	8.30
Rb	94.40	74.30	98.40	101.90	106.90	172.70	85.30	121.30
Ba	828.00	579.00	699.00	714.00	712.00	1165.00	972.00	994.00
Sr	471.60	389.10	360.60	350.80	358.30	204.90	491.70	364.20
Pb	4.10	7.10	2.10	3.00	1.50	3.10	7.00	3.90
Th	14.80	9.30	11.70	13.20	13.10	19.80	9.80	16.30
U	4.20	2.50	3.90	4.00	4.20	4.90	2.90	4.30
Zr	186.50	189.30	163.00	164.40	158.90	166.10	192.90	207.20
Hf	5.30	5.60	4.90	4.60	4.50	4.90	5.50	5.90
Ta						1.50	0.70	1.20
Y	28.80	26.90	18.60	22.00	21.30	22.40	30.30	31.10
Nb	10.50	10.90	10.50	10.80	11.00	14.30	12.50	14.40
Sc	18.00	18.00	12.00	13.00	12.00	5.00	23.00	11.00
Cr				41.06				
Ni	2.20	4.60	4.90	2.50	2.50	1.60	2.00	0.80
Co	62.40	48.90	24.80	38.40	36.70	33.60	36.50	34.70
V	150.00	146.00	98.00	97.00	95.00	27.00	231.00	41.00
La	36.20	28.90	31.60	32.80	32.40	40.40	31.30	38.00
Ce	64.20	54.80	56.20	59.60	58.90	73.70	66.20	75.70
Pr	7.69	6.47	6.29	6.76	6.68	8.38	8.45	9.19
Nd	30.20	25.60	24.40	23.10	26.40	29.60	34.20	36.00
Sm	5.94	5.40	4.29	4.62	4.78	5.16	6.81	6.77
Eu	1.32	1.27	1.03	1.10	1.13	0.87	1.63	1.45
Gd	5.38	5.17	3.96	4.39	4.50	4.43	6.36	6.00
Tb	0.88	0.81	0.62	0.66	0.70	0.74	1.02	1.00
Dy	4.46	4.61	3.05	3.41	3.58	3.68	5.65	5.46
Ho	0.97	0.98	0.66	0.74	0.71	0.76	1.11	1.09
Er	2.73	2.58	1.82	2.09	2.05	2.10	2.96	3.17
Tm	0.43	0.42	0.31	0.35	0.37	0.35	0.44	0.48
Yb	2.66	2.58	1.80	2.06	2.05	2.08	2.77	3.01
Lu	0.42	0.38	0.28	0.33	0.32	0.32	0.42	0.46

Sample	805	806	807	846	847	741	742	G2
Unit	Köprücek volcanites	Köprücek volcanites	Köprücek volcanites	Köprücek volcanites	Köprücek volcanites	Karabacaklar volcanites	Karabacaklar volcanites	Karabacaklar volcanites
Classification	dacite	dacite	andesite	andesite	andesite	trachydacite	trachyte	trachydacite
Affinity	HK-CA	HK-CA	HK-CA	HK-CA	HK-CA	SHO	SHO	SHO
Basin	Emet	Emet	Emet	Emet	Emet	Güre	Güre	Güre
AGE	MM	MM	MM	MM	MM	MM	MM	MM
References	1	1	1	1	1	1	1	1
SiO_2	66.97	67.00	59.97	56.12	58.37	62.37	61.90	62.07
Al_2O_3	15.52	15.94	16.88	16.83	16.45	14.83	14.43	14.63
Fe_2O_3	3.97	3.99	5.84	4.95	7.79	3.87	4.51	4.00
MgO	0.62	0.25	1.78	1.35	1.97	1.39	1.43	1.52
CaO	3.13	2.67	5.44	8.20	6.11	1.92	2.58	1.88
Na_2O	3.88	3.89	3.42	3.29	3.43	1.92	2.61	1.75
K_2O	3.62	3.81	2.77	2.43	2.40	6.88	6.82	6.55
TiO_2	0.64	0.64	1.01	1.06	1.29	1.17	1.15	1.14
P_2O_5	0.22	0.21	0.34	0.42	0.36	0.85	0.86	0.87
MnO	0.08	0.03	0.07	0.14	0.11	0.01	0.18	0.01
LOI	1.10	1.30	2.20	4.90	1.40	4.50	3.10	5.10
Mg#	23.63	11.04	37.65	35.08	33.38	41.58	38.58	42.95
Cs	8.60	31.00	24.10	34.00	31.10	91.10	66.60	64.60
Rb	120.60	140.10	101.40	214.60	82.40	295.50	258.20	302.80
Ba	983.00	960.00	777.00	838.00	982.00	1377.00	1393.00	1554.70
Sr	351.20	354.30	465.30	505.10	520.20	658.70	727.90	628.50
Pb	3.50	2.50	8.50	1.30	9.80	2.50	2.10	4.00
Th	15.40	15.70	11.20	9.40	10.40	17.30	17.00	18.40
U	4.40	4.90	3.70	3.30	3.10	6.50	6.50	6.60
Zr	201.30	213.80	181.10	179.40	200.90	576.30	556.00	605.50
Hf	6.00	6.00	5.10	4.80	5.60	16.80	17.20	17.70
Ta	1.20	1.10	0.90	0.90	0.90	1.50	1.40	1.70
Y	31.40	35.00	30.00	32.80	30.50	21.60	25.50	23.80
Nb	14.80	14.60	12.50	12.40	12.80	25.40	25.20	24.20
Sc	11.00	11.00	17.00	17.00	23.00	9.00	11.00	9.00
Cr						198.43	198.43	184.75
Ni	0.70	2.70	1.80	0.90	2.00	60.80	34.00	89.00
Co	21.60	30.80	35.80	24.80	27.80	18.00	38.30	32.90
V	39.00	30.00	130.00	109.00	238.00	99.00	110.00	92.00
La	37.60	46.80	33.40	32.10	31.20	47.00	43.20	54.50
Ce	74.60	82.00	67.50	66.10	65.60	97.30	90.10	111.90
Pr	9.14	11.61	8.33	8.39	8.45	12.21	11.12	14.05
Nd	35.30	45.00	33.40	36.90	36.70	47.60	44.50	51.70
Sm	6.49	7.91	6.32	6.49	6.77	8.47	7.83	10.30
Eu	1.37	1.56	1.47	1.55	1.72	1.92	1.87	2.03
Gd	5.83	6.91	5.88	6.08	6.43	6.40	6.20	6.76
Tb	0.98	1.11	0.95	1.01	1.06	0.87	0.88	0.84
Dy	5.56	6.36	5.30	5.56	6.11	4.25	4.45	4.72
Ho	1.08	1.15	1.03	1.10	1.11	0.70	0.81	0.78
Er	2.99	3.26	2.89	3.15	3.15	1.84	2.22	2.02
Tm	0.49	0.49	0.44	0.48	0.48	0.25	0.36	0.27
Yb	3.03	3.16	2.81	2.96	2.91	1.69	2.16	1.67
Lu	0.48	0.47	0.42	0.44	0.44	0.23	0.31	0.22

Sample	743	747	748	749	750	751	820	821
Unit	Karabacaklar volcanites	Naşa basalt	Naşa basalt	Naşa basalt	Naşa basalt	Naşa basalt	Kestel volcanites	Kestel volcanites
Classification	trachyte	latite	shoshonite	latite	latite	latite	latite	latite
Affinity	SHO	SHO	SHO	SHO	SHO	SHO	SHO	UK
Basin	Güre	Demirci	Demirci	Demirci	Demirci	Demirci	Emet	Emet
AGE	MM	MM	MM	MM	MM	MM	EM	EM
References	1	1	1	1	1	1	1	1
SiO_2	61.24	54.91	53.13	53.35	54.68	54.53	56.43	52.54
Al_2O_3	15.37	15.58	15.55	15.53	15.74	15.44	16.46	13.63
Fe_2O_3	3.91	7.13	7.05	6.72	7.16	7.17	6.26	6.25
MgO	1.56	4.47	4.42	4.24	3.88	4.06	2.57	4.87
CaO	2.27	6.66	7.38	7.13	7.15	7.40	6.37	8.63
Na_2O	2.32	2.94	2.94	2.89	2.94	3.05	2.68	2.53
K_2O	7.00	4.57	3.97	4.44	4.21	4.15	4.63	5.87
TiO_2	1.20	1.22	1.13	1.19	1.20	1.20	1.10	1.68
P_2O_5	0.92	0.71	0.65	0.68	0.66	0.65	0.58	0.56
MnO	0.01	0.13	0.08	0.09	0.13	0.13	0.10	0.09
LOI	3.90	1.20	3.30	3.40	1.80	1.70	2.50	2.90
Mg#	44.15	55.40	55.40	55.56	51.78	52.87	44.85	60.69
Cs	15.50	3.40	2.70	1.80	3.60	3.20	10.30	7.60
Rb	242.70	162.60	116.50	137.30	159.70	152.10	186.40	292.30
Ba	1571.00	1257.00	1298.00	1200.00	1290.00	1285.00	1180.00	437.00
Sr	675.10	718.20	759.50	745.50	676.20	694.80	655.50	695.30
Pb	4.50	4.90	7.30	5.60	4.30	5.60	6.40	0.90
Th	18.40	13.60	13.60	15.50	13.80	14.00	20.50	10.80
U	7.10	4.50	4.10	4.20	4.70	4.60	5.80	4.90
Zr	575.70	481.90	427.60	456.20	480.30	478.50	299.40	502.70
Hf	17.40	12.90	11.20	12.70	12.90	12.40	8.20	14.20
Ta	1.60	1.70	1.50	1.60	1.70	1.60	1.20	1.90
Y	19.70	33.70	32.10	30.20	35.90	35.10	24.90	23.10
Nb	26.40	29.50	28.50	29.50	30.20	30.70	18.00	31.80
Sc	9.00	19.00	18.00	17.00	19.00	19.00	17.00	17.00
Cr	225.80							
Ni	65.20	54.90	47.20	65.90	56.50	58.60	3.10	89.50
Co	29.70	46.10	32.50	36.40	49.00	54.70	28.70	41.50
V	102.00	157.00	149.00	148.00	153.00	156.00	169.00	166.00
La	43.50	65.40	67.90	65.00	66.20	67.40	40.20	52.10
Ce	89.10	132.80	132.80	132.80	136.30	138.60	85.60	116.10
Pr	10.82	15.85	16.07	16.00	16.64	16.85	10.61	15.26
Nd	41.10	61.50	62.30	60.30	64.30	63.40	42.20	62.20
Sm	7.53	10.29	10.21	9.81	10.72	10.81	7.42	9.97
Eu	1.83	2.24	2.33	2.22	2.39	2.41	1.65	2.14
Gd	5.97	8.04	8.10	7.96	9.02	8.64	5.93	6.95
Tb	0.81	1.15	1.16	1.10	1.24	1.23	0.87	0.91
Dy	4.06	6.24	6.18	5.48	6.47	6.55	4.81	4.61
Ho	0.68	1.20	1.15	1.09	1.26	1.29	0.90	0.80
Er	1.78	3.15	3.10	2.93	3.43	3.38	2.35	2.10
Tm	0.23	0.48	0.48	0.45	0.54	0.53	0.38	0.32
Yb	1.48	3.03	2.97	2.86	3.35	3.34	2.31	1.95
Lu	0.22	0.46	0.46	0.43	0.51	0.51	0.34	0.29

Sample	841	844	845	843	Z1	G3-1	G3-2	839
Unit	Kestel volcanites	Kestel volcanites	Kestel olcanics	Kestel volcanites	Kıran-Zahman basalts	Kıran-Zahman basalts	Kıran-Zahman basalts	Kıran-Zahman basalts
Classification	latite	shoshonite	shoshonite	latite	latite	latite	latite	shoshonite
Affinity	HK-CA	UK-L	UK-L	UK	SHO	UK	UK	UK
Basin	Emet	Emet	Emet	Emet	Güre	Güre	Güre	Güre
AGE	EM	EM	EM	EM	MM	MM	MM	MM
References	1	1	1	1	1	1	1	1
SiO_2	55.77	51.72	52.61	52.38	55.39	54.20	53.98	53.20
Al_2O_3	15.75	13.80	13.90	13.52	16.16	12.49	12.37	14.46
Fe_2O_3	6.05	6.70	6.80	6.77	4.31	6.17	6.26	7.01
MgO	1.72	6.18	5.98	6.20	2.87	5.09	5.17	6.03
CaO	6.18	8.23	7.96	6.60	6.05	6.06	6.08	7.12
Na_2O	2.52	2.75	2.69	2.22	2.51	2.08	1.96	2.38
K_2O	4.65	5.17	5.36	6.12	6.13	6.14	6.25	5.51
TiO_2	0.94	1.66	1.66	1.76	1.84	2.06	2.05	1.51
P_2O_5	0.50	0.58	0.59	0.54	0.73	0.74	0.74	0.68
MnO	0.11	0.10	0.11	0.11	0.04	0.06	0.06	0.11
LOI	5.50	2.70	1.90	3.40	3.50	4.40	4.70	1.50
Mg#	36.03	64.63	63.53	64.47	56.88	62.04	62.07	63.02
Cs	12.60	24.10	20.50	4.10	29.50	13.60	10.80	3.40
Rb	192.90	161.50	181.00	295.70	207.90	202.80	191.20	170.90
Ba	1154.00	502.00	514.00	387.00	1172.20	670.90	683.30	1257.00
Sr	621.70	718.00	736.40	531.80	671.30	672.20	663.40	686.00
Pb	2.90	0.30	0.30	0.20	2.10	0.70	0.70	1.50
Th	20.90	10.20	9.90	9.70	16.00	21.90	21.30	14.90
U	5.90	4.80	4.80	4.50	3.70	5.50	5.70	4.00
Zr	276.30	478.10	477.00	496.60	566.20	942.90	940.40	509.80
Hf	7.60	13.60	12.60	14.00	16.60	26.70	27.60	13.70
Ta	1.10	1.90	1.90	2.00	2.20	3.60	3.60	1.80
Y	23.80	22.70	27.10	22.10	27.30	25.20	25.40	24.50
Nb	17.00	31.20	30.40	30.50	32.00	51.30	51.40	30.20
Sc	14.00	16.00	17.00	18.00	22.00	17.00	17.00	19.00
Cr		218.96	218.96	273.70	328.44	458.45	458.45	328.44
Ni	3.60	74.20	91.30	79.90	64.20	220.60	218.10	122.30
Co	23.20	32.10	36.10	39.20	23.70	28.80	27.70	46.50
V	143.00	173.00	164.00	163.00	163.00	138.00	135.00	162.00
La	39.40	51.50	55.80	50.60	70.80	92.00	94.30	62.10
Ce	82.30	113.80	118.10	113.20	150.50	202.20	200.60	131.60
Pr	10.08	14.82	15.60	14.92	18.59	24.47	25.10	16.24
Nd	39.60	60.40	63.20	61.90	67.10	85.30	84.50	63.30
Sm	6.88	9.79	10.31	9.85	12.40	13.50	13.50	9.87
Eu	1.54	2.12	2.19	2.05	2.71	2.80	2.82	2.18
Gd	5.62	6.58	7.23	6.56	7.93	7.45	6.99	7.16
Tb	0.84	0.89	0.97	0.87	1.10	1.25	1.15	0.97
Dy	4.46	4.22	4.74	4.25	5.43	5.30	5.28	4.55
Ho	0.83	0.77	0.85	0.75	0.90	0.91	0.87	0.85
Er	2.29	2.12	2.47	1.97	2.54	2.20	2.15	2.22
Tm	0.36	0.32	0.35	0.30	0.35	0.30	0.34	0.34
Yb	2.21	1.92	2.13	1.86	2.09	1.92	1.86	2.12
Lu	0.34	0.29	0.32	0.27	0.34	0.28	0.29	0.31

Sample	732	733	734	736	737	822	810	811
Unit	Kıran-Zahman basalts	Kıran-Zahman basalts	Kıran-Zahman basalts	Ilıcasu lamproite	Ilıcasu lamproite	Güre lamproite	Dereköy Basalt	Dereköy Basalt
Classification	latite	latite	latite	latite	latite	shoshonite	shoshonite	latite
Affinity	UK	UK	UK	UK-L	UK-L	UK-L	UK	UK
Basin	Güre	Güre	Güre			Güre	Emet	Emet
AGE	MM	MM	MM	MM	MM	MM	MM	MM
References	1	1	1	1	1	1	1	1
SiO_2	52.82	52.69	51.67	54.90	54.28	50.27	51.03	52.11
Al_2O_3	12.54	12.39	12.23	10.52	10.46	10.85	13.13	13.42
Fe_2O_3	6.52	6.55	6.32	6.16	6.06	7.06	6.70	6.55
MgO	4.76	8.10	7.15	9.61	9.34	9.82	4.80	5.25
CaO	5.93	5.95	6.45	4.10	4.18	6.39	9.15	7.81
Na_2O	1.96	2.20	1.76	1.65	1.51	1.52	2.28	2.39
K_2O	5.73	6.48	6.04	7.25	7.16	5.40	5.60	5.63
TiO_2	1.88	1.78	1.76	1.57	1.56	1.40	1.66	1.69
P_2O_5	0.73	0.77	0.72	1.16	1.18	0.57	0.54	0.53
MnO	0.06	0.11	0.10	0.09	0.09	0.11	0.08	0.10
LOI	6.60	2.30	5.30	2.20	3.40	6.10	4.70	4.10
Mg#	59.12	71.02	69.15	75.56	75.33	73.37	58.67	61.36
Cs	10.90	11.90	3.80	76.70	6.20	8.50	8.70	11.50
Rb	158.50	306.70	167.90	240.20	260.70	267.70	220.10	218.00
Ba	652.00	726.00	696.00	1717.00	1730.00	293.00	485.00	573.00
Sr	665.60	701.70	681.30	920.70	955.20	484.70	547.30	557.20
Pb	1.30	0.60	1.30	6.10	12.50	0.20	1.20	1.40
Th	20.20	28.20	27.70	13.20	14.00	23.70	9.70	11.10
U	4.40	5.90	6.00	5.90	4.80	5.40	4.20	4.50
Zr	894.10	901.50	870.40	739.30	736.50	482.50	468.10	468.20
Hf	26.40	26.50	26.10	22.40	21.10	14.60	13.40	13.50
Ta	3.20	3.30	3.40	2.20	2.30	2.20	1.70	1.70
Y	25.50	23.90	23.80	29.20	29.20	20.70	21.20	21.60
Nb	57.00	59.30	57.10	41.20	45.90	34.90	28.90	29.50
Sc	18.00	19.00	18.00	16.00	16.00	18.00	17.00	17.00
Cr				270.80	243.40	622.67	287.39	287.39
Ni	209.80	302.70	298.40	51.60	43.00	199.60	92.40	99.50
Co	24.90	52.70	42.50	137.00	133.00	48.00	35.70	42.20
V	155.00	158.00	149.00	137.00	133.00	136.00	154.00	152.00
La	88.80	98.90	101.00	53.40	50.50	51.00	48.90	49.80
Ce	188.90	208.20	208.30	120.30	113.30	128.10	107.50	109.50
Pr	23.18	25.03	25.01	16.03	14.93	16.96	14.25	14.32
Nd	85.40	89.20	91.20	67.20	62.20	64.50	58.60	58.40
Sm	12.53	12.72	13.06	11.97	11.08	9.35	9.50	9.43
Eu	2.74	2.65	2.60	2.58	2.51	1.87	2.02	2.02
Gd	8.87	8.72	8.81	8.82	8.69	6.49	6.40	6.34
Tb	1.06	1.04	1.03	1.16	1.21	0.85	0.84	0.84
Dy	5.02	4.70	4.82	5.64	5.75	4.10	4.30	4.25
Ho	0.86	0.78	0.81	1.07	0.98	0.72	0.71	0.74
Er	2.07	2.00	1.93	2.55	2.54	1.89	1.87	2.01
Tm	0.30	0.29	0.28	0.35	0.35	0.28	0.30	0.30
Yb	1.91	1.90	1.89	2.26	2.27	1.68	1.91	1.89
Lu	0.27	0.26	0.26	0.40	0.32	0.25	0.27	0.27

Sample	812	850	851	852	853	726	727	728
Unit	Dereköy Basalt	Gölcük basalt	Gölcük basalt	Gölcük basalt	Gölcük basalt	Taşokçular basalt	Taşokçular basalt	Taşokçular basalt
Classification	latite	Shoshonite	Shoshonite	Shoshonite	Shoshonite	Shoshonite	Shoshonite	Shoshonite
Affinity	UK	CA	CA	CA	CA	SHO	SHO	SHO
Basin	Emet	Bigadiç	Bigadiç	Bigadiç	Bigadiç	Demirci	Demirci	Demirci
AGE	MM	EM	EM	EM	EM	LM	LM	LM
References	1	1	1	1	1	1	1	1
SiO_2	51.95	52.15	49.95	50.19	53.20	49.48	50.50	51.31
Al_2O_3	13.24	17.44	16.01	16.06	17.30	16.55	16.87	17.10
Fe_2O_3	6.64	8.09	7.65	7.53	8.13	8.37	7.89	7.89
MgO	5.38	3.52	7.91	7.92	2.86	4.44	4.31	4.27
CaO	8.21	8.06	7.69	7.57	7.81	8.02	6.97	6.91
Na_2O	2.33	3.59	2.90	2.91	3.52	3.61	3.74	3.58
K_2O	5.82	2.19	2.06	2.05	2.23	3.16	2.99	3.28
TiO_2	1.66	1.15	0.99	1.00	1.14	2.24	2.12	2.09
P_2O_5	0.55	0.46	0.41	0.42	0.46	0.69	0.67	0.68
MnO	0.08	0.09	0.13	0.13	0.08	0.14	0.13	0.12
LOI	3.70	2.90	3.80	3.80	2.90	2.90	3.30	2.40
Mg#	61.62	46.30	67.20	67.57	41.07	51.24	51.98	51.74
Cs	2.70	5.20	11.10	9.90	4.90	2.60	3.50	2.40
Rb	280.30	42.00	54.70	55.70	46.80	86.30	69.70	91.60
Ba	422.00	1027.00	1003.00	982.00	1037.00	1237.00	2174.00	1329.00
Sr	581.30	641.20	557.00	540.20	636.10	690.80	668.90	665.50
Pb	0.70	2.60	3.60	3.70	3.00	2.20	3.10	2.10
Th	10.70	12.50	12.50	11.50	12.90	5.60	6.60	6.40
U	4.50	1.90	3.10	3.10	2.20	3.00	2.90	3.40
Zr	484.10	210.00	171.70	172.60	209.60	236.60	229.20	227.10
Hf	14.50	5.20	4.40	4.60	5.20	5.20	5.50	5.50
Ta	1.70	1.20	0.90	0.90	1.30	4.10	4.00	4.00
Y	22.10	28.80	23.80	23.90	28.60	24.80	23.90	24.00
Nb	29.80	20.30	16.30	16.00	20.30	71.60	69.50	68.00
Sc	17.00	20.00	22.00	21.00	20.00	15.00	15.00	15.00
Cr	273.70	177.91	287.39	287.39	177.91	61.58	61.58	54.74
Ni	91.40	59.20	102.00	105.80	53.10	44.70	45.10	44.50
Co	35.10	36.80	37.80	35.20	31.00	50.10	42.00	43.30
V	158.00	153.00	175.00	170.00	148.00	177.00	183.00	173.00
La	50.10	42.40	37.10	36.90	42.10	37.40	36.50	35.90
Ce	109.10	78.90	72.20	72.30	79.80	71.60	69.80	70.00
Pr	14.45	9.50	8.42	8.44	9.50	8.46	8.43	8.38
Nd	58.40	37.30	33.00	32.50	38.00	33.70	33.50	33.90
Sm	9.47	6.73	5.88	5.97	6.67	6.70	6.58	6.77
Eu	2.08	1.64	1.52	1.49	1.63	2.06	1.95	1.93
Gd	6.38	5.79	5.11	5.19	5.82	5.92	5.91	5.85
Tb	0.85	0.91	0.80	0.80	0.90	0.93	0.94	0.94
Dy	4.31	4.85	4.20	4.21	4.93	4.85	4.58	4.51
Ho	0.75	0.97	0.85	0.85	0.99	0.82	0.81	0.82
Er	1.99	2.75	2.35	2.39	2.83	2.28	2.31	2.17
Tm	0.29	0.44	0.36	0.35	0.41	0.32	0.33	0.34
Yb	1.89	2.62	2.17	2.22	2.52	2.07	1.98	2.03
Lu	0.28	0.40	0.35	0.34	0.40	0.28	0.28	0.28

Sample	729	520-1	520-2	520-3
Unit	Taşokçular basalt	Kabaklar basalt	Kabaklar basalt	Kabaklar basalt
Classification	Shoshonite	K-trachybasalt	K-trachybasalt	K-trachybasalt
Affinity	HK	HK	HK	HK
Region	Demirci	Selendi	Selendi	Selendi
AGE	LM	LM	LM	LM
References	1	2	2	2
SiO_2	49.54	47.85	49.14	48.78
Al_2O_3	16.63	15.34	14.98	15.40
Fe_2O_3	8.42	9.59	8.97	9.13
MgO	3.93	7.61	8.24	8.31
CaO	7.55	9.84	8.73	8.51
Na_2O	4.07	3.35	3.20	3.45
K_2O	2.92	2.28	2.36	2.41
TiO_2	2.22	1.79	1.62	1.66
P_2O_5	0.68	0.66	0.58	0.58
MnO	0.13	0.13	0.12	0.12
LOI	3.60	1.30	1.80	1.40
Mg#	48.05	61.12	64.54	64.33
Cs	7.00	1.50	2.40	2.60
Rb	67.40	51.60	58.00	57.80
Ba	817.00	888.60	888.80	849.70
Sr	673.90	993.90	882.00	886.50
Pb	3.40	4.60	5.40	5.10
Th	6.00	12.30	10.10	11.90
U	2.60	2.10	2.20	1.90
Zr	232.00	206.50	206.60	211.20
Hf	5.30	5.40	4.80	5.60
Ta	3.90	2.50	2.70	2.60
Y	24.10	27.10	25.40	25.80
Nb	68.80	35.90	40.30	42.00
Sc	15.00	0.39	21.00	21.00
Cr	61.58			
Ni	38.50	112.00	192.00	192.00
Co	38.40	71.40	76.40	90.40
V	180.00	211.00	190.00	192.00
La	35.70	56.50	52.40	53.50
Ce	69.10	109.10	100.00	103.80
Pr	8.27	13.00	11.90	11.86
Nd	33.90	49.50	42.90	44.00
Sm	6.82	8.40	8.00	7.70
Eu	1.97	2.55	2.28	2.15
Gd	5.95	6.81	6.01	6.38
Tb	0.89	0.97	1.04	0.97
Dy	4.53	5.00	4.69	4.73
Ho	0.86	0.91	0.85	0.88
Er	2.16	2.58	2.43	2.52
Tm	0.32	0.39	0.41	0.34
Yb	1.95	1.85	2.37	2.02
Lu	0.28	0.32	0.32	0.34

CA: calc-alkaline; HK: high-potassic; MK: medium-potassic; SHO: shoshonitic; UK: ultrapotassic; L: lamproitic.
EM: early Miocene; MM: middle Miocene; LM: late Miocene.